

Experimental Investigation of Mass Flow Rate and Pressure-drop through Rupture Disk Devices with Compressible Two-Phase Flow

Vom Fachbereich Maschinenbau und Verfahrenstechnik
der Universität Kaiserslautern
zur Verleihung des akademischen Grades

Doktor-Ingenieur (Dr.-Ing.)

genehmigte

Dissertation

von

Dipl.-Ing. Mondie Kimandi Mutegi
aus Meru, Kenia

Eingereicht am: 18.11.2019

Mündliche Prüfung am: 03.06.2020

Promotionskommission

Vorsitzender: Prof. Dr.-Ing. Hans Hasse

Berichterstatter: Prof. Dr.-Ing. Jürgen Schmidt

Prof. Dr.-Ing. Jens Denecke

Prof. Dipl.-Ing. Dr. techn. Hans-Jörg Bart

Dekan: Prof. Dr.-Ing. Tilmann Beck

D 386

2020

To my parents,
my siblings,
and
my family of friends,
for their patience and support.

In loving memory of
my father.

This research work was carried out during my stay as a research scientist at the CSE Center of Safety Excellence gGmbH (CSE-Institut), managed by Prof. Dr.-Ing. Jürgen Schmidt and Prof. Dr.-Ing. Jens Denecke, and as an external Ph.D student at the Department of Separation Science and Technology of the University of Kaiserslautern, chaired by Prof. Dipl.-Ing. Dr. techn. Hans-Jörg Bart, from year 2015 to 2019.

The dedicated support by my supervisor, Prof. Dr.-Ing. Jürgen Schmidt has been forthcoming and invaluable. I highly appreciate equally detailed insights and guidance by Prof. Dr.-Ing. Jens Denecke of the Karlsruhe University of Applied Sciences. I remain indebted to all the professors mentioned herein for the opportunity and responsibility given to me to undertake this complex Ph.D study titled “Experimental Investigation of Mass Flow Rate and Pressure-drop through Rupture Disk Devices with Compressible Two-Phase Flow.” The goal of this research work is to improve rupture disk sizing procedures to make our future industries safer.

Special thanks to REMBE® GmbH Safety + Control GmbH, Brilon, Germany for fully supporting me, always, and facilitating the research project. Together with the colleagues at Fraunhofer Institute for Chemical Technology ICT, Pfinztal Germany, and CSE-Institut, you gave valuable technical support which was instrumental in planning and realization of experiments. I humbly applaud all other industrial partners who were involved in the realization of the industry-scale test facility.

I particularly thank my father (departed) and my mother, for their precious and decisive lessons in life, my siblings for inspiring and believing in me and my family of friends for being patient and supportive all the time.

Kaiserslautern, November 2019
Mondie Kimandi Mutegi

The Directive 97/23/EC of the European Parliament and of the Council of 29 May 1997 on the approximation of the laws of the Member States concerning pressure equipment (European Commission, 1997) is the basis of the legal framework for protection of pressure equipment within the European Union. Codes and standards are useful to comply with the legal and regulatory responsibilities stipulated in PED Directive regarding the protection of pressure equipment against overpressure, sizing, and selection safety relief devices.

Rupture disk devices are primary relief devices to protect vessels, pipe, and equipment against overpressure. A rupture disk bursts once the so-called burst pressure is reached in the protected system, thereby discharging flow and preventing further increase in pressure. Currently, rupture disks are sized with standards and codes assuming the worst-case scenario at burst pressure. There is however no standardized procedure for sizing rupture disks with two-phase flow and there lacks suited test-facilities, test-sections, and reliable experimental data for model validation. Sizing rupture disk vent-line systems with current characteristic numbers comes with significant uncertainties, especially for high-velocity compressible flows (Schmidt, 2015).

Zero-Emission and Green Safety are current trends for organizations that seek to attain innovative protection concepts beyond regulatory compliance. A procedure to size a rupture disk vent-line should accurately determine the discharge rate and pressure-drop across a rupture disk, from the point of rupture disk activation to the point when the system depressurizes fully. This procedure is critical for further safety considerations, such as for modeling the dispersion of toxic gases released during emergency-relief and calculating the emissions to the environment with time.

Over-dimensioning is one measure taken today to mitigate uncertainties encountered while sizing with current methods. This is not always an option, as over-dimensioning the rupture disk vent-line system leads to unnecessary financial costs. It may also cause malfunction of the collecting systems downstream when the fluids discharged are more than the design limits. Emissions to the environment are thereby potentially higher than necessary, causing excessive harm to the environment. Under-dimensioning, on the other hand, may lead to hazardous incidents with loss of human life and equipment. This work has therefore focused on the investigation of the mass flow rate and pressure-drop through rupture disk devices with compressible gas and two-phase flow.

The experimental focus was in the design, construction, and commissioning of a high-capacity, high-pressure industry-scale test facility for testing small- to large-diameter rupture disks and other fittings with gas flow. The resulting test facility is suited to test safety devices and pipe fittings at near realistic flow conditions at pressures up to 150 bar. This work also presents the design of a pilot plant for testing rupture disks with air/water two-phase flow. These test facilities open-up new frontiers for capacity testing because they have precise and state-of-the-art measurement and instrumentation. Experimental results from these facilities deliver reliable experimental data to validate proposed sizing procedures for rupture disk devices.

The theoretical focus was on the development of a reliable rupture disk sizing procedure for compressible gas and two-phase flow. This required phenomenological studies of flow through rupture disks with both experiments and CFD studies. Better suited rupture disk characteristic numbers and model parameters for determining the mass flow rate and pressure-drop across rupture disks are identified. The proposed sizing procedure with compressible gas and two-phase flow predicts the dischargeable mass flow rate and pressure-drop across a rupture disk within ± 4 % of measured value. Experimental validation has been undertaken with different types of rupture disks. The procedure is suited for determine the mass flow rate and pressure-drop through rupture disk seamlessly, from the point of rupture disk activation (worst-case scenario) to the point when the system fully depressurizes beyond regulatory compliance.

Der Rechtsrahmen für den Schutz von Druckgeräten in der Europäischen Union basiert auf der Richtlinie 97/23/EG des Europäischen Parlaments und des Rates vom 29. Mai 1997 zur Angleichung der Rechtsvorschriften der Mitgliedstaaten über Druckgeräte (European Commission, 1997). Regelwerke sind nützlich, um die gesetzlichen Verpflichtungen der PED-Richtlinie zum Schutz von Druckgeräten gegen Überdruck, zur Auslegung und Auswahl von Sicherheitseinrichtungen zu erfüllen.

Berstscheibe sind primäre Entlastungsvorrichtungen um Behälter, Rohre und Rohreinbauten vor Überdruck zu schützen. Eine Berstscheibe platzt, wenn der so genannte Berstdruck im geschützten System erreicht ist, wodurch die Strömung abgeführt und ein weiterer Druckanstieg verhindert wird. Derzeit werden Berstscheibe mit Regelwerken ausgelegt, die den schlimmsten Fall (Worst-Case) bei Berstdruck annehmen. Es gibt jedoch kein standardisiertes Verfahren zur Auslegung von Berstscheibe bei Zweiphasenströmung und es fehlen geeignete Prüfeinrichtungen, Prüfrecken und zuverlässige experimentelle Daten für die Modelvalidierung. Die Auslegung von Berstscheibe mit aktuellen Kennzahlen ist mit großen Unsicherheiten behaftet, insbesondere bei kompressiblen Hochgeschwindigkeitsströmungen (Schmidt, 2015).

Zero-Emission und Green Safety sind heute Zukunftstrends für Unternehmen, die innovative Schutzkonzepte über die Einhaltung gesetzlicher Vorschriften hinaus anstreben. Ein Verfahren zur Auslegung einer Berstscheibe sollte die Durchflussrate und den Druckabfall über eine Berstscheibe vom Zeitpunkt der Berstscheibenaktivierung bis zum Zeitpunkt der vollständigen Druckentlastung des Systems genau bestimmen. Dies ist entscheidend für weitere Sicherheitsüberlegungen wie die Modellierung der Ausbreitung von toxischen Gasen, die bei der Notfallentspannung freigesetzt werden, und die Berechnung der Emissionen in die Umwelt mit der Zeit.

Die Überdimensionierung ist eine der Maßnahmen, die heute ergriffen werden um die Unsicherheiten zu verringern die bei der Auslegung mit aktuellen Methoden auftreten. Dies ist nicht immer möglich, da eine Überdimensionierung des Berstscheiben-Entlastungssystems zu unnötigen Kosten führt und zu Fehlfunktionen der nachgeschalteten Sammelsysteme führen kann, wenn die abgeleiteten Medien die zulässigen Grenzwerte überschreiten. Die Emissionen in die Umwelt sind dabei potenziell höher als notwendig und verursachen einen unverhältnismäßigen Schaden für die Umwelt. Unterdimensionierung hingegen kann zu gefährlichen Vorfällen mit Verlust von Menschenleben und Geräten führen. Diese Arbeit hat sich daher auf die Untersuchung des Massenstroms und des Druckabfalls durch Berstscheibe mit kompressiblem Gas und Zweiphasenströmung befasst.

Der experimentelle Schwerpunkt lag in der Planung, dem Bau und der Inbetriebnahme einer leistungsfähigen Hochdruck-Industrieprüfanlage zur Prüfung von Berstscheiben mit kleinem bis große Durchmesser (DN150) und anderen gasführenden Armaturen. Der daraus resultierende Prüfstand eignet sich für die Prüfung von Sicherheitseinrichtungen und Rohrformstücken bei nahezu realistischen Strömungsverhältnissen und Drücken bis 150 bar. Außerdem wird das Konzept einer Pilotanlage zur Prüfung von Berstscheiben mit Luft-/Wasser-Zweiphasenströmung vorgestellt. Diese Prüfeinrichtungen eröffnen neue Grenzen für die Bauteilprüfung, da sie mit präziser und hochmoderner Mess- und Regeltechnik ausgestattet sind. Experimentelle Ergebnisse aus diesen Prüfeinrichtungen werden verwendet, um zuverlässige experimentelle Daten zu liefern und die vorgeschlagenen Auslegungsverfahren für Berstscheibe zu validieren.

Der theoretische Schwerpunkt lag in der Entwicklung eines zuverlässigen Berstscheibenauslegungsverfahrens für kompressible Gase und Zweiphasenströmungen. Dazu wurden phänomenologische Untersuchungen der Strömung durch Berstscheiben sowohl mit Experimenten als auch mit CFD-Studien durchgeführt. Besser geeignete Kennzahlen und Modelparameter zur Bestimmung des Massenstroms und des Druckabfalls wurden beschrieben. Die experimentelle Validierung des vorgeschlagenen Auslegungsverfahrens mit kompressiblem Gas und Zweiphasenströmung zeigt, dass das Verfahren den Massenstrom und Druckabfall über eine Berstscheibe innerhalb von ± 4 % des Messwertes vorhersagt. Das Auslegungsverfahren eignet sich zur Bestimmung des Massenstroms und des Druckabfalls durch die Berstscheibe vom Zeitpunkt der Aktivierung der Berstscheibe (Worst-Case-Szenario) bis zum Zeitpunkt der vollständigen Druckentlastung des Systems – dies geht über die Einhaltung der Vorschriften hinaus.

Dedication	ii
Preface	iii
Abstract	iv
Kurzfassung	v
Contents	vi
List of Figures	ix
List of Tables	xii
Nomenclature	xiv
Latin symbols	xiv
Greek symbols	xv
Dimensionless numbers	xv
Abbreviations	xv
Subscripts	xvi
Superscripts	xvii
1 Introduction and problem	1
2 Aim and methodology	3
3 State of knowledge for sizing rupture disk devices	4
3.1 Dischargeable mass flow rate	5
3.1.1 Free relieving area	6
3.2 Pressure-drop in vent-lines with rupture disk installed	6
3.2.1 Pressure-drop across a rupture disk with gas flow	7
3.2.2 Pressure-drop across a rupture disk with two-phase flow	8
3.2.3 Pressure-drop in an adiabatic straight pipe with gas flow (Fanno flow)	9
3.2.4 Pressure-drop in an adiabatic straight pipe with two-phase flow	10
3.3 Definition of gap in research	12
3.3.1 Summary	14
4 Design, construction and commissioning 150 bar loop	15
4.1 Specification of target measurement range	16
4.2 Design of buffer vessels using demand and capacity analysis	17
4.3 Design of the compression and gas conditioning unit	20
4.4 Design of flow rate measurement and pressure regulation unit	23
4.5 Design of the two-phase rig	24
4.6 Process and Instrumentation Diagram (PID) of the 150 bar loop	24
4.6.1 Buffer tank unit in zone 100	24
4.6.2 Compression and gas processing unit in zone 200	26

4.6.3	Flow measurement and pressure regulation unit in zone 300.....	28
4.6.4	Two-phase rig in zone 400.....	29
4.6.5	Test vessel unit in zone 1000.....	30
4.6.6	Process and Instrumentation Diagram of the 150 bar loop.....	31
4.7	Process Hazard Analysis and Safety Concept of the 150 bar loop.....	32
4.8	Operation manual of 150 bar gas rig.....	32
4.9	Rupture disk test section with measurement and instrumentation.....	33
4.10	Laboratory-scale gas pilot plant for test with air.....	36
4.11	Laboratory-scale two-phase pilot rig for tests with air/water.....	37
5	Development of a sizing procedure for rupture disk devices.....	39
5.1	Visualization of flow through a rupture disk with experiments and CFD.....	39
5.1.1	Visualization of flow with experiments.....	39
5.1.2	Visualization with CFD simulations.....	41
5.2	Modeling of dischargeable mass flow rate across a rupture disk device.....	44
5.2.1	Model representation for flow through a rupture disk.....	44
5.2.2	Method to determine dischargeable mass flow rate with gas flow.....	45
5.2.3	On the dischargeable mass flow rate with two-phase flow.....	52
5.3	Modeling of pressure-drop across a rupture disk device.....	54
5.3.1	Method to determine the pressure-drop with gas flow – CMLC-Theory.....	54
5.3.2	Method to determine pressure-drop with two-phase flow.....	60
5.4	Recommended working equations for liquids, gases and two-phase flow.....	63
5.4.1	The general equation for the rupture disk dischargeable mass flow rate.....	63
5.4.2	The general equation for rupture disk compressible pressure-drop.....	63
6	Experimental validation of a sizing procedure for rupture disk devices.....	64
6.1	Experimental validation of the dischargeable mass flow rate model.....	64
6.1.1	Determination of rupture disk free relieving area with a low-velocity flow.....	64
6.1.2	Prediction of dischargeable mass flow rate with gas flow.....	70
6.1.3	Prediction of dischargeable mass flow rate for two-phase flow.....	82
6.2	Experimental validation of pressure-drop model.....	83
6.2.1	Determination of rupture disk zero-velocity minor loss coefficient, $K_{RD,0}$	83
6.2.2	Prediction of pressure profile in a rupture disk with CMLC theory.....	86
6.2.3	Determination of rupture disk two-phase minor loss coefficient $K_{RD,0,tp}$	93
6.2.4	Prediction of the downstream pressure with a high gas mass flow quality experiment.....	95
7	Conclusion and summary.....	100
8	Bibliography.....	102
9	Annex.....	106
	ANNEX I Dischargeable mass flow rate across a rupture disk device.....	107
	ANNEX II Measurement range of flow measurement unit with $U < 0.5\%$ o.r.....	108

ANNEX III The main components in zone 100	109
ANNEX IV The main components in zone 200.....	110
ANNEX V The main components in zone 300	111
ANNEX VI The main components in zone 400.....	111
ANNEX VII The main components in zone 1000.....	112
ANNEX VIII Process Hazard Analysis of the 150 bar loop	113
ANNEX IX Operation manual for 150 bar gas rig.....	118
ANNEX X Illustration of arrangement for visualization of flow with experiments	123
ANNEX XI Model selected for CFD modelling.....	124
ANNEX XII DN40 pipe roughness measurement results	125
ANNEX XIII DN25 pipe roughness measurement results	128
ANNEX XIV Calibration certificate for Ethernet Intelligent Pressure NetScanner 9116.....	131
ANNEX XV Calibration certificate for Mensor absolute pressure sensor	146
ANNEX XVI Calibration certificate for DN50 Coriolis flowmeter	151
ANNEX XVII Calibration certificate for DN525 Coriolis flowmeter	152
ANNEX XVIII Equations for the proposed method to determine the rupture disk discharge area.....	153
ANNEX XIX The derivation of the dischargeable mass flow rate relationship with gas flow	154
ANNEX XX Recommendations for rupture disk performance testing.....	158
ANNEX XXI Calculation of the gas void fraction in Mathcad.....	159
Publications and conferences	161
Curriculum vitae	162

Figure 1 a. Illustration of a rupture disk installed into a rupture disc holder installation between flanges in a vent-line. b. & c. Two open restrictive rupture disk devices show the complex cross-section of the rupture disk free relieving area, A_{RD} , which is typically not circular.....	2
Figure 2: Closed and burst forward-acting rupture disk device (Schmidt, 2016).....	6
Figure 3 a. Illustration showing the real and model pressure profile with ΔP_{RD} . b. Static pressure profile in the centerline of a sudden pipe contraction measured in a two-phase air/water flow (Schmidt, 1993).....	7
Figure 4 Rupture disk test section	8
Figure 5: Control volume assuming a straight pipe with a constant cross-section according to (Shapiro, 1953)	9
Figure 6 The three stages of the CSE HP loop for tests with air, water and air/water two-phase flow at pressures up to 3000 bar.	15
Figure 7 Block diagram showing the main components of the 150 bar loop covering an area of 1000 m ²	15
Figure 8: Target measurement range of 150 bar rig with data in Table 5.	16
Figure 9: Attainable capacity with B-01 through B-05 with an experiment time of 60 seconds.	17
Figure 10: Attainable capacity with B-01 through B-05 with an experiment time of 300 seconds.....	17
Figure 11: Isentropic drop in temperature while discharging from pressures below 3400 bar.	18
Figure 12: Isentropic drop in temperature while discharging from pressures below 300 bar.	18
Figure 13: Capacity with B-06 and B-07 with experiment time of 60 seconds.	19
Figure 14: Capacity with B-06 and B-07 with an experiment time of 300 seconds.....	19
Figure 15: RCPI comparison of the 13 piston compressors [-].	22
Figure 16: RCPI comparison of 4 screw compressors [-].	22
Figure 17: Measurement range of flow measurement unit with $U < 0.5\%$ o.r. with data in Table 41 through Table 44.....	23
Figure 18: PID of buffer vessels in zone 100 covering an area of about 310 m ²	25
Figure 19 Images of selected components in zone 100.	25
Figure 20: PID of compression and gas processing in zone 200, covering an area of about 50 m ²	27
Figure 21 Images of selected components in zone 200	27
Figure 22: PID of flow measurement and pressure regulation in zone 300, covering an area of about 100 m ²	28
Figure 23 Images of selected components in zone 300.	28
Figure 24 PID of the two-phase rig for tests with air/water at pressure up to 16 bar covering an area of about 100 m ²	29
Figure 25: PID of the test vessel with test benches in zone 1000 covering an area of about 70 m ²	30
Figure 26 Images of selected components in zone 1000.	30
Figure 27: PID of the 150 bar loop covering an area of about 800 m ²	31
Figure 28: Rupture disk test section parts.	33
Figure 29: Rupture disk test section measurement and instrumentation.	35
Figure 30: General overview of laboratory-scale gas pilot plant for test with air.	36
Figure 31: Layout of the two-phase flow pilot rig for tests with air/water up to 10 bar.....	38
Figure 32 Continous line showing the measured static pressure at the center of pipe with a rupture disk installed with the points showing the pressure measured with the wall pressure taps (see also: Figure 28).40	40
Figure 33 Zoom of Figure 32 showing the position of the point with the lowest static pressure near the rupture disk.....	40
Figure 34: Open rupture disk device.	42
Figure 35: Black oxidization to make surface non-reflective.	42
Figure 36: 3D-Laser scanning courtesy of Karlsruhe University of Applied Sciences.	42
Figure 37: Raw data as point cloud from 3D Scanner.....	42
Figure 38: zoom of Figure 37 showing the detailed point cloud.....	42
Figure 39: Surface model generated after triangulation.....	42
Figure 40: Arrows pointing to surface errors in the surface model.	42

Figure 41: Enlarged surface errors after extrusion of the surface by 1 mm	42
Figure 42: Realistic 3D model of rupture disk in Figure 34.	42
Figure 43: Angular perspective view of an open rupture disk with various reference locations.	42
Figure 44 Back-view of an open rupture disk device at reference locations (u), (RD), (r), (*) and (out).....	43
Figure 45: The static pressure computed with the digitalized image of the rupture disk in Figure 42 in a pipe; the static pressure along the pipe axis calculated with a CFD code is plotted.	43
Figure 46 Illustration a control volume assuming a near-circular bore with large area ratio	45
Figure 47: Partial plot of Figure 32 shows the measured static pressure in the middle of a pipe with the rupture disk installed with low-velocity flow with $P_b=100$ mbar.g.	47
Figure 48: C_d per eq.(A-11) as a function of β_{eff} for a range of Re_u	51
Figure 49: K_R per eq.(A-12) as a function of β_{eff} for a range of Re_u	51
Figure 50 Deviation of compressible minor loss coefficient factor, F_g per eq.(49) from eq.(50) for upstream Mach number, $Ma_u < 1.0$ and $\kappa=1.4$	55
Figure 51: Illustration of the key-points, that will be referred to below.....	55
Figure 52 General overview of the computation algorithm for calculating pressure-drop across a rupture disk device.	56
Figure 53 Validation of $K_{RD,0} = \text{const}$ assumption in eq.(53) with L_d per eq.(55) and λ_{av} per eq.(57).	57
Figure 54 Geometry of test objects tested. a. circular bores made of one segment. b. segmental bores made of two segments.....	65
Figure 55 Plot of experimental data in Table 18, with $\beta_{bore}=0.80$ showing pressure in taps $P_{tap,01}$ through $P_{tap,11}$ with test object downstream of $P_{tap,04}$	65
Figure 56 Results for diameter ratio, β_{eff} for DN40 circular and segmental bores per eq.(40) a. DN40 circular bore b. DN40 segmental bore calculated with $\bullet \Omega_{nom}$, $\blacktriangledown \Omega_{min}$ and $\blacktriangle \Omega_{max}$	67
Figure 57 Results for diameter ratio, β_{eff} for DN25 circular and segmental bores per eq.(40) a. DN25 circular bore b. DN25 segmental bore calculated with $\bullet \Omega_{nom}$, $\blacktriangledown \Omega_{min}$ and $\blacktriangle \Omega_{max}$	68
Figure 58: Plots of Ma_{RD} and Ma_r per eq. (29) and Φ per eq.(34), against Ma_u for low- and high-velocity flow with TS0102 DN40.	73
Figure 59: Plots of $\eta_{RD,0}$ and $\eta_{r,0}$ per eq. (38), Φ per eq.(34) against Ma_u for low- and high-velocity flow with TS0102 DN40.	73
Figure 60: Plots of $C_{m,RD}$ and $C_{m,r}$ per eq.(36) and Φ per eq.(34), against $\eta_{RD,0}$ for low- and high-velocity flow with TS0102 DN40.	74
Figure 61: Deviation of predicted mass flow rate $\delta Q_{m,API}$ per eq.(1) and $\delta Q_{m,RD}$ and $\delta Q_{m,r}$ per eq.(27) for low- and high-velocity flow with TS0102 DN40.	74
Figure 62: Plots of Ma_{RD} and Ma_r per eq.(29), Φ per eq.(34), against Ma_u for low- and high-velocity flow with TS0202 DN40.	75
Figure 63: Plots of $\eta_{RD,0}$ and $\eta_{r,0}$ per eq.(38), Φ per eq.(34) against Ma_u for low- and high-velocity flow with TS0202 DN40.	75
Figure 64: Plots of $C_{m,RD}$ and $C_{m,r}$ per eq.(36) and Φ per eq.(34), against $\eta_{RD,0}$ for low- and high-velocity flow with TS0202 DN40.	76
Figure 65: Deviation of predicted mass flow rate $\delta Q_{m,API}$ per eq.(1) and $\delta Q_{m,RD}$ and $\delta Q_{m,r}$ per eq.(27) for low- and high-velocity flow with TS0202 DN40.	76
Figure 66: Plots of Ma_{RD} and Ma_r per eq. (29), Φ per eq.(34), against Ma_u for low- and high-velocity flow with TS0302 DN40.	77
Figure 67: Plots of $\eta_{RD,0}$ and $\eta_{r,0}$ per eq. (38), Φ per eq.(34), against Ma_u for low- and high-velocity flow with TS0302 DN40.	77
Figure 68: Plots of $C_{m,RD}$ and $C_{m,r}$ per eq.(36) and Φ per eq.(34), against $\eta_{RD,0}$ for low- and high-velocity flow with TS0302 DN40.	78
Figure 69: Deviation of predicted mass flow rate $\delta Q_{m,API}$ per eq.(1) and $\delta Q_{m,RD}$ and $\delta Q_{m,r}$ per eq.(27) for low- and high-velocity flow with TS0302 DN40.	78

Figure 70: Plots of $C_{m,RD}$ per eq.(36) against Ma_u showing the $Ma_{u,theo}$ for given upstream conditions for the $P_u \approx 2.3$ bar.a. experiment with rupture disk TS0302. $Q_{m,theo}$ is calculated with $M_{au,theo}$ per eq.(35) and eq.(62)	80
Figure 71: Plots of $C_{m,RD}$ per eq.(36) against $\eta_{RD,0}$ per eq.(38) showing the $\eta_{RD,0} \approx 0.527$ for $Ma_{u,theo} = 0.404$ for given upstream conditions for the $P_u \approx 2.3$ bar.a. experiment with rupture disk TS0302. $Q_{m,theo}$ is calculated with $M_{au,theo}$ per eq.(35) and eq.(62)	80
Figure 72: Process for determining $K_{RD,0}$	85
Figure 73: Pressure ratio profile of a low-velocity experiment for TS0102 with the data in Table 31	85
Figure 74: Predicted pressure profile for TS0102 with low-velocity flow with data in Table 31 with $\Delta P_{RD,g}$ per eq.(61)	87
Figure 75: Predicted pressure profile for TS0102 with high-velocity flow with data in Table 32 with $\Delta P_{RD,g}$ per eq.(61)	87
Figure 76: Predicted pressure profile for TS0102 with low-velocity flow with equations in literature with data in Table 31 with $\Delta P_{RD,lit}$ per eq.(5)	88
Figure 77: Predicted pressure profile for TS0102 with high-velocity flow with equations in literature with data in Table 34 with $\Delta P_{RD,lit}$ per eq.(5)	88
Figure 78 Ratio of effective rupture disk effective length, L_d per eq.(55) to rupture disk zero-velocity length, $L_{RD,0}$ with varying upstream Mach number, Ma_u . HV refers to calculation with high-velocity experimental data in Table 32	89
Figure 79: Rupture disk compressible minor loss coefficient, $K_{RD,g}$ per eq.(60) plotted against Ma_u . HV refers to calculation with high-velocity experimental data in Table 32	89
Figure 80: Calculated pipe loss coefficients: $K_{RD,0}$ per eq.(53), $K_{RD,g}$ per eq.(60) with $F_{g,av}$ for a range of upstream Mach number Ma_u	91
Figure 81: Parity plot of $\Delta P_{RD,g}$ per eq.(51) and $\Delta P_{RD,g}$ per eq.(61)	92
Figure 82: Parity plot of $\Delta P_{RD,g}$ per eq.(51) and $\Delta P_{RD,lit}$ per eq.(5)	92
Figure 83: Plot of $P_i/P_{tap,01}$ against L/D_i from a low gas mass flow quality experiment with TS0102 DN40.	94
Figure 84: Raw data with TS0102 with two-phase flow with a count of 4276 data points with $0.10 < x_g < 0.90$	97
Figure 85: Zoom in of raw data with TS0102 with two-phase flow showing stationary, quasi-stationary and transient flow	97
Figure 86: Raw data with TS0202 with two-phase flow with a count of 3546 data points with $0.1 < x_g < 0.90$	98
Figure 87: Zoom in of raw data with TS0202 with two-phase flow showing stationary, quasi-stationary and transient flow	98
Figure 88: Deviation of the calculated pressure downstream $(P_d - P_{d,exp})/P_{d,exp}$ in % with P_d per eq.(89) to $P_{d,exp}$ for varying x_g with TS0102	99
Figure 89: Deviation of the calculated pressure downstream $(P_d - P_{d,exp})/P_{d,exp}$ in % with P_d per eq.(89) to $P_{d,exp}$ for varying x_g with TS0202	99
Figure 90: Decription of test arrangement to visualize flow with a rupture disk (Schmidt, 2016)	123
Figure 91: Decription of the selected models to visualize flow with CFD's	124
Figure 92: Illustration a control volume assuming a near-circular bore with large area ratio	154

Table 1 Five step-sizing procedure for rupture disk devices (Schmidt, 2015).....	1
Table 2 Target model parameters for two-phase flow in a rupture disk.....	4
Table 3 Advantages and disadvantages of different model representations for predicting pressure gradient with two-phase flow.....	4
Table 4 Test facility specified target measurement range for test objects.....	16
Table 5 Target measurement range of 150 bar rig.....	16
Table 6 Compressor Key Performance Indicators.....	20
Table 7 Piston compressor selection using color scales.....	20
Table 8 Screw compressor selection using color scales.....	20
Table 9 Specific Investment Cost Performance Indicator (CPI01).....	21
Table 10 Specific Investment Cost Performance Indicator (CPI02).....	21
Table 11 Specific Operational Cost Performance Indicator (CPI03).....	21
Table 12 Relative Cost Performance Indicator (RCPI).....	22
Table 13: Location of pressure taps in DN25 and DN40 test sections.....	34
Table 14 Components in two-phase air/water temporary test facility.....	37
Table 15 The variables and parameter to calculate the dischargeable mass flow rate per eq.(27) iteratively.....	45
Table 16 Equations for calculating the rupture disk flow restriction Φ per eq. (34) iteratively.....	47
Table 17 Determination of the $L_{d,tp}$ - function, $L_{d,tp}\{\chi\}$ in eq. (72).....	61
Table 18 Sample measured data set for a regular bore with measured diameter ratio $\beta_{geo}=0.80$ after fabrication for a DN40 test section with air.....	64
Table 19 Dimensions of test objects for validating the proposed method in mm. See also: Figure 54.....	66
Table 20 Measured data with a low-velocity experiment with TS0102 DN40 (II).....	69
Table 21 Measured data with a low-velocity experiment with TS0202 DN40 (III).....	69
Table 22 Measured data with a low-velocity experiment with TS0302 DN40 (IIII).....	70
Table 23 Results for σ_{RD} and A_{RD} determined with the method presented with eq.(40).....	70
Table 24 Measured data with a high-velocity experiment with TS0102 DN40 (II).....	70
Table 25 Measured data with a high-velocity experiment with TS0202 DN40 (III).....	71
Table 26 Measured data with a high-velocity experiment with TS0302 DN40 (IIII).....	71
Table 27 Measured experimental data for three rupture disk types under similar flow conditions.....	71
Table 28 Calculated properties for the experimental data of the three rupture disk types in Table 27.....	72
Table 29 Specified data for sizing a rupture disk vent-line.....	81
Table 30 Results for a rupture disk vent-line with the proposed method.....	81
Table 31: Sample measured data set for a low-velocity (LV) experiment with TS0102.....	83
Table 32: Sample measured data set for a high-velocity (HV) experiment with TS0102.....	84
Table 33 Determined properties for three rupture disk types under similar flow conditions with data in Table 24, Table 25, and Table 26.....	90
Table 34 Determined and calculated properties for the experimental data of the three rupture disk types in Table 33.....	90
Table 35: Sample measured data set for determining $K_{RD,0,tp}$ from a low gas mass flow quality experiment two-phase air/water flow experiment with TS0102.....	93
Table 36: Sample measured data set for determining $K_{RD,0,tp}$ from a low gas mass flow quality experiment two-phase air/water flow experiment with TS0202.....	93
Table 37 Determined and calculated properties for the experimental data of the three rupture disk types in Table 35.....	94
Table 38: Sample measured data set from a high gas mass flow quality experiment two-phase air/water flow experiment with TS0102.....	95
Table 39: Sample measured data set from a high gas mass flow quality experiment two-phase air/water flow experiment with TS0202.....	95

List of Tables

Table 40 Determined and calculated properties for the experimental data of the two rupture disk types in	96
Table 41 Measurement range of FI301 DN150	108
Table 42 Measurement range of FI302 DN80	108
Table 43 Measurement range of FI304 DN40	108
Table 44 Measurement range of FI304 DN25	108
Table 45 Components in Zone 100.....	109
Table 46 Components in Zone 200.....	110
Table 47 Components in Zone 300.....	111
Table 48 Components planned for Zone 400	111
Table 49 Components in Zone 1000	112
Table 50 PHA and Safety concept for zone 100 with SV101 and SV151(solar radiation case)	113
Table 51 PHA and Safety Concept for zone 200 with SV252 (compressor or valve malfunction at V253 case)	113
Table 52 PHA and Safety Concept for zone 200 with SV254 (leakage V254 case)	114
Table 53 PHA and Safety Concept for zone 200 with SV254 (operating error V254 case)	115
Table 54 PHA and Safety Concept for zone 300 with SV301 (Leakage CV301 and CV302)	116
Table 55 PHA and Safety Concept for zone 300 with BS301(Malfunction CV301 and CV302)	116

Latin symbols

Symbol	Name	Unit
A	Area	m ²
C _C	Contraction coefficient	-
C _d	Discharge coefficient	-
C _m	Dimensionless mass flow rate per eq.(36)	-
c _p	Specific heat at constant pressure	(kg·m ²)/(K·s ²)
c _s	Sonic velocity of fluid for given conditions	m/s
c _v	Specific heat at constant volume	(kg·m ²)/(K·s ²)
D	Inner diameter of pipe	m
E _{cost}	Cost of energy	kW/hr
F _g	Rupture disk compressibility factor with gas flow per eq.(49) or eq.(50)	-
F _{tp}	Rupture disk compressibility factor with two-phase flow per eq.(81)	-
G	Mass flux	kg/(s·m ²)
g	Acceleration due to gravity	m/s ²
h	Specific enthalpy	kJ/(kg·K)
H	Height	m
K	Loss coefficient	-
K _{RD,0}	Rupture disk zero-velocity minor loss coefficient	-
K _R	Rupture disk loss coefficient per eq.(6)	-
k _s	Pipe roughness of pipe on the inner surface	m
K _U	Uncertainty correction factor in eq. eq.(1)	-
L	Length in horizontal axis	m
L _{RD,0}	Rupture disk zero-velocity length	m
M _m	Molar mass	kg/mol
P	Pressure	Pa
Q _m	Mass flow rate	kg/s
R	Universal gas constant with R= 8.314 459 8 (kg·m ²)/(s ² ·mol·K)	(kg·m ²)/(s ² ·mol·K)
R _Z	Average maximum height of the profile	m
T	Temperature	K
U	Uncertainty of measurement of respective parameter	-
U _{friction}	Superficial velocity friction quotient per eq.(75)	-
U _s	Superficial velocity	m/s
V	Volume	m ³
w	Velocity	m/s
x _g	Gas quality	-
z	Position in horizontal axis	-
Z	Real gas compressibility factor	-

Greek symbols

Symbol	Name	Unit
β	Diameter ratio with $\beta=d/D$	-
δ	Percent deviation of a variable y from variable x with $\delta=100 \cdot (y-x)/x$	%
Δ	Referring to change of thermodynamic property between two points	-
ε	Void fraction	-
η	Pressure ratio	-
η_C	Viscosity correction factor per (Darby, 2004)	-
κ	Ratio of specific heat $\kappa = c_p/c_v$	-
λ	Darcy friction factor	-
μ	Dynamic viscosity	Pa·s
ν	Specific volume of fluid with $\nu=1/\rho$	m ³ /kg
ω	Omega parameter per eq.(4)	-
ϕ	Rupture disk flow restriction per eq.(34)	-
ρ	Density	kg/m ³
σ	Rupture disk area ratio	-
τ	Shear stress	Pa
θ	Angle of inclination	°
ν	Kinematic viscosity with $\nu=\mu/\rho$	m ² /s

Dimensionless numbers

Symbol	Name	Unit
Ma	Mach-number	-
Re	Reynolds number with $Re=w \cdot D/\nu$	-

Abbreviations

Symbol	Name	Unit
CFD	Computational fluid dynamics	-
CMLC	Rupture disk compressible minor loss coefficient	-
CPI	Cost-Performance-Indicator per chapter 4.3	-
CSE	Referring to the CSE Center of Safety Excellence gGmbH (CSE-Institut)	-
CV	Control Valve	-
DB	Referring to a property from a thermodynamic fluid properties database	-
DP	Referring to design pressure	-
HAZOP	Hazard and operability study	-
HP	High Pressure	-
HV	Referring to a high-velocity experiment	-
KPI	Key-Performance-Indicator per chapter 4.3	-
LV	Referring to a low-velocity flow experiment	-
MNFA	Minimum net flow area	-
PHA	Process hazard analysis	-
PID	Process and instrumentation diagram	-
RCPI	Relative cost performance indicator per chapter 4.3	-
RD	Rupture disk	-
RTD	Resistance temperature detector	-
SV	Safety relief valve	-
VC	Referring to the so called "Vena-Contracta"	-

Subscripts		
Symbol	Name	Unit
0	stagnation conditions	-
1	Conditions in inlet pipe segment	-
a	Ambient conditions	-
acceleration	Referring to changes caused by acceleration of fluid	-
API	Referring to the American Petroleum Institute	-
av	Referring to given averaged thermodynamic properties	-
b	Referring to measured conditions in a reservoir at so called "base conditions"	-
bore	Referring to a bore	-
c	Referring to a set constant gas fraction in eq.(85) and eq.(86)	-
calc	Referring to a calculated value	-
center	Referring to pressure measured at pipe center	-
cost	Referring to the cost of energy	-
d	Referring to the damping factor in eq.85 and eq.(86)	-
eff	Effective value	-
exp	Referring to a measured value	-
friction	Referring to changes caused by friction	-
g	Referring to gas phase	-
geo	Narrowest cross-section of a bore or rupture disk device	-
gravity	Referring to changes caused due to gravity	-
h	Referring to homogeneous thermodynamic property	-
HV	Referring to a high-velocity flow experiment	-
i	Referring to a reference point	-
in	Inlet	-
l	Referring to liquid phase	-
lit	Classic method with equations in literature per eq.(5)	-
LV	Referring to a low-velocity flow experiment	-
m	Referring to mass flow rate	-
max	Referring to maximum of measured values	-
min	Referring to minimum of measured values	-
nom	Referring to nominal measured values	-
nozzle	Referring to a nozzle	-
perfect	Referring to the perfect gas assumption	-
pipe	Referring to inner cross-section of a circular duct	-
r	Referring to rupture disk flow restricting area (r)	-
RD	Rupture disk or rupture disk installation plane	-
real	Referring to real gas assumption	-
s	Referring to the sonic velocity of a fluid	-
seat	Referring to seat diameter of a safety relief valve	-
sizing	Referring to the determined mass flow rate to be discharged	-
start	Referring to the pressure in vessel at the start of discharge	-
stop	Referring to the pressure in vessel at the stop of discharge	-
sum	Referring to the arithmetic sum	-
sys	Referring to a complex rupture disk relief line with all fittings installed	-
tap	Referring to measurement point for pressure or temperature	-
th	Referring to the smallest cross-section of a nozzle	-
theo	Referring to theoretical maximum attainable value	-
tp	Referring to two-phase flow	-
tp	Referring to two-phase flow	-
u	3 diameter lengths upstream of rupture disk	-
u-i	Referring to changes in a property value between (u) and (i)	-
wall	Referring to pressure or temperature measured at a wall	-

Superscripts

Symbol	Name	Unit
*	Referring to a point downstream of rupture disk per Figure 43	-
‡	Referring to the design limits regarding pressure and temperature	-

1 Introduction and problem

In the chemical and petrochemical industry, vessels and pipes are protected against overpressure using safety relief devices, usually rupture disks (also called bursting discs) or safety valves. Rupture disk devices are primary relief devices to protect vessels, pipe, and equipment against overpressure. The safety-related function of a rupture disk device is to limit the pressure to at most 110% of the permissible overpressure in the system or component to be protected (TÜV, 2006).

Once the so-called burst pressure is reached in the protected system, the rupture disk bursts discharging flow through the resulting discharge area, thereby preventing further increase in pressure. The maximum discharge rate prevails at burst pressure, and it reduces until the system fully depressurizes. The system, in this regard, includes the entire relief line with the rupture disk installation together with the inlet and outlet line. Fulfillment of this safety-related function reliably requires proper engineering fabrication, testing, sizing, selection, installation, commissioning, maintenance, and regular inspection (DECHEMA, 2018). Proper sizing of a rupture disk vent-line involves a five-step sizing procedure. This work focuses on Step 4 and Step 5 of the five-step sizing procedure in Table 1.

Table 1 Five step-sizing procedure for rupture disk devices (Schmidt, 2015)

Sizing step	Procedure
Step 1.	Risk analysis to identify the worst-case scenario and definition of sizing case.
Step 2.	Level swell calculation in the pressurized system to determine the flow regime at the entrance of the rupture disk vent line.
Step 3.	Energy and mass balance around the pressurized system to determine the minimum flow rate to be discharged.
Step 4.	Determination of the rupture disk and pipe size that meets the “dischargeable mass flow rate is larger than the minimum flow rate to be discharged” condition.
Step 5.	Detailed pressure-drop calculation in the entire rupture disk vent-line system to validate its capacity

An ideal rupture disk vent-line system has a rupture disk device installed directly on the pressurized system, at best with a short and no inflow line, or with a short outflow line discharging directly to the atmosphere. The law does not always permit discharge to the atmosphere. Therefore, a reasonable number of vent-line systems discharge to a collecting system, a separator, quench, or flare. In these cases, the vent-line includes fittings such as elbows, tees, or enlargements coupled together, resulting in complex rupture disk vent-line systems. It is currently common practice to determine the mass flow and pressure-drop in complex vent-line pipelines using models for pipeline components validated with fully developed and sub-critical flow. The use of small diameter fittings for model validation is typical, while validation is usually under ideal laboratory conditions with ideal test medium.

The vent-line consists of many pipe fittings resulting in an extensive, complex vent-line system. The medium to be discharged is also not ideal, and compressible and high-velocity flow typically prevails. The medium to be discharged is also not ideal. Typically, the medium ranges from vapor only to two-phase flashing for top-venting applications or even liquid only, two-phase flashing for bottom-venting applications. The method used to size a rupture disk vent-line should, therefore, at least vary with flow, geometry of the busted rupture disk, and with the geometry of the vent-line.

The so-called *Minimum Net Flow Area (MNFA)* (API, 2014), is the open rupture disk free relieving area, A_0 in (TÜV, 2006). It is a crucial rupture disk characteristic number for sizing rupture disk vent-line systems. In work, this area is the rupture disk free relieving area, A_{RD} . In contrast to a safety valve, the opening of a bursting disk is a stochastic process leading to a specific range of flow areas, depending on the rupture disk type, as seen in Figure 1. In general, the prediction of this area to the last percent is not possible. It determines the overall pressure loss dominantly, and in case of critical flow, the mass flow rate to be discharged through a rupture disk vent-line system. It is used to predict the contraction of flow through a rupture disk device. The method to determine this rupture disk characteristic number is, however, neither prescribed nor standardized.

The rupture disk minor loss coefficient or rather rupture disk flow resistance factor, K_R (API, 2014), is another essential characteristic number required in sizing a rupture disk vent-line. Standardized tests to determine this characteristic number should be performed under ideal flow conditions with low velocity, subcritical, almost incompressible flow with air or nitrogen with equations in (API, 2014).

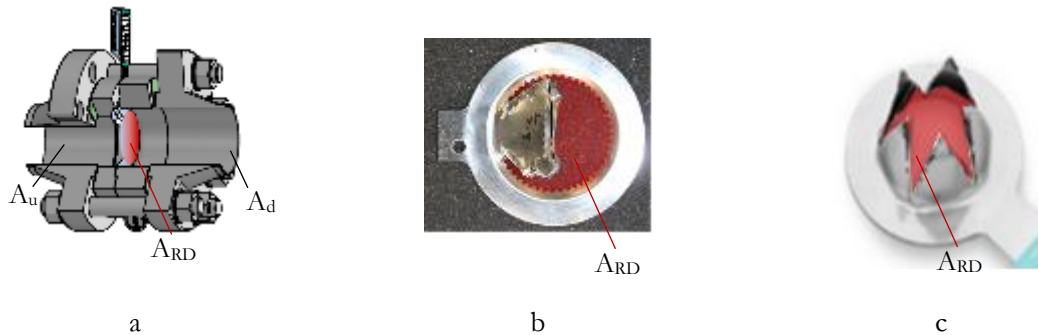


Figure 1 a. Illustration of a rupture disk installed into a rupture disc holder installation between flanges in a vent-line. b. & c. Two open restrictive rupture disk devices show the complex cross-section of the rupture disk free relieving area, A_{RD} , which is typically not circular.

Rupture disk devices are for used over-pressure protection at low burst pressures to very high burst pressures in the range of 2500 bar as in the case in the protection of low-density polyethylene (LDPE) processes. Their sizes also vary from small- to large-diameter devices as large as DN1000. The rupture disk free relieving area A_{RD} and the rupture disk flow resistance factor K_R as characteristic numbers are today indispensable in sizing rupture disk devices installed in complex rupture disk vent-lines. These characteristic numbers should be determined experimentally for a wide range of pressures and sizes. This is, however, not possible today due to limitations in the capacity of test-facilities hence the need to design an industry-scale test-facility for testing small- to large-diameter devices at near realistic flow conditions at pressures up to 3000 bar.

The method used to size a rupture disk vent-line should also be accurate to determine the discharge rate and pressure-drop across a rupture disk, from the point of rupture disk activation to the point when the system depressurizes fully. This information is critical for further safety considerations, such as for modeling the dispersion of accidentally-released toxic gases as well as for calculating the emission load to the environment. (Schmidt, 2015) states that there is overestimation of the rupture disk free relieving area and the dischargeable mass flow rate through rupture disk vent lines in sizing procedures in (API, 2014). For two-phase flow, there is neither a standardized test-section nor any reliable two-phase test results available. There is also no method to predict the pressure-drop and mass flow rate across a rupture disk reliably. As such, there is no suitable method to size a rupture disk with the five step-sizing procedure for rupture disk devices in Table 1, especially for high-velocity flow and two-phase flow.

Sizing rupture disk vent-line systems with characteristic numbers that are not representative of conditions during emergency relief comes with significant uncertainties, especially for high-velocity compressible flow. Over-dimensioning is one measure taken today to mitigate these uncertainties. This is not always an option, as over-dimensioning, the rupture disk vent-line system leads to unnecessary financial costs. It may also cause malfunction of the collecting systems downstream when the fluids discharged are more than the design limits. Emissions to the environment are thereby potentially higher than necessary, causing undue harm to the environment. Under-dimensioning, on the other hand, may lead to hazardous incidents with loss of human life and equipment.

It is imperative that the legal responsibility, as envisioned in the legal framework for protection of pressure equipment as stipulated by the European Union based on the Directive 97/23/EC (European Commission, 1997), is thus not always met by the operator. This is not acceptable, and there is a need to counter the root causes of these uncertainties to prevent a major incidence with possible loss of human life, catastrophic harm to the environment, and loss of property and equipment. A proper sizing procedure for rupture disk devices is indispensable. Also, a large industry-scale test-facility is equally indispensable for proper validation of sizing procedures to reduce the uncertainties and make our future industries safer.

2 Aim and methodology

The aim of this work is the development of a sizing procedure for sizing rupture disk devices for gas flow and two-phase air/water flow based on more reliable rupture disk characteristic numbers. The methodology is listed below:

1. Phenomenological description and investigation of flow through rupture disks.
2. Determination of characteristic numbers and model parameters for determining the mass flow rate and pressure-drop across rupture disks.
3. Development of a reliable sizing procedure for compressible gas and two-phase flow to determine the mass flow rate and pressure-drop across rupture disks.
4. Design, construction, and commissioning of a high-pressure industrial-scale test facility for capacity testing of rupture disks and other fittings with gas flow and construction of a pilot plant for testing rupture disks with air/water two-phase flow.
5. Design of a test section and experimental validation of the new sizing procedure with different types of rupture disks with gas flow and air/water two-phase flow.

3 State of knowledge for sizing rupture disk devices

Flow in high-pressure applications discharging to low-pressure systems is mostly high-velocity flow, and compressibility effects are significant. The flow regime during emergency relief varies from liquid only, gas only, gas/liquid two-phase flow or even flashing liquids. In all these cases, it is necessary to size rupture disk devices reliably to ensure safe operation. If a rupture disk is to be modeled reliably with two-phase flow, then its discharge rate depends largely on the model parameters listed in Table 2 (Fossa & Guglielmini, 2002) (Darby, 2004), (Quibén & Thome, 2007), (Awad & Muzychka, 2008), (Roul & Dash, 2012), (Bhagwat & Ghajar, 2014), (Schmidt, 2015), (Ali & Yeung, 2015), (Hamad, et al., 2017), (Zeghloul, et al., 2017), (Lu, et al., 2018), (Hanafizadeh, et al., 2018), (Kong, et al., 2018).

Table 2 Target model parameters for two-phase flow in a rupture disk

Factor of influence	Model parameters (χ_i) with $i = g, l$ or tp
Rupture disk	Discharge area (A_{RD}), Loss coefficient (K_R), Opening characteristics (circular, star formed, segmental), Discharge coefficient (C_d)
Fluid properties of respective phases	Density (ρ_i), Ratio of specific heat (γ_i), Viscosity (μ_i), Surface tension (σ_i)
Displacement rates of respective phases	Mass flow rate $Q_{m,i}$, Velocity (w_i), Reynolds number (Re_i), Superficial velocity ($U_{s,i}$)
Operating conditions in the relief system	Upstream pressure (P_u), Discharge pressure (P_d), Gravity (g)
Flow pattern around the rupture disk area	Annular, Slug, Intermittent, Stratified, Wavy, Mist, Dryout, Bubbly
Phase distribution	Quality (x_g), Void fraction (ϵ),
Topology of vent-line	Inner pipe diameter (D_i), Friction factor (λ_i), angle of inclination (θ)

The use of empirical (Tribbe & Müller-Steinhagen, 2000), analytical (Schmidt, 2015), or phenomenological model representations (Quibén & Thome, 2007) for sizing devices with two-phase flow, in general, comes with the advantages and disadvantages mentioned in Table 3.

Table 3 Advantages and disadvantages of different model representations for predicting pressure gradient with two-phase flow

Method	Advantages	Disadvantages
Empirical <i>e.g., Lockhart and Martinelli 1949, Friedel 1979, Muller-Steinhagen and Heck 1986</i> <i>See also: Table 2 in (Tribbe & Müller-Steinhagen, 2000)</i>	<ul style="list-style-type: none"> ✚ Minimum knowledge of flow characteristics required ✚ Easy to implement ✚ Provide good accuracy in the validation range 	<ul style="list-style-type: none"> ✚ Limited to validation range
Analytical <i>e.g.</i> <i>See also: Table 2 in (Tribbe & Müller-Steinhagen, 2000)</i>	<ul style="list-style-type: none"> ✚ No empiric information used 	<ul style="list-style-type: none"> ✚ Complex mathematical models resulting in time-consuming calculations ✚ Data required for validation is difficult to obtain
Phenomenological <i>e.g.</i> <i>See also: Table 2 in (Tribbe & Müller-Steinhagen, 2000)</i>	<ul style="list-style-type: none"> ✚ Adequate consideration of flow regimes 	<ul style="list-style-type: none"> ✚ Flow pattern-based models ✚ Some empiricism required to close models ✚ No general flow pattern-based model is available ✚ Require reliable flow pattern mapping

Consider a rupture disk installed to protect a pressure vessel from impermissible over-pressure. The rupture disk is installed in a vent-line, which runs from the pressure vessel and discharges to a catchment system. The rupture disk is activated instantaneously when the burst pressure is reached. Quasi-stationary flow conditions prevail within milliseconds as the fluid is discharged to the catchment system

3.1 Dischargeable mass flow rate

Working standards such as (API, 2014), (TÜV, 2006) are used to size complex relief lines with rupture disk installed. When sizing complex relief lines with (API, 2014), the rupture disk minimum relieving area, A_0 or rather MNFA (ASME, 2017, pp. BPVC-VIII-1 - 2017 Endnote 50) is not required even though A_{RD} is key. The mass flow rate through a rupture disk device installed in a complex vent-line for gas in imperial units with (API, 2014) is per eq.(1).

$$Q_{m,API} = K_U \cdot 1891 \cdot \psi_i \cdot D^2 \cdot \sqrt{\frac{\Delta P_i \cdot P_0}{K_{ys} \cdot v_0}} \text{ with } P \text{ in } PSI, v_0 \text{ in } ft^3/lb \text{ and } D \text{ in } in \quad (1)$$

K_U in eq.(1) is an uncertainty factor with $K_U < 0.9$. ψ_i is the discharge equation for critical or sub-critical flow, ΔP_i is an empiric dimensionless value for critical or sub-critical flow per eq.(A-2) and eq.(A-3) in ANNEX I respectively based on (Crane Co., 2009). Further details regarding eq.(1) are mentioned in ANNEX I.

When sizing similar complex relief lines according to (TÜV, 2006), the minimum rupture disk relieving area A_0 , is mandatory as the resulting flow contraction in a rupture disk device determines the relieving capacity of a rupture disk relief line. The rupture disk minimum relieving area A_0 and the total resistance to flow of the entire relief line with rupture disk installed K_{sys} is required. The rupture disk free relieving area A_{RD} is used correspondingly as MNFA (See: Figure 1). The mass flow rate through a rupture disk device with gas flow with (TÜV, 2006) is per eq.(2).

$$Q_m = A_{RD} \cdot C_d \cdot \psi_i \cdot \sqrt{2 \cdot P_0 \cdot \rho_0} \quad (2)$$

A_{RD} in eq.(2) is the rupture disk discharge area, C_d is a rupture disk's discharge coefficient, ψ_i is a discharge parameter which differentiates between critical and sub-critical flow conditions. Further details regarding eq.(2) are mentioned in ANNEX I.

Nozzle models are also used to model flow through devices. A nozzle's narrowest cross-section, A_{th} is also usually the narrowest flow cross-section. In this case, the thermodynamic conditions at the given nozzle's throat are known. Usually, the rupture disk free relieving area A_{RD} is equated to A_{th} in the following equation to determine the dischargeable mass flow rate with eq.(4) (Schmidt, 2018)

$$Q_{m,nozzle} = \frac{A_{th} \cdot \sqrt{2}}{v_{th}} \cdot \sqrt{-\int_{P_a}^{P_{th}} v \cdot dP - \int de_{diss} + \frac{w_{in}^2}{2} - g \cdot \sin(\theta) \cdot L} \quad (3)$$

(Schmidt, 2019) presents an analytical equation to calculate the dischargeable mass flow rate through a safety relief valve assuming one dimensional, homogeneous, and frictionless nozzle as a hybrid of HNE-DS correlation in the HNE-CSE model for safety relief valves (Schmidt & Claramunt, 2015) per eq.(4).

$$Q_{m,nozzle} = A_{th} \cdot \frac{v_0}{v} \cdot \sqrt{\frac{-\int_{\eta_0}^{\eta} \frac{v}{v_0} \cdot d\eta}{1 - \left(\frac{A_{th}}{A_0}\right)^2 \cdot \left(\frac{\omega(N) \cdot (1 - \eta_0) + \eta_0 \left(\frac{\eta_{th}}{\eta_0}\right)}{\omega(N) \cdot (1 - \eta_{th}) + \eta_{th} \left(\frac{\eta_0}{\eta_0}\right)}\right)^2}} \cdot \sqrt{2 \cdot \frac{P_0}{v_0}} \text{ with } \eta = \frac{P}{P_0} \quad (4)$$

Two-phase equation of state is factored in a rigorous analytical procedure with the definition of omega parameter, ω to consider changes of density with pressure in the nozzle as proposed in Leung (Diener & Schmidt, 2005). The omega-parameter is further corrected to factor the boiling-delay phenomenon in flashing two-phase flows with an imbalance factor N , which contains nozzle-specific correction factor, which should be determined experimentally. Details about this procedure are elaborated in cited references.

3.1.1 Free relieving area

Typical rupture disks are designed to open, resulting in a large effective rupture disk free relieving area, A_{RD} . As such, rupture disks typically have a large diameter ratio, $\beta_{RD} > 0.75$ with $\beta^2 = A_{RD}/A_u$ relative to the inner pipe diameter A_u (Friedel & Kissner, 1988), (Shannak, et al., 1999). The free relieving area of a rupture disk can also not be exactly related to a geographical shape, i.e., circular or rectangular, as seen in Figure 1.

Rupture disks designs vary; there are significant constructive design differences. This means that the opening characteristics and flow conditions also vary depending on the rupture disk type. Small diameter and large diameter rupture disks are not geometrically similar and consequently have different flow characteristics even for rupture disks of the same type. The A_{RD} is requisite in sizing Step 4 in Table 1 as this area significantly influences the magnitude of separation and restriction of flow and therefore, the dischargeable mass flow rate through the device. This is relevant as the dischargeable mass flow rate of a compressible fluid through a rupture disk vent line system depends on the resistance of the piping geometry between the pressurized system and the first cross-section where critical flow condition establishes; the so-called ‘‘choking area.’’ This choking area limits the maximum flow rate through the whole system for prevailing upstream conditions. Any cross-section where there is restriction of flow or any diameter enlargement is potentially a choking area (Mutegei & Schmidt, 2016).

There is no standardized method to determine a rupture disk’s free relieving area directly from experiments. A_{RD} is approximated as the smallest cross-section of the rupture disk holder. This area is, however typically larger than A_{RD} for a reasonable number of rupture disks, as seen in Figure 2. It should be determined experimentally with appropriate consideration of structural members, which reduce the relieving area of an open rupture disk device (ASME, 2017).

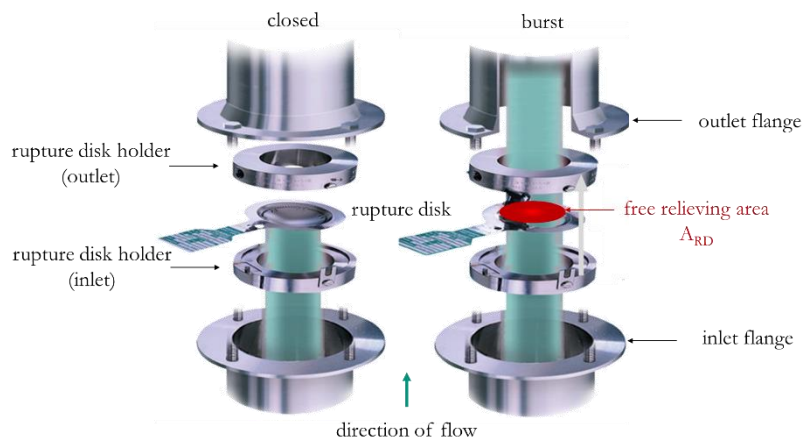


Figure 2: Closed and burst forward-acting rupture disk device (Schmidt, 2016)

3.2 Pressure-drop in vent-lines with rupture disk installed

Flow in high-pressure applications discharging to low-pressure systems is mostly high-velocity flow, and compressibility effects are significant. The general approach in sizing such complex rupture disk vent-lines involves determining the irreversible pressure loss of a pipe with a rupture disk installed and determining the dischargeable mass flow rate. Changes in thermodynamic properties due to acceleration, which arises because of friction and momentum exchange, should be considered.

The fluid accelerates, resulting in pressure-drop starting from the stagnation pressure in the pressure vessel due to exit losses in the pressure vessel flanges. The pressure drops further mainly due to friction and acceleration losses in pipe, from a location in piping upstream of the rupture disk (in) to a location upstream near the rupture disk, (u) as illustrated in Figure 3a.

The pressure-drop in rupture disk is mainly caused by the interaction of rupture disk with fluid due to flow separation and formation of vortices while the pressure-drop in a pipe is mainly due to friction. A rupture disk in pipe causes separation of flow similar or in a lesser magnitude than a contraction. Separation of flow comes with a rapid drop in density and rapid increase in velocity up to the narrowest cross-section of flow, the apparent Vena-contracta.

The ratio of separated flow velocity to inlet pipe velocity increases greatly at high subsonic Mach numbers (Miller, 1984, p. 154). For gas flow, high subsonic Mach numbers prevail in closest proximity downstream of the rupture disk relative to the upstream Mach number. When the Mach number downstream of a rupture disk device attains unity, then the rupture disk is subject to critical flow. The apparent Vena-contracta is more pronounced in gas flow than in two-phase air/water flow, as seen in Figure 3b (Schmidt, 1993). Flow then recovers downstream of the rupture disk, and pressure drops further in the pipe due to friction, as illustrated. The expected real pressure profile in a pipe with a rupture disk installed is as illustrated in the dash-line in Figure 3a. The pressure profile calculated is illustrated by the continuous line plot in Figure 3a. The pressure profile in a vent-line is calculated in the last step, by determining and coupling the upstream and downstream pressure profiles with a step function with the pressure-drop of a rupture disk device, ΔP_{RD} . One peer reviewer in (Mutegi, et al., 2019) observed that proper prediction of pressure-drop was necessary, especially for high-velocity flow, where compressibility effects are significant but are usually ignored in classic methods. Further feedback encouraged the development of new methods to predict the pressure-drop with more reliable characteristic numbers as this would be of benefit for sizing rupture disk relief systems in the chemical and petrochemical industry.

Sizing a rupture disk device thus also involves determining the pressure profile in the vent-line. The pressure-drop of a rupture disk device, ΔP_{RD} is needed to calculate the pressure profile in a rupture disk vent-line reliably for gas flow and two-phase flow.

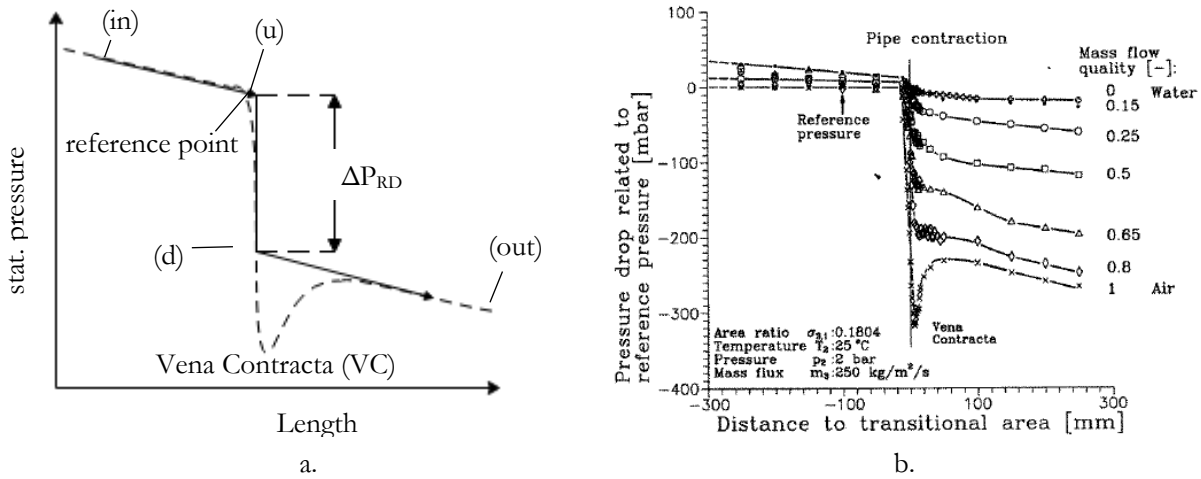


Figure 3 a. Illustration showing the real and model pressure profile with ΔP_{RD} . b. Static pressure profile in the centerline of a sudden pipe contraction measured in a two-phase air/water flow (Schmidt, 1993).

3.2.1 Pressure-drop across a rupture disk with gas flow

The pressure-drop across a rupture disk, ΔP_{RD} in Figure 3a, is usually calculated with equations in literature with the rupture disk resistance factor K_R per eq.(6) (Miller, 1984), (Perry & Green, 2008). It is calculated with the rupture disk loss coefficients for gas $K_{R,g}$, and liquid service $K_{R,l}$ with eq.(5) respectively. It is usually referenced at a point upstream of the rupture disk at (u) in the unseparated flow region.

$$\Delta P_{RD,li} = -\frac{G_u^2}{2 \cdot \rho_u} \cdot K_R \quad (5)$$

Even though a rupture disk is used as a primary relief device, the rupture disk flow resistance coefficients determined under ideal laboratory conditions are not precisely applicable for compressible gas, vapor, liquid, or multiphase flow. Experimental studies with restrictive rupture disk devices show that indeed, the rupture disk resistance factor, K_R varies significantly with test pressure, as observed by previous unpublished work by (Huff, 2001).

3.2.1.1 Rupture disk loss coefficient

The rupture disk loss coefficient, K_R is today determined during rupture disk capacity testing with ASME PTC-25 (ASME, 2014) subject to ASME BPVC VIII Div. 1 (ASME, 2017). A rupture disk is first busted with water or with air in a separate test-section.

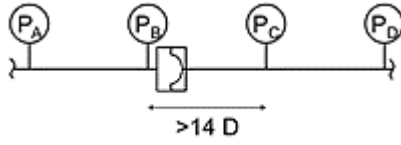


Figure 4 Rupture disk test section

K_R is then determined with the burst rupture disk in the standardized test section in ASME PTC-25 (ASME, 2014). The test section has four pressure taps A, B, C and D. The first set of tests are run with only pipe, while the second tests are run with rupture disk device installed between the pressure tap B and C. The length of pipe between pressure tap B and C pressure taps is $>14D$.

K_R is taken to be the difference between the resistance factor of pipe segment between pressure taps B and C with rupture disk installed, $K_{B-C, RD}$, and without rupture disk installed, $K_{B-C, pipe}$.

The loss coefficients, $K_{B-C, RD}$, and $K_{B-C, pipe}$ are determined from the experimental data using eq.(5) based on equations in literature (Levenspiel, 1977) and (Perry and Green 2008). Once determined, K_R is taken to be constant for all plausible gas flows.

$$K_R = \Delta K_{B-C, RD} - \Delta K_{B-C, pipe} \quad (6)$$

3.2.2 Pressure-drop across a rupture disk with two-phase flow

For two-phase flow, the pressure-drop in a rupture disk, $\Delta P_{RD, tp}$ is mainly due to friction. Unlike in gas low, there is no characteristic number like K_R to calculate the pressure drop. The work by (Friedel & Kissner, 1988) proposes a method to predict $\Delta P_{RD, tp}$ per eq.(7). This equation is empiric, and it comes with the limitations in Table 3. This equation does not consider most of the model parameters listed in Table 2.

$$\Delta P_{RD, tp} = \frac{G^2}{2 \cdot \rho_{tp, m}} \cdot \frac{1}{\beta_{RD}^4} \cdot \left(\frac{1}{2} \cdot (1 - \beta_{RD}^2) + \sqrt{2} \cdot (1 - \beta_{RD}^2)^{3/2} + (1 - \beta_{RD}^2)^2 \right) \quad (7)$$

$\rho_{tp, m}$ in eq.(7) is the two-phase momentum density and β_{RD} as the given rupture disk diameter ratio, which is determined empirically.

The work by (Shannak, 2010) proposes a method to predict the rupture disk two-phase frictional pressure $\Delta P_{RD, tp, friction}$ is per eq.(8). This equation is also empiric, and it comes with the limitations in Table 3. This equation does not consider most of the model parameters listed in Table 2.

$$\Delta P_{RD, tp, friction} = - \frac{G^2}{2 \cdot \rho_{tp, h}} \cdot \left(a_{RD} \cdot Re_{tp}^{b_{RD}} \cdot C_{C, tp} \cdot \exp(x_g) \cdot \eta_C \right) \quad (8)$$

$\rho_{tp, h}$ in eq.(8) is the homogenous two-phase density, Re_{tp} is the two-phase Reynolds-number correlation according to Shannak, $C_{C, tp}$ is the empiric two-phase contraction coefficient correlation according to Shannak and η_C is the safety valve viscosity correction factor for liquids according to (Darby, 2004) while a_{RD} , and b_{RD} , are rupture disk specific constants that are given for a rupture disk device (Shannak, 2010).

Correlations for predicting the pressure-drop across orifice with two-phase flow have been reviewed in (Zeghloul, et al., 2017). They are expressed as functions of gas quality, x_g , and the densities of the gas and liquid phases. Effects of viscosity, surface tension, and gravity if the orifice is placed in a vertical plane, are not taken into consideration. Further, only the correlation of Chisholm (B-equation) is reported to consider geometrical parameters of the orifice (thickness and open area) on the two-phase multiplier. Correlations for orifice should not be used for sizing rupture disk devices directly without further studies, because the rupture disk differs significantly from an orifice.

3.2.3 Pressure-drop in an adiabatic straight pipe with gas flow (Fanno flow)

Changes in thermodynamic properties of a gas flowing through a pipe with a constant cross-section are mainly due to friction and change in momentum resulting in pressure drop. The geodetic head is usually negligible for gases (Shannak, 2008). Literature models for calculating the pressure-drop in a straight pipe are derived assuming an infinitely small control volume assuming a rough, circular, straight pipe with a constant cross-section. Adiabatic and steady-state flow prevails. Changes in thermodynamic properties attributable to friction in pipe are as illustrated in Figure 5.

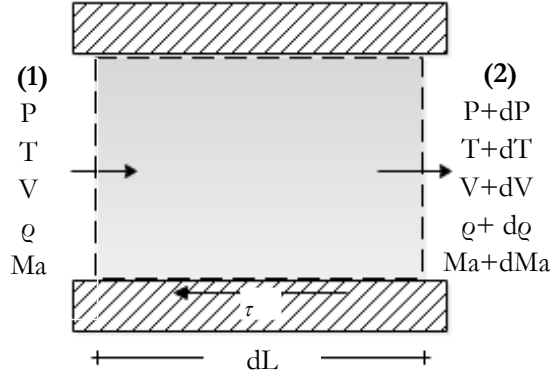


Figure 5: Control volume assuming a straight pipe with a constant cross-section according to (Shapiro, 1953)

The definition of a loss coefficient of a pipe segment due to friction (Miller, 1984), (Levenspiel, 1998), (Perry and Green 2008) is introduced assuming the Darcy friction factor, λ is equal to the arithmetic average in the control volume.

$$K = \frac{\lambda_w}{D} \cdot L \quad \text{and} \quad \Delta P = -\frac{G^2}{2 \cdot \rho} \cdot K \quad \text{with} \quad \lambda_w = \frac{1}{L} \cdot \int_0^L \lambda \{L\} \cdot dL \quad (9)$$

Several solutions for the Darcy friction factor λ in the Colebrook equation have been reviewed (Brkić, 2011). The explicit approximation of Colebrook's equation solution according to (Chen, 1979) for a given pipe roughness is used because it is one of the most accurate approximations and it deviates by less than 0.5% from Colebrook's equation. The mean roughness depth, R_z , is equated to k_s based on the relationship between measured surface roughness to the equivalent sand grain roughness, k_s as studied by (Adams & Grant, 2012).

$$\lambda \{L\} = \left(-2 \cdot \log \left[\frac{k_s}{3.7065 \cdot D} - \frac{5.0452}{\text{Re} \{L\}} \cdot \log \left(\frac{1}{2.8257} \cdot \left(\frac{k_s}{D} \right)^{1.1098} \right) + \frac{5.8506}{\text{Re}^{0.8981} \{L\}} \right] \right)^{-2} \quad (10)$$

The relationship between the Mach number, Ma and the Darcy friction factor λ , and ratio of specific heats, κ , assuming adiabatic flow for a perfect gas with friction in the control volume illustrated Figure 5, is derived in (Shapiro, 1953). This working equation is also referenced in current literature such as (Perry and Green 2008). The Shapiro-equation may be formulated in terms of loss coefficient per eq.(11).

$$\int_{L_1}^{L_2} \lambda \{L\} \cdot \frac{dL}{D} = \int_{Ma_1}^{Ma_2} \frac{1 - Ma^2}{\kappa \cdot Ma^4 \cdot Y \{Ma\}} \cdot dMa^2 \quad \text{with} \quad Y \{Ma\} = 1 + \frac{\kappa - 1}{2} \cdot Ma^2 \quad (11)$$

The works by (Levenspiel, 1977) and (Truckenbrodt, 2008) integrate eq.(11) with the Mach-number as an independent variable to deliver the explicit solution for pipe loss coefficient, assuming adiabatic flow with friction in a round pipe with constant cross-sectional area between location (u) and (d). (See: Figure 45a). The averaged Darcy friction factor, λ_{av} per eq.(9) is used in the definition of loss coefficient in eq(12).

$$K \{Ma_1, Ma_2\} = \frac{\lambda_w}{D} \cdot L_{1-2} = \left[\frac{1}{\kappa} \cdot \left(\frac{1}{Ma_1^2} - \frac{1}{Ma_2^2} \right) + \frac{\kappa + 1}{2 \cdot \kappa} \cdot \ln \left(\frac{2 + (\kappa - 1) \cdot Ma_2^2}{2 + (\kappa - 1) \cdot Ma_1^2} \cdot \left(\frac{Ma_1}{Ma_2} \right)^2 \right) \right] \quad (12)$$

The pressure profile in pipe segments upstream and downstream of a rupture disk device is typically calculated by integrating the pressure gradient, $(dP/dL)_g$ per eq.(13) in respect of pipe length assuming steady-state, adiabatic and fully developed flow with a perfect gas (Truckenbrodt, 2008).

$$\left(\frac{dP}{dL}\right)_g = -\frac{\lambda_g \{L\}}{D} \cdot \frac{G^2}{2 \cdot \rho \{L\}} \cdot \frac{1 + (\kappa - 1) \cdot Ma \{L\}^2}{1 - Ma \{L\}^2} \quad (13)$$

The pressure profile in pipe segments may also be calculated by integrating $(dP/dL)_{go}$ equation per eq.(14) in respect of pipe length assuming steady-state, adiabatic, and fully developed flow with a real gas (Thévenin & Janiga, 2014, p. 155).

$$\left(\frac{dP}{dL}\right)_g = -\frac{\lambda_g \{L\}}{D} \cdot \frac{G^2}{2 \cdot \rho \{L\}} \cdot \frac{1}{Ma \{L\}^2 - 1} \cdot \left(1 + \frac{P_i}{c_v \{L\}} \cdot \frac{Ma \{L\}^2}{\rho \{L\} \cdot T \{L\}}\right) \quad (14)$$

The strategy in this work is to determine the friction component to correlate losses observed with low-velocity flow to losses expected on high-velocity flow using equations for predicting losses in rough pipes. Therefore, equations for predicting the pressure gradient $(dP/dL)_{tp,friction}$ in pipes are relevant in this work.

3.2.4 Pressure-drop in an adiabatic straight pipe with two-phase flow

Compressible two-phase flow in a straight pipe has been studied extensively over-time, and a wide range of models are available in literature. The pressure gradient in a straight pipe for two-phase flow, $(dP/dL)_{tp}$ is generally attributable to three components, i. Acceleration, ii. Gravity and iii. Friction between pipe inner wall and fluid. For steady-state flow, assuming circular and constant flow cross-section with an inner diameter, the pressure gradient is per eq.(15) (Thome & Cioncolini, 2015).

$$\left(\frac{dP}{dL}\right)_{tp} = \left(\frac{dP}{dL}\right)_{tp,acceleration} + \left(\frac{dP}{dL}\right)_{tp,friction} + \left(\frac{dP}{dL}\right)_{tp,gravity} \quad (15)$$

The acceleration term accounts for pressure-drop during evaporation in a channel or pressure recovery during condensation in a channel is usually neglected in adiabatic channels (Awad & Muzychka, 2008) and non-boiling two-phase flows such as air-water two-phase flows. The acceleration term is per eq. (Lu, et al., 2018).

$$\left(\frac{dP}{dL}\right)_{tp,acceleration} = -\frac{d}{dz} \cdot \left(\frac{G_l^2}{\rho_l \cdot (1 - \epsilon_{fp})} + \frac{G_g^2}{\rho_g \cdot \epsilon_{fp}}\right) \quad (16)$$

Various methods are available in literature to calculate the frictional component. The methods may be classified as either empirical, analytical, (Tribbe & Müller-Steinhagen, 2000) or phenomenological (Quibén & Thome, 2007), and they come with advantages and disadvantages mentioned in Table 3. The work by (Tribbe & Müller-Steinhagen, 2000) evaluated 24 empirical and phenomenological methods in literature and observed that the precision of empirical and phenomenological methods is comparable. (Ould-Didi, et al., 2002) compared popular methods in literature and found that the (Müller-Steinhagen & Heck, 1986) method and the (Grønnerud, 1979) method provided the most accurate predictions. The (Friedel, 1979) method came in third. A later work by (Thome & Cioncolini, 2015) undertook a conclusive comparison of more than 20 methods in literature from the year 1942 to 2009. These methods were compared against an extensive database and the (Müller-Steinhagen & Heck, 1986) and the (Sun & Mishima, 2009) which is a modification of the (Lockhart & Martinelli, 1949) were found to predict the pressure gradient most accurately. (Hamad, et al., 2017) presents and compares a drift-flux model against popular models and finds that the model their work predicts the pressure gradient best within an average percent error of <3% with two-phase compressible flows.

The frictional component may be calculated with the Müller-Steinhagen and Heck correlation per eq.(17). This correlation is preferred in this work as it expresses the pressure-drop attributable to friction as components of liquid-only and gas-only. This correlation has been reviewed in (Thome & Cioncolini, 2015) and is reported to be the second-best frictional pressure-drop correlation out of nine correlations in that study, and it has also been validated with 9313 data points with pipe diameter up to 392 mm.

$$\left(\frac{dP}{dL}\right)_{tp, friction} = \left[\left(\frac{dP}{dL}\right)_l + 2 \cdot \left\{\left(\frac{dP}{dL}\right)_g - \left(\frac{dP}{dL}\right)_l\right\} \cdot x_g\right] \cdot (1-x_g)^{0.33} + \left(\frac{dP}{dL}\right)_g \cdot x_g^3 \quad (17)$$

The single-phase pressure gradients are calculated with Darcy friction factor per eq.(18) as described in (Müller-Steinhagen & Heck, 1986).

$$\left(\frac{dP}{dL}\right)_l = \frac{\lambda_l \{Re_l\}}{D_i} \cdot \frac{G^2}{2 \cdot \rho_l}; \quad \left(\frac{dP}{dL}\right)_g = \frac{\lambda_g \{Re_g\}}{D_i} \cdot \frac{G^2}{2 \cdot \rho_g}; \quad (18)$$

Calculation of two-phase mixture density ρ_{tp} requires reliable prediction of the two-phase void fraction ϵ_{tp} . Void fraction correlations based on the drift-flux model, are found to be best performing in a study which compares seventeen slip ratio-correlations, thirteen K- ϵ_H -correlations, nineteen drift-flux-correlations and twenty general void fraction correlations in open literature (Melkamu A. & J.Ghajar, 2007).

Void fraction, ϵ_{tp} varies with flow pattern, the orientation of pipe, pipe diameter, and fluid properties. This work uses the (Bhagwat & Ghajar, 2014) two-phase void fraction correlation ϵ_{tp} , which is independent flow pattern maps. It is based on a one-dimensional drift-flux model assuming that the two-phase flow properties do not change in a pipe cross-section (Bhagwat & Ghajar, 2014). This correlation is based on the drift-flux model and has been validated with 8255 experimental data points and predicts two-phase void fraction best when compared against 11 correlations in that study. Even though it is not as detailed as the separated flow model, it is recommendable due to its simplicity and flexibility.

With this, the gravity component in the pressure gradient in two-phase flow with two-phase mixture density ρ_{tp} is predicted with two-phase void fraction ϵ_{tp} with Bhagwat & Ghajar co-correlation (Lu, et al., 2018).

$$\left(\frac{dP}{dL}\right)_{tp, gravity} = -(\rho_{tp}) \cdot g \cdot \sin(\theta) \quad \text{with } \rho_{tp} = \epsilon_{tp} \cdot \rho_g + (1 - \epsilon_{tp}) \cdot \rho_l \quad (19)$$

The pressure gradient in adiabatic pipes is, therefore per eq.(15) with acceleration term per eq.(16), the friction term per eq.(17) and the gravity term per eq.(19).

$$\left(\frac{dP}{dL}\right)_{tp} = \left(\frac{dP}{dL}\right)_{tp, gravity} + \left(\frac{dP}{dL}\right)_{tp, friction} \quad (20)$$

Methods and technology to determine the density, velocity and void fraction with two-phase flow, based on tomography i.e. Electrical Resistance Tomography (ERT), Electromagnetic Tomography (EMT), Microwave Tomography (MWT), Electrical Impedance Tomography (EIT), Optical Tomography or Gamma Densitometry are mentioned in (Hansen, et al., 2019) and are not the focus in this work.

3.3 Definition of gap in research

The following gaps in research are identified for adiabatic, steady-state flow across a rupture disk device and listed in the order in which they will be processed in this work:

Gap I. Test facility and test sections for rupture disk capacity testing

The procedures proposed to close the gaps in research should be validated adequately with reliable experimental results. Conclusive studies should involve testing of small-diameter devices to large-diameter devices at a wide range of pressures to reflect the wide range of use of rupture disk devices and other fittings.

Currently, no test facility is found in open literature with adequate capacity and capability to also test large-diameter rupture disks with single-phase, or with two-phase flow. There is also no suited standardized test section and, therefore, no standards available for sizing rupture disks for two-phase flow, primarily because there is no standardized industry-scale test facility to deliver reliable experimental results (Mutegi & Schmidt, 2016). This work should, design, construct, and commission achieve a suited facility based on the feasibility study by (Mutegi, 2014).

Gap II. Development of a model to calculate the dischargeable mass flow rate across a rupture disk device

The dischargeable mass flow rate across a rupture disk device per eq.(1) and eq.(2) is calculated based on the total system pressure loss coefficient, K_{sys} calculated with K_R , which ignores compressibility effects, especially for high-velocity effects. Beyond this, it is necessary to study if the rupture disk is subject to choking so that the dischargeable mass flow rate through a rupture disk at burst pressure is calculated accurately, especially for high-velocity gas flows and for compressible two-phase flows. This is necessary to find a relationship to determine the smallest rupture disk and pipe size which fulfills the “dischargeable mass flow rate is larger than the minimum flow rate to be discharged” sizing criterion reliably and accurately using the rupture disk free relieving area, A_{RD} at sizing Step 4 in Table 1. The developed methodology should be valid to determine the dischargeable mass flow rate, from the point of activation of the rupture disk to the point when the system depressurizes fully. This information is critical for further safety considerations, such as for modeling the dispersion of accidentally-released toxic gases.

Gap III. Determination of rupture disk free relieving area

Sizing of throttling devices with the nozzle-based equation per eq.(2), eq.(4) and other area-based models require accurate values for the rupture disk free relieving area A_{RD} . Eq. (4) would, for example, require A_{RD} to equate it to the nozzle’s narrowest flow cross-section in that model representation, i.e., throat. A_{RD} is an essential rupture disk characteristic number in sizing Step 4 in Table 1 and should be determined experimentally for a rupture disk device reliably. Visualization of flow in a rupture disk, to investigate how a rupture disk interacts with fluid is crucial to predict a rupture disk’s narrowest flow cross-section reliably.

Gap IV. Development of a model to calculate the pressure-drop across a rupture disk device

Proper prediction of pressure-drop is necessary especially for high-velocity flow, where compressibility effects are significant but are usually ignored in classic methods as observed by one peer reviewer during the review of (Mutegi, et al., 2019). The development of new methods to predict the pressure-drop across a rupture disk, ΔP_{RD} is necessary, especially for high-velocity gas flow and two-phase flow (See also: in Figure 3a.). For two-phase flow, there is neither a characteristic number for characterizing losses in rupture disk device nor a method to calculate the pressure-drop across a rupture disk, ΔP_{RD} . This even though ΔP_{RD} is essential for the pressure-drop calculation in the entire rupture disk vent-line system to validate its capacity in sizing Step 5 in Table 1.

This work should also focus on sizing Step 5 in Table 1 and should investigate losses in the rupture disk device. The rupture disk should be characterized reliably with more reliable characteristic numbers. For two-phase flow, new characteristic numbers and a method to determine the pressure-drop across a rupture disk ΔP_{RD} should be proposed.

Gap V. Determination of prevailing rupture disk minor loss coefficient

Eq.(10) through eq.(12) are meant for use in straight pipes with constant cross-sectional area assuming adiabatic flow of a perfect gas (fanno flow). Separation and restriction of flow is not considered during their derivation. The rupture disk flow resistance factor K_R is determined with the said equations per eq. (6) and is therefore blind to compressibility effects, separation, and restricting of flow, especially for high-velocity flow, as is typically the case during emergency relief.

Studies regarding the rupture disk loss coefficients are necessary to determine and define rupture disk characteristic numbers reliably. Studies with high-velocity and compressible gas flows, as well as compressible air/water two-phase flows, are especially relevant because compressibility effects are dominant in such flows.

3.3.1 Summary

The *experimental focus* in this work is in the design, construction, and commissioning of the “150 bar loop for testing small-diameter devices to large-diameter devices at a wide range of pressures below 150 bar with air, and air/water two-phase mixture. The 150 bar loop as the first stage of the CSE HP loop, is essential for the realization of other stages. Once complete, the CSE HP loop will be a high-capacity, high pressure industry-scale test-facility safety devices and other fittings at near realistic flow conditions at pressures up to 3000 bar (see also: Figure 6 – The three stages of the CSE HP loop for tests with air, water and air/water two-phase flow at pressures up to 3000 bar). The 150 bar loop will be used to deliver reliable experimental data, deeper understanding, and know-how for rupture disk device, resulting in improved models. Once in operation, the Gap I (Test facility and test sections for rupture disk capacity testing) will be closed.

The *theoretical focus* of this work will be to find a relationship to determine the dischargeable mass flow rate through a rupture disk device so as to close Gap III (Determination of rupture disk free relieving area) and Gap II (Development of a model to calculate the dischargeable mass flow rate across a rupture disk device). Both gaps in research are essential to determine the smallest rupture disk and pipe size, which fulfills the “dischargeable mass flow rate is larger than the minimum flow rate to be discharged” sizing criterion in sizing Step 4 in Table 1 reliably.

The *theoretical focus* of this work will also be on the prediction of the pressure-drop across a rupture disk device for gas flow and two-phase flow. The aim here will be to find a relationship that is valid, more generally, to correlate rupture disk losses observed in low-velocity flow to losses expected in high-velocity flow by factoring compressibility fully. This is indispensable to close Gap IV (Development of a model to calculate the pressure-drop across a rupture disk device) and Gap V (Determination of prevailing rupture disk minor loss coefficient). Both gaps in research are essential to achieve a detailed pressure-drop calculation in the entire rupture disk vent-line system to validate its capacity in sizing Step 5 in Table 1 reliably.

4 Design, construction and commissioning 150 bar loop

The requisite components in the 150 bar loop will be selected, procured, fabricated, and constructed as specified based on a feasibility study previously conducted within the scope of a Diplom-thesis (Mutegi, 2014). The 150 bar loop is the first stage of the CSE HP loop, a high-capacity, high-pressure industry-scale test-facility for testing small- to large-diameter devices at near realistic flow conditions at pressures up to 3000 bar. The CSE HP loop in the third stage will deliver much-needed suitable experimental data, deeper understanding, and know-how for rupture disk device and other fittings. This ambitious large-scale project is to be implemented in three stages as illustrated in Figure 6, in constant consultation and cooperation with specialist companies and qualified partners. The 150 bar gas rig is a prerequisite for all the other rigs.

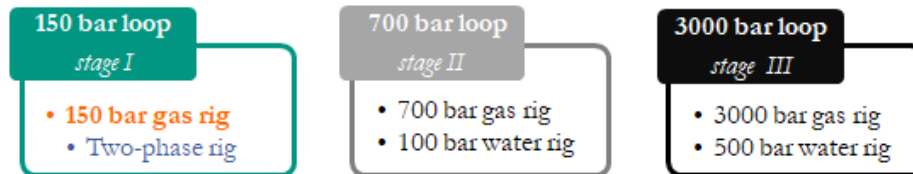


Figure 6 The three stages of the CSE HP loop for tests with air, water and air/water two-phase flow at pressures up to 3000 bar.

To attain two-phase flow testing capabilities in the 150 bar loop, the two-phase rig should additionally be designed later and coupled with the 150 bar gas rig.

Further, a laboratory-scale test facility should be constructed as a pilot facility for testing various techniques before they are implemented in the 150 bar loop. The 150 bar loop should be a multi-purpose, industry-scale, Europe-wide unique test facility for testing small to large diameter safety-devices and other fittings with air at pressures up to 150 bar with water, air and air/water two-phase mixtures, at pressures up to 15 bar in the basic configuration. Flow conditions will be representative of flow conditions during emergency relief. Gas flow in this work is with air, while the two-phase flow is with a mixture of initially subcooled water and air.

The requisite parts needed to design, construct, and commission the CSE 2-phase flow loop on an industrial scale will be described in the following. For this stage, I of the CSE HP loop for tests with air up to 150 bar is highlighted. It is referred to as the “150 bar gas rig” in this work. The 150 bar gas rig will be designed as a modular test facility for testing rupture disk devices and other industrial fittings. It consists of the following units: *i. compression and gas conditioning*, *ii. Buffer vessels*, *iii. flow measurement and pressure regulation*, *iv. test vessel*. The test section varies with the test object. It is to be installed downstream of a test vessel and will be designed separately for testing rupture disk devices. The CSE 150 bar loop is to be constructed spread out in a plot of land with an area of about 1000 m² in the premises of Fraunhofer Institute for Chemical Technology (ICT) in Pfinztal, (near Karlsruhe), Germany.

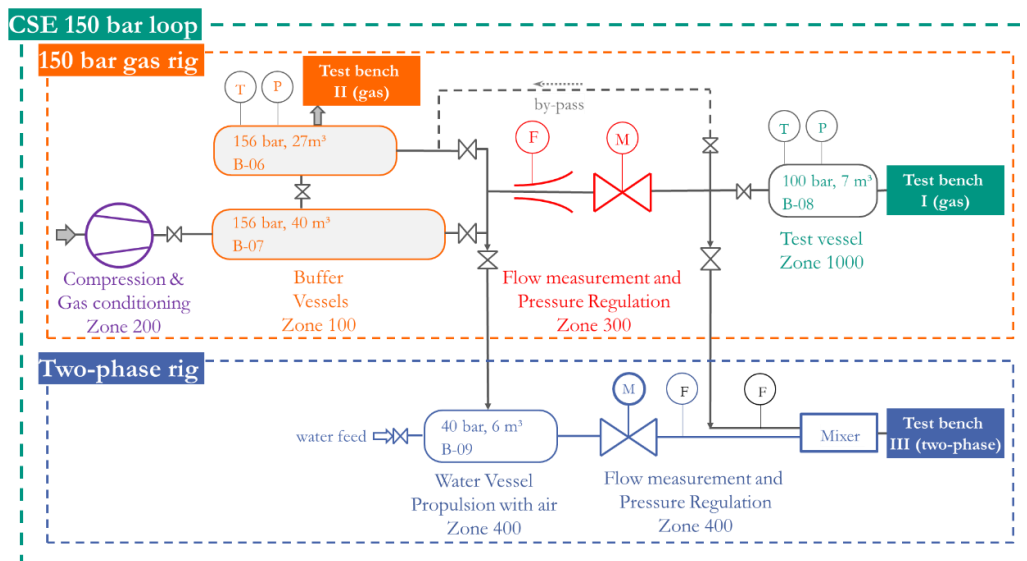


Figure 7 Block diagram showing the main components of the 150 bar loop covering an area of 1000 m².

4.1 Specification of target measurement range

To size the main components, the target measurement range and specifications about the nominal pipe size of the rupture disk devices and safety relief valves were made. For this, demand analysis was done to determine the required mass flow rate for experiments at pressures up to 100 bar.

Table 4 Test facility specified target measurement range for test objects

Target parameter	Value
Nominal pipe size of rupture disc	up to 150 mm
Seat diameter of safety relief valve	up to 63 mm
Test pressure	up to 100 bar for smaller diameter devices up to 40 bar for large diameter devices
Test temperature	> -60 °C in test vessel

For safety valves (SV), the required mass flow rate for experiments is calculated as the dischargeable mass flow rate with AD2000-A2 (TÜV, 2015). For rupture disk devices (RD), the demand was determined by calculating the mass flow rate, which would result in a pressure-drop of at least -0.050 bar in a specified pipe length. The pipe length is specified to 30 diameter lengths to match the length between the first two pressure taps in the current standardized test section for testing rupture disk devices (ASME, 2014) since the test facility should have capability for rupture disk capacity testing subject to that standard.

$$Q_{m,exp} \leftarrow -\frac{dP}{dL} = -\frac{\lambda}{D} \cdot \frac{Q_{m,exp}^2}{2 \cdot A^2 \cdot \rho \{L\}} \cdot \frac{1 + (\kappa - 1) \cdot Ma^2}{1 - Ma^2} \cdot 30 \cdot D = -0.050 \text{ bar} \quad \text{with } Ma = \frac{Q_{m,exp}}{\rho \cdot A \cdot c_s} \quad (21)$$

Rupture disk (RD) with nominal pipe size DN50 (RD-50), DN100 (RD-100), and DN200 (RD-200), as well as safety valves (SV) with inner throat diameter of 15 mm (SV-15), 50 mm (SV-50) and 63 mm (SV-63) are selected for specification of target measurement range. The target measurement range for these devices is found to be between 65 kg/hr and 291,807 kg/hr as seen in Figure 8.

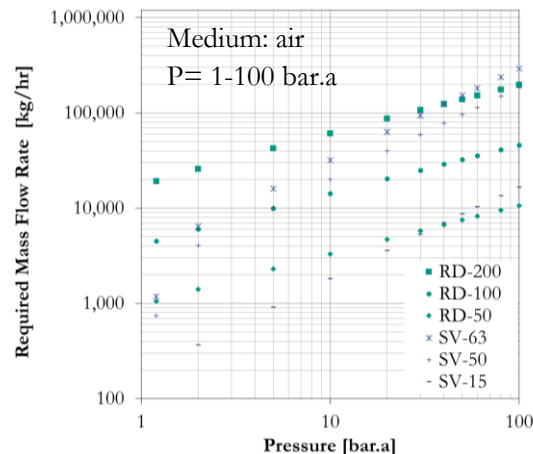


Figure 8: Target measurement range of 150 bar rig with data in Table 5.

Table 5 Target measurement range of 150 bar rig

Required mass flow rate to test object in kg/hr						
P in bar	Rupture disks (RD) with $D_i =$			Safety valves (SV) with $D_{seat} =$		
	50 mm	100 mm	200 mm	15 mm	50 mm	63 mm
1.2	1,056	4,524	19,251	65	743	1,179
2	1,408	6,047	25,820	366	4,063	6,450
5	2,302	9,920	42,502	911	10,120	16,066
10	3,301	14,240	61,091	1,811	20,117	31,938
20	4,710	20,330	87,271	3,579	39,763	63,128
30	5,791	25,003	107,350	5,308	58,973	93,625
40	6,703	28,943	124,280	7,000	77,779	123,482
50	7,507	32,413	139,188	8,659	96,214	152,749
60	8,232	35,547	152,649	10,288	114,306	181,473
80	9,515	41,087	176,448	13,462	149,578	237,471
100	10,635	45,922	197,215	16,542	183,804	291,807
ID	RD-50	RD-100	RD-150	SV-15	SV-50	SV-63

4.2 Design of buffer vessels using demand and capacity analysis

Having determined the measurement range for flow measurement, the next step was to design buffer vessels for storing compressed gas. They should be large enough to hold enough compressed air to run experiments. *Capacity* is defined as the mass of compressed gas, $\Delta M_{\text{capacity}}$ which can be discharged from a buffer vessel at a given pressure, within a given time. The capacity of a pressurized vessel volume V , discharging gas from starting pressure P_{start} and stopping discharge at pressure P_{stop} was estimated per eq.(22) assuming isentropic discharge conditions.

$$\Delta M_{\text{capacity}} = \frac{M_m \cdot V}{Z \cdot R} \cdot \left(\frac{P_{\text{stop}}}{T_{\text{start}} \cdot \left(\frac{P_{\text{start}}}{P_{\text{stop}}} \right)^{\frac{1-\kappa}{\kappa}}} - \frac{P_{\text{start}}}{T_{\text{start}}} \right) \quad (22)$$

Demand in this work is defined as the mass flow rate required to test a fitting at a given pressure over a given time with $\text{Demand} = \text{Mass flow rate} \times \text{Time}$. For an experiment to be done, the capacity of the test facility has to be larger than the demand in terms of air needed to test a device where the time is specified as the time it takes to run an experiment ($\text{Capacity} > \text{Demand}$).

The capacity of the test facility was specified with an experiment time between 60 s and 300 s to get the minimum and maximum capacity. Three identical pressure vessels (B01, B02 and B03) with the maximum allowable working pressure, MAWP of 3400 bar and two identical vessels (B04 and B05) with permissible pressure of 730 bar were examined for their suitability for use as buffer volume for the 150 bar rig since they were already in the inventory list. To get the capacity of the 150 bar rig with B-01 through B-05, it was assumed that these vessels could be compressed to their respective design pressure and discharged for 60 s and 300 s.

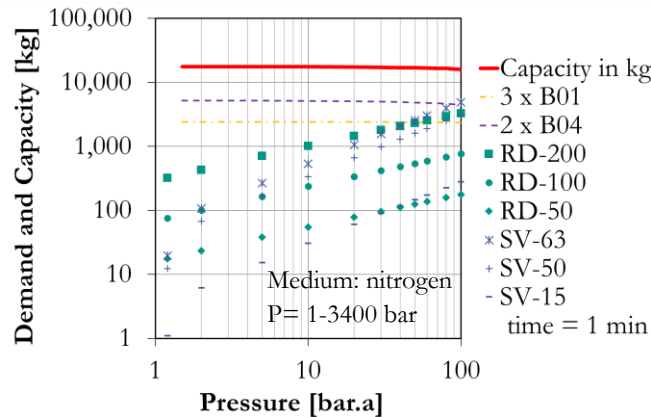


Figure 9: Attainable capacity with B-01 through B-05 with an experiment time of 60 seconds.

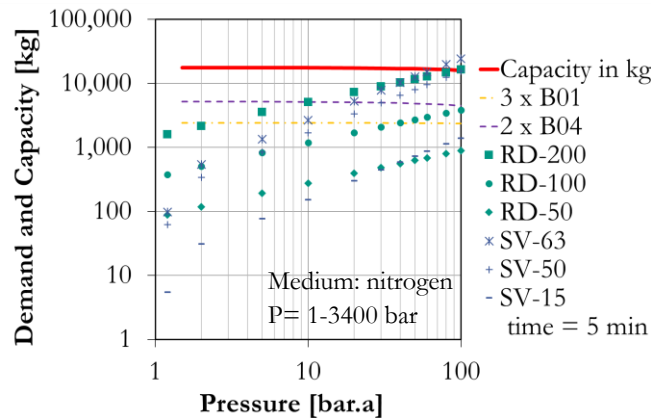


Figure 10: Attainable capacity with B-01 through B-05 with an experiment time of 300 seconds.

The orange and purple dash lines in Figure 9 and Figure 10 represent attainable capacity with only 3400 bar vessels ($3 \times B01$) and only 730 bar vessels ($2 \times B04$). The thick red line represents the total capacity with 3400 bar vessels ($3 \times B01$) and 730 bar vessels ($2 \times B04$). The points represent the demand for gas while testing various devices at a pressure below 100 bar for a specified time of 60 s and 300 s. All points that are below the red line could be tested at the facility since the $Capacity > Demand$ condition could be met.

Though B-01 through B-05 had capacity to meet the demand as seen in Figure 9 and Figure 10, they were not suited because the gas temperature would fall to -130°C during discharge from 3400 bar and to -100°C during discharge from 730 bar to 100 bar as seen in Figure 11. These temperatures would be below -60°C against specification. The use of more expensive cold-resistant steels would also have been necessary. This would not have been feasible from a technical and economic point of view. The use of these vessels was abandoned at this stage.

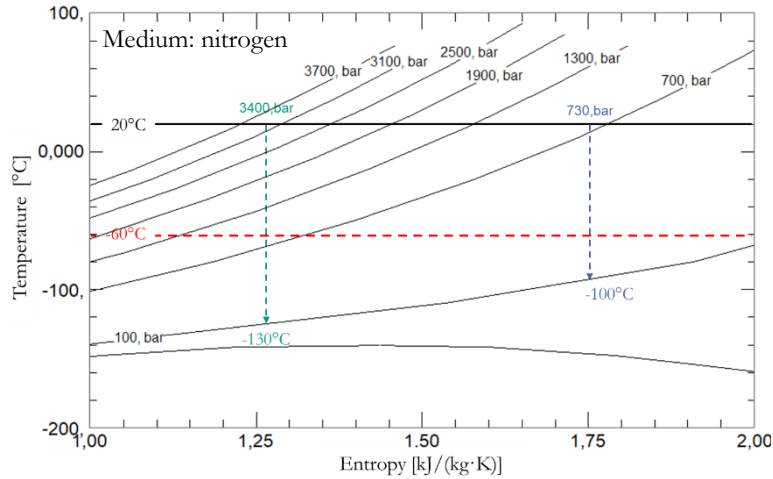


Figure 11: Isentropic drop in temperature while discharging from pressures below 3400 bar.

Since the gas temperature after discharge from pressure vessel was specified to be above -60°C , it was necessary to discharge gas at lower pressures. The maximum discharge pressure to attain gas temperatures above -60°C was found to be 300 bar. This option would have however required that the vessel have a pressure rating of Cl.2500 (PN420). This option was also very near the boundary limit regarding specified minimum gas temperature, as seen in Figure 12. The optimum specification for the vessel pressure rating was found to be Cl.1500 (PN250) and the design pressure (DP) was set to be in the range of 156 bar. Under these conditions, the gas temperature after discharge from 156 bar to 100 bar is -22°C way above the specified temperature for the buffer vessels. Therefore, stationary flow conditions can be attained for the measurement target measurement range.

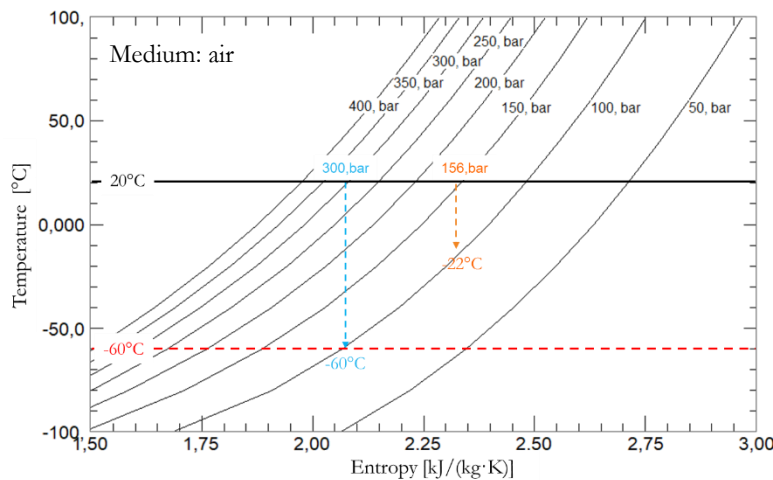


Figure 12: Isentropic drop in temperature while discharging from pressures below 300 bar.

To get the required volume of the buffer vessels with enough capacity, it was assumed that the buffer volume could be compressed to design pressure, DP=156 bar and discharged for 60 s and 300 s. The required buffer volume was found to be in the range of 60 m³ after undertaking capacity-demand analysis.

The next challenge was to realize such a large pressure vessel. For this, custom-made pressure vessels were designed to use gas pipeline segments like those used in the Nord Stream gas pipeline (Nord Stream AG, 2013). Five pipeline segments were made available for use by EUROPIPE, which was one of the suppliers in that project. The inner pipe diameter of each pipe segment is 1220 mm, the material thickness is 26.6 mm and the length is 12 m.

Fabricating a pressure vessel with all the 5 segments would have resulted in a 60 m long vessel; such space was not available at the construction site. A decision was made to fabricate two pressure vessels (B06 and B07) with a combined volume larger than 60 m³. Design and fabrication of B06 and B07 was done in close collaboration with Friedrich Vorwerk. Pressure vessel B06 was fabricated with two pipe segments, while B07 was fabricated with the remaining 3 pipe segments. B06 has V= 25.5 m³ (L≈24 m) and B07 has V=37.77 m³ (L≈36 m). The specifications of B-06 and B-07 regarding temperature and pressure are in Figure 27. To get the capacity of the 150 bar rig with B-06 and B-07, it was assumed that these vessels could be compressed to their respective design pressure, DP=156 bar and discharged for 60 s and 300 s.

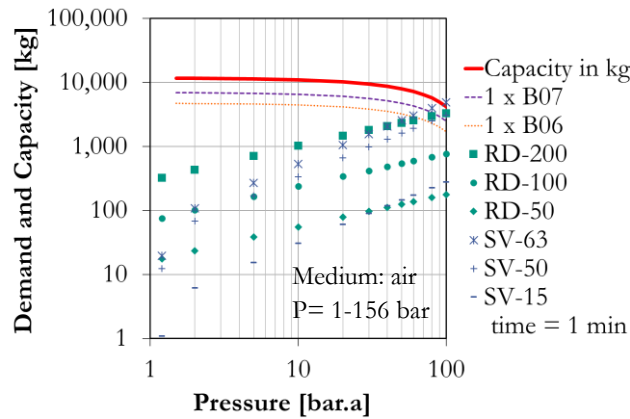


Figure 13: Capacity with B-06 and B-07 with experiment time of 60 seconds.

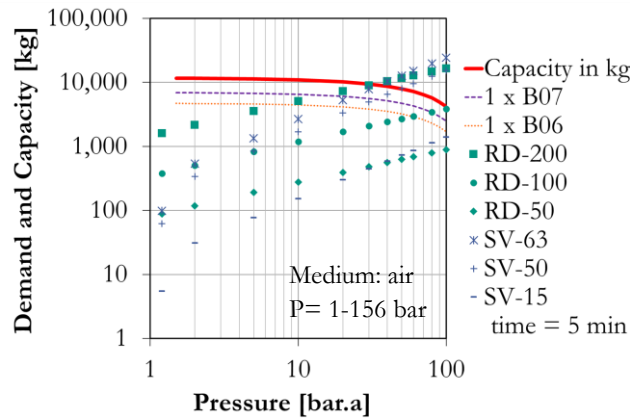


Figure 14: Capacity with B-06 and B-07 with an experiment time of 300 seconds.

The orange and purple lines in Figure 13 and Figure 14 represent attainable capacity with only B06 (V=25.5 m³) and only B07 (V=37.77 m³), respectively. The thick red line represents the total capacity with B06 and B07. The points represent the demand for gas while testing various devices at pressure below 100 bar for specified time of 60 s and 300 s. All points are below the red line can be tested at the facility since the *Capacity* > *Demand* condition is met. Figure 13 and Figure 14 show that B06 and B07 have enough total capacity to meet the demand while discharging air from 156 bar to 100 bar so as to keep the discharge temperature above the specified minimum temperature of -20°C in B06 and B07 as seen in Figure 12.

4.3 Design of the compression and gas conditioning unit

The buffer volume in B06 and B07 should be compressed to the design pressure, DP=156 bar. The compressors should work with both air and nitrogen because the 730 bar and 3400 bar stages should operate with nitrogen. The compressed gas should be free of particles and oil-free to keep the buffer-volume clean. It should also be dry to prevent corrosion of pressure vessel and piping, and to prevent potential icing of the gas rig during discharge. The purity of gas was specified to be better than class 2 regarding particles, oil content and moisture content (ISO 8573-1, 2010).

Since the compression unit is substantial for the 150 bar gas rig, inquiries were made to five compressor suppliers and manufacturers. These five manufacturers offered 13 piston compressors. The list price range for the piston compressor was between 38,590€ and 296,000€. This represented an unexpected price difference of 257,410€ between compressors offered based on the same inquiry. Procurement could therefore not be done only based on only pricing. The compressors were initially evaluated based on the compressor KPI's in Table 6.

Table 6 Compressor Key Performance Indicators

Abbreviation	Compressor KPI's	Indicator for	Preference
KPI01	Net price in € in per pc.	Initial investment costs	Lowest
KPI02	Displacement rate in Nm ³ /hr	Time it takes to compress medium	Highest
KPI03	Max. pressure in bar.a	Suitability for application	Highest
KPI04	Rotation speed in min ⁻¹	Maintenance costs during operation	Lowest
KPI05	Power in kW	Operating costs	Lowest
KPI06	Acoustic pressure in dB	Noise pollution	Lowest
KPI07	max. inlet pressure in bar	Specification for screw compressor	Lowest

Color scales were used for selection in the first instance with green indicating a preference and red indicating non-preference in Table 7.

Table 7 Piston compressor selection using color scales

#	Description	1	2	3	4	5	6	7
KPI01	Net price in € in per pc.	163,305	52,520	45,040	43,260	38,590	167,000	103,050
KPI02	Displacement in Nm ³ /hr	700	293	280	190	200	250	330
KPI03	Max. pressure in bar.a	64	80	80	100	100	71	350
KPI04	Rotation speed in min ⁻¹	600.0	1800.0	1800.0	1800.0	1800.0	380.0	1485.0
KPI05	Power in kW	90.0	87.0	87.0	64.0	64.0	55.0	75.0
KPI06	Acoustic pressure in dB	82.0	94.0	96.0	88.0	90.0	85.0	91.0
KPI07	max. inlet pressure in bar	7.0	8.0	8.0	8.0	8.0	6.0	10.0
#	Description	8	9	10	11	12	13	
KPI01	Net price in € in per pc.	118,250	129,000	296,000	158,000	146,000	102,000	
KPI02	Displacement in Nm ³ /hr	210	330	660	204	285	285	
KPI03	Max. pressure in bar.a	150	150	100	201	101	150	
KPI04	Rotation speed in min ⁻¹	1180.0	1095.0	1230.0	1230.0	517.0	451.0	
KPI05	Power in kW	75.0	75.0	150.0	90.0	84.0	14.2	
KPI06	Acoustic pressure in dB	90.0	93.0	95.0	95.0	85.0	85.0	
KPI07	max. inlet pressure in bar	1.0	10.0	8.0	8.0	1.0	80.0	

Most compressors in Table 7 required pressurized gas at the compressor intake. This meant that it was necessary also to use a screw compressor upstream of the piston compressor. The screw compressor should work in tandem with the piston compressor. The selection of the best-suited compressor using color scales was also not reliable as seen in Table 8.

Table 8 Screw compressor selection using color scales

#	Description	14	15	16	17
KPI01	Net price in € in per pc.	28,000	24,925	18,495	5,750
KPI02	Displacement in Nm ³ /hr	771	486	301	75
KPI03	Max. pressure in bar.a	12	15	15	20
KPI04	Rotation speed in min ⁻¹	2593.0	2980.0	2980.0	2950.0
KPI05	Power in kW	110.0	76.0	75.0	15.0
KPI06	Acoustic pressure in dB	73.0	75.0	45.0	70.0

Color scaling could not identify the most suitable compressor reliably, as seen in Table 7 and Table 8, e.g., while compressor 5 in Table 7 had the lowest list price, it had low displacement rates and very high rotation speeds. Additionally, while compressor 1 had the highest displacement rate, it had the lowest maximum operating pressure. Complex interdependency between the compressor KPI's was identified.

To counter this challenge of identifying the best-suited screw compressor and piston compressor, Specific Cost-Performance-Indicators, CPI's to compare the compressors were there proposed and used to select the most suitable compressor based on initial investment and operational costs as presented in eq.(23) through eq.(25).

Table 9 Specific Investment Cost Performance Indicator (CPI01)

Name	Specific Investment Cost Performance Indicator
Abbreviation	CPI01
Formula	$CPI01 = \frac{KPI01}{KPI02 \times (KPI03 - KPI07)} \left[\frac{\text{€}}{\frac{\text{m}^3}{\text{h}} \cdot \text{bar}} \right] \quad (23)$
Indicator for	Investment costs for every bar compressed at a given displacement rate.
Preference	Lowest

Table 10 Specific Investment Cost Performance Indicator (CPI02)

Name	Specific Energy Cost Performance Indicator
Abbreviation	CPI02
Formula	$CPI02 = \frac{KPI05 \cdot 1h}{(KPI03 - KPI07) \cdot KPI02} \left[\frac{\text{kW} \cdot h}{\text{bar} \cdot \frac{\text{m}^3}{\text{h}}} \right] \quad (24)$
Indicator for	Energy consumption in one hour, for every bar, compressed at a given displacement rate
Preference	Lowest

Table 11 Specific Operational Cost Performance Indicator (CPI03)

Name	Specific Operational Cost Performance Indicator
Abbreviation	CPI03
Formula	$CPI03 = CPI02 \times E_{\text{cost}} \left[\frac{\text{€}}{\frac{\text{m}^3}{\text{h}} \cdot \text{bar}} \right] \quad E_{\text{cost}} \text{ in } \frac{\text{€}}{\text{kWh}} \quad (25)$
Indicator for	Operational costs in for every bar compressed at displacement rate
Preference	Lowest

Unique *Relative Cost Performance Indicator* RCPI was finally formulated from the CPI's and applied to compare various compressors with dimensionless values between 0 and 1. Here a value 0 represents the best-suited compressor, while value 1 represents the least suited compressor option.

Table 12 *Relative Cost Performance Indicator (RCPI)*

Name	Relative Cost Performance Indicator
Abbreviation	RCPI
Formula	$RCPI = \frac{1}{2} \cdot \left[\frac{CPI01_i}{\max(CPI02_i)} + \frac{CPI03_i}{\max(CPI03_i)} \right] \quad i = 1 \dots N \quad (26)$
Indicator for Preference	Dimensionless Relative Cost Performance Indicator Lowest

Compressor 7 (*Bauer GIB24 12 -75*) is the most suited piston compressor based on the Relative Cost Performance Indicator (RCPI) calculated per eq.(26) with the compressors in Table 7 as seen in Figure 15.

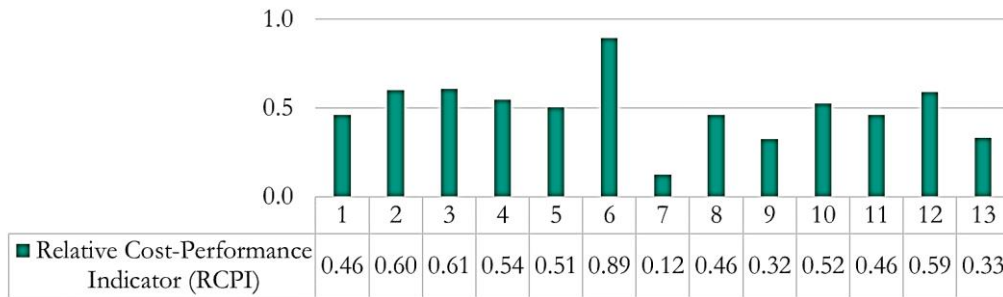


Figure 15: RCPI comparison of the 13 piston compressors [-].

Compressor 15 (*Renner RSF 75-12*) is the most suited screw compressor based on the Relative Cost Performance Indicator (RCPI) calculated per eq.(26) with the compressors in Table 8, as seen in Figure 16.

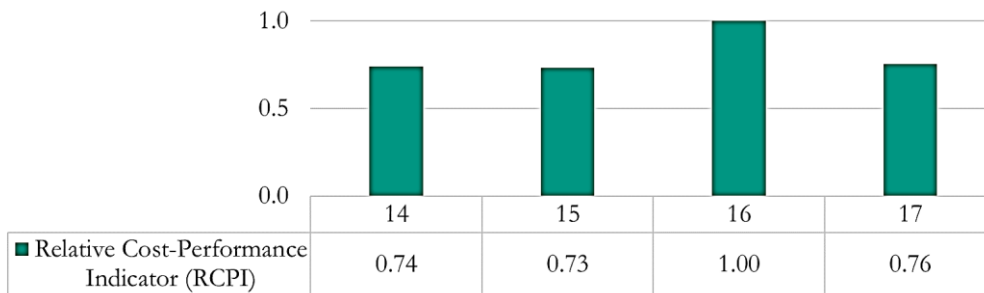


Figure 16: RCPI comparison of 4 screw compressors [-].

All compressors were further configured in detail with the respective suppliers to meet the specification about the compressed air quality and functionality. A pressure vessel B-K-01 (V=3.6 m³) was installed to act as a buffer between the two compressors.

4.4 Design of flow rate measurement and pressure regulation unit

Various conventional flow measurement techniques were considered: i. differential pressure flowmeters (e.g., orifice plate, flow nozzle, venturi meter) ii. velocity flowmeters (e.g., turbine, vortex shedding, swirl, electromagnetic, ultrasonic) iii. mass flowmeters (e.g., Coriolis, thermal or gravimetric flow measurement). Coriolis flowmeters were identified to be the most suited in the feasibility study by (Mutegi, 2014). This technique is a state-of-the-art flow measurement and offers direct mass flow rate measurement capability. The devices are also very compact.

Upon comparison of devices from various manufacturers. Endress+Hauser Promass F 300 Coriolis flowmeters were considered to have the most suitable measurement range to fulfill the requirements in this work. Four devices with DN150 (FI-301), DN80 (FI-302), DN40 (FI-303), and DN25 (FI-304) all in PN100 were found to cover the identified measurement range best. PN100 was the highest pressure rating listed in the manufacturer's standard product catalog at the time of selection.

The measurement range with uncertainty of measurement U , less than 0.5% of range ($U < 0.5\%$ o.r), is highlighted in green in Figure 17 below. The broken lines in blue, orange, purple and black represent the measurement range of FI-301, FI-302, FI-303 and FI-304, respectively. The horizontal lines represent the lowest measurable flow rate with $U < 0.5\%$ o.r, while the angled lines represent the highest measurable flow rate with $U < 0.35\%$ o.r. The thick and continuous angled line in green represents the maximum measurable flow rate when all the four devices are operated in parallel with $U < 0.35\%$ o.r. The data used to plot the measurement range of the flow measurement unit in Figure 17 is in ANNEX II.

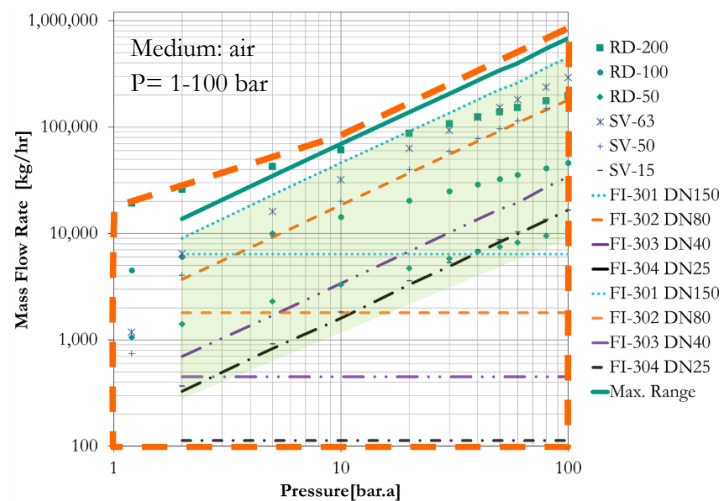


Figure 17: Measurement range of flow measurement unit with $U < 0.5\%$ o.r. with data in Table 41 through Table 44.

The flow measurement unit has a design pressure of 100 bar because of the pressure rating of the Coriolis flowmeters. The pressure vessels, B-06 and B-07 have a design pressure of 150 bar. It was therefore necessary to install pressure regulators upstream of the flowmeters to reduce pressure from 150 bar to a maximum of 100 bar.

It was also necessary to install pressure regulators downstream of the flowmeters to regulate the pressure in the test vessel (B08, $V=5.5 \text{ m}^3$) from a maximum of 100 bar to ambient pressure. The nominal pressure regulation range is highlighted in green in Figure 17. The extended pressure regulation range is marked with orange borders in Figure 17. The latter is necessary to increase the capacity of the 150 bar gas rig in the future.

This pressure regulation range was challenging and only one manufacturer offered a solution. The supplier offered two pressure valves upstream of flowmeters; CV301 (DN150 PN150) and CV302 (DN100 PN150) and three control valves downstream of the flowmeters; CV306 (DN250 PN100), CV307 (DN150 PN100) and CV308 (DN25 PN150). To allow for future capacity expansion, an extra control valve CV308 (DN80 PN100) may also be installed optionally downstream of flow-meters. A decision was made to install only CV302, CV307 and CV308 and install the rest in future expansion stages.

4.5 Design of the two-phase rig

To attain two-phase capability in the 150 bar loop, a two-phase rig was designed as illustrated in the Process Instrumentation Diagram (PID) in Figure 24. The design of the two-phase rig in zone 400 does not require the use of pumps since propulsion is by using compressed air from B-K-01 ($V=3.6 \text{ m}^3$) in zone 200 to displace water.

The construction and commissioning of the two-phase rig designed was abandoned at this point and scheduled for implementation in the future due to operational reasons. A laboratory-scale two-phase pilot rig was therefore implemented with the existing inventory below to study two-phase flow in rupture disks (see also: chapter 4.11).

4.6 Process and Instrumentation Diagram (PID) of the 150 bar loop

The design of the 150 bar gas rig involved a rigorous and intensive process involving communication between all the suppliers. The resulting design with all the requisite components was documented in the form of a Process and Instrumentation Diagram. The design involved multiple parts in multiple functional units.

The 150 bar gas rig was therefore subdivided into 3 zones during design based on the identified functional units. Zoning made it possible to know where various fittings are installed easily. Zone 100-199 was allocated to the buffer vessels, zone 200-299 to the compression and gas conditioning unit, zone 300-399 to the flow measurement and pressure regulation unit, and zone 1000 was allocated to the test section with test bench 01-A and test bench 01-B.

These main design functional units are highlighted as various zones based on the resulting PID of the 150 bar gas rig in Figure 27. The Process Hazard Analysis and Safety Concept for the entire 150 bar rig has already been incorporated in the PID in Figure 27, as described in chapter 4.7. Unless otherwise stated, piping and fitting are according to ASME standards.

4.6.1 Buffer tank unit in zone 100

The buffer tank section in the CSE HP loop (150 bar stage) consists of the tanks (B06) and (B07), which are designed for a pressure of 156 bar g and have a volume of 25.2 m^3 and 37.3 m^3 respectively. The tanks are fed from the compressor part through feed lines and serve as a buffer for the test medium. The buffer tank section is controlled by the control valves (CV202, CV205, CV251) from the compressor section, which are monitored by temperature sensors (TIz 101, TIz 102, TIz 103, TIz 104, TIz 151, TIz 152, TIz 153) and pressure sensors (PI 101, PI 102, PI 103, PI 151, PI 152, PI 153). The design of zone 100 is presented in detail as a PID diagram in Figure 18. A list of the main components in zone 100 is listed in ANNEX I. The following are the key features highlighted for zone 100:

1. Pressure vessel B06 and B07 have a 24" manhole each.
2. Pressure vessel B06 and B07 may be used independently by separating them at the connection between nozzle S05 on B07 (10") and nozzle S18 on B06 (10").
3. Upon separation, B06 may be used as a test vessel. It has blinded test flanges in DN200, DN50.
4. The exit nozzles are equipped with 8" (Cl. 1500) valves. Smaller valves 1" (Cl. 1500) are installed in a by-pass to preserve the mechanical integrity of these valves. The smaller valves should be used to reduce the pressure ratio across 8" valves.

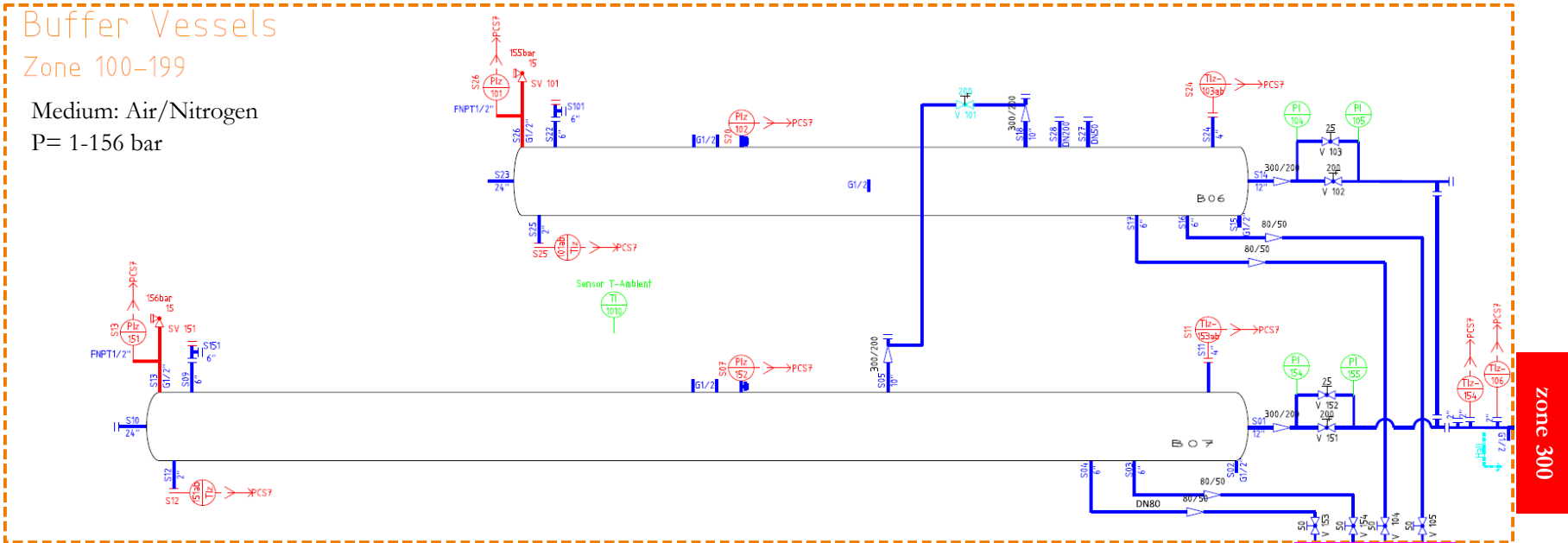


Figure 18: PID of buffer vessels in zone 100 covering an area of about 310 m².

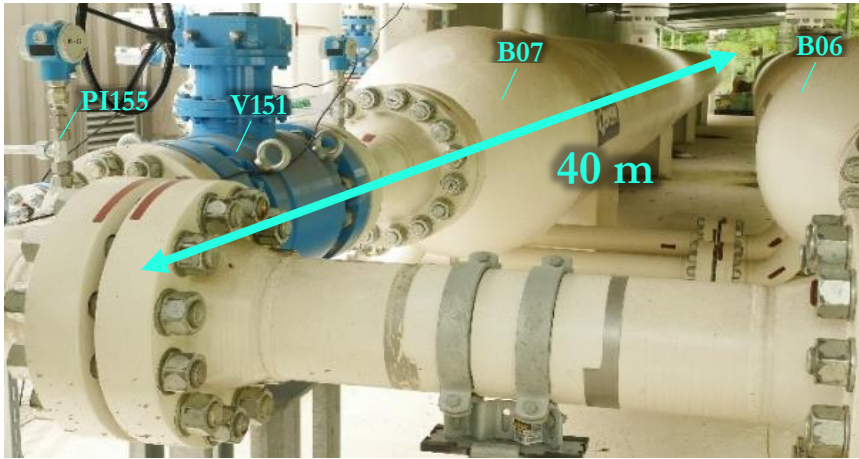


Figure 19 Images of selected components in zone 100.

4.6.2 Compression and gas processing unit in zone 200

The compression unit in the CSE HP loop (150 bar stage) consists of two separate stages, which are used to fill the buffer tanks B06 and B07. In the first stage, the medium is pre-compressed in a screw compressor (RSF 75-15) up to a maximum of 15 bar, then the air is cleaned of oil and water and dried. To avoid impurities, an oil filter (RF-C 0750) is used to separate oil, and water is separated by a fine droplet separator (AC-0550). The shut-off valve (V201) is required for start-up and shut-down processes. After drying air in (HL MSD 550), the air in the second compression stage is compressed further to the selected pressure. This is done by a piston compressor (GIB 24.12-75), which is supplied with cooling water by a pump (CY-6091) and an air cooler (GFH 067B). Screw compressor and piston compressor are connected via a pressure vessel (B-K-01). It is a surge tank to buffer air, especially for start-up and shut-down processes, in order to provide enough initial pressure for the piston compressor. After the medium has been compressed to the maximum pressure of 156 bar.g, the air must be purified again (AKC-0870). The piston compressor can be bypassed via a bypass through the shut-off valve (V203) if tests are to be carried out up to a maximum of 15 bar only. Furthermore, there is a branch through the shut-off valve (V253), which is designed as the interface for the 700 bar loop (see also: Figure 20). The compression section is controlled by the control valves (CV202, CV205, CV251) and the compressor control units, which are monitored by the temperature sensors (TI201, TI204) and pressure sensors (PI201, PI202, PI203, PI204, PI205).

The entire air treatment and compressor unit is installed as a separate module in two containers. The operator can read operating states and error messages and operate the compressors directly. The main system parts in Zone 200 are listed in Table 46. The design of zone 200 is presented in detail as a PID diagram in Figure 20. A list of the main components in zone 200 is listed in ANNEX IV. The following are the key features highlighted for zone 200:

1. The compressor RSF 75-15 runs independently and is used to compress B06 and B07 to a pressure of 15 bar. For this, a bypass for the piston compressor was implemented between V202 and V254
2. Most of the moisture separated with the RF-C 0750 and cyclone separator
3. The dew point of the unit is designed to be below -50°C to ensure the air downstream has humidity below $0.11 \text{ gm}/\text{m}^3$ downstream of the HL MSD 550 drier unit.
4. The residual oil content downstream of AKC-0550 active-carbon adsorber is designed to be below $0.04 \text{ mg}/\text{m}^3$
5. The piston compressor GIB24. 12-75 intake is connected to B-K-01; it should only run if the screw compressor is online.
6. The piston compressor GIB24. 12-75 can compress both air and nitrogen up to 350 bar. It is set-up currently to stop compression at 150 bar.
7. The residual oil content downstream of the two AKC-0870 active-carbon adsorbers is designed to be below $0.04 \text{ mg}/\text{m}^3$ as specified.

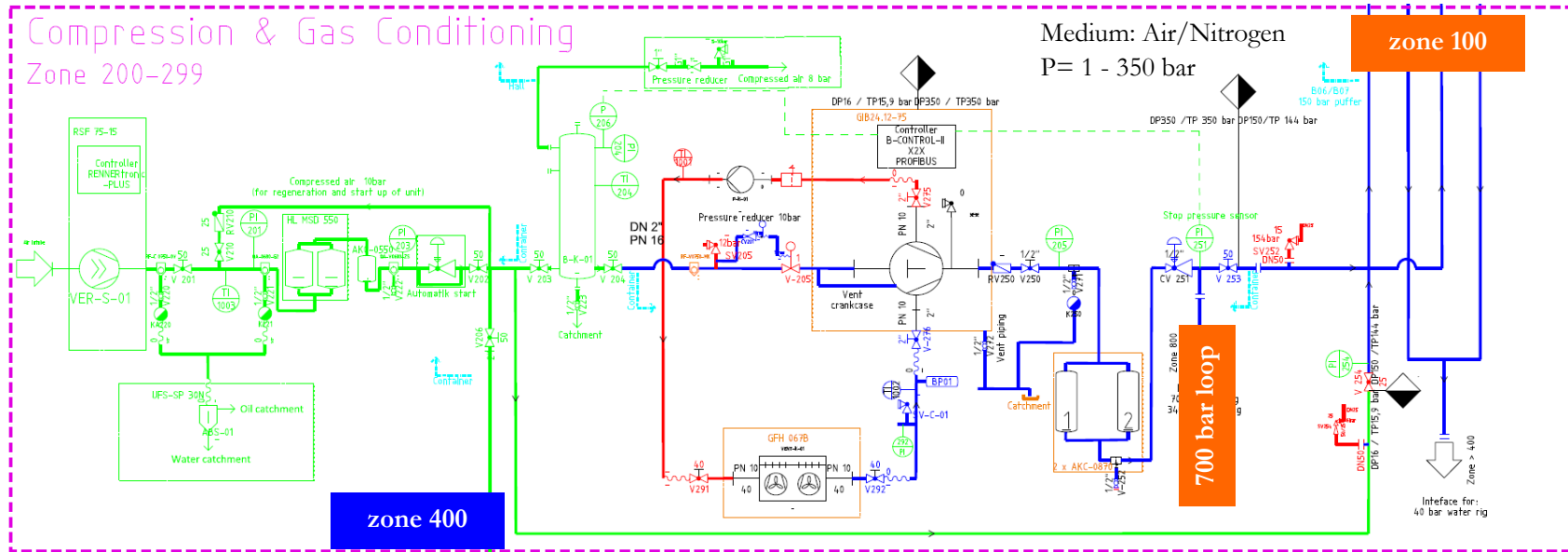


Figure 20: PID of compression and gas processing in zone 200, covering an area of about 50 m².



Figure 21 Images of selected components in zone 200

4.6.3 Flow measurement and pressure regulation unit in zone 300

The buffer tanks (B06) and (B07) supply the flow measurement and pressure control unit with air at a maximum pressure of 156 bar. Flow measurement and pressure regulation unit has a design pressure, DP=100 bar g. Therefore, control valves (CV301, CV302) with the functionality of reducing the pressure from 156 bar to a maximum of 100bar are installed upstream of the flowmeters. The flow measurements (FI301, FI302, FI303, FI304) can be selected for use via the shut-off valves (V304, V305, V306, V307) depending on the required capacity. The pressure regulation for tests is implemented with the control valves (CV306, CV307, CV308). All control valves can be controlled by the operator via a 0-20 mA signal. The safety-relevant shut-off valve (V310) is also controlled via a 0-20 mA signal. (V310) should be shut in case of any anomaly. The design of zone 300 is presented in detail as a PID diagram in Figure 22. A list of the main components in zone 300 is listed in ANNEX V. The following are the key features highlighted for zone 300:

1. All parts downstream of (CV301, CV302) have a pressure rating of PN100 and below.
2. All control valves (CV302, CV307, CV308) fail by closing, e.g., when the compressed air supply pressure is low
3. All control valves can be controlled by the operator via a 0-20 mA
4. V-310 is the master shut-off valve for the 150 bar gas rig. It should be closed promptly during any anomaly. The valve also fails in the closed position.

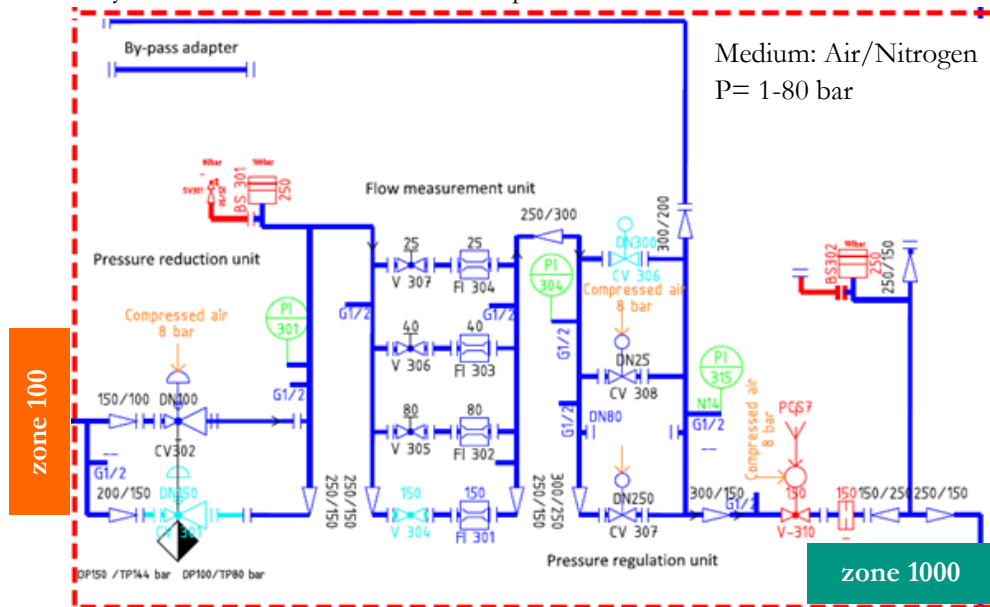


Figure 22: PID of flow measurement and pressure regulation in zone 300, covering an area of about 100 m².



Figure 23 Images of selected components in zone 300.

4.6.4 Two-phase rig in zone 400

Compressed air enters the two-phase sub-rig in zone 400 via control valve CV401 (DN25 PN16). The purpose of this control valve is to regulate the pressure in the gas puffer vessel B401 ($V=1.0\text{ m}^3$) to pressures below 15 bar. B401 has a pressure sensor (P401) and a temperature sensor (T401). The operator regulates the pressure at P401 with CV401.

A stainless steel water vessel B402 ($V=3.0\text{ m}^3$) is installed downstream of B401. B402 also has a pressure sensor P402 and temperature sensor T402. The operator regulates the pressure at P402 also with CV401. Pressure vessel B402 has a water intake flange where water is fed in at the highest point of the vessel. This flange is then closed before experiments.

Flow measurement in the water sub-loop downstream of B402 is by a Coriolis flowmeter FI405 (DN50 PN40). Flow measurement in the air sub-loop downstream of B401 is by a Coriolis flowmeter FI406 (DN25 PN40).

Air and water are fed into a mixer, which is connected to the test section described in chapter 4.9 (Rupture disk test section with measurement and instrumentation).

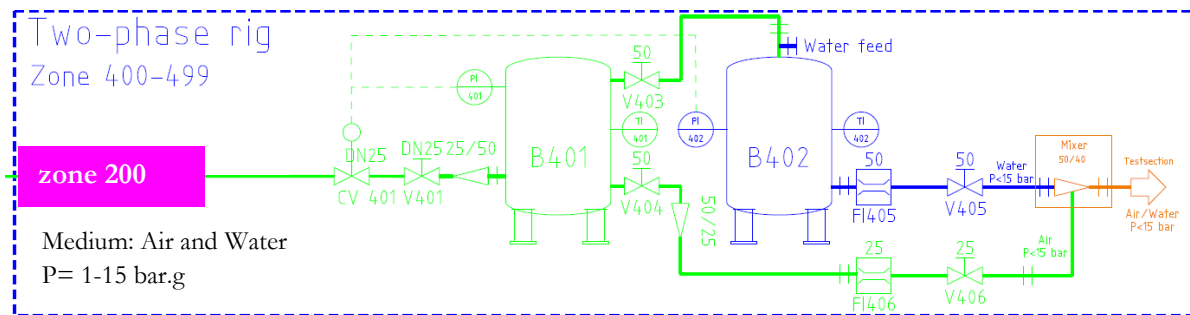


Figure 24 PID of the two-phase rig for tests with air/water at pressure up to 16 bar covering an area of about 100 m².

4.6.5 Test vessel unit in zone 1000

Zone 1000 is the zone where tests are done. It is fed with compressed air from zone 300. It has a pressure vessel (B08) with a design pressure, DP=100bar.g. Two DN400 test benches are installed on either side of the vessel. All experiments can be adapted to use these two test benches. The design of zone 1000 is presented in detail as a PID diagram in Figure 25. A list of the main components in zone 100 is listed in ANNEX VI.

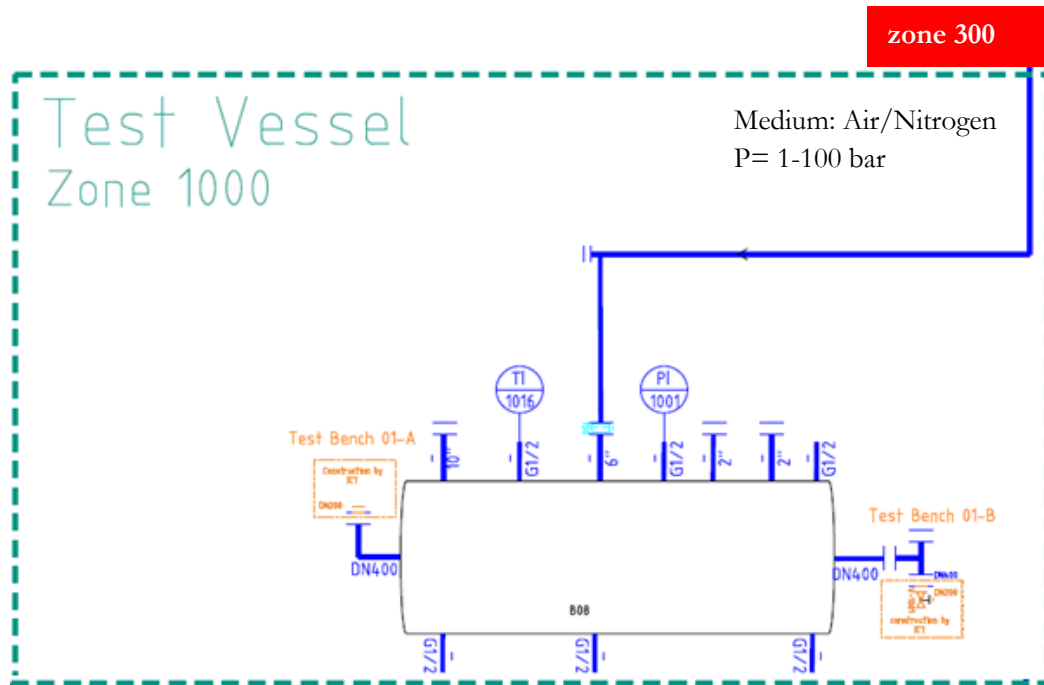


Figure 25: PID of the test vessel with test benches in zone 1000 covering an area of about 70 m².



Figure 26 Images of selected components in zone 1000.

The full design of the 150 bar gas rig is composed of zone 100, zone 200, zone300 and zone 1000. The main system parts in the 150 bar gas rig are listed in Table 45, Table 46, Table 47 and Table 49. The design of the 150 bar gas rig is documented in detail as the PID of the 150 bar in Figure 27. The PID was used by the company that was contracted to construct the test facility. This company first created a 3D-diagram of the 150 bar rig, fabricated the piping, and mounted the parts as specified in the PID.

4.6.6 Process and Instrumentation Diagram of the 150 bar loop

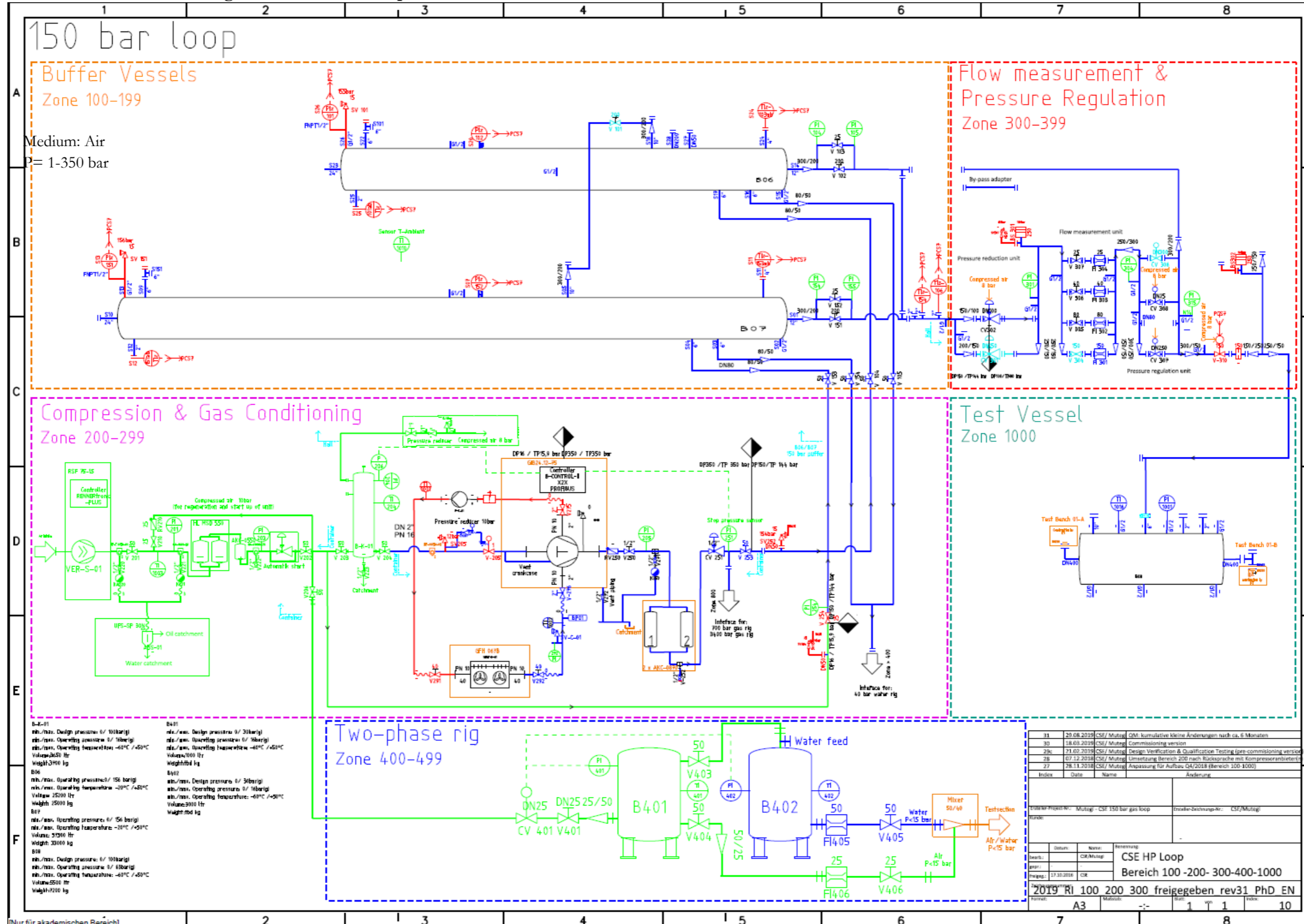


Figure 27: PID of the 150 bar loop covering an area of about 800 m².

4.7 Process Hazard Analysis and Safety Concept of the 150 bar loop

The following Process Hazard Analysis, (PHA) and the safety concept was done and implemented in the 150 bar gas rig as illustrated in the respective PID diagrams for zone 100 (Figure 18), zone 200 (Figure 20), zone 300 (Figure 22), and zone 1000 (Figure 25), and cumulatively in the PID of the entire 150 bar gas rig (Figure 27). The details are in ANNEX VIII (Process Hazard Analysis of the 150 bar loop).

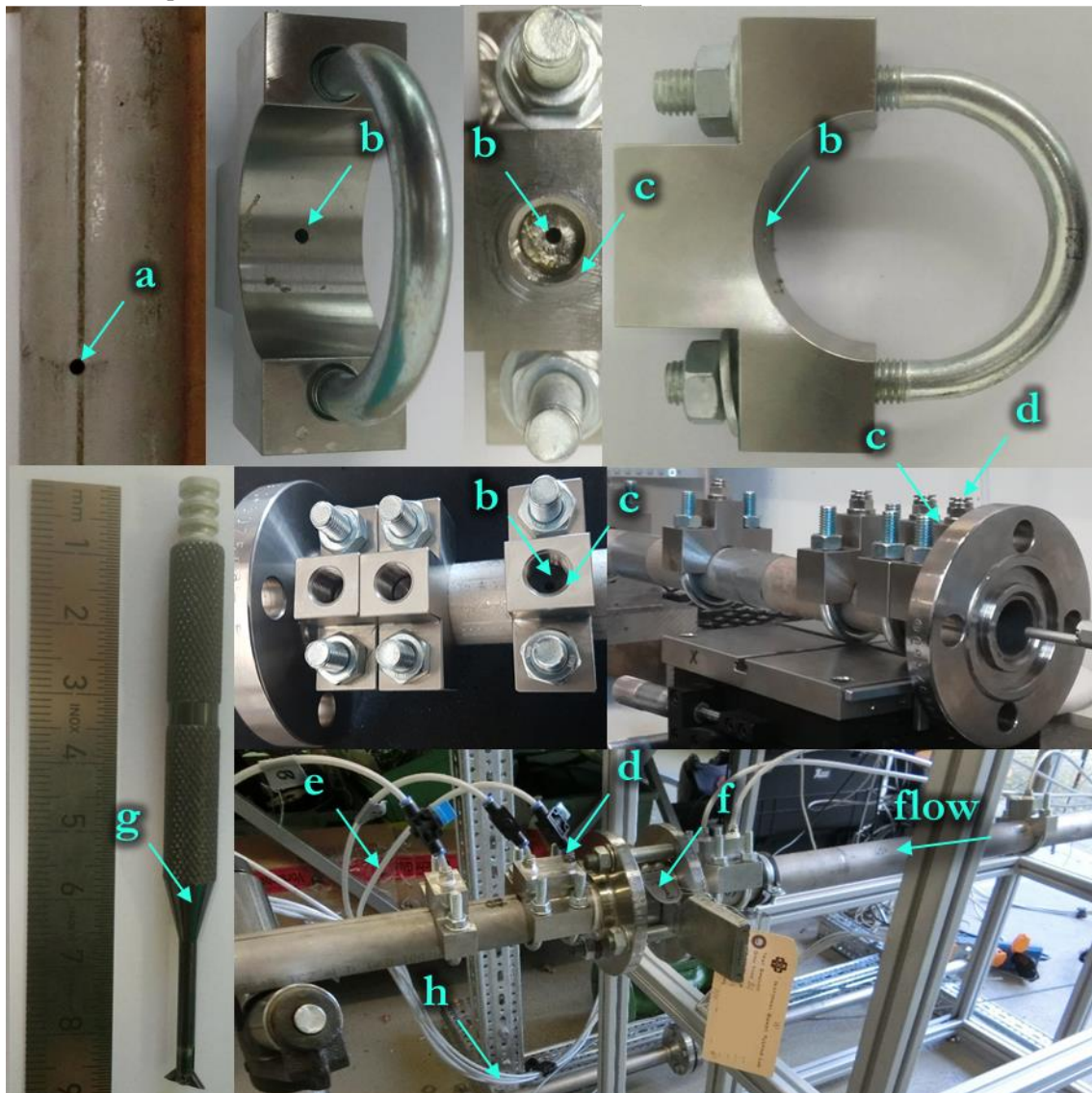
4.8 Operation manual of 150 bar gas rig

The operation manual of the 150 bar gas rig attached in ANNEX IX.

4.9 Rupture disk test section with measurement and instrumentation

The rupture disk test section and its measurement and instrumentation will be described below. The same test section was used with gas and air/water two-phase flow. The parts that form the test section are depicted in Figure 28 and the measurement and instrumentation are depicted in Figure 29.

Rupture disk test section parts are depicted in Figure 28. The test section consists of two straight precision circular stainless-steel pipe segments in DN25 ($D_i=26.64\pm 0.58$ mm) and DN40 ($D_i=40.90\pm 0.59$ mm). Precision steel pipes with material inspection certificates were used to guarantee low uncertainty in the determination of the inner pipe diameter. All the pressure probes in the test section are 3 mm bores that are deburred with a deburring gadget. Every probe has a clamp-on adapter that adapts the pressure probe to the joint where the 6 mm pneumatic tube is connected. This clamp-on adapter also has a 3 mm bore on the pipe side and a standard M14 joint on the opposite side. The pressure-probe bore and the clamp-on adapter bore are carefully centered and sealed. A Festo adapter (NPQM-D-G14-Q6-P1) is connected to the clamp-on adapter. Standard 6 mm pneumatic tube is connected to the Festo adapter and connected to the NetScanner 9116 pressure transducer.



- | | |
|--|---|
| (a) 3 mm bore on test section pipe | (e) Standard 6 mm pneumatic tube from (d) |
| (b) 3 mm bore on clamp-on adapter | (f) Rupture disk in test section (see also: Figure 2) |
| (c) Connection point for (d) with standard M14 joint | (g) Deburring gadget for (a) |
| (d) Festo adapter type NPQM-D-G14-Q6-P1 | (h) (e) to NetScanner 9116 pressure transducer |

Figure 28: Rupture disk test section parts.

The length of pipe between the test section inlet and pressure probe $P_{\text{tap},01}$ is within range of 60 inner pipe diameter lengths to ensure fully developed flow upstream of pressure probe $P_{\text{tap},01}$. The inlet segment has five pressure probes, $P_{\text{tap},01}$ through $P_{\text{tap},05}$.

Table 13: Location of pressure taps in DN25 and DN40 test sections.

	inlet	$P_{\text{tap},01}$	$P_{\text{tap},02}$	$P_{\text{tap},03}$	$P_{\text{tap},04}$	$P_{\text{tap},05}$	RD
DN25	0 m	1.569 m	1.969 m	2.110 m	2.330 m	2.344 m	2.404 m
DN40	0 m	2.470 m	3.110 m	3.320 m	3.670 m	3.710 m	3.795 m
	$P_{\text{tap},06}$	$P_{\text{tap},07}$	$P_{\text{tap},08}$	$P_{\text{tap},09}$	$P_{\text{tap},10}$	$P_{\text{tap},11}$	outlet
DN25	2.475 m	2.500 m	2.552 m	2.697 m	2.857 m	3.502 m	3.872 m
DN40	3.870 m	3.910 m	3.990 m	4.230 m	4.475 m	5.195 m	5.775 m

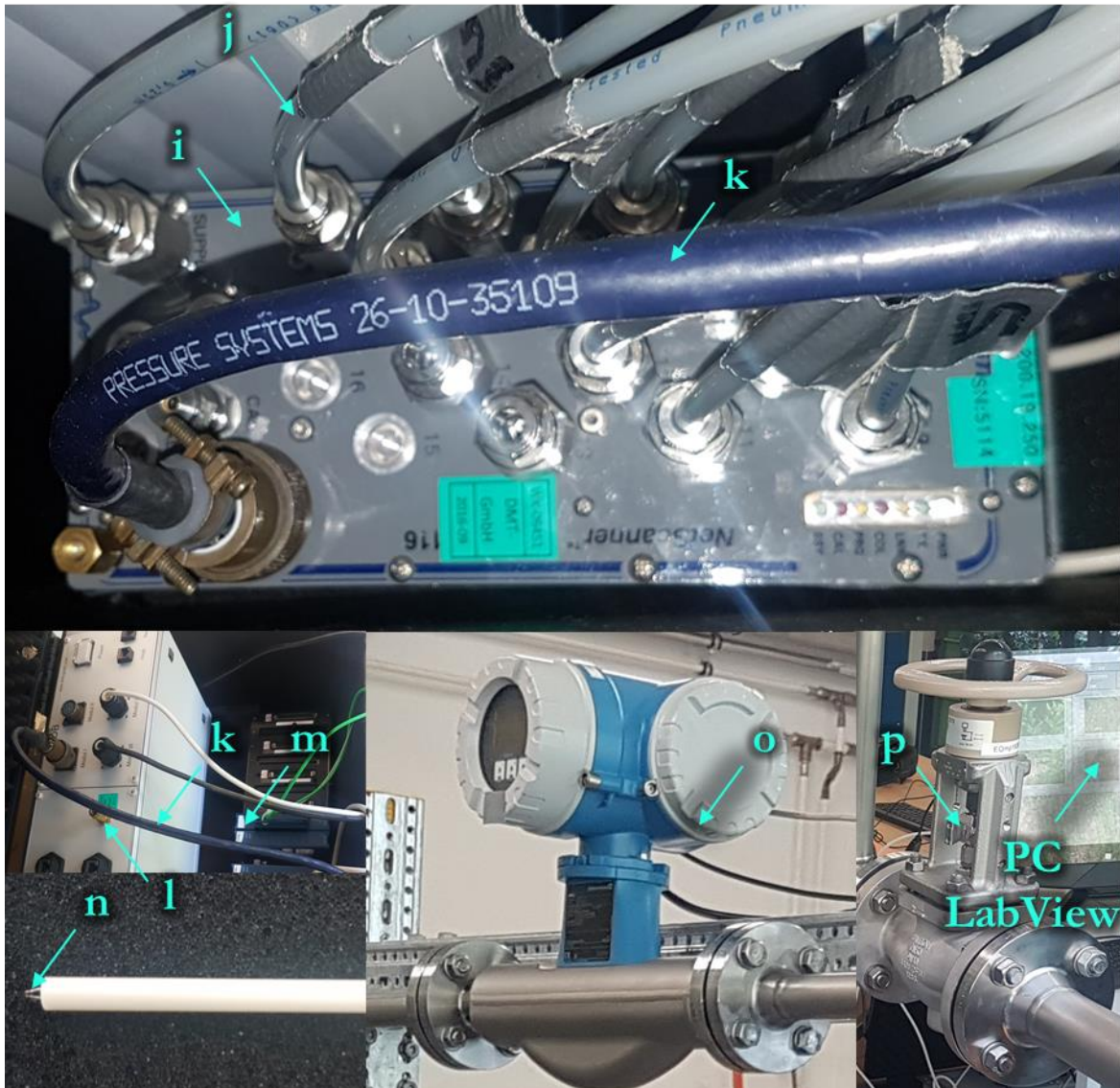
A rupture disk is installed centered 3 inner pipe diameter lengths downstream of pressure probe $P_{\text{tap},04}$ with its holder. The holder and the test object are carefully installed centered and sealed with tongue-and-groove flanges. The outlet segment downstream has 6 pressure probes, $P_{\text{tap},06}$ through $P_{\text{tap},11}$. Pressure taps $P_{\text{tap},05}$ through $P_{\text{tap},08}$ are in the separated flow region to measure the static pressure in the region around the rupture disk. Pressure probe $P_{\text{tap},09}$ is 10.64 inner diameter lengths from the test object to ensure that fully developed flow prevails consistent with the finding by (TORIZUMI, 1990), (Ebrahimi, et al., 2017), (Straka, et al., 2018).

The inner pipe roughness $k_s=R_z=13\cdot 10^{-6}$ m for the DN40 test section and $k_s=R_z=11\cdot 10^{-6}$ m for the DN25 test section. The pipe roughness is measured with a Hommel-Etamic T8000 device on the inner surface of the outlet pipe segment. The test section discharges to the environment freely.

Rupture disk test section measurement and instrumentation is depicted in Figure 29. The stagnation pressure is transmitted to the NetScanner 9116 pressure transducer with an air-tight, 6 mm pneumatic tube. The probe, T_b , to measure the stagnation temperature in the test vessel, is a NiCr-Ni (K) thermocouple without a guard tube to ensure fast response to changes in temperature. This probe constructively placed is in the middle of the vessel. The outer wall temperature probe T_{wall} is on the outer surface and is also of type NiCr-Ni (K). The ambient temperature probe T_a is an RTD (PT-100) probe. These three temperature probes are used to check that near adiabatic conditions prevail during experiments. The flow and temperature measurement based in National Instruments NI cFP-1808 Compact FieldPoint with two versatile temperature input modules. The module type NI cFP-TC-120 is for NiCrNi (K) thermocouples and the module type NI cFP-RTD-124 is for PT-100 thermocouples. A 8-Channel analog voltage and current input module of type NI cFP-AI-110 is used for flow measurement.

The 4 mA – 20 mA signal from the calibrated Coriolis flow measurement devices with error below 0.5 % FS (see: 0 and ANNEX XVII) is connected on two isolated channels on the NI cFP-AI-110 module. Thermocouples, T_b and T_{wall} are of type NiCrNi (K) while T_a is of type RTD (PT-100). The ambient pressure, P_a is measured with a calibrated precision pressure transducer of type Mensor CPT6100 (see: ANNEX XV). The stagnation pressure, P_b and static pressure measurements $P_{\text{tap},01}$ through $P_{\text{tap},11}$ are based on the Ethernet Intelligent Pressure NetScanner 9116, which is a pneumatic intelligent pressure transducer with up to 16 piezoresistive pressure sensors. The sensors used were selected and calibrated in a DAkkS accredited calibration laboratory (see: ANNEX XIV). All channels used in this work have uncertainty of measurement better than 3.0 mbar after re-zero in the measurement range. Re-zero, is a self-contained feature that sets the pressure of all transducers to the zero before the start of every experiment.

All signals from NI cFP-1808, Mensor CPT6100 and NetScanner 9116 are accumulated and finally acquired in a PC where a custom-made LabVIEW program runs. This program also helps the operator visualize key parameters such as the stagnation pressure and flow rate when regulating the flow and maintaining stationary conditions with precision control valve V-01 during experiments.



- | | |
|--|--|
| (i) Calibrated NetScanner 9116 pressure transducer | (m) NI cFP-1808 (with NI cFP modules) connected to (l) |
| (j) Standard 6 mm pneumatic tube from (d) | (n) Standard NiCrNi (K) thermocouple without guard |
| (k) Connection point for (i) to (l) | (o) Calibrated Endress+Hauser Promass 83F to (m) |
| (l) TCP/IP signal box to PC with Mensor CPT6100 | (p) Control valve (V-01) of type Samson Type 3241 |

Figure 29: Rupture disk test section measurement and instrumentation.

The pipe roughness measurements for the DN40 and DN25 test sections are attached in ANNEX XII and ANNEX XIII, respectively. The calibration certificates for NetScanner 9116 pressure transducer, Mensor absolute pressure sensor, DN50 Coriolis flowmeter and DN25 Coriolis flowmeter are attached in ANNEX XIV, ANNEX XV, ANNEX XVI, ANNEX XVII respectively.

4.10 Laboratory-scale gas pilot plant for test with air

The laboratory described below was also designed, constructed and used as a pilot-plant for experiments with gases. This laboratory runs with air and has 5 pressure vessels, each with maximum allowable pressure of 25 bar.g upstream of the motor-operated valve V-01. Compressed clean air enters the test section via V-01 and flow is then measured directly with a calibrated Coriolis flow measurement device of type Endress+Hauser Promass 83F. Two devices are available; one is in DN 25 (F-01) and the other in DN50 (F-02). Only one device is used at a time, depending on the required accuracy and the size of the test object. Flow is regulated manually with a precision control valve of type Samson Type 3241 in DN50 (CV01). The gas then enters the test vessel where the stagnation pressure and temperature are measured with P_b and T_b respectively. The test vessel has a capacity of 2.5 m³ and a maximum allowable working pressure of 25 bar.g. The vessel is protected from overpressure with a rupture disk. The stagnation pressure is measured on P_0 positioned at the top of the vessel.

The gas then flows into a carefully designed test section (See also: chapter 4.9) where pressure is measured at 4 locations upstream of test object and 7 locations downstream with probes $P_{tap,01}$ through $P_{tap,11}$. The test section is calibrated before the tests.

The pressure in the test vessel is gradually increased until the target pressure and stationary flow conditions are attained by gradually opening the precision control valve V-01, manually. These stationary flow conditions are then held constant for at least 5 seconds at a sample rate of 10 data-points per second, to collect at least 40 data points.

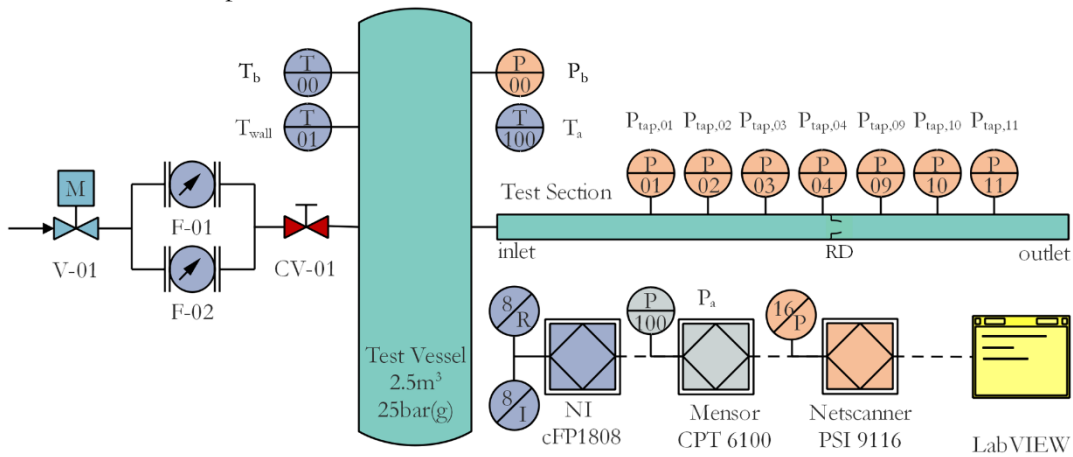


Figure 30: General overview of laboratory-scale gas pilot plant for test with air.

4.11 Laboratory-scale two-phase pilot rig for tests with air/water

The two-phase temporary test facility was designed as a pilot rig using existing inventory as illustrated in Figure 31 to implement experiments with air/water two-phase flow. The gas loop in the two-phase flow pilot rig test facility was connected to the 150 gas rig in zone 1000 at the test-bench 01-B downstream of V1002. The mass flow rate of air was measured with a Coriolis flowmeter FI-1001 (DN40 PN40). The flow rate was regulated with V-1010.

Compressed clean air enters the test section via V1001 in test bench 01-B in the 150 bar gas rig and flow is then measured directly with a calibrated Coriolis flow measurement device of type Endress+Hauser Promass 83F DN50 (FI1002).

The water source was a fire-fighting water hydrant (DN100). This hydrant delivered water at pressure below 5 bar.g. The mass flow rate of water was also measured with a Coriolis flowmeter FI-1002 (DN25 PN40). Mixing of air/water to generate two-phase flow was at the T-joint and at the control valve CV1012. The same test section and measurement and instrumentation as the one used for gas experiments, as described in chapter 4.9, is installed downstream of CV1012.

Table 14 Components in two-phase air/water temporary test facility

Component	Tag	Function/Technical data
Control valve	CV1012	Mixing of air and water
Flow measurement	FI1001	Flow measurement for test specimen
Flow measurement	FI1002	Flow measurement for test specimen
Shut-off valve	V1001	Open-Close
Shut-off valve	V1010	Open-Close
Shut-off valve	V1011	Open-Close

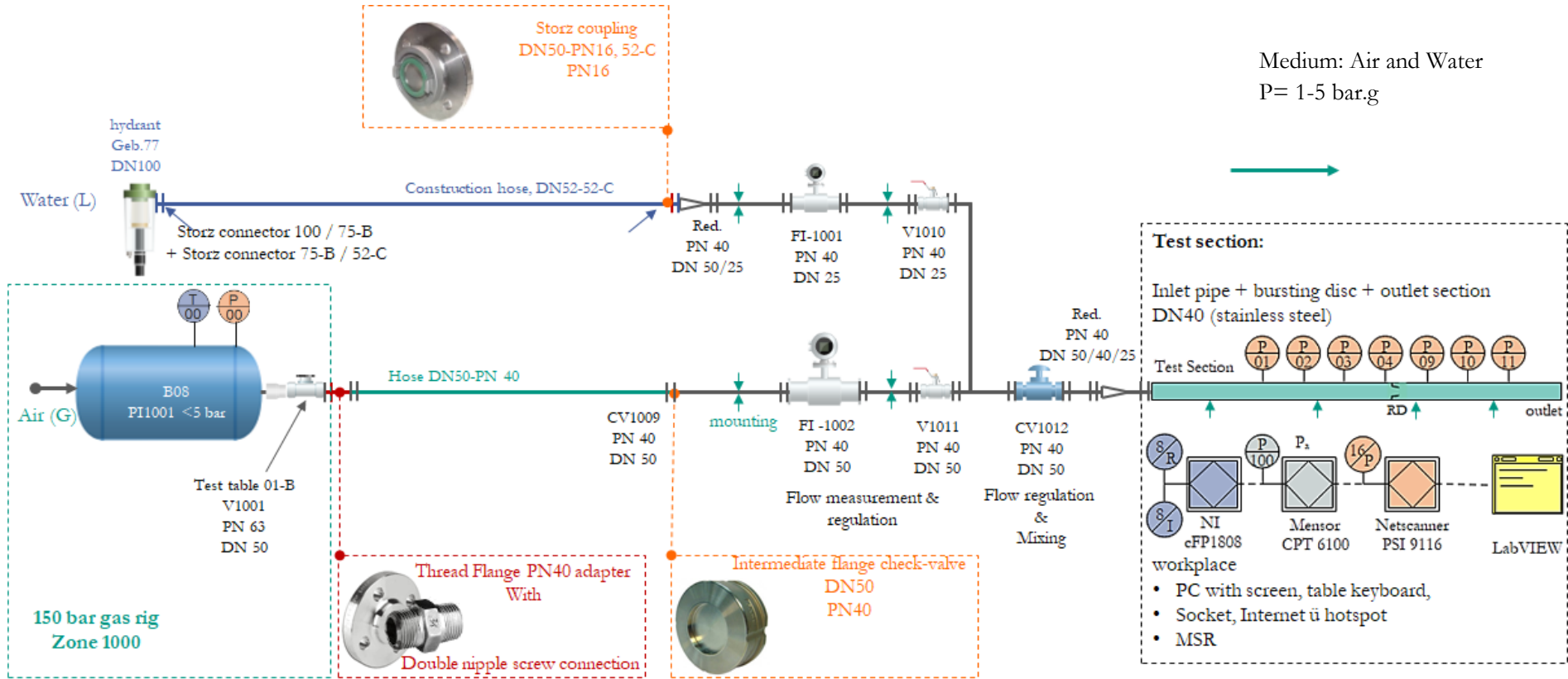


Figure 31: Layout of the two-phase flow pilot rig for tests with air/water up to 10 bar.

5 Development of a sizing procedure for rupture disk devices

A relationship to calculate the dischargeable mass flow rate through a rupture disk will be presented. This relationship is essential to determine the smallest rupture disk and pipe size, which fulfills the “dischargeable mass flow rate is larger than the minimum flow rate to be discharged” sizing criterion in sizing Step 4 in Table 1 to comply with regulations.

After that, a relationship to predict the pressure-drop will be presented as this is essential to achieve a detailed pressure-drop calculation in the entire rupture disk vent-line system to validate its capacity in sizing Step 5 in Table 1 to comply with regulations.

Flow phenomena in rupture disk devices based on their free relieving area and opening characteristic of a rupture disk will be visualized and investigated experimentally as a first step, to generate a better understanding of how a rupture disk interacts with fluid with a view to developing better and more reliable approaches for sizing rupture disk devices. Where possible, model parameters listed in Table 2 will be applied to develop models, methods or procedures for closing Gap II through Gap V. The advantages listed in Table 3 will be kept while the disadvantages will be countered in the following. The developed relationships will go beyond regulation and compliance to calculate the dischargeable mass flow rate and pressure-drop across a rupture disk from the point of rupture disk activation to the point when the system is fully depressurized seamlessly.

5.1 Visualization of flow through a rupture disk with experiments and CFD

A common technique to study flow phenomena in devices such as orifices, nozzles, bends, safety valves is to visualize flow either experimentally (Schmidt, 1993), (Shannak, 1998), (Diener, 1999) or with CFD-models (Beune, 2009). Flow phenomena such as separation and restriction of flow in a rupture disk will be visualized in the following to study differences in visualizations of flow through orifices (Ebrahimi, et al., 2017), (Straka, et al., 2018). This is particularly useful to identify the most suited model representation for a rupture disk with restriction model, orifice-model or nozzle model as possible model representations. This is crucial for developing models that consider flow phenomena in rupture disk devices properly. The experiments in this section were done with the test section and measurement and instrumentation described in chapter 4.9 in the laboratory-scale gas pilot plant described in chapter 4.10 with air.

5.1.1 Visualization of flow with experiments

An open rupture disk device was installed in a test section and the static pressure in the center of the pipe cross-section P_{center} was measured continuously under stationary flow conditions with the test facility illustrated in Figure 30. A pressure probe was installed centered and moved carefully from the outlet, through the rupture disk, to the upstream end at a speed of about 2 mm/s in a suited test arrangement (Schmidt, 2016) to do this. (See also: Figure 90 in ANNEX X).

The line plots in Figure 32 represents the static pressure measured experimentally at about 2 mm intervals continuously with the pressure probe in the middle of the pipe, while the scatter plot represents the static pressure measured at the wall pressure taps. P_{wall} is marked with points, while P_{center} is marked with lines in Figure 45. These measurements were taken under stationary flow conditions with air.

Figure 32 is the pressure profile in the entire test section while Figure 33 is the zoom-in Figure 32 in the region near the rupture disk device. Flow 2D upstream of rupture disk and about 4D downstream of rupture disk is disturbed. The intensity of the point with the lowest pressure, Vena-contracta, increases with upstream pressure (increasing flow rate). The Vena-contracta also moves towards the rupture disk installation plane with an increase in pressure as seen in Figure 33. Flow is seen to be fully developed up to about 2D upstream of a device inlet. Flow is accelerated rapidly from about 2D upstream, to the installation plane and further downstream of rupture disk in closest proximity. This is characterized by the sharp drop in pressure which is typical for the formation of a Vena-contracta; therefore, a rupture disk is subject to flow separation and restriction. The flow is seen to recover almost fully after about 6D downstream of the device. The axial pressure measurement with classic wall pressure taps (see also: Figure 28) is enough to capture the pipe pressure profile.

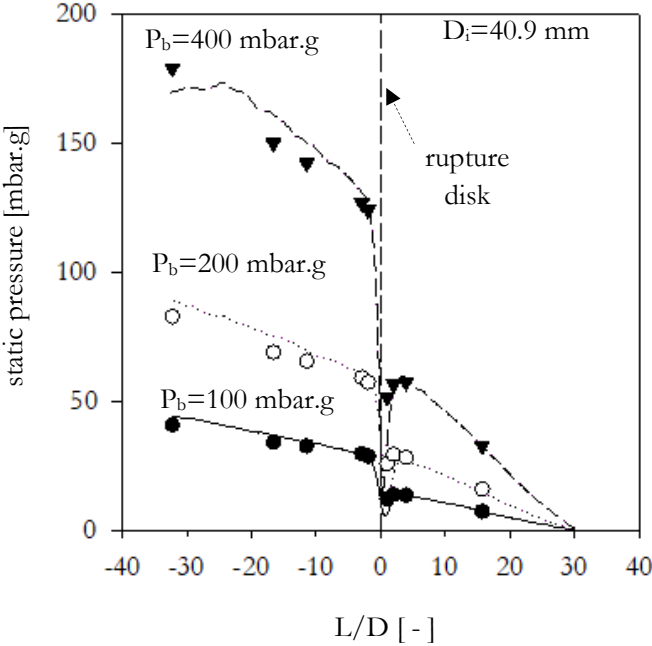


Figure 32 Continuous line showing the measured static pressure at the center of pipe with a rupture disk installed with the points showing the pressure measured with the wall pressure taps (see also: Figure 28).

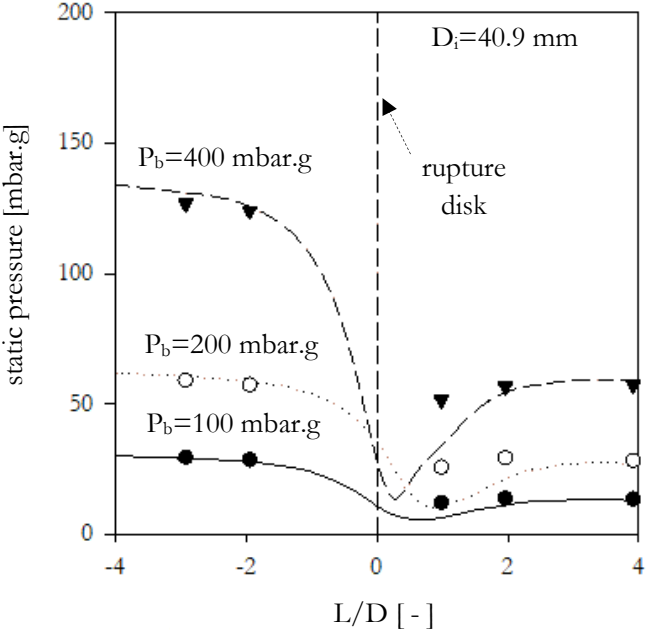


Figure 33 Zoom of Figure 32 showing the position of the point with the lowest static pressure near the rupture disk.

5.1.2 Visualization with CFD simulations

To further visualize flow restriction across a rupture disk, an activated DN25 rupture disk was digitalized and implemented in Siemens Star CCM+ CFD code. Computational fluid dynamics (CFD) is a powerful fluid mechanics approach for undertaking flow phenomena studies using numerical analysis. It has been successfully applied in diverse applications such as airplanes, cars, heat-exchangers, orifice, safety relief valves, etc.

CFD-studies have various advantages against experimental studies (Ebrahimi, et al., 2017). They are alternatives to cost-intensive prototyping (Straka, et al., 2018) and studies can be done even with hazardous substances. To enjoy these advantages, a methodology to generate a realistic 3D model of an open rupture disk was necessary. The challenge was to develop a reliable method to acquire a realistic 3D model of an open rupture disk to deliver precise insights regarding flow phenomena using CFD.

Figure 34 is the image of an open rupture disk device. The following steps were followed to generate the rupture disk 3D model for use in CFD simulations (Blank, 2018).

I Black oxidation:

Since the rupture disk had a reflective surface, and it would not be suitable for 3D-laser scanning, a thin layer of cold black oxide was applied. *Result:* Figure 35.

II 3D Laser scanning:

The blackened rupture disk was scanned with a 3D-Laser-Scanner. The distance between two points in the scanner should be smaller than the sheet thickness so that the 3D model can then be derived automatically. Otherwise, the rupture disk should be scanned from the backside in flow direction to avoid ambiguity in the surface definition. Figure 36 shows the implementation with “Romer Absolute Arm Scanner with FP1 Scanning Pack”. The Software combines the scanner operating program with the post-processing tasks for the raw data (Figure 36). *Result:* Point cloud in Figure 37 & Figure 38 with over 1.57 million measuring points.

III Triangulation:

The most important parameter when cross-linking the measuring points with triangular surfaces is the maximum number of triangles supported by the scanner software. The higher the limit, the finer the mesh and the more precise the geometry. The surface model shown in Figure 39 was generated with 100,000 triangles. *Result:* Raw surface model in Figure 39 with almost one million triangles.

IV Post-processing:

After triangulation, errors became visible in the surface model, e.g. holes and heels or individual outliers that lead to sharp-edged surfaces on the surface model. These are deleted and new elements are inserted into the resulting holes. The file is saved in .STL format. *Result:* Detailed surface in Figure 39 & Figure 40.

V 3D-model generation:

The STL file is imported into a CFD-3D-Model and re-meshed. The distance between two points in the 3D scanner caused ambiguity in the definition of surface because of the rupture disk’s small rupture sheet thickness of 0.1 mm. The back-surface was, therefore extruded by 1 mm first to make surface errors larger and more visible in the surface model after import (Figure 41). Errors were selected and deleted. The resulting holes in the geometry were closed. Once all errors were corrected, the surface model was extruded by 0.1 mm to match the original sheet thickness. *Result:* Final error-free 3D-model of rupture disk in Figure 42.



Figure 34: Open rupture disk device.

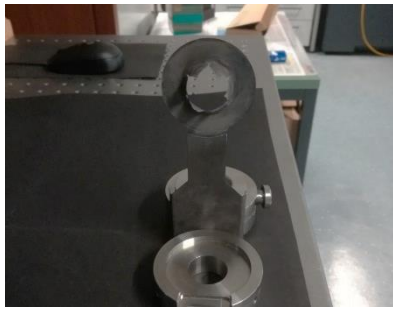


Figure 35: Black oxidization to make surface non-reflective.

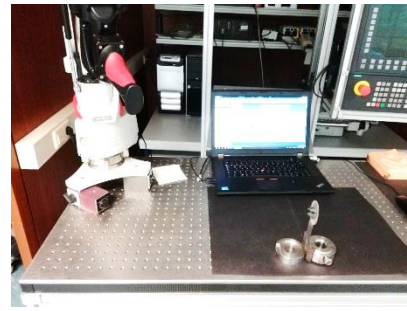


Figure 36: 3D-Laser scanning courtesy of Karlsruhe University of Applied Sciences.

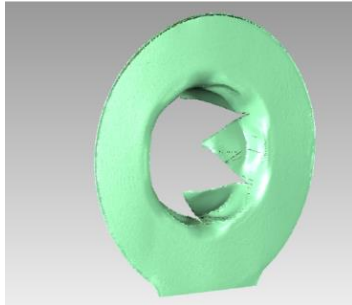


Figure 37: Raw data as point cloud from 3D Scanner.

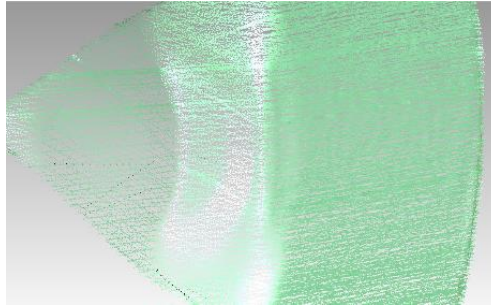


Figure 38: zoom of Figure 37 showing the detailed point cloud.

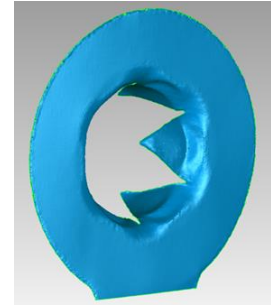


Figure 39: Surface model generated after triangulation.

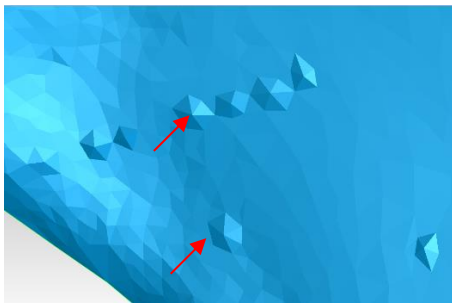


Figure 40: Arrows pointing to surface errors in the surface model.

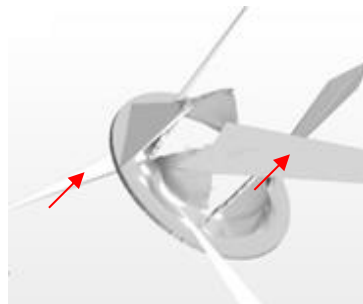


Figure 41: Enlarged surface errors after extrusion of the surface by 1 mm

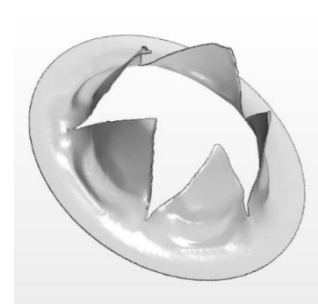


Figure 42: Realistic 3D model of rupture disk in Figure 34.

The results after implementation in a suited CFD code are presented in Figure 43 where Mach-number is plotted (Blank, 2018), (Kacic & Nitschke, 2018), (Flösch & Klumpp, 2019). The models selected are as illustrated in Figure 91 in ANNEX XI. Color blue indicates low-velocity flow regions, while color red indicates high-velocity flow regions as per the color-scale in Figure 43.

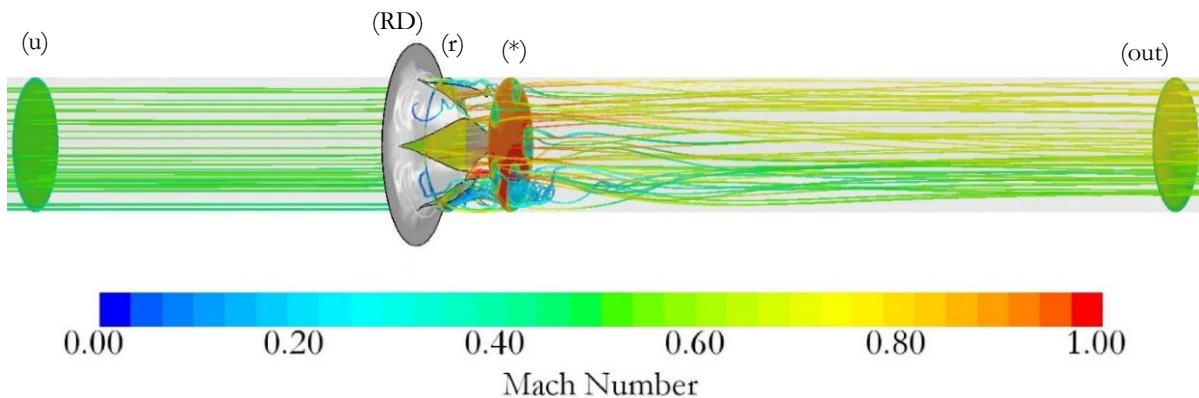


Figure 43: Angular perspective view of an open rupture disk with various reference locations.

Looking at Figure 43, the presence of an open rupture disk causes significant acceleration of flow between the rupture disk installation plane at (RD), through a location downstream at (r), to a cross-section with the highest velocity at (*). Flow downstream of (*) then expands and recovers.

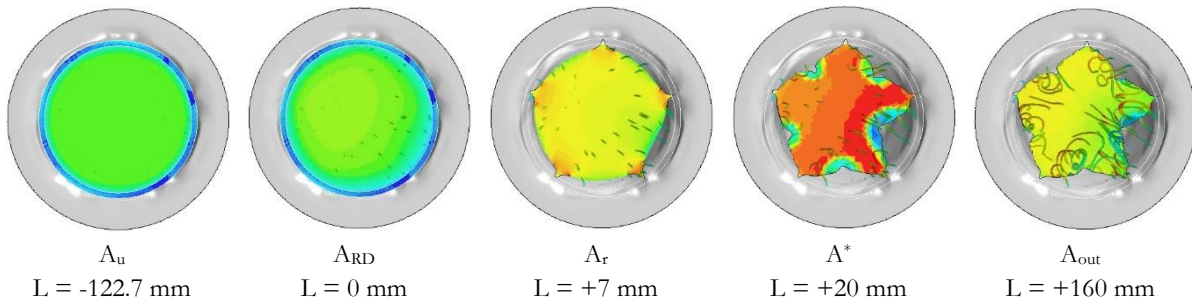


Figure 44 Back-view of an open rupture disk device at reference locations (u), (RD), (r), (*) and (out).

There is a significant increase in velocity between locations (RD) and (r), even though the distance between these two locations is just 7 mm, as seen in Figure 44. The velocity of fluid increases further downstream of (r) and shock-waves with $Ma > 1$ are observed at A^* . (Reader-Harris, 2015) observes that the cross-sectional area with the highest velocity at (A^*) cannot practically be measured. A^* is therefore impracticable for modeling flow in a rupture disk since — a location upstream of (A^*) is better suited to model flow across a rupture disk device.

Figure 45 is the plot of the static pressure computed with the digitalized image of the rupture disk in Figure 42.

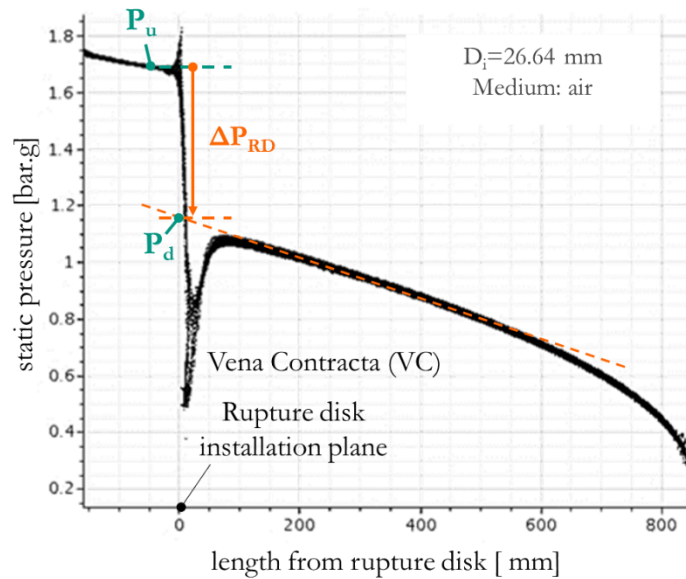


Figure 45: The static pressure computed with the digitalized image of the rupture disk in Figure 42 in a pipe; the static pressure along the pipe axis calculated with a CFD code is plotted.

The static pressure profile along the pipe axis computed with CFD is qualitatively like the pressure profile measured experimentally in Figure 32. Flow acceleration or expansion is characterized by a rapid drop in static pressure, which is caused by the interaction of the parts of an open rupture disk device with the fluid resulting in the increase in Mach number.

5.2 Modeling of dischargeable mass flow rate across a rupture disk device

An analytical method to determine the dischargeable mass flow rate through a rupture disk device so as to close Gap II (Development of a model to calculate the dischargeable mass flow rate across a rupture disk device) will be presented. This requires determination of the rupture disk free relieving area, A_{RD} experimentally as a model parameter, so as to close Gap III (Determination of rupture disk free relieving area). The result is a procedure to determine the smallest rupture disk and pipe size, which fulfills the “dischargeable mass flow rate is larger than the minimum flow rate to be discharged” sizing criterion in sizing Step 4 in Table 1 reliably. The procedure is meant to accurately determine the discharge rate from the point of rupture disk activation to the point when the system is fully depressurized seamlessly.

5.2.1 Model representation for flow through a rupture disk

High-velocity flow with significant compressibility effects is typical in emergency relief sizing. Restriction of flow in a rupture disk device is important in modelling rupture disk devices. High-velocity and compressible flow in a circular bore is characterized by an elaborate Vena-Contracta (Schmidt, 1993). Studies with constant area fittings such as orifices have been studied with high pressure cavitating flow with liquids (Ebrahimi, et al., 2017). The discharge rate in orifice plates has been shown to vary with orifice thickness (Ward-Smith, 1979). Orifices, in general, have regular and constant geometry and are usually characterized with regular geometric shapes and have a contraction area that is characterized with a regular shape. On the contrary, rupture disk devices have an irregular and complex discharge area and contraction area. Figure 1 b and c, as well as Figure 43 and Figure 44 show that open rupture disk devices typically have a discharge area with complex shape and may not be characterized exactly as a circular bore without further studies.

The rupture disk will be modeled as an infinitely thin asymmetric bore with a large diameter ratio to determine the dischargeable mass flow rate across a rupture disk. The separated flow region in a rupture disk will be modeled as an *apparent asymmetric nozzle with a large throat area*, A_{th} . The apparent throat area, A_{th} will be equated to the rupture disk discharge area, A_{RD} . The free relieving area of an open rupture disk A_{RD} is neither a concentric bore nor squired- or knife-edged nor symmetric nozzle, as seen in Figure 1 as well as Figure 42, Figure 43 and Figure 44. It has a form that could be characterized as a combination of all these geometric forms and it also depends on rupture disk type. However, the measured pressure profile in Figure 32 is similar to that of a restriction, as seen in Figure 3b (Schmidt, 1993) and that of an orifice (Shannak, 1998). The pressure profile calculated with the rupture disk CFD model is also qualitatively like that of an orifice CFD model in (Roul & Dash, 2012), (Ebrahimi, et al., 2017).

To determine the pressure-drop across a rupture disk, a relationship that is valid more generally will be developed by correlating rupture disk losses observed in low-velocity flow to losses expected in high-velocity flow by factoring compressibility fully. This is based on (Thévenin & Janiga, 2014) where it is stated that friction leads to modifications of the flow velocity like a reduction of flow cross-section. Since visualization of flow has shown that a rupture disk reduces the flow cross-section as an infinitely thin asymmetric bore, the separated flow region in the rupture disk will be modeled as a pipe and the pressure-drop will be calculated with the equations for pipe.

One-dimensional analysis has been successfully applied in the equations for flow in a pipe, as described in chapter 3.2.3 and 3.2.4. The rupture disk device model should be coupled with the pipe models using the model parameters listed in Table 2 analogous to the modeling approaches listed in Table 3. Further, (Ebrahimi, et al., 2017) have shown that that one-dimensional analysis in industrial applications is comparable to rigorous multi-dimensional numerical approaches like those in CFD models when compared to experimental results with orifices. One-dimensional analysis seems to be widely used in the industry successfully- It is therefore correspondingly be applied to develop models to determine the mass flow rate and pressure-drop across the rupture disk in the following.

5.2.2 Method to determine dischargeable mass flow rate with gas flow

The rupture disk will be modeled as an infinitely thin asymmetric bore with a large diameter ratio. The separated flow region in a rupture disk will be modeled as an *apparent asymmetric nozzle with a large throat area*, as described in chapter 5.2.1 and as illustrated in Figure 46.

The relationship between the rupture disk free relieving area, A_{RD} and the dischargeable mass flow rate across a rupture disk is derived with isentropic nozzle model assumptions below. The control volume is marked with a green dash-line, in Figure 46, is in the region between location (u) and (i).

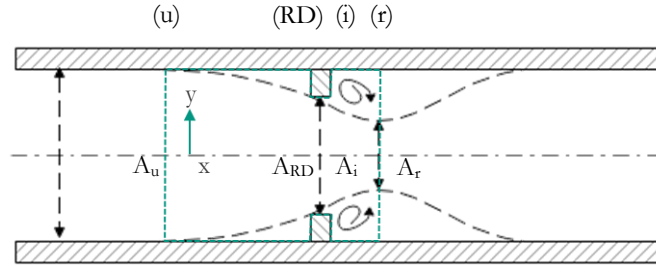


Figure 46 Illustration a control volume assuming a near-circular bore with large area ratio

Separated flow in the control volume is modeled with two nozzles upstream of an abrupt expansion correspondingly. The first nozzle is between (u) and (RD) while the second nozzle is between (u) and (r). Coupling of mass and energy balance with polytropic equation of state yields the general equation for calculating the mass flow rate through (i) for given Ma_u per eq.(27). Isentropic flow assumption is applied between (u) and a cross-section between (RD) and (r), which is denoted by the location (i). The full derivation of the equation to determine the dischargeable mass flow rate across a rupture disk iteratively is derived fully in ANNEX XIX and is adopted from eq.(A-27) as eq.(27).

$$Q_{m,i} = \rho_u \cdot A_u \cdot \phi_j \cdot \sigma_{RD} \cdot \eta_{u-i,j}^{1/\kappa} \cdot \left(-\Delta h_{u-i,j} \cdot \frac{2}{\left[1 - \phi_j^2 \cdot \sigma_{RD}^2 \cdot \eta_{u-i,j}^{2/\kappa} \right]} \right)^{1/2} \quad (27)$$

with $i = RD; r$ and $j = LV; HV$

Table 15 The variables and parameter to calculate the dischargeable mass flow rate per eq.(27) iteratively.

Property	Eq.
i. General relationship to calculate stagnation pressure P_0 , temperature T_0 and density ρ_0	(28)
ii. Classic relationship for Mach number between two cross-sections for given Ma_u and σ_{RD}	(29)
iii. Static pressure ratio $\eta_{u-i,HV}$ between (u) and (i) for given Ma_u and resulting Φ_{HV} (high-velocity)	(30)
iv. Approximation of drop in enthalpy between (u) and (i) $\Delta h_{u-i,HV}$ (high-velocity)	(31)
v. Static pressure ratio $\eta_{u-i,LV}$ between (u) and (i) for given Ma_u and resulting Φ_{LV} (low-velocity)	(32)
vi. Approximation of drop in enthalpy between (u) and (i) $\Delta h_{u-i,LV}$ (low-velocity)	(33)
vii. Rupture disk flow restriction, Φ	(34)
viii. Rupture disk area ratio, σ_{RD}	(40)

The variables and parameter required in eq.(27) are listed in Table 15 and described below.

The general relationship to calculate stagnation pressure, temperature and density for given conditions at (u), (RD) and (r) is per eq.(28). The static pressure at a random point (i) between (u) and (r) may also be calculated from the same relationships correspondingly (Levenspiel, 1998), (Perry & Green, 2008), (Truckenbrodt, 2008).

$$P_0 = P_i \cdot \left(1 + \frac{\kappa-1}{2} \cdot Ma_i^2 \right)^{\frac{\kappa}{\kappa-1}} \quad T_0 = T_i \cdot \left(1 + \frac{\kappa-1}{2} \cdot Ma_i^2 \right) \quad \rho_0 = \rho_i \cdot \left(1 + \frac{\kappa-1}{2} \cdot Ma_i^2 \right)^{\frac{1}{\kappa-1}} \quad i = u; RD; r \quad (28)$$

The relationship to determine the dischargeable mass flow rate across a rupture disk with gas flow, $Q_{m,g}$ is calculated with $\Phi=1$ in eq.(27) for a given σ_{RD} . For this, the Mach number at location (RD) is calculated iteratively with the classic relationship for Mach number between two cross-sections for given Ma_u and σ_{RD} (Thévenin & Janiga, 2014).

$$Ma_i \leftarrow \frac{Ma_u}{\sigma_{RD} \cdot \phi_j} \cdot \left(\frac{1 + \frac{\kappa-1}{2} \cdot Ma_i^2}{1 + \frac{\kappa-1}{2} \cdot Ma_u^2} \right)^{\frac{1}{2} \frac{\kappa+1}{\kappa-1}} - Ma_i = 0 \quad \text{with } i=RD; r \quad (29)$$

5.2.2.1 *Enthalpy drop with high-velocity flow:*

The pressure ratio between (u) and (i) with high-velocity flow is calculated per eq.(30) as a function of the upstream Mach number, Ma_u , the experimentally determined rupture disk area ratio σ_{RD} and the now unknown rupture disk restriction Φ_{HV} and the resulting Mach number at the apparent restriction at (i) as Ma_i .

$$\eta_{u-i,HV} = \frac{P_i}{P_u} = \left(1 + \frac{\kappa-1}{2} \cdot Ma_u^2 \right)^{\frac{\kappa}{\kappa-1}} \cdot \left[1 + \frac{\kappa-1}{2} \cdot \left(\frac{Ma_u}{\sigma_{RD} \cdot \phi_{HV}} \cdot \left(\frac{1 + \frac{\kappa-1}{2} \cdot Ma_i^2}{1 + \frac{\kappa-1}{2} \cdot Ma_u^2} \right)^{\frac{1}{2} \frac{\kappa+1}{\kappa-1}} \right)^2 \right]^{-\left(\frac{\kappa}{\kappa-1} \right)} \quad i=RD; r \quad (30)$$

For high-velocity flow, the general equation for calculating the enthalpy drop for a given Ma_u and σ_{RD} assuming isentropic flow between (u) and (i) has been derived in detail in ANNEX XIX and is adopted from eq.(A-21) per eq.(31).

$$\Delta h_{u-i,HV} = h_i - h_u = \frac{\kappa}{\kappa-1} \cdot \frac{P_u}{\rho_u} \cdot \left(\left(\eta_{u-i,HV} \right)^{\frac{\kappa-1}{\kappa}} - 1 \right) \quad i=RD; r \quad (31)$$

5.2.2.2 *Enthalpy drop with low-velocity flow*

Looking at Figure 32 and Figure 33 with $P_b=100$ mbar.g, the pressure gradient upstream and the pressure gradient downstream of the rupture disk is constant, as seen in the measured static pressure at the center of a pipe with rupture disk installed (See also: chapter 5.1). Compressibility effects with low-velocity flow are negligible and the pressure ratio between (u) and (i) is therefore calculated per eq.(32).

$$\eta_{u-i,LV} = \frac{P_i}{P_u} = \frac{P_u - \Delta P_{u-i,LV}}{P_u} = \frac{P_u - \frac{Q_m^2 \cdot K_R}{2 \cdot A_u^2 \cdot \rho_u}}{P_u} \quad i=RD; r \quad (32)$$

Looking at Figure 43 and Figure 44, the enthalpy drop with incompressible flow and low-velocity flow $\Delta h_{u-i,LV}$ in the complex turbulent area between (u) and a random point (i) between (u) and (r) in the model representation is attributed to pressure drop, ΔP_{u-i} between (u) and (i). For incompressible flow, the drop in enthalpy $\Delta h_{u-i,LV}$ is approximated with ΔP_{RD} and K_R (Zande, et al., 1998) per eq.(33).

$$\Delta h_{u-i,LV} = \frac{1}{\rho_u} \cdot \Delta P_{u-i,LV} = -\frac{1}{\rho_u} \cdot \frac{Q_m^2 \cdot K_R}{2 \cdot A_u^2 \cdot \rho_u} \quad i=RD; r \quad (33)$$

The second term in eq.(33) is the rupture disk permanent pressure loss, which is usually calculated with the rupture disk loss coefficient, K_R per eq.(6). Linear extrapolation of pressure profile upstream and downstream to get $\Delta P_{u-i,LV}$ assuming low-velocity and incompressible flow is applied, as seen in Figure 47.

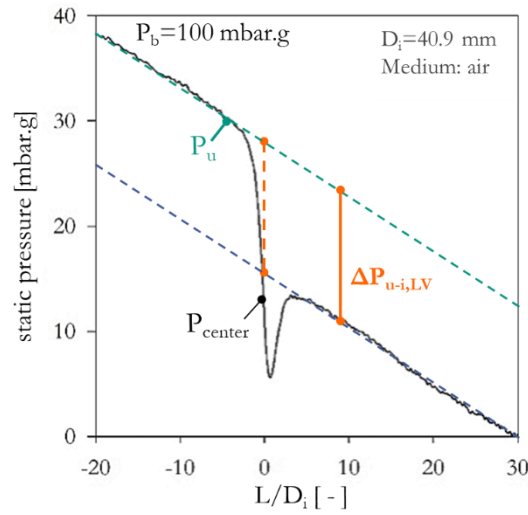


Figure 47: Partial plot of Figure 32 shows the measured static pressure in the middle of a pipe with the rupture disk installed with low-velocity flow with $P_b=100$ mbar.g.

This is valid because the pressure gradient upstream and downstream of the rupture disk is linear and similar, as seen in Figure 47 for the low-velocity experiment with $P_b=100$ mbar.g. This is a requisite model simplification of the complex dissipation region between (u) and (i). This model simplification will be validated experimentally.

The location (RD) is more suited to determine the mass flow rate across the rupture disk than at (r) since $\Phi=1$ at (RD). Furthermore, the region between (RD) and (r) is not practically measurable (Reader-Harris, 2015) and this region is characterized by flow with high shear as demonstrated in Figure 43 and Figure 44.

5.2.2.3 Rupture disk flow restriction

The general equation for calculating rupture disk flow restriction, Φ for given Ma_u and σ_{RD} assuming isentropic flow between (u) and (i) has been derived in detail in ANNEX XIX and is adopted from eq.(A-25) per eq.(34). The model parameter, Φ is calculated per eq.(34) by inserting $\Delta h_{u-i,HV}$ per eq.(31) for high-velocity flow or $\Delta h_{u-i,LV}$ per eq.(33) for low-velocity flow into eq.(34).

Rupture disk flow restriction, Φ is a measure of the magnitude of restriction of flow with the drop in enthalpy for low-velocity and high-velocity flow. Eq.(34) is solved for the prevailing rupture disk flow restriction, Φ for given upstream conditions at (u). The rupture disk area ratio σ_{RD} , is determined experimentally for a rupture disk type as described in chapter 5.2.2.5 per eq.(40).

$$\phi = \phi_j \{Ma_u, \phi_j\} = \frac{Q_m}{\rho_u \cdot A_u \cdot \sigma_{RD} \cdot \eta_{u-i,j} \{Ma_u, \phi_j\}^{1/k}} \cdot \left(-\Delta h_{u-i,j} \cdot \frac{2}{\left[1 - \phi_j^2 \cdot \sigma_{RD}^2 \cdot \eta_{u-i,j} \{Ma_u, \phi_j\}^{2/k} \right]} \right)^{-\frac{1}{2}} \quad (34)$$

with $i=RD; r$ and $j=LV; HV$

Table 16 Equations for calculating the rupture disk flow restriction Φ per eq. (34) iteratively

Property	Eq.
i. Static pressure ratio $\eta_{u-i,HV}$ between (u) and (i) for given Ma_u and resulting Φ_{HV} (high-velocity)	(30)
ii. Approximation of drop in enthalpy between (u) and (i) $\Delta h_{u-i,HV}$ (high-velocity)	(31)
iii. Static pressure ratio $\eta_{u-i,LV}$ between (u) and (i) for given Ma_u and resulting Φ_{LV} (low-velocity)	(32)
iv. Approximation of drop in enthalpy between (u) and (i) $\Delta h_{u-i,LV}$ (low-velocity)	(33)
v. Rupture disk area ratio, σ_{RD} (see also chapter 5.2.2.5)	(40)

The model representation differentiates between low-velocity and high-velocity flow. A boundary condition to determine when high-velocity flow with $\Delta h_{u-i,HV}$ per eq.(31) transitions to low-velocity flow with $\Delta h_{u-i,LV}$ per eq.(33) depending on Ma_u is required in eq.(34) because $\Phi_{HV} \rightarrow 0$ with $\eta_{u-i,HV}$ per eq.(30) for $Ma_u \rightarrow 0$. This would be inconsistent with previous works that found $C_C > 0.5$ for liquid and gas flows (Shannak, et al., 1999), (Ebrahimi, et al., 2017). The boundary condition is set to the upstream Mach-number, $Ma_{u,boundary}$ when $\Phi_{LV} = \Phi_{HV}$. With this, Φ_{LV} is valid $Ma_u \leq Ma_{u,boundary}$ while Φ_{HV} is valid for $Ma_u > Ma_{u,boundary}$. The relationship between the flow conditions at rupture disk (RD) and at (r) are calculated with calculated rupture disk flow restriction, Φ .

5.2.2.4 Area-choking in rupture disk devices

Once a rupture disk is activated, it opens and attains the highest mass flow rate at burst pressure, Q_{m,RD^*} if the pressure in the system to be protected does not rise further. The mass flow rate at rupture disk, $Q_{m,RD}$ then reduces with time as the system is depressurized. In the following equation to determine the theoretical mass flow rate $Q_{m,theo}$ in a rupture disk device is derived. The mass flow rate at burst pressure, Q_{m,RD^*} is calculated with the dimensionless mass flow rate at burst pressure, C_{m,RD^*} .

The separated flow region in a rupture disk between (u) and (r) is modeled as a thin asymmetric isentropic nozzle. (Ward-Smith, 1979) theoretically proves that $\Phi \rightarrow 1$, for *area-choking* to occur in square-edged orifice with a small ratio of thickness t to rupture disk effective diameter, d with $t/d \rightarrow 0$. If a rupture disk is handled analogously, then its t/d ratio must be very small. For example, the rupture disk could have a thickness of just 1 mm if the rupture disk discharge area is located at the rupture disk installation plane. This is possible because the slits which are formed by an open rupture disk part begin in closest proximity to the rupture disk installation plane, as seen in Figure 42 and Figure 43. In this case, $t/d \rightarrow 0$.

If a similar analogy is valid for the rupture disk, then the theoretical choking dimensionless mass flow rate must approach unity, $C_{m,theo} \rightarrow 1$ for area-choking to occur at $\Phi \rightarrow 1$ (Miller, 1996; Dayev & Sultanov, 2018).

Therefore, the choking area is at A_{RD} with $Ma_r \rightarrow 1.0$. There is, therefore, a theoretical maximum upstream Mach number $Ma_{u,theo}$ when area-choking shall occur. $Ma_{u,theo}$ is calculated by solving for Ma_u iteratively for a given σ_{RD} per eq.(35) at (RD) with $\Phi = 1$. Ma_r in eq.(35) is set to 0.99 for numerical convergence reasons. A value of Ma_{RD} closer to 1.0 may be chosen if needed.

$$Ma_{u,theo} \leftarrow \frac{Ma_u}{\sigma_{RD} \cdot Ma_{RD}} \cdot \left(\frac{1 + \frac{\kappa-1}{2} \cdot Ma_{RD}^2}{1 + \frac{\kappa-1}{2} \cdot Ma_u^2} \right)^{\frac{1}{2} \frac{\kappa+1}{\kappa-1}} - Ma_{RD} = 0 \quad \text{with } Ma_{RD} = 0.99 \quad (35)$$

The theoretical mass flow rate $Q_{m,theo,g}$ with area-choking is calculated in the final step at (RD) with eq.(27) with $Ma_u = Ma_{u,theo}$ and $\Phi = 1$ with $Ma_{u,theo}$ per eq.(35). Choking in rupture disks with a large diameter ratio of $\beta_{RD} > 0.75$ is not typical. Theoretically, the choking point can prevail if the pressure ratio P_d/P_u is lowered to the point when $Ma_u \rightarrow Ma_{u,theo}$.

The rupture disk dimensionless mass flow rate at burst pressure, C_{m,RD^*} is the ratio of prevailing mass flow rate at burst pressure, Q_{m,RD^*} to maximum theoretical mass flow rate with area-choking, $Q_{m,theo,g}$ at burst pressure per eq.(36). C_{m,RD^*} is a measure of how near the prevailing upstream burst conditions are to area-choking conditions since area-choking is when $Q_{m,RD} = Q_{m,theo,g}$.

The dimensionless mass flow rate at burst pressure, C_{m,RD^*} should be measured experimentally at burst pressure and assumed to be constant for a rupture disk type. C_{m,RD^*} should then be used to determine the dischargeable mass flow rate at burst pressure, Q_{m,RD^*} with eq.(36) assuming that the pressure in the system to be protected does not rise above the burst pressure.

$$C_{m,i} = \frac{Q_{m,i}}{Q_{m,theo,g}} \quad C_{m,i^*} = \frac{Q_{m,i^*}}{Q_{m,theo,g}} \quad \text{with } i=RD; r \quad (36)$$

Non-choking rupture disk designs do not limit the dischargeable mass flow rate at the rupture disk itself. These designs are sized to operate at $Ma_u < Ma_{u,theo}$. A detailed pressure-drop calculation for the entire rupture disk vent-line system with all fittings installed should be done to calculate the capacity of the rupture disk vent-line system. This is because the dischargeable mass flow rate with these designs depends on both the flow conditions upstream of the rupture disk device and on the downstream conditions.

Choking rupture disk designs limit the dischargeable mass flow rate at the rupture disk itself. These designs are sized to operate at $Ma_u = Ma_{u,theo}$. The dischargeable mass flow rate with these designs only depends on the flow conditions upstream of rupture disk device and not on the downstream conditions since the rupture disk behaves like a sonic nozzle when the rupture disk dimensionless mass flow rate at burst pressure $C_{m,RD} = 1.0$ is attained.

Given the flow conditions upstream of the rupture disk, the general equation for determining the dischargeable mass flow rate across a rupture disk with gas flow, $Q_{m,g}$ is computed by coupling the non-choked and choked flow regions per eq.(37) for a given upstream Mach-number, Ma_u . The condition of $Ma_u \geq Ma_{u,theo}$ in eq.(37) is to limit the maximum possible flow rate if $Ma_u \geq Ma_{u,theo}$ is assumed during rupture disk sizing.

$$Q_{m,g} = \begin{cases} Q_{m,RD,g} & \text{if } 0 \leq Ma_u < Ma_{u,theo} \\ Q_{m,theo,g} & \text{if } Ma_u \geq Ma_{u,theo} \end{cases} \quad (37)$$

Typically, the pressure ratio referenced to stagnation conditions as $\eta_{i,0}$ per eq.(38) with index “0” denoting stagnation conditions per eq.(28). This relationship will be used to present the experimental results during experimental validation of this procedure.

$$\eta_{i,0} = \frac{P_i}{P_0} = \left(1 + \frac{\kappa - 1}{2} \cdot Ma_i^2 \right)^{-\frac{\kappa}{\kappa - 1}} \quad \text{with } i = RD; r \quad (38)$$

5.2.2.5 Rupture disk free relieving area

The rupture disk is often modeled as a bore with a known area ratio, σ_{RD} (Friedel & Kissner, 1988), (Shannak, et al., 1999), (Shannak, 2010). σ_{RD} is also a model parameter in the equations to determine the rupture disk flow restriction, Φ per eq.(34) and mass flow rate through a rupture disk Q_m per eq.(27). It should be determined experimentally for a rupture disk type. Flow measurement with orifice is a well-known differential pressure flow measurement technique where the discharge rate is predicted for a given bore area and measured differential pressure.

Inversely, A_{RD} can be determined experimentally with low-velocity flow using equations for flow measurement with orifice plates. A_{RD} is determined experimentally by equating it to the area of an equivalent orifice with the same discharge rate under the same flow conditions. This area is considered as the Minimum Net Flow Area, MNFA (API, 2014), a value that most rupture disk manufacturers give. The relationship between the rupture disk diameter ratio β_{RD} , rupture disk area ratio σ_{RD} and A_{RD} is, $\beta_{RD} = (\sigma_{RD})^{0.5} = (A_{RD}/A_u)^{0.5}$. A_{RD} is often taken to be constant for a restrictive rupture disk device (TÜV, 2006).

This section presents an alternative method to directly determine the A_{RD} with Mach-number at three diameter lengths upstream of the device below 0.30. The opening characteristic of the rupture disk device is taken to be ideal; the rupture disk device opens fully, resulting in the maximum possible discharge area for the rupture disk design. The challenge here is to get precise and reliable experimental data with low-velocity flow, as the pressure-drop across the rupture disk device and pipe is very low. The requirements regarding the precision of the instruments especially regarding pressure measurement instrumentation are high because relative pressure below 10 mbar.g should be measured reliably.

Consider a rupture disk installed in a pipe and characterized as a fictitious bore with a large diameter ratio, $\beta_{\text{bore}} = (\sigma_{\text{bore}})^{0.5} = (A_{\text{bore}}/A_u)^{0.5}$ with $\beta_{\text{bore}} > 0.75$. The upstream pipe cross-section (A_u) is the same as the downstream cross-section (A_d) and A_u is the reference point. Whenever a random test object, with an arbitrary but constant discharge area, is installed in a properly calibrated test section, it interacts with flow causing constant dissipation of energy under stationary flow conditions.

Dissipation of energy can be measured experimentally with precision instruments as irreversible pressure-drop with stationary, incompressible low-velocity gas flow and characterized with a minor loss coefficient K_R , which may also be characterized as discharge area, A_{bore} . The minor loss coefficient of a concentric orifice is correspondingly applicable to both eccentric and segmental orifice (TORIZUMI, 1990). The minor loss coefficient between points location (u) and (d) with all the pressure loss being attributable to only the fitting installed in an infinitely small pipe segment, for incompressible fluid flow is per eq.(39)

$$K_R = 2 \cdot \frac{\Delta P_{RD} \cdot A_u^2 \cdot \rho_u}{Q_m^2} \quad (39)$$

K_R is determined experimentally with low-velocity flow analogous to the standardized method in ASME PTC-25 (ASME, 2014). The irreversible pressure loss, ΔP_{RD} and the mass flow rate Q_m are measured experimentally in a properly calibrated test section while the density ρ_u is calculated from the measured values (See also: Chapter 4.9). The (Urner, 1997) equation gives the relationship between an orifice's minor loss coefficient, K_R measured with incompressible flow, β_{bore} and C_d . The relationship between C_d and β_{RD} is per and (Reader-Harris & Sattary, 1996) equation. This equation is a result of decades of research and it relates the orifice discharge coefficient C_d to the diameter ratio, β_{bore} and the prevailing upstream Reynold's number Re_u .

The (Urner, 1997) equation and (Reader-Harris & Sattary, 1996) equation are part of a working standard for measurement of fluid flow with orifice plates ISO 5167-2 (ISO, 2003). The (Reader-Harris & Sattary, 1996) eq.(A-11) in ANNEX XVIII is factored into the (Urner, 1997) eq.(A-12) also in ANNEX XVIII, resulting to an implicit equation which gives the relationship between a fitting's K_R , and C_d as a function of the fittings β_{eff} and the upstream Reynolds number, Re_u . This equation is solved for β_{eff} iteratively.

$$\beta_{\text{eff}} \leftarrow \beta_{\text{eff}} - \left(C_d \{Re_u, \beta_{\text{eff}}\}^2 \cdot \left(K_{RD}^{1/2} + 1 \right)^2 + \left(1 - C_d \{Re_u, \beta_{\text{eff}}\}^2 \right)^{0.25} \right) = 0 \quad (40)$$

$$A_{RD} = A_{\text{eff}} = 0.25 \cdot \pi \cdot (\beta_{\text{eff}} \cdot D_u)^2 \quad \text{and} \quad \sigma_{RD} = A_{RD}/A_u \quad \text{with} \quad C_d = \frac{Q_{m,\text{exp}}}{Q_{m,\text{theo}}}$$

The diameter ratio of a random test object β_{eff} is determined by solving eq.(40) iteratively and the minimum discharge area of a test object, A_{eff} , is taken to be its narrowest cross-section, A_{RD} . All the terms in eq. (40) are calculated from measured experimental data, with the exception of the diameter ratio β_{eff} , which is solved for iteratively (Kurz, 2017).

Below is a contour plot of the discharge coefficient as a function of the effective diameter ratio β_{eff} and the Reynolds number. The effective diameter β_{eff} of typical rupture disks is expected to be in the range $\beta_{\text{eff}} > 0.70$ (Friedel & Kissner, 1988). Flow during determination of the effective diameter of should also be turbulent with $Re_u \geq 10^5$ to ensure that turbulent flow prevails, and the Mach number Ma_u should be below 0.30 to avoid compressibility effects. The discharge coefficient equation is meant for use with flow measurement with orifice devices with $0.25 \leq \beta_{\text{eff}} \leq 0.75$. The validity of the discharge coefficient equation outside its intended range with $\beta_{\text{eff}} > 0.75$ will be validated experimentally.

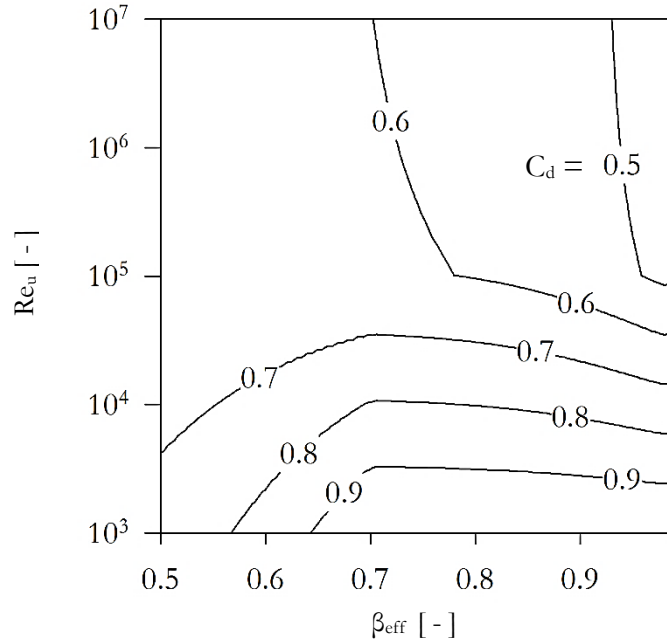


Figure 48: C_d per eq.(A-11) as a function of β_{eff} for a range of Re_u .

The rupture disk resistance factor K_R , of typical rupture disks is expected to be in the range $0.1 \leq K_R < 10$ (Friedel & Kissner, 1988), (NBBPVI, 2019). Looking at the plot for effective diameter ratio, β_{eff} with eq.(40) as a function of minor loss coefficient, K_R in Figure 48, $\beta_{\text{eff}} \rightarrow 1$ for $K_R \rightarrow 0$ as expected. The bend in the plot in Figure 48 is inherent to the (Urner, 1997) eq.(A-12) in ANNEX XVIII. The validity of the (Urner, 1997) with $\beta_{\text{eff}} > 0.75$ will be validated experimentally.

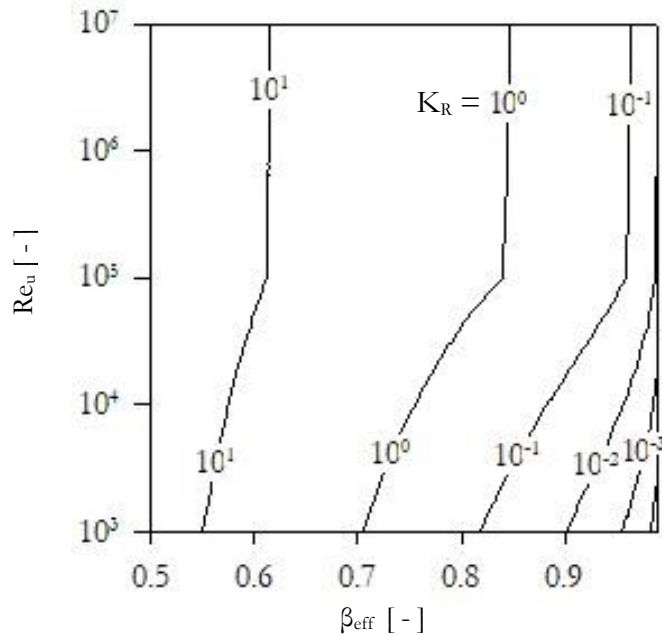


Figure 49: K_R per eq.(A-12) as a function of β_{eff} for a range of Re_u .

5.2.3 On the dischargeable mass flow rate with two-phase flow

The dischargeable mass flow rate across a rupture disk with two-phase flow, just like the pressure drop, depends on all the parameters listed in Table 2. The advantages of using empiric, analytical or phenomenological methods have also been listed in Table 3.

The density of the two-phase mixture, $\rho_{tp,RD}$ at (RD), is calculated iteratively per eq.(41) (Petrovic & Stevanovic, 2016).

$$\frac{\rho_{tp,RD}}{\rho_{tp,u}} = \left(\frac{1 + \left(\frac{\kappa_{tp} - 1}{2} \right) \cdot \left(\frac{\rho_{tp,RD}}{\rho_{tp,u}} \right)^{\kappa_{tp} + 1}}{\left(\frac{\kappa_{tp} + 1}{2} \right)} \right)^{\frac{1}{(\kappa_{tp} - 1)}} \quad (41)$$

The detailed work by (Bhagwat & Ghajar, 2014) introduces a flow-pattern independent void fraction, ε_{tp} , that is valid generally. This two-phase mixture void fraction, ε_{tp} formulation is key because it significantly simplifies two-phase flow. It is the first general flow pattern-based model available in literature that does not require flow maps at all. It also considers the inclination of the pipe. Since it is a drift-flux based model, it is independent of the slip velocity. Therefore ε_{tp} in eq.(42) and eq.(45) is calculated with the method and equations in (Bhagwat & Ghajar, 2014) with as described in ANNEX XXI.

The two-phase mixture isentropic expansion coefficient κ_{tp} varies with conditions upstream of RD at (u) and, therefore, also with ε_{tp} , per eq.(42). κ_{tp} is calculated analogously to eq.(45) per eq.(42). The change in κ_{tp} between (u) and (RD) is assumed to be approximately constant. ε_{tp} in eq.(42) is calculated with the method and equations in (Bhagwat & Ghajar, 2014).

$$\kappa_{tp} = \varepsilon_{tp} \cdot \kappa_g + (1 - \varepsilon_{tp}) \kappa_l \quad (42)$$

The two-phase mixture velocity, $w_{tp,RD}$ at (RD) for given upstream conditions is calculated with continuity equations with $\rho_{tp,RD}$ per eq.(41) per eq.(43).

$$w_{tp,RD} \{Q_{m,RD}\} = \frac{Q_{m,RD}}{A_{RD} \cdot \rho_{tp,RD}} \quad (43)$$

(Shannak, et al., 1999) experimentally proved that flow contraction with two-phase flow is limited to mass flow qualities in the range $0.012 < x_g < 0.90$ where the flow regimes are specified as bubble and spray flow, respectively. The mass flow rate across a rupture disk with two-phase flow is calculated per eq.(44).

$$Q_{m,tp} = A_{RD} \cdot \rho_{tp,RD} \cdot w_{tp,RD} \quad (44)$$

The theoretical mass flow rate with a two-phase flow mixture, $Q_{m,theo,tp}$ at the rupture disk with given discharge area A_{RD} prevails when the two-phase mixture velocity at A_{RD} equals sonic velocity. Two-phase in this work is restricted to air/water two-phase mixture, where frozen flow with no change in the gas quality, x_g is assumed. The *frozen two-phase sonic velocity*, $c_{s,tp}$ in (Grolmes & Fauske, 1969) has been derived in (Petrovic & Stevanovic, 2016) assuming 1-D, homogeneous flow per eq.(45) with the homogeneous two-phase mixture density.

$$c_{s,tp} = \left(\frac{\varepsilon_{tp} \cdot \rho_{tp,hom}}{\rho_l \cdot c_{s,l}^2} + \frac{(1 - \varepsilon_{tp}) \cdot \rho_{tp,hom}}{\rho_g \cdot c_{s,g}^2} \right)^{-\frac{1}{2}} \text{ with } \rho_{tp,hom} = \varepsilon_{tp} \cdot \rho_g + (1 - \varepsilon_{tp}) \rho_l \quad (45)$$

The theoretical mass flow rate with a two-phase flow mixture at A_{RD} prevails when $w_{tp,RD} \{Q_{m,tp}\}$ per eq.(43) equals $c_{s,tp}$ per eq.(45). Therefore, the theoretical mass flow rate with a two-phase flow mixture, $Q_{m,tp,theo}$ across A_{RD} is computed by per eq.(46).

$$Q_{m,tp,theo} = A_{RD} \cdot \rho_{tp,RD} \cdot c_{s,tp} \quad (46)$$

The two-phase dimensionless mass flow rate at, $C_{m,tp}$ describes the ratio of the actual mass flow rate, $Q_{m,tp}$ to the theoretical maximum mass flow rate, $Q_{m,tp,theo}$ per eq.(46). Therefore, the dimensionless mass flow rate across a rupture disk is per eq.(47).

$$C_{m,tp} = \frac{Q_{m,tp}}{Q_{m,tp,theo}} \quad (47)$$

Given the flow conditions upstream of the rupture disk, the general equation for determining the dischargeable mass flow rate across a rupture disk with two-phase flow mixture, $Q_{m,tp}$ is computed by coupling the non-choked and choked flow regions per eq.(48). The validity of this equation is subject to experimental validation.

$$Q_{m,tp} = \begin{cases} \text{if } Q_{m,tp} < Q_{m,theo,tp} & Q_{m,tp} \\ \text{else} & Q_{m,theo,tp} \end{cases} \quad (48)$$

5.3 Modeling of pressure-drop across a rupture disk device

An analytical method to determine the pressure-drop across a rupture disk device to close Gap IV (Development of a model to calculate the pressure-drop across a rupture disk device) will be presented. This requires determination of the rupture disk compressible minor loss coefficient, K_{RD} experimentally as a model parameter, so as to close Gap V (Determination of prevailing rupture disk minor loss coefficient).

The compressible pressure-drop across a rupture disk, ΔP_{RD} is requisite in determining the pressure-drop in a rupture disk vent line accurately. This is especially the case in high-velocity compressible gas flow, with significant separation of flow. To model the pressure profile upstream and downstream of the rupture disk installation plane is rather challenging, as seen in Figure 32, Figure 33, Figure 43, Figure 44 and Figure 45. A more practical approach is to model this area between the upstream location (u) and downstream location (out) with a step function, as illustrated in Figure 45. The assumption here is that the flow is from left to right, the flow conditions at (u) are known and steady-state flow of a perfect gas prevails.

5.3.1 Method to determine the pressure-drop with gas flow – CMLC-Theory

It is proposed that a rupture disk be characterized with rupture disk zero-velocity minor loss coefficient, $K_{RD,0}$ to consider the dissipation of energy in the separated flow region (Mutegi, et al., 2019). Here, $K_{RD,0}$ is a characteristic number for a rupture disk. It is equated to a pipe segment length with the same pressure loss as a rupture disk under the same flow conditions. $K_{RD,0}$ is determined with low-velocity flow with $Ma_u \rightarrow 0$, because compressibility effects are negligible and incompressible flow assumptions are valid. Once determined, $K_{RD,0}$ is taken to be constant for gas flow.

$K_{RD,0}$ will be used in this work to predict the rupture disk compressible minor loss coefficient, $K_{RD,g}$ seamlessly for low-velocity and high-velocity gas flow. The basis of this hypothesis is inspired by the work of (Thévinin and Janiga 2014), where it is proven that friction qualitatively induces changes in thermodynamic parameters, i.e., velocity, like a reduction in cross-section. The pressure-drop across a flow-restricting device such as a rupture disk may thus be modeled with equations for frictional pressure-drop in a pipe.

The pressure gradient in a pipe $(dP/dL)_g$ with perfect gas assumption is calculated per eq.(13). The Mach number dependent term to the right in eq.(13) will be used to factor in the compressibility and to correlate the rupture disk loss coefficient observed in low-velocity flow to those expected in high-velocity flow. This term is also used to relate the prevailing loss coefficient to flow conditions upstream of the rupture disk device. This term is collected conveniently in this work into one term for given steady-state flow conditions and introduced as the rupture disk compressibility factor with gas flow, F_g per eq. (49).

$$F_g \{L\} = F_{g,perfect} \{L\} = -\frac{1 + (\kappa - 1) \cdot Ma \{L\}^2}{1 - Ma \{L\}^2} \quad (49)$$

The Mach number dependent term to the right in eq.(14) is also similarly suited for computing the rupture disk compressibility factor with gas flow, F_g as eq.(49) with perfect gas assumption, as seen in Figure 50.

$$F_g \{L\} = F_{real} \{L\} = -\frac{1}{Ma \{L\}^2 - 1} \cdot \left(1 + \frac{P \{L\}}{c_v \{L\}} \cdot \frac{Ma \{L\}^2}{\rho \{L\} \cdot T \{L\}} \right) \quad (50)$$

F_g in eq.(49) or eq.(50) is a dimensionless measure of compressibility of a fluid at any reference condition. It tends towards the absolute value of 1 for $Ma \rightarrow 0$ and towards $+\infty$ for $Ma \rightarrow 1.0$. The deviation of F_g per eq.(49) from F_g per eq.(50) is less than 10% for $Ma\{L\} < 0.60$ and pressure below 200 bar, as seen in Figure 50. F_g in eq.(50) is not limited to perfect gas assumptions. This work, however, uses F_g per eq.(49) in the following to stay consistent with the perfect gas assumption.

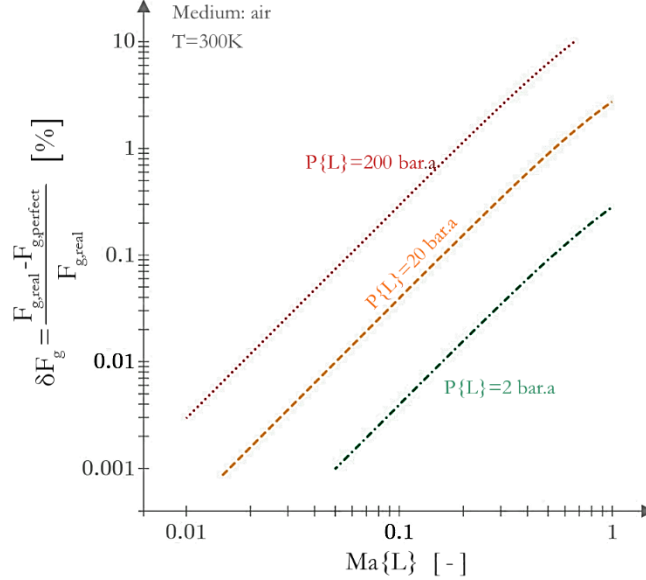


Figure 50 Deviation of compressible minor loss coefficient factor, F_g per eq.(49) from eq.(50) for upstream Mach number, $Ma_u < 1.0$ and $\kappa = 1.4$.

A rupture disk is modeled as a variable pipe, with a characteristic minimum length, which is introduced as rupture disk zero-velocity length, $L_{RD,0}$. This is the length of a pipe, with the same loss coefficient as a rupture disk device as seen in Figure 51.



Figure 51: Illustration of the key-points, that will be referred to below.

The proper way to determine the pressure-drop in a pipe between locations (u) and (d) with length L_d is by integrating eq.(49) fully per eq.(51). The challenge here is to determine the $Ma\{L\}$, $\rho\{L\}$, $\lambda\{L\}$ profiles for given Ma_u and the upper integration boundary at $L=L_d$.

$$\Delta P_{RD,g} = \int_{P\{L=0\}}^{P\{L=L_d\}} dP = -\frac{1}{D_u} \cdot \frac{G_u^2}{2} \cdot \int_{L=0}^{L=L_d} \frac{\lambda_g\{L\}}{\rho\{L\}} \cdot \frac{1 + (\kappa - 1) \cdot Ma\{L\}^2}{1 - Ma\{L\}^2} dL \quad (51)$$

$\Delta P_{RD,g}$ above is simplified without significant loss of accuracy by integrating the variables $Ma\{L\}$, $\rho\{L\}$, $\lambda\{L\}$ separately in respect of L per eq.(52).

$$\Delta P_{RD,g} = -\frac{G_u^2}{2 \cdot \rho_{g,av}} \cdot \frac{\lambda_{g,av}}{D_u} \cdot L_d \cdot F_{g,av} \quad \text{with } x_{i,av} = \frac{\int_0^{L_d} x\{L\} \cdot dL}{L_d}; x = \lambda_g; \rho_g; F_g \quad (52)$$

5.3.1.1 The zero-velocity minor loss coefficient, $K_{RD,0}$ characteristic number

Applying dimensional analysis to eq. (52) yields the rupture disk zero-velocity minor loss coefficient, $K_{RD,0}$ as presented in eq.(53). $K_{RD,0}$ is a constant rupture disk characteristic number, which represents the lowest magnitude of equivalent pipe loss coefficient $K_{RD,g}$ that would prevail for Mach number, $Ma_u \rightarrow 0$ and turbulent flow. It will be used to predict the pressure-drop for gas flows (Mutegi, et al., 2019).

$$K_{RD,0} = \frac{K_{RD,g}}{F_{C,g,0}} = const \quad (53)$$

The loss coefficient $K_{RD,g}$ in eq.(53) is determined just like the rupture disk zero-velocity minor loss coefficient K_R per eq.(6) with $Ma_u < 0.30$ and $Re_u > 10^5$. Determination of $K_{RD,g}$ therefore requires the loss coefficient for a pipe segment per eq.(12), and is therefore also a function of the Darcy friction factor λ per eq.(10). $K_{RD,g}$ therefore also varies with Reynolds number. The $K_{RD,0}$ however seems to be mostly constant even with change in λ , with change of Reynolds number as seen in Figure 53.

5.3.1.2 The rupture disk compressible minor loss coefficient, $K_{RD,g}$ with gas flow

It is stated that the pressure-drop of a rupture disk has a characteristic number $K_{RD,0}$ (Mutegi, et al., 2019). When Ma_u is increased, the variable pipe length, L_d increases and the Mach number, Ma_d at L_d , also increase due to frictional losses. To integrate variables in eq.(51) and (52) the following variables are required: i the upper boundary limit for integration, L_d and ii. the Mach-number profile in a pipe with variable length, $Ma\{L\}$. Both L_d and $Ma\{L\}$ are calculated from given conditions at location (u) and $K_{RD,0}$. For this, the super-positioning of the Mach number at location (d) is applied in eq.(54) and eq.(55) with $K_{RD,0}$, as illustrated in Figure 52, where it is shown that $K_{RD,0}$ is constant for varying friction factor and length, as explained below.

The Mach number at location (d), $Ma_d\{K_{RD,0}\}$ per eq.(54) is calculated by solving for Ma_d iteratively for a given $K_{RD,0}$ and given conditions at (u) assuming constant ratio of specific heats κ_u , and perfect gas (Levenspiel, 1998). The ratio of specific heats is calculated with the static conditions at (u) with the loss coefficient per eq.(12).

$$Ma_d\{K_{RD,0}\} \leftarrow K\{Ma_u, Ma_d\} - K_{RD,0} = 0 \quad (54)$$

The rupture disk equivalent length, L_d , which would result in $Ma_d\{K_{RD,0}\}$ at the exit is calculated iteratively per eq. (55) as a function of given $K_{RD,0}$ and Ma_u by solving for L_d .

$$L_d \leftarrow K\{Ma_u, Ma_d\{K_{RD,0}\}\} - \int_0^{L_d} \lambda\{L\} \cdot dL = 0 \quad (55)$$

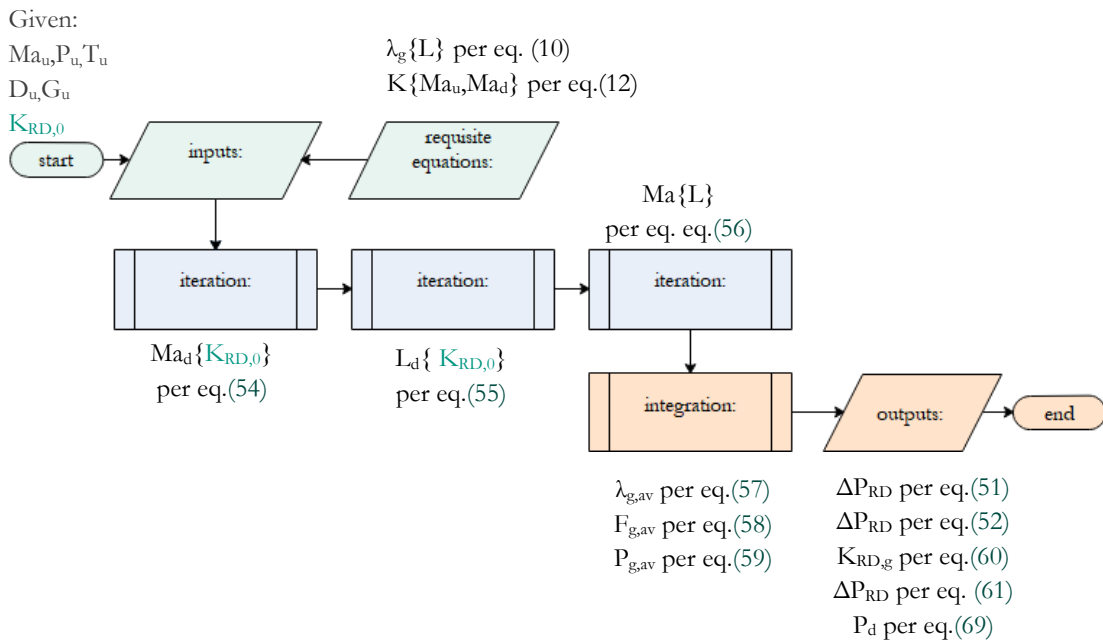


Figure 52 General overview of the computation algorithm for calculating pressure-drop across a rupture disk device.

Finally, the Mach number profile $Ma\{L\}$ is calculated per eq.(56) by solving for the Mach number at a random location between (u) and (d) by iteration.

$$Ma\{L\} \leftarrow K\{Ma_u, Ma_d\} - \frac{\int_0^L \lambda\{L\} \cdot dL}{D_u} = 0 \quad (56)$$

The averaged Darcy friction factor, λ_g is calculated by integrating eq.(10) with respect to L with L_d per eq.(55) as the upper integration boundary limit.

$$\lambda_{g,av} = \frac{\int_0^{L_d} \lambda\{L\} \cdot dL}{L_d} \quad (57)$$

The rupture disk compressibility factor, $F_{g,av}$ follows from the integration of eq.(49) with $Ma\{L\}$ per eq.(56) and L_d per eq.(55).

$$F_{g,av} = \frac{\int_0^{L_d} \frac{1 + (\kappa - 1) \cdot Ma\{L\}^2}{1 - Ma\{L\}^2} \cdot dL}{L_d} \quad (58)$$

Averaged fluid density, $\rho_{g,av}$ is determined by integration eq.(59) with L_d per eq.(55) and $Ma\{L\}$ per eq.(56) (Truckenbrodt, 2008).

$$\rho_{g,av} = \frac{\int_0^{L_d} \left(\rho_u \cdot \frac{Ma_u}{Ma\{L\}} \cdot \frac{2 + (\kappa_u - 1) Ma\{L\}^2}{2 + (\kappa_u - 1) \cdot Ma_u^2} \right) \cdot dL}{L_d} \quad (59)$$

The resulting rupture disk compressible minor loss coefficient, $K_{RD,g}$ is introduced based on equations above. $K_{RD,g}$ is the rupture disk minor loss coefficient with prevails for any given flow conditions at (u) with gas flow. $K_{RD,g}$ is calculated from $K_{RD,0}$ and the averaged compressible minor loss coefficient factor, $F_{g,av}$ for given steady-state conditions at the location (u) per eq.(60).

$$K_{RD,g} = K_{RD,0} \cdot F_{g,av} \quad (60)$$

5.3.1.3 The compressible pressure-drop across a rupture disk with gas flow

The compressible pressure-drop across a rupture disk, $\Delta P_{RD,g}$ is formulated by simplifying eq.(52) symbolically, using averaged thermodynamic properties per eq.(61).

$$\Delta P_{RD,g} = - \frac{G_u^2}{2 \cdot \rho_{g,av}} \cdot K_{RD,g} \quad (61)$$

While L_d per eq. eq.(52) and $\lambda_{g,av}$ per eq.(57) vary significantly with Ma_u , the resulting $K_{RD,0}$ per must be constant, as seen in Figure 53.

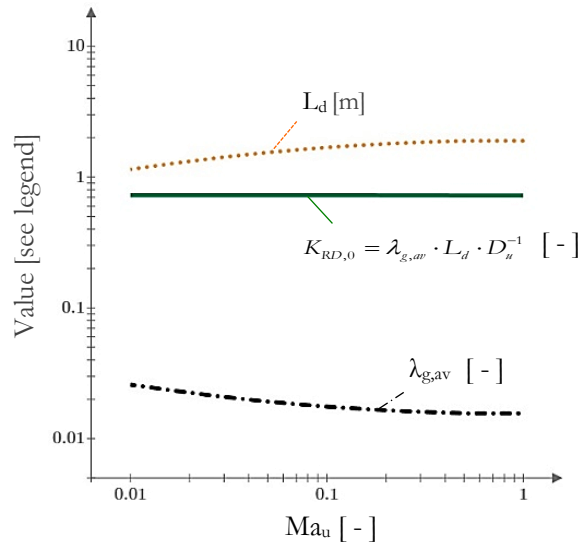


Figure 53 Validation of $K_{RD,0} = \text{const}$ assumption in eq.(53) with L_d per eq.(55) and λ_{av} per eq.(57).

Losses observed in low-velocity turbulent gas flow have been correlated to losses expected in high-velocity flow with equations for pipe in the CMLC-theory (Mutegei, et al., 2019). The separated flow region between (u) and (d) is modeled as a pipe with a variable length (see also: Figure 3a). The pipe loss coefficient between (u) and (d) is calculated per eq.(60). The maximum upstream Mach number $Ma_{u,theo}$ according to CMLC-theory is attained when the Mach number at the exit of the equivalent pipe length attains unity ($Ma_d \rightarrow 1.0$) for a given rupture disk zero-velocity loss coefficient, $K_{RD,0}$ with $K\{Ma_u, Ma_d\}$ per eq.(12).

$$Ma_{u,theo} \leftarrow K\{Ma_u, Ma_d\} - K_{RD,0} = 0 \quad \text{with } Ma_d = 0.99 \quad (62)$$

The maximum rupture disk equivalent length, $L_{d,theo}$ which would result in $Ma_{u,theo}=0.99$ at the exit is calculated iteratively per eq. (63) It is a function of a given $K_{RD,0}$ and $Ma_{u,theo}$ by solving for L_d with $Ma_{u,theo}$ from eq.(62).

$$L_{d,theo} \leftarrow K\{Ma_u, Ma_{d,theo}\} - \frac{\int_0^{L_d} \lambda_g \{L\} \cdot dL}{D_u} = 0 \quad (63)$$

The maximum rupture disk compressibility factor, $F_{g,av,theo}$ is calculated by integrating eq.(49) with $Ma\{L\}$ per eq.(56) and $L_{d,theo}$ per eq.(63).

$$F_{g,av,theo} = \frac{\int_0^{L_{d,theo}} \frac{1 + (\kappa - 1) \cdot Ma\{L\}^2}{1 - Ma\{L\}^2} \cdot dL}{L_{d,theo}} \quad (64)$$

The maximum rupture disk compressible minor loss coefficient, $K_{RD,g,theo}$ is calculated from $K_{RD,0}$ and the maximum averaged compressible minor loss coefficient factor, $F_{g,av,theo}$ for given steady-state conditions at location (u) per eq.(65).

$$K_{RD,g,theo} = K_{RD,0} \cdot F_{g,av,theo} \quad (65)$$

The maximum averaged fluid density, $\rho_{g,av,theo}$ is calculated by integrating eq.(66) with $L_{d,theo}$ per eq.(63) and $Ma\{L\}$ per eq.(56) (Truckenbrodt, 2008).

$$\rho_{g,av,theo} = \frac{\int_0^{L_{d,theo}} \left(\rho_u \cdot \frac{Ma_u}{Ma\{L\}} \cdot \frac{2 + (\kappa_u - 1) Ma\{L\}^2}{2 + (\kappa_u - 1) \cdot Ma_u^2} \right) \cdot dL}{L_{d,theo}} \quad (66)$$

The maximum compressible pressure-drop across a rupture disk, $\Delta P_{RD,g,theo}$ is calculated with the averaged thermodynamic properties in eq.(65) and eq.(66) per eq.(67).

$$\Delta P_{RD,g,theo} = - \frac{Q_m^2}{A_u^2} \cdot \frac{K_{RD,g,theo}}{2 \cdot \rho_{g,av,theo}} \quad (67)$$

Given the flow conditions upstream of the rupture disk, the general equation for determining the compressible pressure-drop across a rupture disk with gas flow, $\Delta P_{RD,g}$ is computed by coupling the non-choked and choked flow regions per eq.(68). The condition of $Ma_u \geq Ma_{u,theo}$ in eq.(68) is to limit the maximum possible pressure-drop if $Ma_u \geq Ma_{u,theo}$ is assumed during rupture disk sizing.

$$\Delta P_{RD,g} = \begin{cases} \text{if } 0 \leq Ma_u < Ma_{u,theo} & \Delta P_{RD,g} \\ \text{else if } Ma_u = Ma_{u,theo} & \Delta P_{RD,g,theo} \end{cases} \quad (68)$$

The downstream pressure with gas flow P_d , as illustrated in Figure 45, is calculated with a step function with $\Delta P_{RD,g}$ per eq.(68) at (RD).

$$P_{d,g} = P_u + \Delta P_{RD,g} \quad (69)$$

5.3.1.4 **Method to predict fanno-choking in rupture disk devices**

To further analyze the validity of the area-choking per eq.(35) based on the isentropic nozzle choking model, *Fanno-choking* is applied to calculate $Ma_{u,theo}$. Fanno-choking occurs when the Mach number at the exit of a rough adiabatic pipe attains unity. Losses observed in low-velocity gas flow have been correlated to losses expected in high-velocity flow with equations for pipes in the CMLC-theory in (Mutegi, et al., 2019). The separated flow region between (u) and (r) in Figure 43 is modeled as a fanno duct with a variable length (see also: Figure 51). The pipe loss coefficient between (u) and (r) is calculated per eq.(12).

Fanno-choking shall occur if the theoretical value for the choking Mach number $Ma_{u,theo}$ upstream of RD with CMLC-theory is attained. Under these conditions, the Mach number at the exit of the equivalent duct length attains unity ($Ma_r \rightarrow 1.0$) for a given rupture disk zero-velocity loss coefficient, $K_{RD,0}$ with $Ma_r = Ma_{u,theo}$ per eq.(62).

The consistency of *area-choking* in an apparent isentropic nozzle with $Ma_{u,theo}$ per eq.(35) and *fanno-choking* with equivalent pipe model and $Ma_{u,theo}$ per eq.(62) will be investigated in chapter 6.1.2.1 . For this, $Ma_{u,theo}$ will be calculated with area-choking and with fanno-choking under the same conditions and compared against each other. The two model representations are considered to be consistent if $Ma_{u,theo}$ with area-choking per eq.(35) is of the same magnitude as $Ma_{u,theo}$ with fanno-choking per eq.(62).

5.3.2 Method to determine pressure-drop with two-phase flow

The pressure-drop in a rupture disk is modeled using equations for pipes with gas flow. The strategy in this work is to correlate losses observed with low-velocity and incompressible flow to losses expected in high-velocity and compressible flow with an effective pipe length, as illustrated in Figure 51. A similar approach is also adopted for two-phase flow.

The pressure-drop across a rupture disk with the two-phase flow is modeled based on the (Müller-Steinhagen & Heck, 1986) method. Its advantage is in its simplicity in terms of computation effort, and its extensive validation. The advantages of this approach are listed in Table 3. The model parameters listed in Table 2 will be applied to develop this procedure. The pressure gradient in a pipe assuming liquid-only $(dP/dL)_l$ or gas-only $(dP/dL)_g$ is per eq.(70).

$$\left(\frac{dP}{dL}\right)_l = \frac{Q_m^2}{A_u^2} \cdot \frac{1}{D_i \cdot \rho_l} \cdot K_{RD,0,tp} \quad \left(\frac{dP}{dL}\right)_g = \frac{Q_m^2}{A_u^2} \cdot \frac{1}{D_i \cdot \rho_g} \cdot K_{RD,0,tp} \quad (70)$$

$K_{RD,0,tp}$ in eq.(70) is set to be the rupture disk minor loss coefficient for two-phase flow. It shall be determined experimentally for two-phase flow with mass flow rate gas quality $x_g < 0.30$.

The pressure gradient of two-phase flow $(dP/dL)_{friction,tp}$ is per eq.(71) analogous to the equation to calculate the pressure gradient in a pipe with (Müller-Steinhagen & Heck, 1986) per eq.(17). Here the empirical term in the original eq.(17) is set to 1 from 3 in eq.(71) to make the equation valid generally.

$$\left(\frac{dP}{dL}\right)_{friction,tp} = \left(F \cdot (1-x_g)^{1/C} + \left(\frac{dP}{dL}\right)_g \cdot x_g^C \right) \text{ with } C = 1 \quad (71)$$

with $F = \left(\frac{dP}{dL}\right)_l + 2 \cdot \left(\left(\frac{dP}{dL}\right)_g - \left(\frac{dP}{dL}\right)_l \right) \cdot x_g$

The pressure-drop across a rupture disk with now unknown rupture disk two-phase effective pipe length $L_{d,tp}$ -function, $L_{d,tp}\{\chi\}$ with eq.(71) is per eq.(72).

$$\Delta P_{RD,friction,tp} = - \left(\frac{dP}{dL}\right)_{friction,tp} \cdot L_{d,tp}\{\chi\} \quad (72)$$

Two-phase flow is especially characterized by complex interaction between multiple parameters in Table 2. In the case of $L_{d,tp}\{\chi\}$, more than 31 potential model parameters for modeling $L_{d,tp}\{\chi\}$ are identified based on Table 2 with $i = l, g, tp$. Here the flow patterns are not considered since they do not have numerical order but are taken into consideration since the void fraction ϵ_{tp} is determined according to (Bhagwat & Ghajar, 2014) as described in ANNEX XXI. The approach in (Bhagwat & Ghajar, 2014) describes how to determine the void fraction ϵ_{tp} independent of flow regime maps. This drift-flux model approach simplifies two-phase flow significantly. The accuracy of the (Bhagwat & Ghajar, 2014) correlation is found to predict void fraction ϵ_{tp} consistently mainly within $\pm 10\%$ of measured value over the entire range of the void fraction ($0 < \epsilon_{tp} < 1$) and is recommended to predict void fraction without any reference to flow regime maps.

A general relationship to determine $L_{d,tp}$ -function, $L_{d,tp}\{\chi\}$ with two-phase flow is required in eq. (73) so as to determine the pressure drop across a rupture disk with two phase flow. The target function for reducing the parameters of influence in $L_{d,tp}\{\chi\}$ is per eq.(73). Dimensional analysis is applied to find the $L_{d,tp}\{\chi\}$. A valid solution for this equation is defined as to be a finite set of real numbers between 0.90 and 1.0. This range corresponds to the convergence radius for the $L_{d,tp}\{\chi\}$, and to ensure that the proposed function predicts the pressure-drop within $\pm 10\%$ of measured value. The dimension for $L_{d,tp}\{\chi\}$ is set to Length L.

$$\frac{\Delta P_{tp,exp}}{\left(\frac{dP}{dL}\right)_{tp} \cdot L_{d,tp}\{\chi\}} = M_{tp} \in \{0.90...1.0\} \quad (73)$$

Three experiments, with gas mass flow quality $x_g < 0.3$, are used to find the model parameters for $L_{d,tp}$ -function. Low quality is selected because the target model should be based on the density of the liquid phase (incompressible flow). All the 31 model parameters are structured in a model parameter find-algorithm with their dimensions and combined until a valid solution is found for all three experimental data-points.

Table 17 Determination of the $L_{d,tp}$ -function, $L_{d,tp}\{\chi\}$ in eq. (72)

	C1	C2	C3	C4	C5	C6	C7	C8	C9	C10
R1	Parameter	x_g	$P_{u,exp}$	G_{exp} in	$\Delta P_{tp,exp}$	$P_{d,tp,exp}$	M_{tp}	$L_{d,tp}$	$\Delta P_{RD,calc}$	$P_{d,tp,calc}$
R2	unit	-	bar.a	kg/(s·m ²)	bar.a	bar.a	-	mm	bar.a	bar.a
R3	Exp. I	0.163	1.692	314.278	-0.181	1.493	0.961	62.492	-0.174	1.517
R4	Exp. II	0.201	1.619	304.879	-0.176	1.430	0.939	48.834	-0.166	1.453
R5	Exp. III	0.258	1.524	295.504	-0.160	1.356	0.97	35.930	-0.156	1.368

The parameter find-algorithm reduces the model parameters required to model the pressure-drop in a rupture disk to six, namely, upstream inner pipe diameter (D_u), two-phase friction factor (λ_{tp}) which is a function of the two-phase Reynolds number, Re_{tp} , upstream pressure (P_u), discharge pressure (P_a) superficial velocity of gas ($U_{s,g}$) and superficial velocity of liquid ($U_{s,l}$). The rupture disk two-phase effective pipe length $L_{d,tp}$ -function, $L_{d,tp}\{\chi\}$ is proposed as:

$$L_{d,tp} = \frac{4 \cdot D_u}{\lambda_{tp}} \cdot \frac{P_a}{P_u} \cdot U_{friction} \quad (74)$$

Here the *superficial velocity friction ratio*, $U_{friction}$ is per eq.(75). It is a dimensionless number that accounts for the two-phase frictional losses based on the superficial velocity of the gas-phase and liquid-phase.

$$U_{friction} = \frac{U_{s,g} \cdot U_{s,l}}{(U_{s,g} + U_{s,l})^2} \quad (75)$$

The gas-phase superficial velocity, $U_{s,g}$ and liquid phase superficial velocity, $U_{s,l}$ are defined in (Thome & Cioncolini, 2015) per eq.(76) where the two-phase mixture velocity, U_m is the sum of the superficial velocities of the gas and liquid phase (Awad & Muzychka, 2008).

$$U_{s,g} = \frac{x_g}{\rho_g} \cdot \frac{Q_m}{A_u} \quad U_{s,l} = \frac{(1-x_g)}{\rho_l} \cdot \frac{Q_m}{A_u} \quad U_m = U_{s,g} + U_{s,l} \quad (76)$$

The two-phase Reynolds number in (Bhagwat & Ghajar, 2014) is per eq.(77) and it is referenced to the thermodynamic properties of the liquid phase.

$$Re_{tp} = \frac{U_m \cdot \rho_{l,u} \cdot D_i}{\eta_{l,u}} \quad (77)$$

The two-phase Darcy friction factor in eq.(74) is solved for iteratively by solving for the Fanning factor for two-phase flow, $f_{friction,tp}$ from the definition of $f_{friction,tp}$ in (Bhagwat & Ghajar, 2014) per eq.(78).

$$\lambda_{tp} \leftarrow 4 \cdot \left[\left(-4 \cdot \log \left(\frac{k}{3.7 \cdot D_i} + \frac{1.256}{Re_{tp} \cdot f_{friction,tp}} \right) \right)^{-2} - f_{friction,tp} \right] \quad (78)$$

Eq.(74) is inserted in eq.(72) yielding the model length-based pressure drop, $\Delta P_{tp,L}$ with two-phase flow per eq.(79).

$$\Delta P_{tp,L} = - \left(\frac{dP}{dL} \right)_{friction,tp} \cdot L_{d,tp} \quad (79)$$

5.3.2.1 *The rupture disk incompressible minor loss coefficient for two-phase flow*

This work proposes the rupture disk incompressible minor loss coefficient for two-phase flow $K_{RD,0,tp}$, as a characteristic number for determining the two-phase pressure-drop across a rupture disk consistent with the proposed convention for gases and analogous to eq.(53) with $K_{RD,0,tp}$ per eq.(80).

$$K_{RD,0,tp} = const \quad (80)$$

Here, $K_{RD,0,tp}$ is a characteristic number for a rupture disk with two-phase flow. It is determined with low gas mass flow quality low with $x_g \rightarrow 0$. Once determined, $K_{RD,0,tp}$ is taken to be constant for two-phase flow. The validity of this assumption will be proven experimentally.

In two-phase flow, it is practicable to reference the pressure-drop across a rupture disk to the density of liquid-phase because it results to better accuracy. This approach is practicable because it does away with the need to determine the two-phase mixture density, ρ_{tp} upstream of rupture disk. In the following, the model parameters are referenced to the liquid-phase.

For this, the rupture disk two-phase compressibility factor, F_{tp} is introduced analogous to F_g , for gas flow per eq.(49) to factor compressibility and to correlate the rupture disk loss coefficient observed in low gas mass flow quality, to those expected in all other two-phase flows. This term is also used to relate the prevailing loss coefficient with two-phase flow to flow conditions upstream of the rupture disk device. It is also for referencing the model parameters to the thermodynamic properties of the liquid phase with model length-based pressure drop, $\Delta P_{tp,L}$ per eq.(79).

$$F_{tp} = \frac{A_u^2}{Q_{m,tp}^2} \cdot \frac{2 \cdot \rho_{l,u} \cdot \Delta P_{tp,L}}{K_{RD,0,tp}} \quad (81)$$

The resulting **rupture disk compressible two-phase minor loss coefficient**, $K_{RD,0,tp}$ is introduced based on eq.(71), eq.(74), eq.(79), eq.(80) and eq.(81). $K_{RD,tp}$ is the rupture disk minor loss coefficient with prevails for any given flow conditions at (u). $K_{RD,tp}$ is calculated from the rupture disk incompressible minor loss coefficient for two-phase flow $K_{RD,0,tp}$ and the rupture disk two-phase compressibility factor, F_{tp} for given steady-state conditions at the location (u) per eq.(60).

$$K_{RD,tp} = K_{RD,0,tp} \cdot F_{tp} = \Delta P_{tp,L} \cdot \frac{A_u^2}{Q_{m,tp}^2} \cdot 2 \cdot \rho_{l,u} = - \left(\frac{dP}{dL} \right)_{friction,tp} \cdot \frac{4 \cdot D_u}{\lambda_{tp}} \cdot \frac{P_u}{P_u} \cdot U_{friction,tp} \cdot \frac{A_u^2}{Q_{m,tp}^2} \cdot 2 \cdot \rho_{l,u} \quad (82)$$

The rupture disk compressible two-phase pressure-drop referenced to liquid density, $\Delta P_{RD,tp}$ is formulated by rearranging eq.(82) symbolically and adding the geodetic pressure loss in eq.(19) resulting in eq.(83). The contribution of the gas phase to geodetic pressure losses are negligible in a rupture disk and can be neglected in eq. (83).

$$\Delta P_{RD,tp} = \frac{Q_{m,tp}^2}{A_u^2} \cdot \frac{1}{2 \cdot \rho_{l,u}} \cdot K_{RD,tp} - \left(\varepsilon_{tp} \cdot \rho_{g,u} + (1 - \varepsilon_{tp}) \cdot \rho_{l,u} \right) \cdot g \cdot \sin(\theta) \cdot \Delta H_{RD} \quad (83)$$

The pressure downstream of the rupture disk (RD) with two-phase flow, $P_{d,tp}$ is per eq.(84).

$$P_{d,tp} = P_u + \Delta P_{RD,tp} \quad (84)$$

5.4 Recommended working equations for liquids, gases and two-phase flow

The phenomenological relations to determine the dischargeable mass flow rate across a rupture disk for gas flow, $Q_{m,g}$ per eq.(37), with for two-phase flow $Q_{m,tp}$ per eq. (48), as well as the phenomenological equations to determine the pressure-drop across a rupture disk, $\Delta P_{RD,g}$ per eq.(68) and $\Delta P_{RD,tp}$ per eq.(83) have been determined. In the following, mathematical closure relationships will be applied to couple these phenomenological relations for the range of gas mass flow quality $0.95 < x_g \leq 1.0$ with the tanh-trigonometric function. This eliminates the need to use logical computation, for example, with an IF-clause, which might otherwise result in a non-monotonous step-function.

5.4.1 The general equation for the rupture disk dischargeable mass flow rate

The dischargeable mass flow rate with two phase-flow $Q_{m,tp}$ per eq. (48) is only valid for $0 \leq x_g < 1$. Therefore a closure relationship for $x_g \rightarrow 1$ is applied for this range with $Q_{m,g}$ for gas flow per eq.(37) is needed. The closure relationship is by using the tanh trigonometric function to compute for the rupture disk dischargeable mass flow rate, $Q_{m,g}$ for the full range of $0 \leq x_g \leq 1$ per eq.(85).

$$Q_{m,RD} = Q_{m,tp} + \frac{1 + \tanh(D_d \cdot (x_g - x_{g,c}))}{2} \cdot (Q_{m,g} - Q_{m,tp}) \quad (85)$$

Here the constant $x_{g,c}=0.95$ is the closure point at $x_g=0.95$ and the constant $D_d=100$ is the damping factor to close the region between $0.95 < x_g \leq 1.0$ with a smooth function, where the trigonometric tanh-function is suited (Miller & Ross, 1993).

5.4.2 The general equation for rupture disk compressible pressure-drop

The pressure-drop across a rupture disk with two phase-flow $\Delta P_{RD,tp}$ per eq.(83) is only valid for $0 \leq x_g < 1$ since the superficial velocity of liquid $U_{s,l} \rightarrow -\infty$ in eq.(74) for $x_g \rightarrow 1.0$. Therefore a closure relationship for $x_g \rightarrow 1$ is applied for this range with $\Delta P_{RD,g}$ for gas flow per eq.(68) is needed analogous to the mass flow rate in the previous section. The closure relationship is by using the tanh trigonometric function to compute for the rupture disk compressible pressure drop, ΔP_{RD} for the full range of $0 \leq x_g \leq 1$ per eq.(86).

$$\Delta P_{RD} = \Delta P_{RD,tp} + \frac{1 + \tanh(D_d \cdot (x_g - x_{g,c}))}{2} \cdot (\Delta P_{RD,g} - \Delta P_{RD,tp}) \quad (86)$$

As for the mass flow rate approach, the constant $x_{g,c}=0.95$ is the closure point at $x_g=0.95$ and the constant $D_d=100$ is the damping factor to close the region between $0.95 < x_g \leq 1.0$ with a smooth function also with the trigonometric tanh-function (Miller & Ross, 1993).

$$\Delta P_{RD,g} = \frac{Q_{m,tp}^2}{A_u^2} \cdot \frac{1}{2 \cdot \rho_{g,u}} \cdot K_{RD,0} \cdot F_{g,u} \quad \text{with } F_{g,u} = -\frac{1 + (\kappa_g - 1) \cdot Ma_{g,u}^2}{1 - Ma_{g,u}^2} \quad (87)$$

The upstream Mach number of gas the phase, $Ma_{g,u}$ in eq.(87) is computed assuming gas-only with gas void fraction, $\varepsilon_{tp}=1.0$ because $\varepsilon_{tp} \rightarrow 1.0$ for gas mass flow quality $x_g > 0.95$.

$$Ma_{g,u} = \left(\frac{Q_{m,tp}}{\varepsilon_{tp} \cdot A_u} \cdot \frac{x_g}{\rho_g \cdot c_{s,g}} \right) \quad (88)$$

A step function simplifies the downstream pressure P_d as illustrated in Figure 45 with ΔP_{RD} per eq.(86) for gas and two-phase flow.

$$P_d = P_u + \Delta P_{RD} \quad (89)$$

6 Experimental validation of a sizing procedure for rupture disk devices

In the following the proposed methodology for “Experimental validation of the dischargeable mass flow rate model” as described in chapter 6.1 will be validated in chapter 6.1 while the proposed methodology for “Modeling of pressure-drop across a rupture disk device” as described in chapter 5.3 will be validated in chapter 6.2. Experiments with gas flow are done with the “Laboratory-scale gas pilot plant for test with air,” which is described in chapter 4.10, while experiments with two-phase flow are done with the “Laboratory-scale two-phase pilot rig for tests with air/water” in chapter 4.11. The same “Rupture disk test section with measurement and instrumentation” is used for all experiments, as described in chapter 4.9.

6.1 Experimental validation of the dischargeable mass flow rate model

The method to determine the dischargeable mass flow rate will be validated in the following order:

- i. The method to determine the rupture disk discharge area, A_{RD} per eq.(40) will be determined experimentally.
- ii. The determined A_{RD} will be used to validate the method to determine the dischargeable mass flow rate across a rupture disk, $Q_{m,RD}$ per eq.(85) with gas flow and $x_g=1.0$ with three different types of rupture disk. The validity of the equations to predict area-choking per eq.(35) and fanno-choking per eq.(62) will also be investigated.
- iii. The proposed method to determine the dischargeable mass flow rate across a rupture disk with gas flow, $Q_{m,g}$ per eq.(37) and dischargeable mass flow rate with two-phase flow, $Q_{m,tp}$ per eq.(48) will be calculated as described and the methods proposed will be validated experimentally. $Q_{m,g}$ per eq.(37) and $Q_{m,tp}$ per eq.(48) are incorporated in the general equation for the rupture disk dischargeable mass flow rate, $Q_{m,RD}$ for the full range of $0 \leq x_g \leq 1$, with $Q_{m,RD}$ per eq.(85).

6.1.1 Determination of rupture disk free relieving area with a low-velocity flow

The validation of the proposed method to determine the rupture disk relieving area experimentally is presented below. Experiments with gas flow are done in the test facility described in chapter 4.10.

The rupture disk discharge area A_{RD} is a model parameter that is required for gas flow and two-phase flow. It is determined once with low-velocity gas flow and used to determine the dischargeable mass flow rate with gas flow, as described in chapter 3.2.1.1.

A rupture disk device is installed centered between the inlet and outlet pipe segment. The test section is calibrated before the tests. The pressure in the test vessel is gradually increased until the target pressure and stationary flow conditions are attained by gradually opening the precision control valve, CV-01 manually (see: Figure 30). These stationary flow conditions are then held constant for at least 5 seconds at a sample rate of 10 data-points per second, to collect at least 40 data points as listed in column C7 in Table 18. The following sample measured data set is acquired for each experiment.

Table 18 Sample measured data set for a regular bore with measured diameter ratio $\beta_{geo}=0.80$ after fabrication for a DN40 test section with air.

	C1	C2	C3	C4	C5	C6	C7
R1	Channel	Symbol	Mean	$\pm U$	Unit	L in mm	n
R2	Base pressure	P_b	201.58	0.69	mbar.g	-	95
R3	Pressure at tap 01	$P_{tap,01}$	115.14	0.21	mbar.g	2470	95
R4	Pressure at tap 02	$P_{tap,02}$	105.80	0.32	mbar.g	3110	95
R5	Pressure at tap 03	$P_{tap,03}$	101.95	0.37	mbar.g	3320	95
R6	Pressure at tap 04	$P_{tap,04}$	98.28	0.83	mbar.g	3670	95
R7	Pressure at tap 09	$P_{tap,09}$	30.06	0.22	mbar.g	4230	95
R8	Pressure at tap 10	$P_{tap,10}$	21.85	0.28	mbar.g	4475	95
R9	Pressure at tap 11	$P_{tap,11}$	7.43	0.31	mbar.g	5195	95
R10	Mass flow rate	$Q_{m,exp}$	131.19	0.04	g/s	-	95
R11	Base temperature	T_b	296.35	1.00	K	-	95
R12	Ambient temperature	T_a	294.21	1.00	K	-	95
R13	Ambient pressure	P_a	992.37	0.40	mbar, a	-	95

6.1.1.1 **Test objects for validating the method to determine the rupture disk discharge area**

Test objects for validating the implicit method to determine A_{RD} experimentally are seven circular bores and six segmental bores for both the DN25 and DN40 test sections. The surfaces of the bores are fabricated per ISO 5167-2 (ISO, 2003) (See: Figure 54). These bores are fabricated to have a target diameter ratio, β_{bore} of 0.70 through 0.95 in steps of 0.05 relative to the inner pipe diameter D_1 with $\beta_{bore} = (A_{bore}/A_1)^{0.5}$ as seen in Table 19 column C1. This range of diameter ratio is primarily selected because rupture disk devices are expected to have a similar range of diameter ratios (Friedel & Kissner, 1988) and secondarily to check for the validity of eq.(40) for diameter ratios larger than 0.75 as intended. Circular bores and segmental bores are installed with a custom-made holder with the same inner diameter as the pipe, while a rupture disk device is installed with its designated holder.

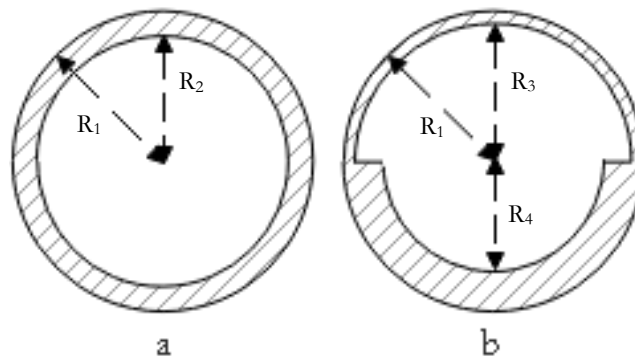


Figure 54 Geometry of test objects tested. a. circular bores made of one segment. b. segmental bores made of two segments.

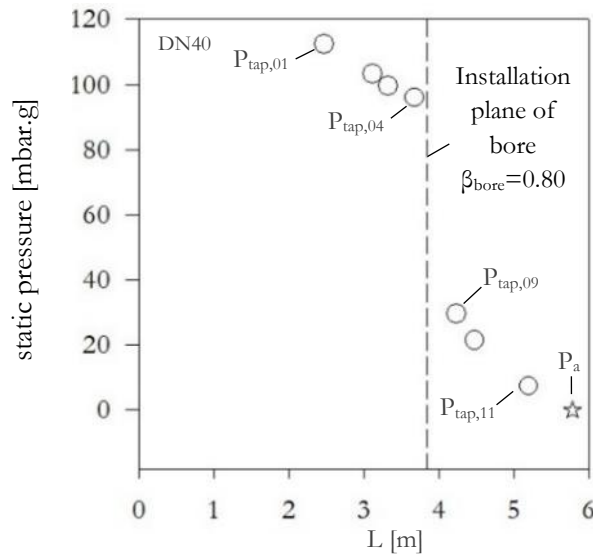


Figure 55 Plot of experimental data in Table 18, with $\beta_{bore}=0.80$ showing pressure in taps $P_{tap,01}$ through $P_{tap,11}$ with test object downstream of $P_{tap,04}$.

The effective diameter ratio β_{eff} of each test object is calculated with measured values Ω_{nom} , with $\Omega_{min} = \Omega_{nom} - U$ and with $\Omega_{max} = \Omega_{nom} + U$ with U as the uncertainty of measurement for the respective channel to sample the sensitivity of the method. These values are the nominal, minimum and maximum values, respectively. The certified fabrication tolerance for the inner diameter ($2 \cdot R_1$) for the DN25 pipe and DN40 pipe is 0.58 mm and 0.59 mm respectively. The dimensions of the test objects are constant as presented in Table 19.

The aim is to validate that the method presented is suitable for determining a bore's diameter ratio irrespective of the shape and symmetry of the bore for diameter ratio of bore larger than 0.75 as rupture disk devices are typically also not circular and the rupture disk diameter ratio is expected to be larger than 0.75. The dimensions of circular and segmental DN25 and DN40 test objects depicted in Figure 54.

The dimensions of the circular bores are given in Table 19 column C2 and C5, respectively, with R_2 . Segmental bores consist of two semi-circular segments with R_3 and R_4 which are combined and installed centered in a holder; they have the same discharge area as circular bores. The dimensions of DN25 and DN40 segmental bores with $D_{geo,2}$ & $D_{geo,3}$ are in Table 19 column C3 & C4 and C6 & C7, respectively.

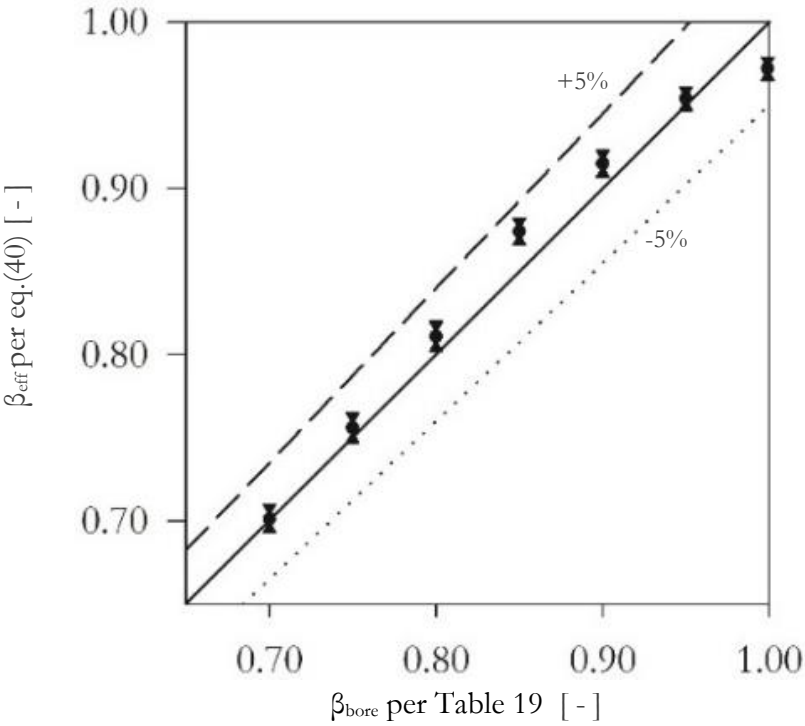
Table 19 Dimensions of test objects for validating the proposed method in mm. See also: Figure 54.

		DN25			DN40		
	C1	C2	C3	C4	C5	C6	C7
R1	β_{bore}	$2 \cdot R_2$	$2 \cdot R_3$	$2 \cdot R_4$	$2 \cdot R_2$	$2 \cdot R_3$	$2 \cdot R_4$
R2	1.00	26.64	-	-	40.90	-	-
R3	0.95	25.31	26.64	23.90	38.86	40.90	36.70
R4	0.90	23.98	25.31	22.57	36.81	38.86	34.64
R5	0.85	22.64	23.98	21.23	34.77	36.81	32.59
R6	0.80	21.31	22.64	19.89	32.72	34.77	30.54
R7	0.75	19.98	21.31	18.55	30.68	32.72	28.48
R8	0.70	18.65	19.98	17.21	28.63	30.68	26.43
Ref: Figure 54		a	b		a	b	

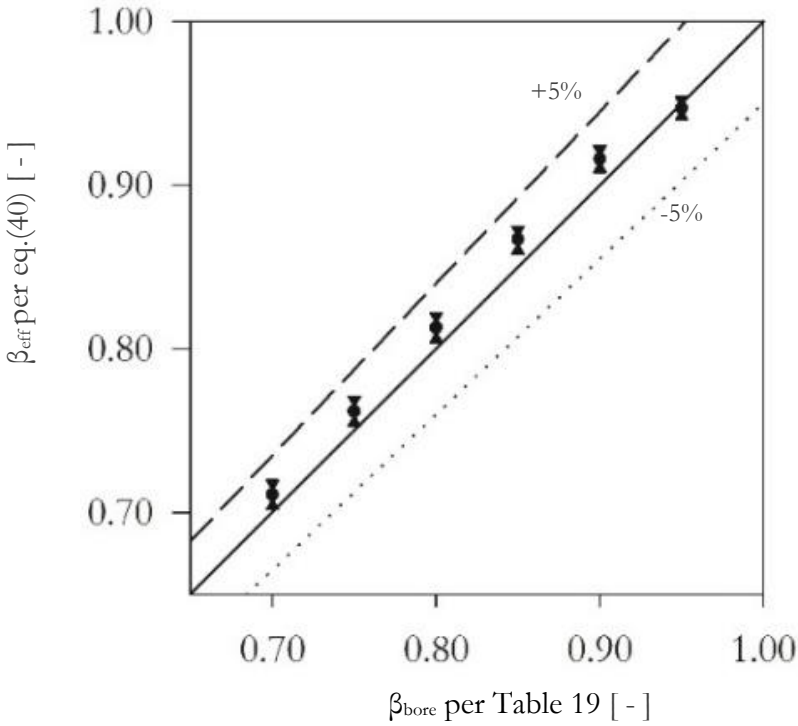
6.1.1.2 Determination of rupture disk discharge area from experimental results

The flow resistance method is applied to determine a test object's minor loss coefficient, which is required in eq.(40) from the measured data, analogous to the method prescribed in ASME PTC- (ASME, 2014) with dry air. The upstream Reynolds number is calculated with the pressure and temperature at pressure tap, $P_{tap,04}$ which is 3 inner pipe diameters upstream of the test object. Reference fluid thermodynamic and transport properties for air are derived from the CoolProp database (Bell, et al., 2014).

The method to determine A_{RD} is first validated with 26 experiments. The diameter ratio β_{eff} of fourteen circular bores and twelve segmental bores with dimension per Table 19 is determined with an implicit method to determine the discharge area experimentally with eq.(40). Experiments in this work show that the equations used to reproduce the relationship between K_R , β_{bore} and C_d reliably for bores with $\beta_{bore} > 0.70$ as seen below.

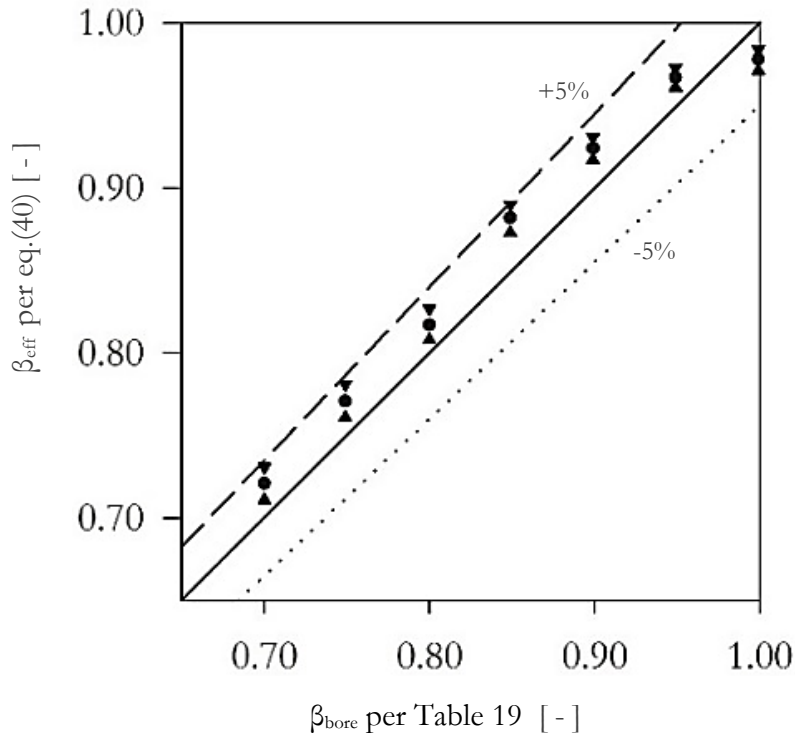


a

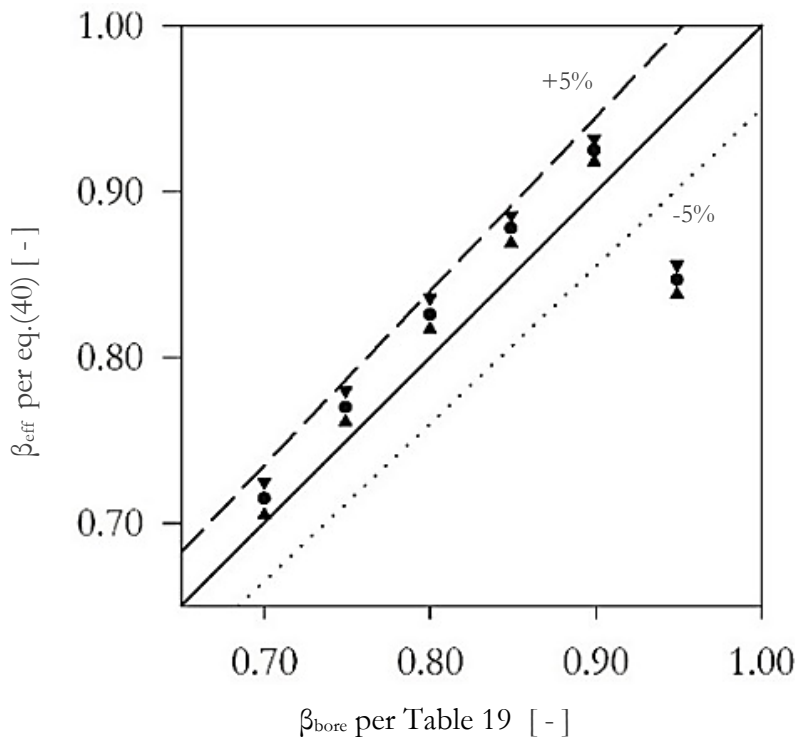


b.

Figure 56 Results for diameter ratio, β_{eff} for DN40 circular and segmental bores per eq.(40)
 a. DN40 circular bore b. DN40 segmental bore calculated with \bullet Ω_{nom} , \blacktriangledown Ω_{min} and \blacktriangle Ω_{max} .



a



b.

Figure 57 Results for diameter ratio, β_{eff} for DN25 circular and segmental bores per eq.(40)
 a. DN25 circular bore b. DN25 segmental bore calculated with \bullet Ω_{nom} , \blacktriangledown Ω_{min} and \blacktriangle Ω_{max} .

The implicit method to determine the discharge area experimentally determines the discharge area of both the circular and segmental bores within $\pm 5\%$ of the actual area. This is within the range of fabrication tolerances for the objects with β_{bore} ranging from 0.70 through 0.95 for the DN40 bores and 0.90 for DN25 bores as seen in Figure 56 and Figure 57. No explanation was found for the outlier in Figure 57b for the segmental bore with $\beta_{\text{bore}}=0.95$ in the DN25 test section. The method presented may therefore be used to determine the rupture disk effective minimum discharge area, A_{RD} by characterizing A_{RD} which is typically not circular as a circular bore. Based on the experimental results, the method proposed is reliable to predict the area for $\beta_{\text{eff}} > 0.70$ and $\beta_{\text{eff}} < 0.95$ for DN40 and $\beta_{\text{eff}} < 0.90$ for DN25. The use of this method to predict the area for smaller or larger diameter ratios is subject to additional experimental validation.

The rupture disk minimum discharge area, A_{RD} of three different types of rupture disk devices, TS0102 DN40, TS0202 DN40 and TS0302 DN40 (identified as TI, TII, TIII) was determined with eq.(40) using low-velocity experimental data in Table 20, Table 21 and Table 22, respectively.

Table 20 Measured data with a low-velocity experiment with TS0102 DN40 (TI).

	C1	C2	C3	C4	C5	C6	C7
R1	Channel	Symbol	Mean	$\pm U$	Unit	L in mm	n
R2	Base pressure	P_b	200.15	0.69	mbar.g	-	98
R3	Pressure at tap 01	$P_{\text{tap},01}$	97.95	0.21	mbar.g	2470	98
R4	Pressure at tap 02	$P_{\text{tap},02}$	86.76	0.32	mbar.g	3110	98
R5	Pressure at tap 03	$P_{\text{tap},03}$	82.05	0.37	mbar.g	3320	98
R6	Pressure at tap 04	$P_{\text{tap},04}$	77.32	0.83	mbar.g	3670	98
R7	Pressure at tap 09	$P_{\text{tap},09}$	34.67	0.22	mbar.g	4230	98
R8	Pressure at tap 10	$P_{\text{tap},10}$	25.47	0.28	mbar.g	4475	98
R9	Pressure at tap 11	$P_{\text{tap},11}$	8.24	0.31	mbar.g	5195	98
R10	Mass flow rate	$Q_{\text{m,exp}}$	142.39	0.04	g/s	-	98
R11	Base temperature	T_b	296.07	1.00	K	-	98
R12	Ambient temperature	T_a	294.19	1.00	K	-	98
R13	Ambient pressure	P_a	992.35	0.40	mbar.a	-	98

Table 21 Measured data with a low-velocity experiment with TS0202 DN40 (TII).

	C1	C2	C3	C4	C5	C6	C7
R1	Channel	Symbol	Mean	$\pm U$	Unit	L in mm	n
R2	Base pressure	P_b	200.87	0.69	mbar.g	-	97
R3	Pressure at tap 01	$P_{\text{tap},01}$	91.42	0.21	mbar.g	2470	97
R4	Pressure at tap 02	$P_{\text{tap},02}$	79.37	0.32	mbar.g	3110	97
R5	Pressure at tap 03	$P_{\text{tap},03}$	74.34	0.37	mbar.g	3320	97
R6	Pressure at tap 04	$P_{\text{tap},04}$	69.19	0.83	mbar.g	3670	97
R7	Pressure at tap 09	$P_{\text{tap},09}$	36.39	0.22	mbar.g	4230	97
R8	Pressure at tap 10	$P_{\text{tap},10}$	26.99	0.28	mbar.g	4475	97
R9	Pressure at tap 11	$P_{\text{tap},11}$	9.30	0.31	mbar.g	5195	97
R10	Mass flow rate	$Q_{\text{m,exp}}$	147.30	0.04	g/s	-	97
R11	Base temperature	T_b	292.65	1.00	K	-	97
R12	Ambient temperature	T_a	293.32	1.00	K	-	97
R13	Ambient pressure	P_a	978.50	0.40	mbar.a	-	97

Table 22 Measured data with a low-velocity experiment with TS0302 DN40 (TIII).

	C1	C2	C3	C4	C5	C6	C7
R1	Channel	Symbol	Mean	$\pm U$	Unit	L in mm	n
R2	Base pressure	P_b	200.56	0.69	mbar.g	-	98
R3	Pressure at tap 01	$P_{tap,01}$	120.78	0.21	mbar.g	2470	98
R4	Pressure at tap 02	$P_{tap,02}$	112.17	0.32	mbar.g	3110	98
R5	Pressure at tap 03	$P_{tap,03}$	108.76	0.37	mbar.g	3320	98
R6	Pressure at tap 04	$P_{tap,04}$	105.00	0.83	mbar.g	3670	98
R7	Pressure at tap 09	$P_{tap,09}$	27.85	0.22	mbar.g	4230	98
R8	Pressure at tap 10	$P_{tap,10}$	20.51	0.28	mbar.g	4475	98
R9	Pressure at tap 11	$P_{tap,11}$	7.43	0.31	mbar.g	5195	98
R10	Mass flow rate	$Q_{m,exp}$	126.05	0.04	g/s	-	98
R11	Base temperature	T_b	286.01	1.00	K	-	98
R12	Ambient temperature	T_a	290.95	1.00	K	-	98
R13	Ambient pressure	P_a	977.92	0.40	mbar.a	-	98

The results for the determined discharge area for the data with the three different types of rupture disk, according to the method presented, found that the rupture disks tested have $0.790 < \beta_{RD} < 0.890$ as seen in Table 23.

 Table 23 Results for σ_{RD} and A_{RD} determined with the method presented with eq. (40).

Rupture disk	P_b	G_u	P_u	T_u	ρ_u	Ma_u	Re_u	β_{RD}	σ_{RD}
unit	mbar.a	kg/(s·m ²)	mbar.a	K	kg/m ³	-	-	-	-
TS0102DN40 (TI)	1192	108.4	1070	293	1.274	0.2480	2.44E+05	0.877	0.769
TS0202DN40 (TII)	1192	106.3	1063	294	1.256	0.2458	2.38E+05	0.890	0.792
TS0302DN40 (TIII)	1178	95.9	1083	283	1.331	0.2135	2.21E+05	0.796	0.634
								Eq.(40)	Eq.(40)

6.1.2 Prediction of dischargeable mass flow rate with gas flow

Similar experiments were done with three rupture disk types by keeping the pressure upstream of the rupture disk with constant pressure upstream $P_u \approx 2.3$ bar.a to determine the dimensionless mass flow rate, $C_{m,RD*}$ at a burst pressure of 2.3 bar.a.

Table 24 Measured data with a high-velocity experiment with TS0102 DN40 (TI).

	C1	C2	C3	C4	C5	C6	C7
R1	Channel	Symbol	Mean	$\pm U$	Unit	L in mm	n
R2	Base pressure	P_b	2336.37	0.69	mbar.g	-	49
R3	Pressure at tap 01	$P_{tap,01}$	1568.89	0.21	mbar.g	2470	49
R4	Pressure at tap 02	$P_{tap,02}$	1479.40	0.32	mbar.g	3110	49
R5	Pressure at tap 03	$P_{tap,03}$	1435.90	0.37	mbar.g	3320	49
R6	Pressure at tap 04	$P_{tap,04}$	1399.20	0.83	mbar.g	3670	49
R7	Pressure at tap 09	$P_{tap,09}$	876.56	0.22	mbar.g	4230	49
R8	Pressure at tap 10	$P_{tap,10}$	748.17	0.28	mbar.g	4475	49
R9	Pressure at tap 11	$P_{tap,11}$	470.90	0.31	mbar.g	5195	49
R10	Mass flow rate	$Q_{m,exp}$	611.35	0.18	g/s	-	49
R11	Base temperature	T_b	301.08	1.00	K	-	49
R12	Ambient temperature	T_a	293.92	1.00	K	-	49
R13	Ambient pressure	P_a	992.37	0.40	mbar.a	-	49

Table 25 Measured data with a high-velocity experiment with TS0202 DN40 (TII).

	C1	C2	C3	C4	C5	C6	C7
R1	Channel	Symbol	Mean	$\pm U$	Unit	L in mm	n
R2	Base pressure	P_b	2377.55	0.69	mbar.g	-	40
R3	Pressure at tap 01	$P_{tap,01}$	1582.23	0.21	mbar.g	2470	40
R4	Pressure at tap 02	$P_{tap,02}$	1490.74	0.32	mbar.g	3110	40
R5	Pressure at tap 03	$P_{tap,03}$	1447.54	0.37	mbar.g	3320	40
R6	Pressure at tap 04	$P_{tap,04}$	1406.02	0.83	mbar.g	3670	40
R7	Pressure at tap 09	$P_{tap,09}$	907.05	0.22	mbar.g	4230	40
R8	Pressure at tap 10	$P_{tap,10}$	782.10	0.28	mbar.g	4475	40
R9	Pressure at tap 11	$P_{tap,11}$	500.97	0.31	mbar.g	5195	40
R10	Mass flow rate	$Q_{m,exp}$	628.84	0.19	g/s	-	40
R11	Base temperature	T_b	296.13	1.00	K	-	40
R12	Ambient temperature	T_a	291.07	1.00	K	-	40
R13	Ambient pressure	P_a	991.61	0.40	mbar.a	-	40

Table 26 Measured data with a high-velocity experiment with TS0302 DN40 (TIII).

	C1	C2	C3	C4	C5	C6	C7
R1	Channel	Symbol	Mean	$\pm U$	Unit	L in mm	n
R2	Base pressure	P_b	2021.72	0.69	mbar.g	-	96
R3	Pressure at tap 01	$P_{tap,01}$	1491.99	0.21	mbar.g	2470	96
R4	Pressure at tap 02	$P_{tap,02}$	1434.71	0.32	mbar.g	3110	96
R5	Pressure at tap 03	$P_{tap,03}$	1408.97	0.37	mbar.g	3320	96
R6	Pressure at tap 04	$P_{tap,04}$	1385.23	0.83	mbar.g	3670	96
R7	Pressure at tap 09	$P_{tap,09}$	574.78	0.22	mbar.g	4230	96
R8	Pressure at tap 10	$P_{tap,10}$	483.22	0.28	mbar.g	4475	96
R9	Pressure at tap 11	$P_{tap,11}$	263.20	0.31	mbar.g	5195	96
R10	Mass flow rate	$Q_{m,exp}$	508.85	0.15	g/s	-	96
R11	Base temperature	T_b	288.18	1.00	K	-	96
R12	Ambient temperature	T_a	290.83	1.00	K	-	96
R13	Ambient pressure	P_a	977.70	0.40	mbar.a	-	96

The key properties from these three experiments with Table 24, Table 25 and Table 26 are tabulated in Table 27. The rupture disk zero-velocity loss coefficient, $K_{RD,0}$ is calculated with the CMLC-theory (Mutegi, et al., 2019).

Table 27 Measured experimental data for three rupture disk types under similar flow conditions.

	C1	C2	C3	C4	C5	C6
R1	Given property	Symbol	unit	TS0102 DN40	TS0202 DN40	TS0303 DN40
R2	Inner pipe diameter	D_i	mm	40.9	40.9	40.9
R3	Discharge area A_{RD}	A_{RD}	mm ²	1010.5	1040.7	832.5
R4	Loss coefficient	$K_{RD,0}$	-	0.725	0.646	1.978
R5	Molar mass of air	M_m	gm/mol	28.97	28.97	28.97
R6	Ratio of specific heat	κ	-	1.405	1.405	1.405
R7	Base pressure	P_b	bar.a	3.329	3.369	2.999
R8	Base temperature	T_b	K	301.1	296.7	288.2
R9	Ambient pressure	P_a	bar.a	0.992	0.992	0.978
R10	Ambient temperature	T_a	K	293.9	291.1	290.8
R11	Mass flow rate discharged	$Q_{m,exp}$	kg/hr	2200.9	2220.4	1831.9
R12	Pressure upstream of RD	P_u	bar.a	2.392	2.370	2.363

Looking at Table 27, TS0302 has the smallest A_{RD} (R3) and lowest $Q_{m,exp}$ (R11). The discharge area significantly affects the discharge rate under similar discharge conditions. Also, the smaller the size of A_{RD} (R3), the higher the $K_{RD,0}$ (R4). This is consistent with Figure 48. The proposed theory is now used to evaluate the experimental data for the three experiments in Table 33. The following properties are calculated for the $P_b \approx 3.3$ bar.g experiments.

Table 28 Calculated properties for the experimental data of the three rupture disk types in Table 27.

C1	C2	C3	C4	C5	C6	C7	
R1	Calculated property	Symbol	unit	Eq.	TS0102 DN40	TS0202 DN40	TS0303 DN40
R2	Mass flux	G_u	$kg/(s \cdot m^2)$	-	465.3	469.5	387.3
R3	Pressure upstream of RD	P_u	bar.a	-	2.392	2.370	2.363
R4	Temperature upstream of RD	T_u	K	-	289.2	284.7	280.2
R5	Density of fluid	ρ_u	kg/m^3	-	2.884	2.903	2.941
R6	Velocity of fluid	w_u	m/s	-	161.37	161.74	131.69
R7	Mach number	Ma_u	-	-	0.463	0.468	0.386
R8	Reynolds number	Re_u	$\cdot 10^6$	-	1.033	1.055	0.887
R9	Stagnation pressure	$P_{0,u}$	bar.a	(28)	2.772	2.754	2.620
R10	Stagnation temperature	$T_{0,u}$	K	(28)	301.8	297.3	288.7
R11	Stagnation density	$\rho_{0,u}$	kg/m^3	(28)	3.203	3.230	3.165
R12	Flow restriction	Φ	-	(35)	0.917	0.897	0.965
R13	Pressure at A_{RD}	P_{RD}	bar.a	(28)	1.985	2.029	1.709
R14	Temperature at A_{RD}	T_{RD}	K	(28)	274.1	272.3	255.2
R15	Mach number at A_{RD}	Ma_{RD}	-	(29)	0.706	0.674	0.805
R16	Stagnation pressure ratio	$\eta_{RD,0}$	-	(38)	0.716	0.737	0.652
R18	Predicted mass flow rate at A_{RD}	$Q_{m,RD,g}$	kg/hr	(27)	2154.6	2172.8	1804.8
R19	Pressure ratio at A_r	P_r	bar.a	(28)	1.462	1.453	1.382
R20	Temperature at A_r	T_r	K	(28)	250.9	247.3	240.1
R21	Mach number at A_r	Ma_r	-	(29)	1.000	1.000	1.000
R22	Stagnation pressure A_r	$\eta_{r,0}$	-	(38)	0.527	0.527	0.527
R23	Predicted mass flow rate at A_r	$Q_{m,r,g}$	kg/hr	(27)	2154.6	2172.8	1804.8
R24	Theoretical upstream Mach number	$Ma_{u,theo}$	-	(29)	0.527	0.545	0.404
R25	Theoretical mass flow rate with $Ma_{u,theo}$	$Q_{m,theo}$	kg/hr	(27)	2427.3	2531.9	1885.0
R26	Dimensionless mass flow rate	$C_{m,RD}$	-	(36)	0.888	0.858	0.957

The TS0302 rupture disk had the highest value of Φ row (R12), as seen in Table 28. Ma_{RD} (R15) is higher than Ma_u (R7), while Ma_r (R15) is significantly higher than Ma_u and Ma_{RD} (R15). This shows that rupture disks devices cause significant restriction of flow. $Ma_{u,theo}$ (R24), is highest in TS0202. This means that TS0202 also has the highest $Q_{m,theo}$ (R25). $Q_{m,RD}$ (R15) and $Q_{m,r}$ (R23) are within range of mass flow rate discharged $Q_{m,exp}$ in Table 27 (R11).

In the following, the rupture disk dischargeable mass flow rate, $Q_{m,RD}$ with $x_g=1$ per eq.(85) will be evaluated the remaining 250 data points from experiments done with low-velocity incompressible and high-velocity compressible flows with rupture disk type I, type II and type III analogous to Table 28. Experimental data was collected with the three DN40 rupture disk samples in Table 23 (TS0102 with 75 data-points, TS0202 with 96 data-points & TS0302 with 82 data-points). The three rupture disk types exhibit significant differences in the shape of the free discharge area, A_{RD} .

The values of Φ per eq.(35), Ma_{RD} and Ma_r per eq. (29) and $\eta_{RD,0}$ and $\eta_{r,0}$ per eq.(38), are first calculated and plotted against Ma_u . The dimensionless mass flow rate $C_{m,RD}$ at (RD) and $C_{m,r}$ at (r) per eq.(36) is then calculated with Φ per eq.(34) and plotted against pressure ratio at (RD) referenced to stagnation conditions $\eta_{RD,0}$ per eq.(38). The deviation of the predicted mass flow rate with (API, 2014) , $\delta Q_{m,API}$ per eq.(1) and the proposed method with $\delta Q_{m,RD}$ at (RD) and $\delta Q_{m,r}$ at (r) per eq.(27) from the measured mass flow rate $\delta Q_{m,exp}$ is also calculated and plotted against Ma_u to evaluate the accuracy of these two methods.

Results for rupture disk type I:

The proposed theory is examined with 75 data-points with test object TS0102 DN40.

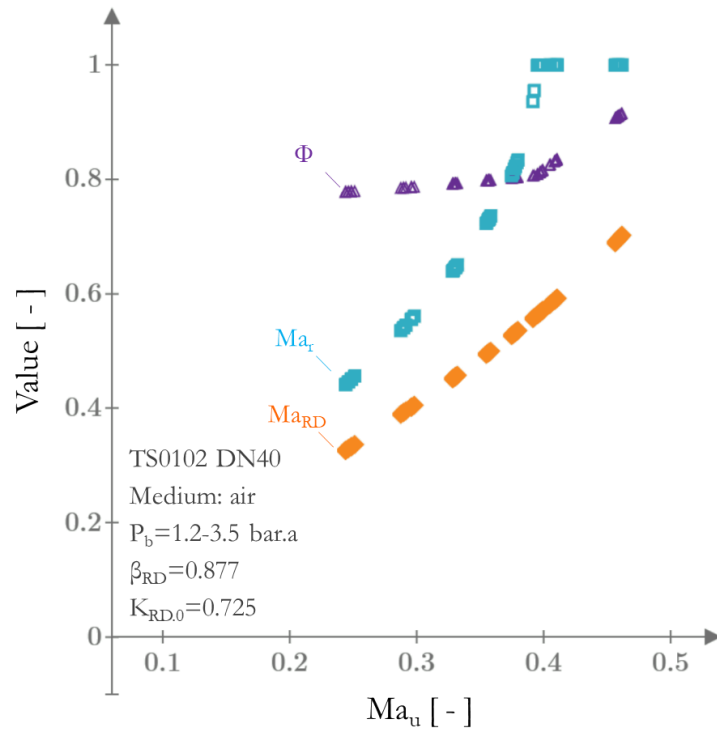


Figure 58: Plots of Ma_{RD} and Ma_r per eq. (29) and Φ per eq.(34), against Ma_u for low- and high-velocity flow with TS0102 DN40.

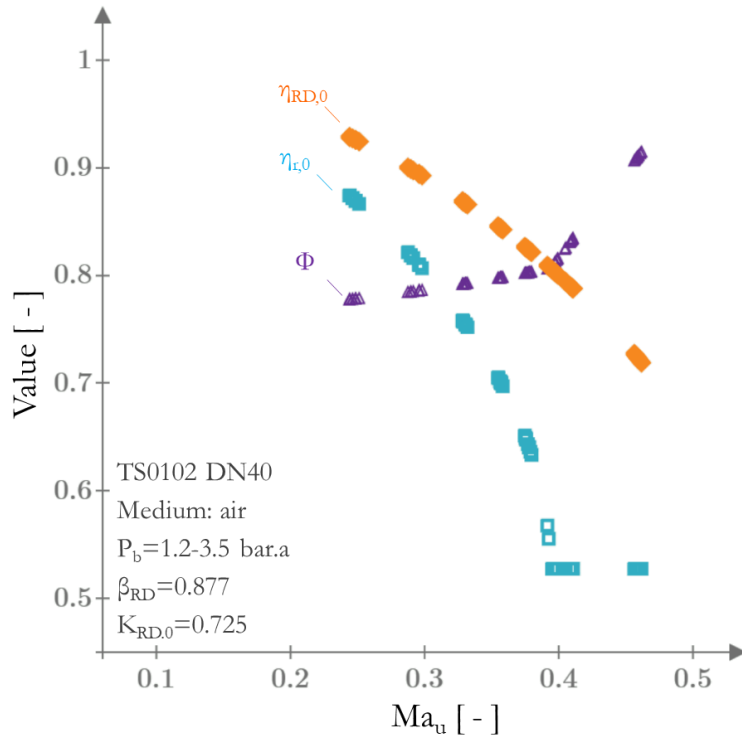


Figure 59: Plots of $\eta_{RD,0}$ and $\eta_{r,0}$ per eq. (38), Φ per eq.(34) against Ma_u for low- and high-velocity flow with TS0102 DN40.

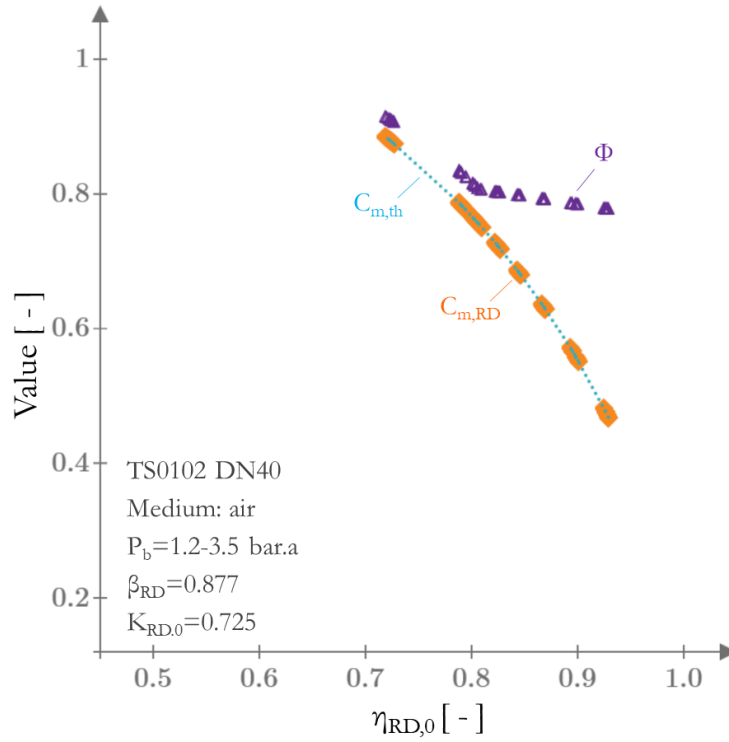


Figure 60: Plots of $C_{m,RD}$ and $C_{m,r}$ per eq.(36) and Φ per eq.(34), against $\eta_{RD,0}$ for low- and high-velocity flow with TS0102 DN40.

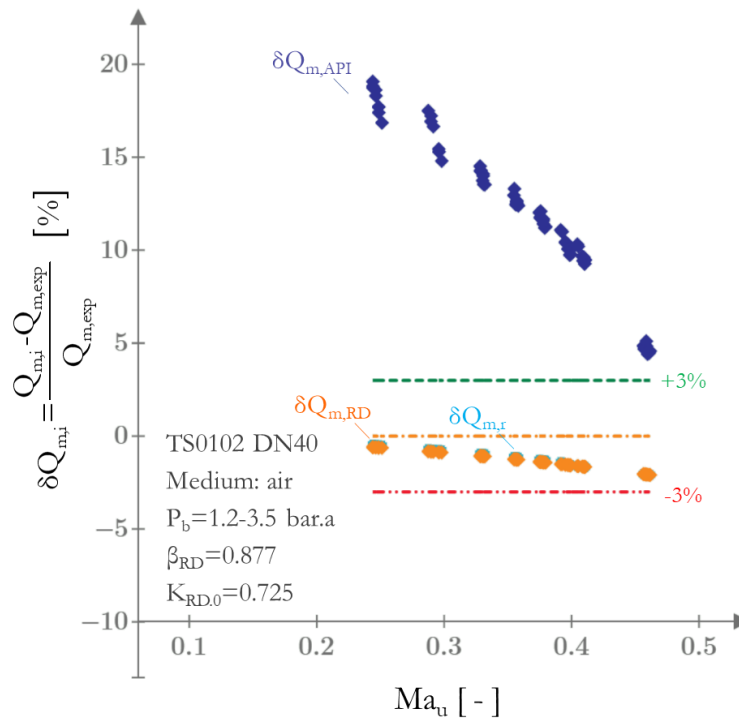


Figure 61: Deviation of predicted mass flow rate $\delta Q_{m,API}$ per eq.(1) and $\delta Q_{m,RD}$ and $\delta Q_{m,r}$ per eq.(27) for low- and high-velocity flow with TS0102 DN40.

Results for rupture disk type II:

Similar studies were done with another rupture disk type II with 96 data-points with test object TS0202 DN40.

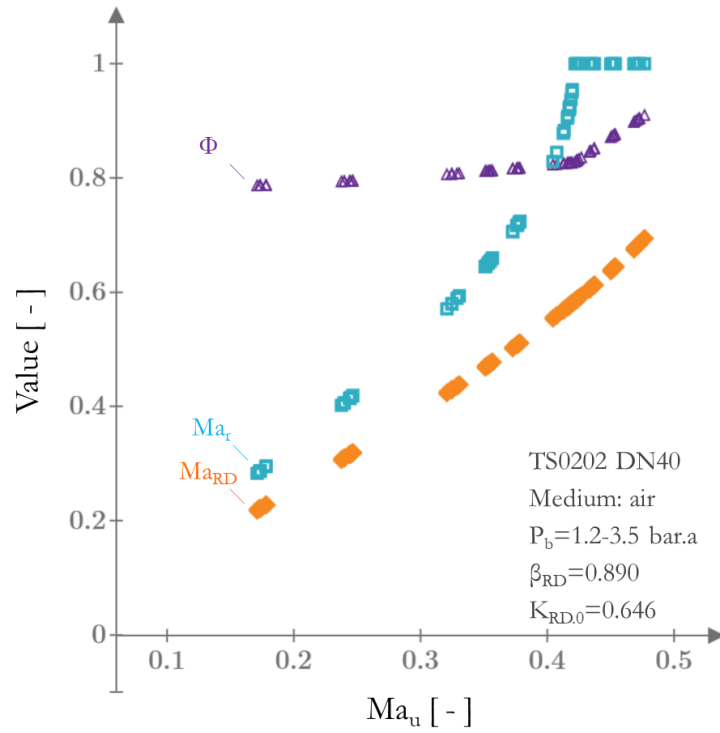


Figure 62: Plots of Ma_{RD} and Ma_r per eq.(29), Φ per eq.(34), against Ma_u for low- and high-velocity flow with TS0202 DN40.

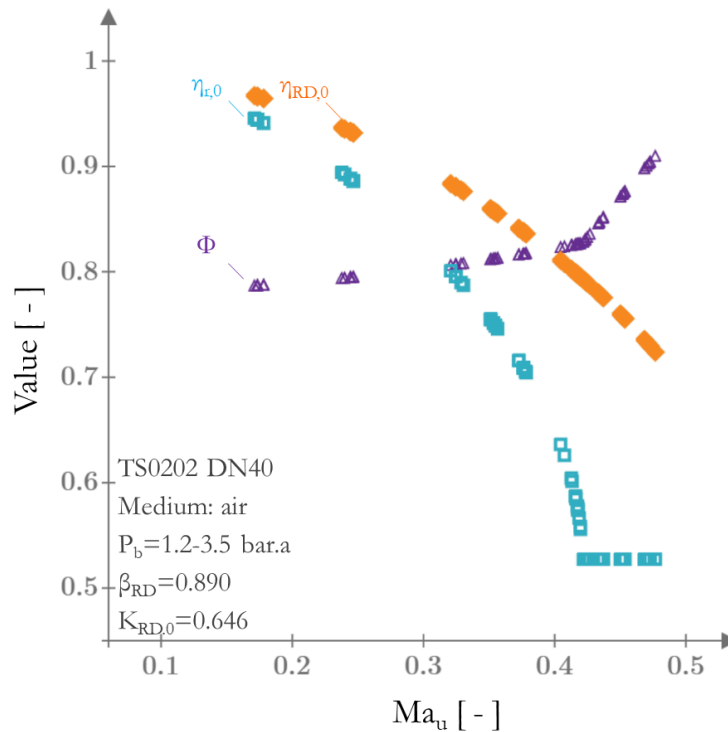


Figure 63: Plots of $\eta_{RD,0}$ and $\eta_{r,0}$ per eq.(38), Φ per eq.(34) against Ma_u for low- and high-velocity flow with TS0202 DN40.

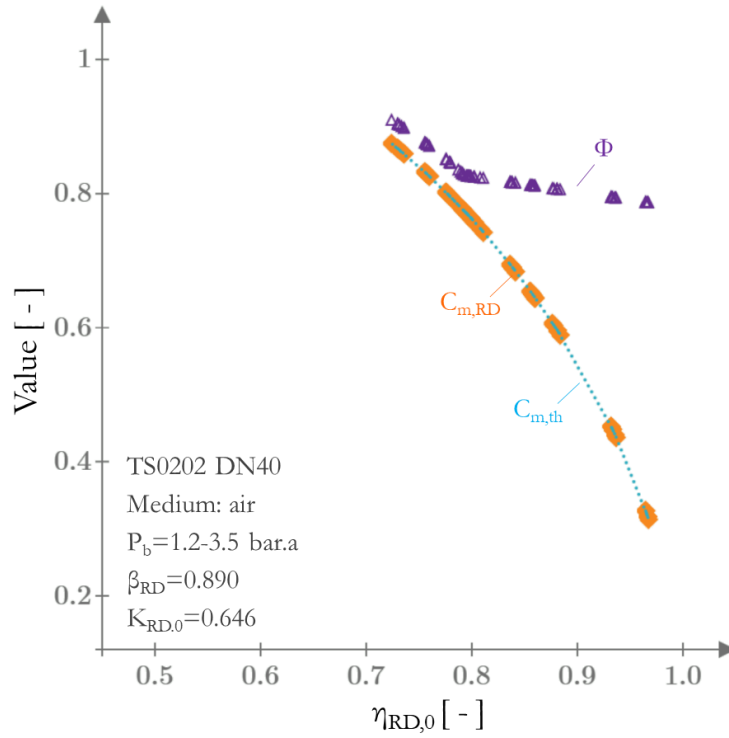


Figure 64: Plots of $C_{m,RD}$ and $C_{m,r}$ per eq.(36) and Φ per eq.(34), against $\eta_{RD,0}$ for low- and high-velocity flow with TS0202 DN40.

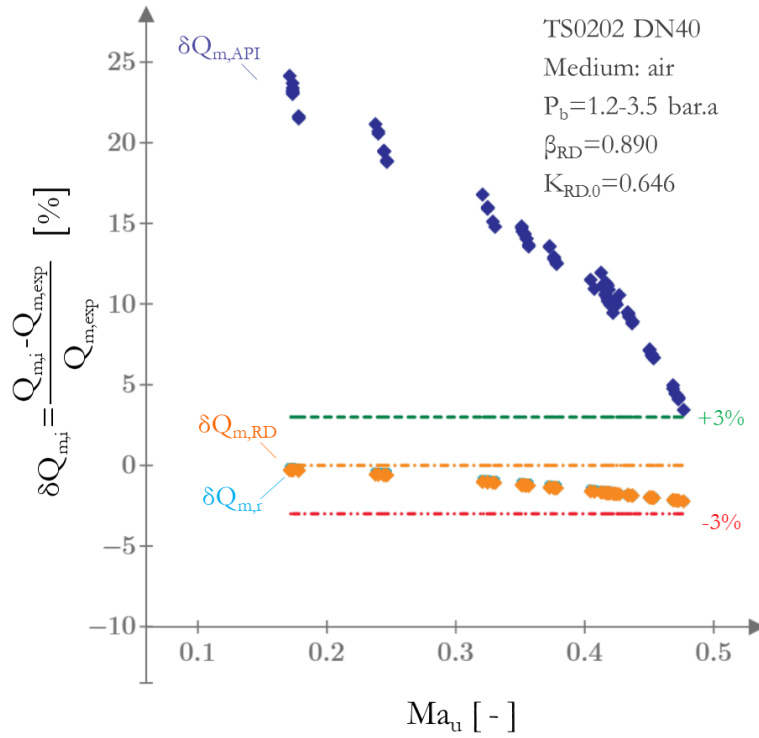


Figure 65: Deviation of predicted mass flow rate $\delta Q_{m,API}$ per eq.(1) and $\delta Q_{m,RD}$ and $\delta Q_{m,r}$ per eq.(27) for low- and high-velocity flow with TS0202 DN40.

Results for rupture disk type III:

Further studies were done with another rupture disk type III with 82 data-points from test object TS0302 DN40.

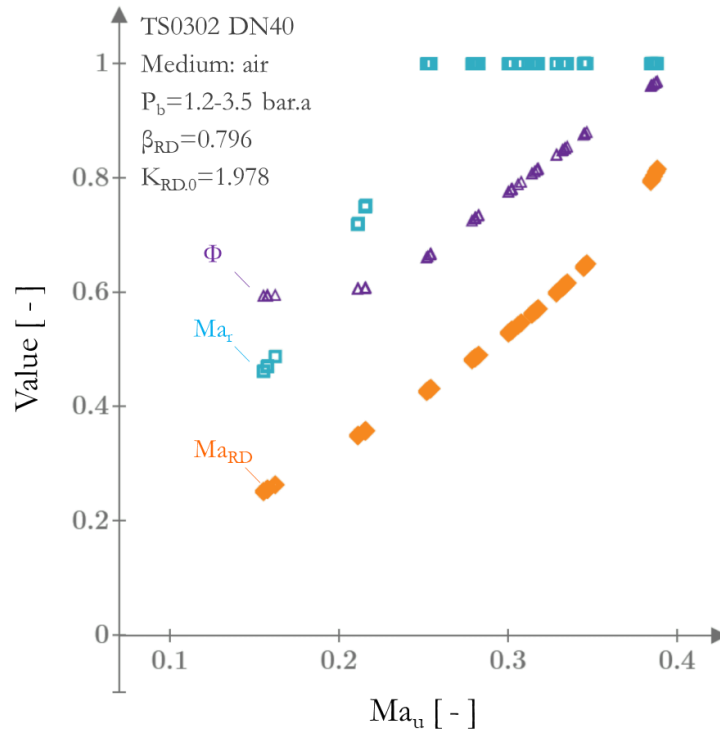


Figure 66: Plots of Ma_{RD} and Ma_r per eq. (29), Φ per eq.(34), against Ma_u for low- and high-velocity flow with TS0302 DN40.

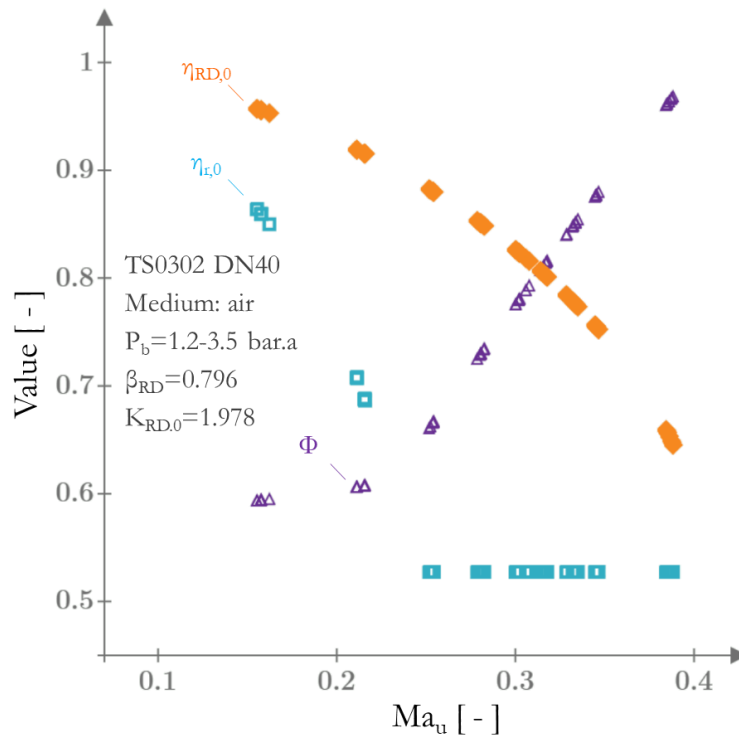


Figure 67: Plots of $\eta_{RD,0}$ and $\eta_{r,0}$ per eq. (38), Φ per eq.(34), against Ma_u for low- and high-velocity flow with TS0302 DN40.

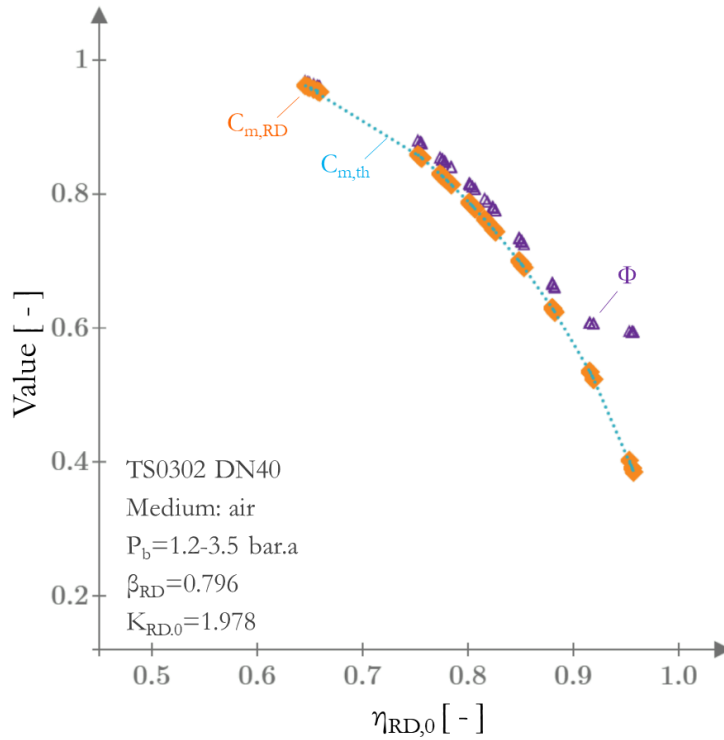


Figure 68: Plots of $C_{m, RD}$ and $C_{m, r}$ per eq.(36) and Φ per eq.(34), against $\eta_{RD, 0}$ for low- and high-velocity flow with TS0302 DN40.

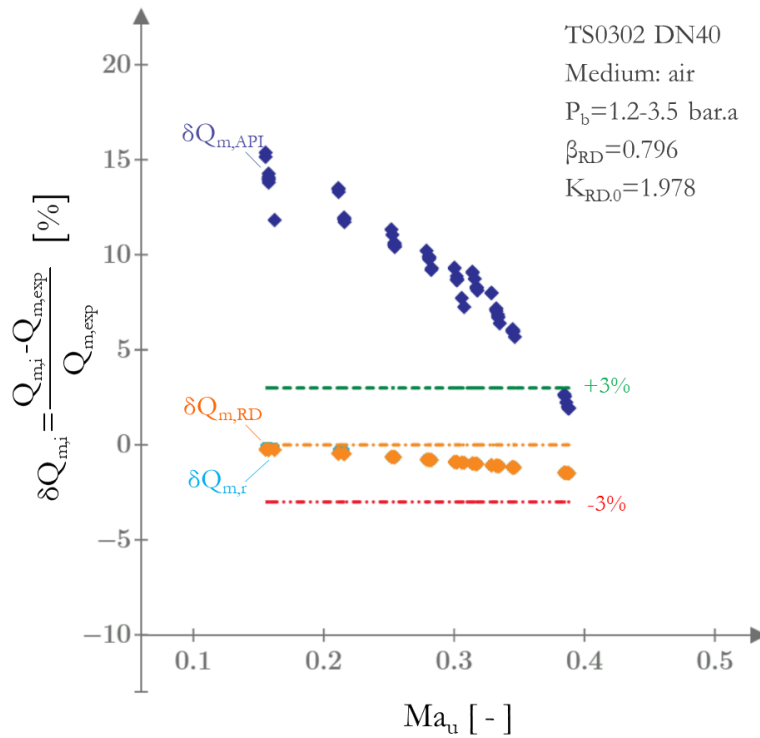


Figure 69: Deviation of predicted mass flow rate $\delta Q_{m, API}$ per eq.(1) and $\delta Q_{m, RD}$ and $\delta Q_{m, r}$ per eq.(27) for low- and high-velocity flow with TS0302 DN40.

Figure 58, Figure 62 and Figure 66 show that experiments were done for a range of upstream Mach numbers $0.15 < Ma_u \leq 0.5$. This is representative of low-velocity and high-velocity flows. Looking at Figure 66 (TS0302), one, for example, observes that $Ma_{RD}=0.81$ while $Ma_r=1.0$ even though $Ma_u=0.486$. This further proves significant contraction of flow as illustrated in Figure 43 and Figure 44.

Increasing fluid velocity with Ma_u leads to an increase of velocity at (RD) and (r) and with $Ma_{RD} < 1$ while $Ma_r \rightarrow 1$. The proposed theory states that the maximum dischargeable mass flow rate is attained if $\eta_{RD,0} = \eta_{r,0}$. This happens when $\Phi = 1.0$ and $Ma_u = Ma_{u,theo}$. At this point, $A_r = A_{RD}$ and $Ma_r = Ma_{RD}$ and Φ , $C_{m,RD}$ and $C_{m,r}$ attain unity. Figure 59, Figure 63 and Figure 67 illustrate how $\Phi \rightarrow 1.0$ leads to $\eta_{RD,0} = \eta_{r,0}$. This is when the dimensionless mass flow rate $C_{m,RD}$ at (RD) and $C_{m,r}$ at (r) attains unity, as seen in Figure 60, Figure 64 and Figure 68. This is consistent with the proposed model representation which states that $A_r = A_{RD}$ and $Ma_r = Ma_{RD}$ when Φ , $C_{m,RD}$ and $C_{m,r}$ attain unity.

Once a rupture disk is activated, it opens and attains the highest mass flow rate at burst pressure, Q_{m,RD^*} . This is when the highest upstream Mach number Ma_u and the corresponding highest discharge rate prevails. The mass flow rate at the rupture disk, $Q_{m,RD}$ then reduces with time as the system is depressurized. The deviation of the predicted mass flow rate $Q_{m,API}$ per eq.(1) deviates by up to 25% from the experimental mass flow rate, as seen in Figure 61, Figure 65, Figure 69. The deviation is mainly attributed to not considering the rupture disk discharge area, while determining the dischargeable mass flow rate per eq.(1). The deviation in that method varies significantly with the rupture disk type. The deviation reduces as the Ma_u increases. Therefore eq.(1) is better suited to predict the dischargeable mass flow rate at burst pressure with high-velocity flow and less suited for a depressurizing system since it overpredicts the dischargeable mass flow rate with reduction of fluid velocity significantly.

The proposed method with $Q_{m,RD}$ and $Q_{m,r}$ per eq. (27) is suited to calculate the dischargeable mass flow rate for all flows from the time a rupture disk is activated to the time when the system is fully depressurized as seen in Figure 61, Figure 65, Figure 69. The deviation of the predicted mass flow rate is within $\pm 3\%$ of measured discharge rate $Q_{m,exp}$ for all 253 data-points in this study. The dischargeable mass flow rate across a rupture disk should therefore be calculated per eq. (27) at (RD) because this point is defined uniquely with A_{RD} and $\Phi = 1.0$.

6.1.2.1 Area-choking in rupture disk device

To elaborate further on the choking criteria for rupture disks, C_{m,RD^*} per eq.(36) is plotted against Ma_u and $\eta_{RD,0}$ per eq.(38) for the $P_u \approx 2.3$ bar.a. experiment with rupture disk TS0102. The calculated properties are listed in Table 34 (C5). The maximum theoretical upstream Mach-number, $Ma_{u,theo}$ which results in area-choking, is calculated with the nozzle theory per eq.(35). It is also calculated effective pipe theory, which results in fanno-choking per eq.(62).

Rupture disk TS0102 is not choked, and choking would occur if the Ma_u would be increased to 0.522 and the pressure ratio $\eta_{RD,0}$ decreased to 0.527. This can, for example, be attained by installing the rupture disk further downstream, increasing the stagnation pressure upstream of (RD), or reducing the discharge pressure downstream of (RD). The points marked with a red triangle in Figure 70 and Figure 71, have been calculated assuming *area-choking* per eq.(35) while those marked with blue triangle have been calculated assuming *Fanno-choking* eq.(62). Both area-choking and fanno-choking predict the same value of $Ma_{u,theo} \approx 0.404$, because the mass flow rate is limited by $Ma_{u,theo}$ per eq.(35) for the determined A_{RD} per eq.(40), as can be seen in Figure 70 and Figure 71. Therefore, $Ma_{u,theo}$ may be calculated with either method. Overall the area-choking model with $Ma_{u,theo}$ per eq.(35) is more practicable since it is easier to compute numerically.

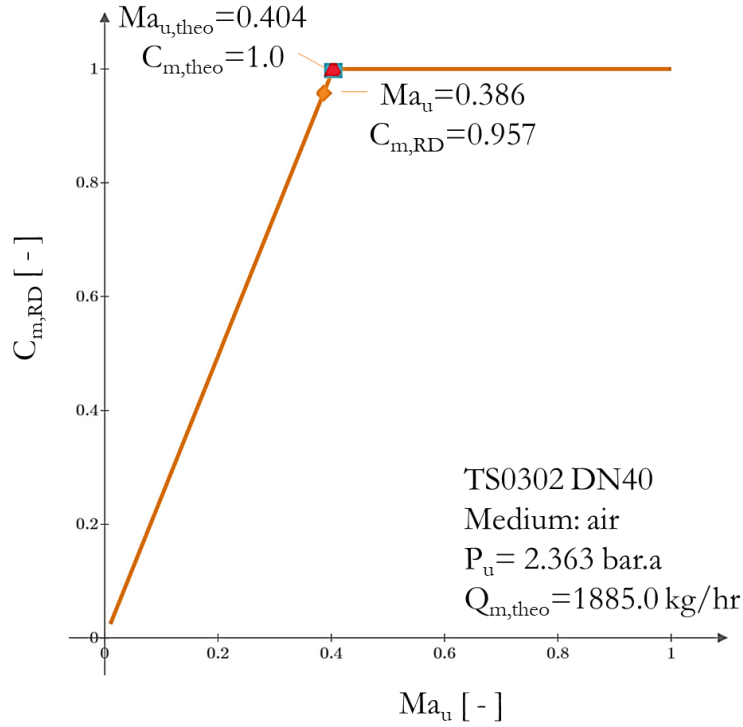


Figure 70: Plots of $C_{m,RD}$ per eq.(36) against Ma_u showing the $Ma_{u,theo}$ for given upstream conditions for the $P_u \approx 2.3$ bar.a. experiment with rupture disk TS0302. $Q_{m,theo}$ is calculated with $Ma_{u,theo}$ per eq.(35) and eq.(62).

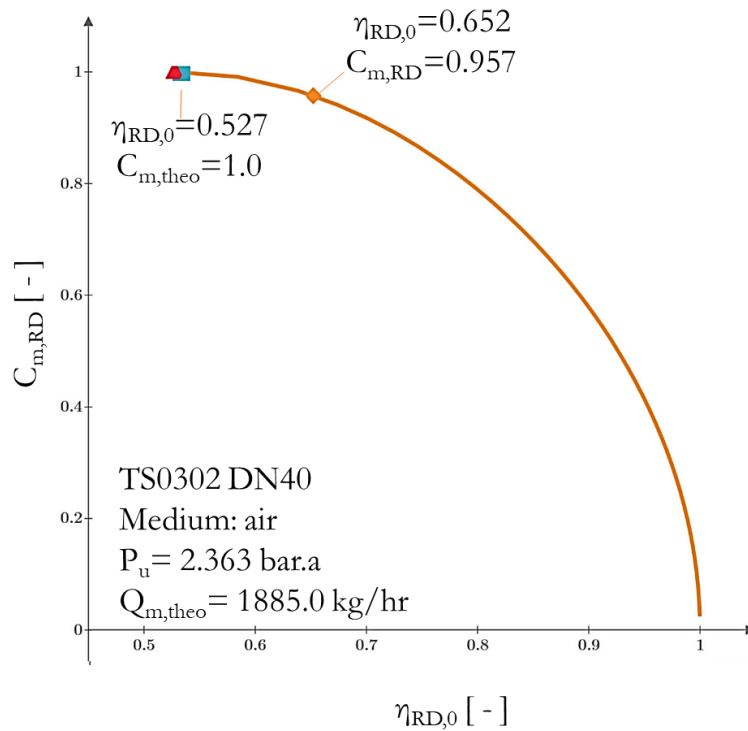


Figure 71: Plots of $C_{m,RD}$ per eq.(36) against $\eta_{RD,0}$ per eq.(38) showing the $\eta_{RD,0} \approx 0.527$ for $Ma_{u,theo} = 0.404$ for given upstream conditions for the $P_u \approx 2.3$ bar.a. experiment with rupture disk TS0302. $Q_{m,theo}$ is calculated with $Ma_{u,theo}$ per eq.(35) and eq.(62)

6.1.2.2 Sample sizing case to determine minimum rupture disk and pipe size.

Now that the rupture disk devices TS0102, TS0202 and TS0302 have been characterized, the dischargeable mass flow rate across a rupture disk will be calculated in a sample sizing case. After HAZOP analysis, the properties for sizing a rupture disk vent line are specified by the plant operator per Table 29. A_{RD} has been determined by a certified authority. Further, the flow regime is given as a gas-only and medium to be discharged is arbitrary selected as Hydrogen Sulfide (H_2S). The conditions upstream of the rupture disk device during relief are known. The design engineer has 3 types of rupture disk devices to choose from the rupture disk product catalogs; TS0102, TS0202 and TS0302. The design engineer should determine the required nominal pipe size of the rupture disk and vent-line, which meets the “dischargeable mass flow rate at burst pressure is larger than the minimum flow rate to be discharged.” $Q_{m,RD} > Q_{m,sizing}$ sizing criterion using the proposed method with the specified data in Table 29.

Table 29 Specified data for sizing a rupture disk vent-line.

	C1	C2	C3	C4	C5	C6
R1	Given property	Symbol	unit	TS0102	TS0202	TS0302
R2	Inner pipe diameter	D_i	mm	40.9		
R3	Molar mass of H_2S	M_m	gm/mol	34.08		
R4	Ratio of specific heat	κ	-	1.336		
R5	Ambient pressure	P_a	bar.a	0.992		
R6	Ambient temperature	T_a	K	294.2		
R7	Specified pressure upstream of RD	P_u	bar.a	8.00		
R8	Specified temperature upstream of RD	T_u	K	400		
R9	Specified minimum flow rate to be discharged	$Q_{m,sizing}$	kg/hr	6000		
R10	Specified discharge area A_{RD}	A_{RD}	mm ²	1010.5	1040.7	832.5
R11	Specified loss coefficient	$K_{RD,0}$	-	0.723	0.646	1.978

The calculated properties for the sample rupture disk sizing case are tabulated in Table 30 for rupture disk types TS0102, TS0202 and TS0302. $Q_{m,RD}$ is the “dischargeable mass flow rate” under the specified conditions.

Table 30 Results for a rupture disk vent-line with the proposed method.

	C1	C2	C3	C4	C5	C6	C7
R1	Calculated property	Symbol	unit	Eq.	TS0102	TS0202	TS0302
R2	Determined mass flux	G_u	kg/(s·m ²)	-	1268.6		
R3	Determined density of fluid	ρ_u	kg/m ³	-	8.400		
R4	Determined upstream Mach number	Ma_u	-	-	0.422		
R5	Predicted mass flow rate at A_{RD}	$Q_{m,RD,g}$	kg/hr	(37)	5910.9	5910.9	5683.6
R6	Predicted upstream Mach number	Ma_u	-	-	0.4224	0.4224	0.406
R7	Predicted Mach number at A_{RD}	Ma_{RD}	-	(29)	0.686	0.648	1.000
R8	Theoretical upstream Mach number	$Ma_{u,theo}$	-	(29)	0.525	0.537	0.406
R9	Theoretical mass flow rate with $Ma_{u,theo}$	$Q_{m,theo}$	kg/hr	(27)	7340.9	7665.7	5683.6

Choking rupture disk designs and non-choking rupture disk designs have been introduced in chapter 5.3.1.4. Looking at Table 30 row R7, rupture disk TS0302 DN40 is a choking rupture disk design in this sample sizing case because of $Ma_u = Ma_{u,theo}$ condition. Flow in this rupture disk is choked under the specified conditions. As such, the dischargeable mass flow rate is limited in TS0302 by the rupture disk itself at $Q_{m,RD} = Q_{m,theo} = 5683.6$ kg/hr. The dischargeable mass flow rate, in this case, only depends on the pressure upstream of the rupture disk. If flow limitation at the rupture disk itself is desired, TS0302 should be preferred and if permissible, the specified minimum flow rate to be discharged $Q_{m,sizing}$ should be reduced below $Q_{m,RD} = 5683.6$ kg/hr to meet the dischargeable mass flow rate is larger than the minimum flow rate to be discharged”, $Q_{m,RD} > Q_{m,sizing}$ sizing criterion.

Looking at Table 30 row R7 rupture disks TS0102 and TS0202 are non-choking rupture disk designs in this sample sizing case. Flow in is not limited at the rupture disk itself under specified conditions as $Ma_u < Ma_{u,theo}$ per Table 30 (R4&R8). Dischargeable mass flow rate depends on the downstream pressure and a detailed pressure-drop calculation must be done with the rupture disk CMLC-Theory (Mutegi, et al., 2019) considering all the fittings installed in the entire vent line. Both rupture disk types are also suited for the sizing case. The specified minimum flow rate to be discharged $Q_{m,sizing}$ should be reduced below $Q_{m,RD}=5910.9$ kg/hr to meet the dischargeable mass flow rate is larger than the minimum flow rate to be discharged”, $Q_{m,RD} > Q_{m,sizing}$ sizing criterion with rupture disks TS0102 and TS0202.

6.1.3 Prediction of dischargeable mass flow rate for two-phase flow

(Shannak, et al., 1999) finds that contraction of flow is not dominant for a wide range of gas mass flow quality $0.012 < x_g < 0.90$ experimentally. The dischargeable mass flow rate for $x_g > 0.90$ can be approximated with the equation for gas flow with $Q_{m,g}$ per eq.(37) which has been validated with gas flow above. The dischargeable mass flow rate across a rupture disk is predicted per eq.(48). Choking in rupture disks can be predicted per eq.(46). It is, however, not typical and the general equation rupture disk dischargeable mass flow rate, $Q_{m,RD}$ per eq.(85) for $x_g < 1$ is assumed to be valid.

6.2 Experimental validation of pressure-drop model

The method to determine the rupture disk zero-velocity minor loss coefficient, $K_{RD,0}$ with gas flow per eq.(53) will be validated experimentally first. The determined $K_{RD,0}$ will be used to validate the method to determine the rupture disk compressible pressure-drop per eq.(86) with gas flow and $x_g=1.0$ with three different types of rupture disk.

The proposed method to determine the compressible pressure-drop across a rupture disk with gas flow, $\Delta P_{RD,g}$ per eq.(68) in chapter 5.3.1 and the rupture disk compressible two-phase pressure-drop with two-phase flow, $\Delta P_{RD,tp}$ per eq.(83) in chapter 5.3.2 will be calculated as described and the methods proposed will be validated experimentally. $\Delta P_{RD,g}$ per eq.(68) and $\Delta P_{RD,tp}$ per eq.(83) are incorporated in general equation for rupture disk compressible pressure drop, ΔP_{RD} for the full range of $0 \leq x_g \leq 1.0$, with ΔP_{RD} per eq.(86).

The general strategy for predicting the pressure-drop across a rupture disk with gas and two-phase flow is to correlate losses observed with low-velocity and incompressible flow to losses expected in high-velocity and compressible flow with an effective pipe length. For this, the rupture disk characteristic numbers $K_{RD,0}$ per eq.(53) and $K_{RD,0,tp}$ per eq.(80) are determined experimentally with low-velocity flow. They are taken to be constant rupture disk characteristic numbers for a rupture disk type and nominal pipe size. These characteristic numbers are then used to predict the pressure-drop across a rupture disk for all other flows.

6.2.1 Determination of rupture disk zero-velocity minor loss coefficient, $K_{RD,0}$

A rupture disk device is installed centered in between the inlet and outlet pipe segment. The test section is calibrated before the tests. The pressure in the test vessel is gradually increased until the target pressure and stationary flow conditions are attained by gradually opening the precision control valve, CV-01 manually (see also: Figure 30). These stationary flow conditions are then held constant for at least 5 seconds to collect at least 40 data points as listed in column C8 in Table 31 and Table 32. The following sample measured data set is acquired for each experiment.

Table 31: Sample measured data set for a low-velocity (LV) experiment with TS0102.

	C1	C2	C3	C4	C5	C6	C7
R1	Channel	Symbol	Mean	$\pm U$	Unit	L in mm	n
R2	Base pressure	P_b	200.15	0.69	mbar.g	-	98
R3	Pressure at tap 01	$P_{tap,01}; P_{tap,A}$	97.95	0.21	mbar.g	2470	98
R4	Pressure at tap 02	$P_{tap,02}$	86.76	0.32	mbar.g	3110	98
R5	Pressure at tap 03	$P_{tap,03}$	82.05	0.37	mbar.g	3320	98
R6	Pressure at tap 04	$P_{tap,04}; P_{tap,B}$	77.32	0.83	mbar.g	3670	98
R7	Pressure at tap 09	$P_{tap,09}$	34.67	0.22	mbar.g	4230	98
R8	Pressure at tap 10	$P_{tap,10}; P_{tap,C}$	25.47	0.28	mbar.g	4475	98
R9	Pressure at tap 11	$P_{tap,11}; P_{tap,D}$	8.24	0.31	mbar.g	5195	98
R10	Mass flow rate	Q_m	142.39	0.04	g/s	-	98
R11	Base temperature	T_b	296.07	1.00	K	-	98
R12	Ambient temperature	T_a	294.19	1.00	K	-	98
R13	Ambient pressure	P_a	992.35	0.40	mbar.a	-	98

$K_{RD,0}$ is first determined from a low-velocity experiment with $Ma_u < 0.30$ and $Re_u > 105$ as described in the sample calculation below. Once determined, $K_{RD,0}$ is taken to be a constant rupture disk characteristic number for a rupture disk type and nominal pipe size (Mutegi, et al., 2019).

Table 32: Sample measured data set for a high-velocity (HV) experiment with TS0102

	C1	C2	C3	C4	C5	C6	C7
R1	Channel	Symbol	Mean	$\pm U$	Unit	L in mm	n
R2	Base pressure	P_b	2336.37	0.69	mbar.g	-	49
R3	Pressure at tap 01	$P_{tap,01}; P_{tap,A}$	1568.89	0.21	mbar.g	2470	49
R4	Pressure at tap 02	$P_{tap,02}$	1479.40	0.32	mbar.g	3110	49
R5	Pressure at tap 03	$P_{tap,03}$	1435.90	0.37	mbar.g	3320	49
R6	Pressure at tap 04	$P_{tap,04}; P_{tap,B}$	1399.20	0.83	mbar.g	3670	49
R7	Pressure at tap 09	$P_{tap,09}$	876.56	0.22	mbar.g	4230	49
R8	Pressure at tap 10	$P_{tap,10}; P_{tap,C}$	748.17	0.28	mbar.g	4475	49
R9	Pressure at tap 11	$P_{tap,11}; P_{tap,D}$	470.90	0.31	mbar.g	5195	49
R10	Mass flow rate	Q_m	611.35	0.18	g/s	-	49
R11	Base temperature	T_b	301.08	1.00	K	-	49
R12	Ambient temperature	T_a	293.92	1.00	K	-	49
R13	Ambient pressure	P_a	992.37	0.40	mbar.a	-	49

The first step is to determine $K_{RD,0}$ with the data from the low-velocity experiment in Table 31 with $Ma_u < 0.30$ and $Re_u > 10^5$. The process to be followed to determine $K_{RD,0}$ is presented in the following and illustrated in Figure 73 and can be described as follows:

1. A low-velocity flow experiment was done with a pipe with a rupture disk installed. The experimental data is tabulated in Table 31.
2. The pressure profile of the upstream segment was determined by inserting the best straight line of fit through $P_{tap,01}$ through $P_{tap,04}$.
3. The temperature and Mach number at $P_{tap,04}$ was calculated as described in ASME PTC-25 (ASME, 2014).
4. The location of $P_{tap,04}$ was set as the upstream location (u). It is located 3 inner pipe diameter lengths upstream of the rupture disk. The pressure profile in the inflow pipe segment was calculated from location (u). The following data was recorded for (u):

$$G_u = 108.4 \frac{\text{kg}}{\text{s} \cdot \text{m}^2} \quad \frac{P_u}{P_b} = \frac{1.070 \text{ bar.a}}{1.193 \text{ bar.a}} = 0.897 \quad T_u = 293 \text{ K} \quad Ma_u = 0.247 \quad (90)$$

5. The pressure profile of the downstream segment was determined by inserting the best straight line of fit through $P_{tap,06}$ through $P_{tap,11}$ with the pressure at pipe exit as P_a as seen in Figure 73
6. P_d is calculated per eq.(69) with $\Delta P_{RD,g}$. P_d is the static pressure downstream of the rupture disk device. It is marked with a circular dot, which intersects with the downstream linear pressure profile at the rupture disk installation plane at $P_d/P_b = 0.870$ in Figure 73. For this, the prevailing value of $K_{RD,0}$ was determined as follows:
 - a. Initial value of $K_{RD,0}$, was set to 0.723 (estimated value)
 - b. The downstream Mach number, $Ma_d \{K_{RD,0}\}$ is calculated per eq.(54); the equivalent length of pipe, L_d is per eq.(55) and downstream Mach number, $Ma \{L_d\}$ is per eq.(56).

$$Ma_d = Ma_d \{K_{RD,0}\} = 0.255 \quad L_d = 1.700 \text{ m} \quad Ma \{L_d\} = 0.255 \quad (91)$$

- c. The compressible minor loss coefficient factor, F_c is integrated from the upstream location with $L_u = 0 \text{ m}$ to $L_d = 1.700 \text{ m}$ with $F_g \{L\}$ per eq.(49) and $Ma \{L\}$ per eq.(56). The rupture disk compressible minor loss coefficient, $K_{RD,g}$ is calculated per eq.(60).

$$F_{g,app} = \frac{\int_{0 \text{ m}}^{1.700 \text{ m}} F_g \{L\} \cdot dL}{1.700 \text{ m}} = 1.094 \quad (92)$$

$$K_{RD,g} = K_{RD,0} \cdot F_{g,app} = 0.794$$

- d. The rupture disk pressure drop, $\Delta P_{RD,g}$ is calculated per eq.(61).

$$\Delta P_{RD,g} = -\frac{G_u^2}{2 \cdot \rho_{av}} \cdot K_{RD,g} = -0.037 \text{ bar with } \rho_{av} = 1.253 \frac{\text{kg}}{\text{m}^3} \quad (93)$$

- e. The pressure downstream of the rupture disk and the pressure ratio relative to base pressure P_b is calculated per eq.(94).

$$P_d = P_u + \Delta P_{RD,g} = 1.032 \text{ bar} \quad \frac{P_d}{P_b} = \frac{1.032 \text{ bar.a}}{1.193 \text{ bar.a}} = 0.866 \quad T_d = 290K \quad Ma \{L_d\} = 0.255 \quad (94)$$

- f. $K_{RD,0}$ at step 6a is manually changed until the round dot representing P_d is within the range of $\pm 5\%$ of $P_{d,exp}$ which is determined by extrapolation of downstream pressure profile. At this point, $P_d = P_{d,exp}$ and $K_{RD,0}=0.725$. The experimental data, the upstream and downstream pressure profile, as well as the pressure downstream of the rupture disk, P_d are plotted in Figure 73.

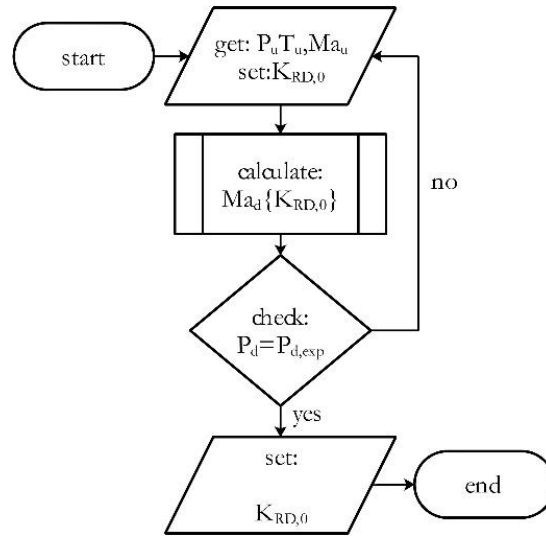


Figure 72: Process for determining $K_{RD,0}$.

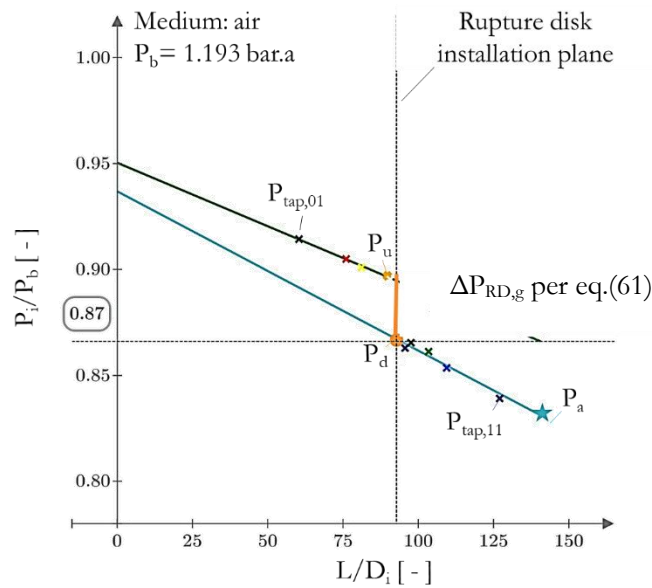


Figure 73: Pressure ratio profile of a low-velocity experiment for TS0102 with the data in Table 31.

6.2.2 Prediction of pressure profile in a rupture disk with CMLC theory

In practice, the mass flow rate and the conditions upstream of the rupture disk are given. In this example, the flow conditions at the location of $P_{\text{tap},04}$ are set as the inlet conditions. $K_{RD,0}$ is used to determine the pressure-drop for low-velocity and high-velocity flow for given upstream flow conditions, as described in chapter 6.2.2. and the pressure profile is predicted backward and forwards from this location as follows:

7. The following data was recorded for (u) and taken as the given conditions upstream of the rupture disk device.

$$G_u = 465.3 \frac{\text{kg}}{\text{s} \cdot \text{m}^2} \quad \frac{P_u}{P_b} = \frac{2.392 \text{ bar.a}}{3.329 \text{ bar.a}} = 0.718 \quad T_u = 289.2 \text{ K} \quad Ma_u = 0.463 \quad (95)$$

8. The pressure profile of the inlet is calculated from conditions at the location (u) and (d), respectively, by integrating eq.(13). The flow conditions at the rupture disk installation plane upstream are:

$$\frac{P_{RD}}{P_b} = \frac{2.367 \text{ bar.a}}{3.329 \text{ bar.a}} = 0.711 \quad T_{RD} = 289.0 \text{ K} \quad Ma_{RD} = 0.468 \quad (96)$$

9. The flow conditions downstream of the rupture disk are calculated analogously to 6.b with flow conditions at the rupture disk installation plane and $K_{RD,0}=0.725$.

$$Ma_d = Ma_d \{K_{RD,0}\} = 0.557 \quad L_d = L_d \{K_{RD,0}\} = 1.883 \text{ m} \quad Ma \{L_d\} = 0.557 \quad (97)$$

10. $F_{g,av}$ and $K_{RD,g}$ are calculated analogously to 6.c

$$F_{g,av} = \frac{\int_{0 \text{ m}}^{1.883 \text{ m}} F_C \{L\} \cdot dL}{1.875 \text{ m}} = 1.484 \quad K_{RD,g} = K_{RD,0} \cdot F_{g,av} = 1.077 \quad (98)$$

11. The rupture disk pressure drop, $\Delta P_{RD,g}$ is calculated analogously to 6.d.

$$\Delta P_{RD,g} = -\frac{G_u^2}{2 \cdot \rho_{av}} \cdot K_{RD,g} = -0.436 \text{ bar} \quad (99)$$

$$\text{with } G_u = 465.3 \frac{\text{kg}}{\text{s} \cdot \text{m}^2} \quad \rho_{av} = 2.674 \frac{\text{kg}}{\text{m}^3} \quad K_{RD,g} = 1.077$$

12. The flow conditions downstream of the rupture disk at (d) are calculated analogously to 6.e.

$$P_d = P_u + \Delta P_{RD,g} = 1.956 \text{ mbar} \quad \frac{P_d}{P_b} = \frac{1.956 \text{ mbar}}{3.329 \text{ mbar}} = 0.587 \quad T_d = 273 \text{ K} \quad Ma \{L_d\} = 0.577 \quad (100)$$

13. The pressure profile of the outlet segment is calculated from conditions at (d) forwards by integrating eq.(13).
14. The pressure profile in the entire test section is calculated by coupling the inlet- and outlet segment pressure profiles. For this, a step function at the rupture disk installation plane is used with $\Delta P_{RD,g}$ and P_d as seen in Figure 74 through Figure 77.

For comparison, the downstream pressure P_d is also predicted for the same experiments. Here, the differential pressure-drop $\Delta P_{RD,fit}$ is calculated per eq.(5) with the fitting's rupture disk coefficient K_R per eq.(6). The pressure profile of the test section with the rupture disk installed for rupture disk sample TS0102 DN40 is then predicted for the low-velocity flow experiment and high-velocity flow experiment. The results are presented in Figure 76 and Figure 77, respectively.

The pressure profile calculated for low-velocity experimental data in Table 31 and high-velocity experimental data in Table 32 with $\Delta P_{RD,g}$ per eq.(68) is presented in Figure 74 and Figure 75 respectively.

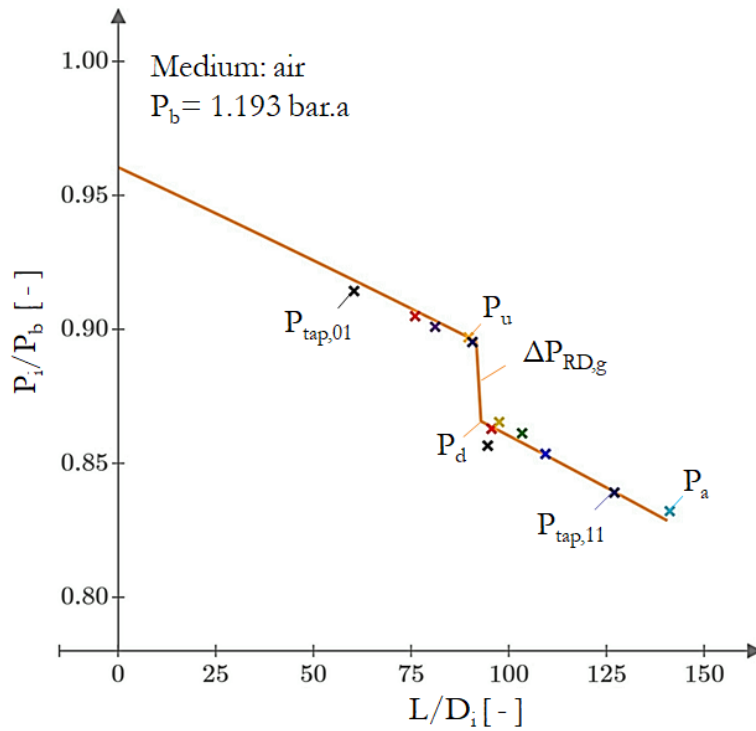


Figure 74: Predicted pressure profile for TS0102 with low-velocity flow with data in Table 31 with $\Delta P_{RD,g}$ per eq.(61).

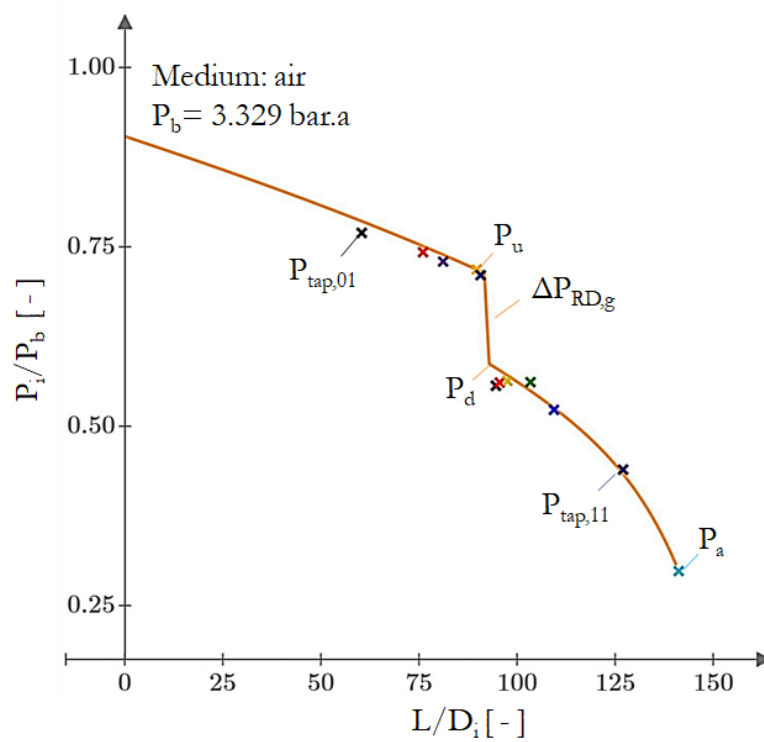


Figure 75: Predicted pressure profile for TS0102 with high-velocity flow with data in Table 32 with $\Delta P_{RD,g}$ per eq.(61).

The pressure profile calculated for low-velocity experimental data in Table 31 and high-velocity experimental data in Table 32 with $\Delta P_{RD, lit}$ (classic method) per eq.(5) is presented in Figure 76 and Figure 77 respectively.

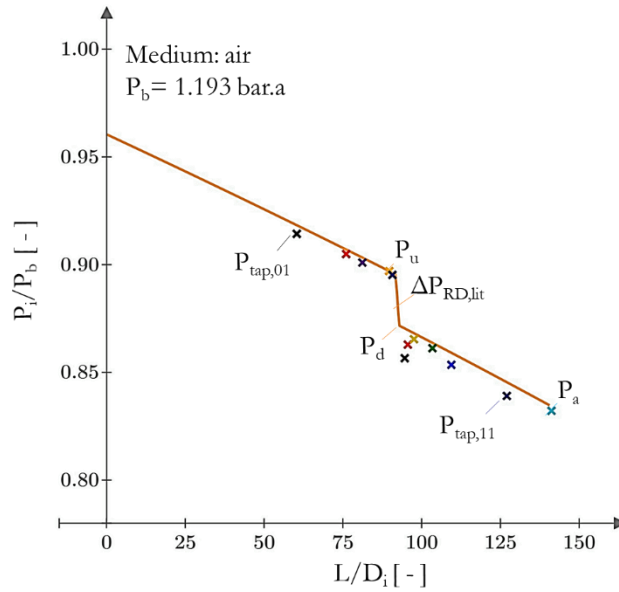


Figure 76: Predicted pressure profile for TS0102 with low-velocity flow with equations in literature with data in Table 31 with $\Delta P_{RD, lit}$ per eq.(5).

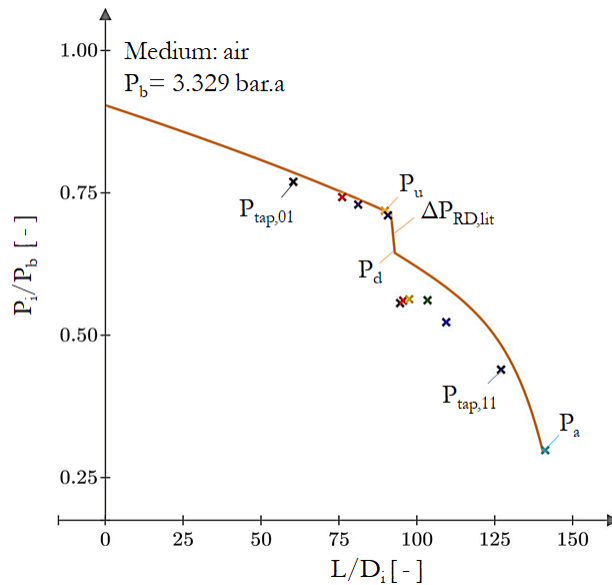


Figure 77: Predicted pressure profile for TS0102 with high-velocity flow with equations in literature with data in Table 34 with $\Delta P_{RD, lit}$ per eq.(5).

The proposed method for calculating $K_{RD, g}$ per eq.(60) and the method in literature with K_R per eq.(6) predict the pressure profile for low-velocity flow accurately as seen in Figure 74 and Figure 76 respectively. The literature method with K_R is however less suited for high-velocity flows that are typical in rupture disk relief lines as seen in Figure 77; the use of eq.(6) to determine a rupture disk's loss coefficient with high-velocity compressible flow with flow separation comes is the root cause of uncertainties while determining the pressure-drop across a rupture disk. This is because this equation is derived for adiabatic flow in a rough pipe with straight cross-section as seen in the control volume in Figure 5. Its derivation does not consider changes in the cross-sectional area. This contrasts with a pipe with a rupture disk device installed where the cross-sectional area varies significantly.

The pressure-drop across a rupture disk should consider the dissipation of energy due to the acceleration of flow which occurs due to changes in the cross-sectional area. The rupture disk should be modeled with rupture disk equivalent pipe length, L_d per eq.(56), which increases with upstream Mach number, Ma_u as seen in Figure 78. The industrial assumption is that $L_d/L_{RD,0}=1.0=const$ for all plausible gas flows. This assumption does not represent the reality as L_d per eq.(55) is not constant. Beyond this choked flow in rupture disk prevail when L_d attains a maximum length. This is when $Ma\{L_d\} \rightarrow Ma_{u,theo}$ and Ma_d per eq.(62) tends towards unity.

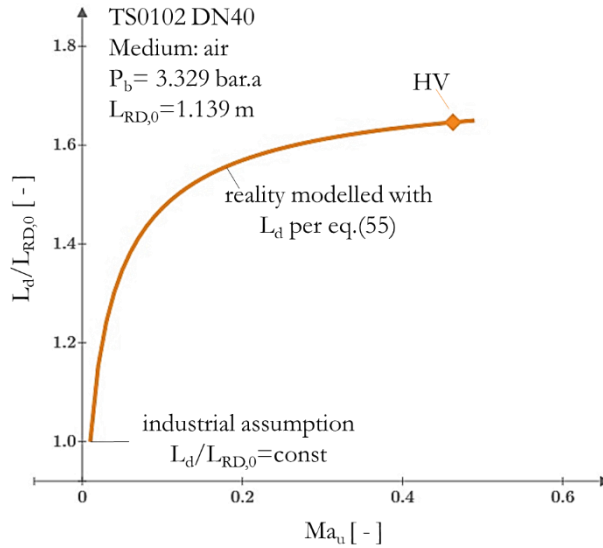


Figure 78 Ratio of effective rupture disk effective length, L_d per eq.(55) to rupture disk zero-velocity length, $L_{RD,0}$ with varying upstream Mach number, Ma_u . HV refers to calculation with high-velocity experimental data in Table 32.

The rupture disk compressible minor loss coefficient $K_{RD,g}$ per eq.(60) also increases with Ma_u from zero-velocity loss coefficient, $K_{RD,0}$ which represents the lowest magnitude of rupture disk loss coefficient for $Ma_u \rightarrow 0$. This contrasts with the industrial assumption that K_R is constant as assumed in eq.(5) and as seen in Figure 79. Dissipation varies with flow velocity, or rather with variation in Reynolds number. Dissipation of energy due to acceleration of flow is factored into $K_{RD,g}$ per eq.(60) with the rupture disk compressibility factor, $F_{g,av}$ per eq.(58). This results in an exponential increase of $K_{RD,g}$ with Ma_u .

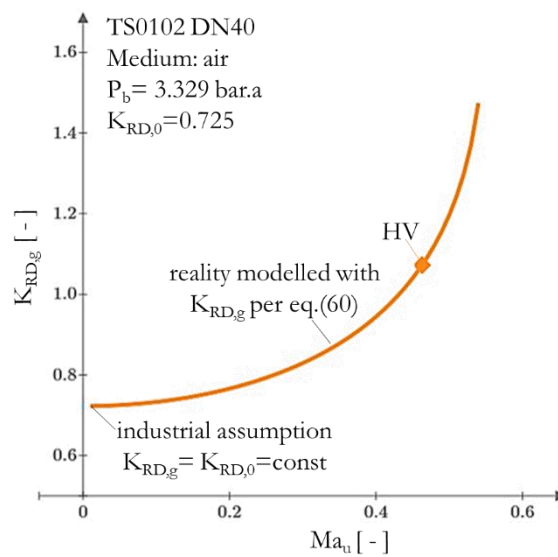


Figure 79: Rupture disk compressible minor loss coefficient, $K_{RD,g}$ per eq.(60) plotted against Ma_u . HV refers to calculation with high-velocity experimental data in Table 32.

To compare pressure-drop across a rupture disk $\Delta P_{RD,g}$ calculated with proposed method per eq.(61) three similar experiments with three different types of rupture disk are highlighted. Similar experimental conditions were reproduced by keeping measured pressure at $P_{tap,04}$ constant at $P_{tap,04} \approx 2.400$ bar.a. The key properties from these three experiments are tabulated in Table 33 with high-velocity flow.

Table 33 Determined properties for three rupture disk types under similar flow conditions with data in Table 24, Table 25, and Table 26 .

	C1	C2	C3	C4	C5	C6
R1	Property	Symbol	unit	TS0102	TS0202	TS0302
R2	Base pressure	P_b	bar.a	3.329	3.373	2.999
R3	Base temperature	T_b	K	301.1	296.7	288.2
R4	Ambient pressure	P_a	bar.a	0.992	0.992	0.978
R5	Ambient temperature	T_a	K	293.9	291.1	290.8
R6	Mass flow rate discharged	$Q_{m,exp}$	kg/hr	2200.9	2220.4	1831.9
R7	Pressure upstream of RD	P_u	bar.a	2.392	2.370	2.363
R8	Pressure at tap 04	$P_{tap,04}$	bar.a	2.392	2.370	2.363
R9	Pressure at tap 09	$P_{tap,09}$	bar.a	1.869	1.919	1.552
R10	Pressure at tap 10	$P_{tap,10}$	bar.a	1.741	1.790	1.461
R11	Pressure at tap 11	$P_{tap,11}$	bar.a	1.463	1.508	1.241

The following properties are determined or calculated for the $P_{tap,04} \approx 2.400$ bar.a experiments. Looking at Table 34, TS0302 has the smallest A_{RD} (R3) and lowest $Q_{m,exp}$ in Table 33 (R6). The discharge area significantly affects the discharge rate under similar discharge conditions. Also, the smaller the size of A_{RD} (R3), the higher the $K_{RD,0}$ (R4). The proposed theory is now used to evaluate the experimental data for the three experiments in Table 33.

Table 34 Determined and calculated properties for the experimental data of the three rupture disk types in Table 33.

	C1	C2	C3	C4	C5	C6	C7
R1	Calculated property	Symbol	unit	Eq.	TS0102	TS0202	TS0302
R2	Inner pipe diameter	D_i	mm	-	40.9	40.9	40.9
R3	Discharge area A_{RD}	A_{RD}	mm ²	-	1011	1041	833
R4	Loss coefficient	$K_{RD,0}$	-	-	0.725	0.646	1.978
R5	Molar mass of air	M_m	gm/mol	-	28.97	28.97	28.97
R6	Ratio of specific heat	κ	-	-	1.405	1.405	1.405
R7	Mass flux	G_u	kg/(s·m ²)	-	465.3	469.5	387.3
R8	Temperature upstream of RD	T_u	K	-	289.2	284.7	280.2
R9	Density of fluid at (u)	ρ_u	kg/m ³	-	2.884	2.903	2.941
R10	Velocity of fluid at (u)	w_u	m/s	-	161.4	161.7	131.7
R11	Mach number at (u)	Ma_u	-	-	0.463	0.468	0.386
R12	Mass flux	G_u	kg/(s·m ²)	-	465.3	469.5	387.3
R13	Mach number	$Ma_d\{K_{RD,0}\}$	-	(54)	0.557	0.551	0.578
R14	Pipe length	L_d	m	(55)	1.883	1.678	5.098
R15	Mach number	$Ma\{L_d\}$	-	(56)	0.557	0.551	0.578
R16	Rupture disk compressibility factor	$F_{g,av}$	-	(58)	1.484	1.485	1.389
R17	Compressible minor loss coefficient	$K_{RD,g}$	-	(60)	1.077	0.959	2.748
R18	Averaged density	ρ_{av}	kg/m ³	(59)	2.674	2.712	2.535
R19	Predicted pressure drop	$\Delta P_{RD,g}$	bar.a	(61)	0.436	0.390	0.813
R20	Predicted downstream pressure	P_d	bar.a	(69)	1.956	1.980	1.550
R21	Predicted downstream Mach number	Ma_d	-	(54)	0.557	0.551	0.578
R22	Predicted downstream Temperature	T_d	K	-	272.9	270.0	248.0
R23	Predicted pressure at tap 09	$P_{calc,09}$	bar.a	(13)	1.828	1.856	1.441
R24	Predicted pressure at tap 10	$P_{calc,10}$	bar.a	(13)	1.749	1.778	1.372
R25	Predicted pressure at tap 11	$P_{calc,11}$	bar.a	(13)	1.443	1.488	1.041

In the following CMLC-theory will be evaluated further by evaluating more data points from experiments done with low-velocity and high-velocity flow, with rupture disk type TS0102, TS0202 and TS0302 with 78, 122, and 84 data points respectively. $K_{RD,0}$ is determined as intended at eq.(53) with measured data with $Ma_u < 0.30$ and $Re_u > 10^5$ (ref: Figure 80) and $K_{RD,g}$ is determined with CMLC theory per eq.(60).

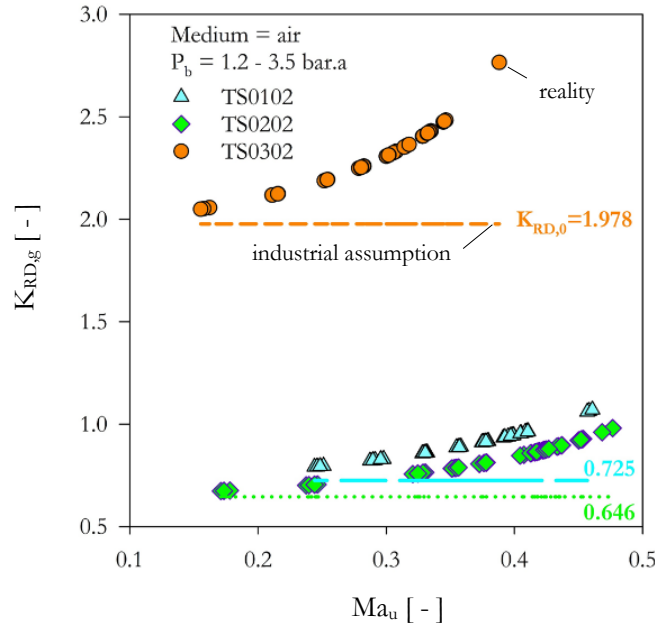


Figure 80: Calculated pipe loss coefficients: $K_{RD,0}$ per eq.(53), $K_{RD,g}$ per eq.(60) with $F_{g,av}$ for a range of upstream Mach number Ma_u .

Figure 80 shows that experiments were done for a range of upstream Mach numbers Ma_u . This is representative of low-velocity and high-velocity flows. It also shows that the rupture disk loss coefficients vary significantly and exponentially with Ma_u .

$\Delta P_{RD,g}$ per eq.(51) is representative of the experimental pressure drop. $\Delta P_{RD,g}$ deviates marginally by up to 3% from $\Delta P_{RD,g}$ per eq.(51) for all three rupture disk types tested. A relationship that is valid more generally, to correlate rupture disk losses observed in low-velocity flow with $K_{RD,0}$ to losses expected in high-velocity flow with $K_{RD,g}$ by factoring compressibility fully in the proposed method has so far been validated with 284 data points with low- and high-velocity flow with air. Experimental data was collected from three DN40 rupture disk samples (TS0102 DN40 with 78 data-points, TS0202 DN40 with 122 data-points & TS0302 DN40 with 84 data-points). This representing three rupture disk types (TI, TII & TIII). Extrapolation of method for large diameter rupture disks is subject to experimental validation.

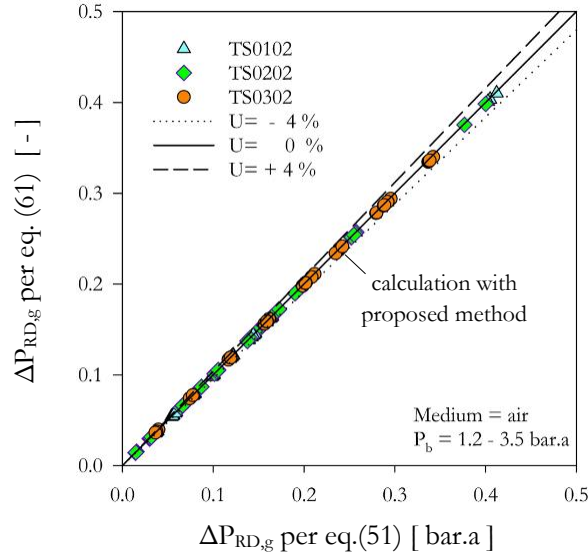


Figure 81: Parity plot of $\Delta P_{RD,g}$ per eq.(51) and $\Delta P_{RD,g}$ per eq.(61).

$\Delta P_{RD,g}$ is also calculated with proposed theory per eq.(61) and $\Delta P_{RD,lit}$ is calculated with equations in literature per eq.(5), which is representative of the industrial assumption.

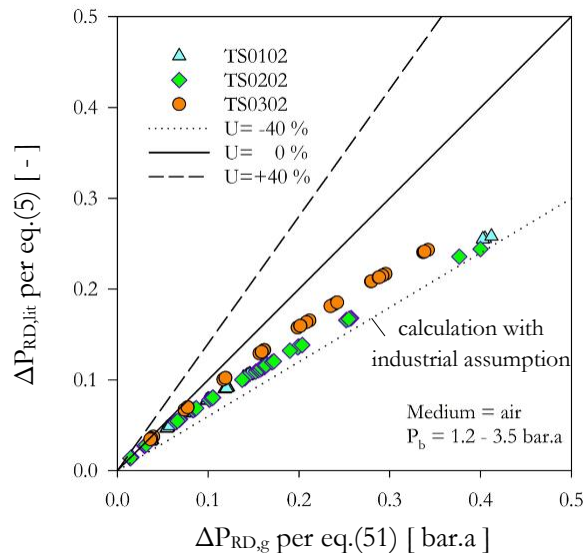


Figure 82: Parity plot of $\Delta P_{RD,g}$ per eq.(51) and $\Delta P_{RD,lit}$ per eq.(5).

$\Delta P_{RD,lit}$ deviates by up to - 40% from $\Delta P_{RD,g}$ per eq.(51) with the deviation increasing with an increase in fluid velocity. The industrial assumption is not valid for high-velocity flow, as is typically the case during emergency relief.

6.2.3 Determination of rupture disk two-phase minor loss coefficient $K_{RD,0,tp}$

Am air/water two-phase experiment with a low gas-quality experiment with $x_g < 0.20$ is done in the pilot rig described in the test facility described in chapter 4.11. The test section and instrumentation described in chapter 4.9. A rupture disk device is installed centered between the inlet and outlet pipe segment. The test section is calibrated before the tests.

Table 35: Sample measured data set for determining $K_{RD,0,tp}$ from a low gas mass flow quality experiment two-phase air/water flow experiment with TS0102.

	C1	C2	C3	C4	C5	C6	C7
R1	Channel	Symbol	Mean	$\pm U$	Unit	L in mm	n
R2	Pressure at tap 01	$P_{tap,01}$	476.07	0.21	mbar, g	2470	56
R3	Pressure at tap 02	$P_{tap,02}$	424.96	0.32	mbar, g	3110	56
R4	Pressure at tap 03	$P_{tap,03}$	414.70	0.37	mbar, g	3320	56
R5	Pressure at tap 04	$P_{tap,04}$	380.04	0.83	mbar, g	3670	56
R6	Pressure at tap 09	$P_{tap,09}$	192.41	0.22	mbar, g	4230	56
R7	Pressure at tap 10	$P_{tap,10}$	163.16	0.28	mbar, g	4475	56
R8	Pressure at tap 11	$P_{tap,11}$	66.25	0.31	mbar, g	5195	56
R9	Temperature at tap 01	$T_{tap,01}$	287.21	1.00	K	-	56
R10	Temperature at tap 04	$T_{tap,04}$	286.69	1.00	K	-	56
R11	Ambient temperature	T_a	300.12	1.00	K	-	56
R12	Ambient pressure	P_a	987.74	0.40	mbar, a	-	56
R13	Mass flow rate (air)	$Q_{m,g}$	60.52	0.02	g/s	-	56
R14	Mass flow rate (water)	$Q_{m,l}$	249.08	0.07	g/s	-	56
R15	Mass flow rate (2ph)	$Q_{m,tp}$	309.59	0.09	g/s	-	56
R16	Gas mass flow quality	x_g	0.200	0.02	-	-	56
R17	Liquid quality	x_l	0.800	0.07	-	-	56

Table 36: Sample measured data set for determining $K_{RD,0,tp}$ from a low gas mass flow quality experiment two-phase air/water flow experiment with TS0202.

	C1	C2	C3	C4	C5	C6	C7
R1	Channel	Symbol	Mean	$\pm U$	Unit	L in mm	n
R2	Pressure at tap 01	$P_{tap,01}$	230.07	0.21	mbar, g	2470	39
R3	Pressure at tap 02	$P_{tap,02}$	206.77	0.32	mbar, g	3110	39
R4	Pressure at tap 03	$P_{tap,03}$	201.67	0.37	mbar, g	3320	39
R5	Pressure at tap 04	$P_{tap,04}$	189.04	0.83	mbar, g	3670	39
R6	Pressure at tap 09	$P_{tap,09}$	105.18	0.22	mbar, g	4230	39
R7	Pressure at tap 10	$P_{tap,10}$	83.26	0.28	mbar, g	4475	39
R8	Pressure at tap 11	$P_{tap,11}$	31.55	0.31	mbar, g	5195	39
R9	Temperature at tap 01	$T_{tap,01}$	290.84	1.00	K	-	39
R10	Temperature at tap 04	$T_{tap,04}$	290.66	1.00	K	-	39
R11	Ambient temperature	T_a	299.54	1.00	K	-	39
R12	Ambient pressure	P_a	987.86	0.40	mbar, a	-	39
R13	Mass flow rate (air)	$Q_{m,g}$	46.20	0.01	g/s	-	39
R14	Mass flow rate (water)	$Q_{m,l}$	170.01	0.05	g/s	-	39
R15	Mass flow rate (2ph)	$Q_{m,tp}$	216.21	0.06	g/s	-	39
R16	Gas mass flow quality	x_g	0.210	0.01	-	-	39
R17	Liquid quality	x_l	0.790	0.05	-	-	39

The measured data in Table 35 is plotted in Figure 83 for TS0102. The upstream pressure profile is determined by inserting the best straight line of fit through $P_{\text{tap},01}$ through $P_{\text{tap},04}$. The downstream stream pressure profile $P_{\text{tap},09}$ through $P_{\text{tap},11}$ and P_a

To validate the prediction of pressure-drop ΔP_{RD} per eq.(86) and downstream pressure P_a per eq.(89) an experiment with low gas mass flow quality $x_g=0.20$ is evaluated. The pressure profile upstream and downstream is determined by inserting the best straight line of fit through pressure taps $P_{\text{tap},01}$ to $P_{\text{tap},04}$ and $P_{\text{tap},09}$ to $P_{\text{tap},11}$ respectively.

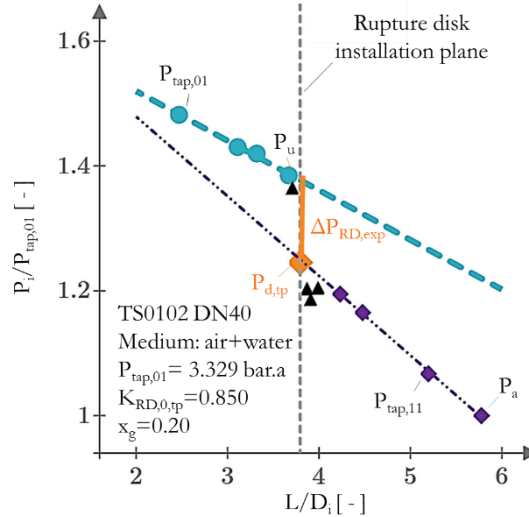


Figure 83: Plot of $P_i/P_{\text{tap},01}$ against L/D_i from a low gas mass flow quality experiment with TS0102 DN40.

All these pressure taps are in the unseparated flow region, as seen in Figure 83. Pressure taps $P_{\text{tap},05}$ through $P_{\text{tap},08}$ marked with a black triangle are in the separated flow region and are therefore not used for evaluation in this work. The downstream pressure with two-phase flow P_a is calculated per eq.(89) assuming a random value of $K_{\text{RD},0,\text{tp}}$. The following values are thereby calculated. The following data-points were determined for the two rupture disks TS0102 DN40 and TS0202 DN40 with the data in Table 35 and Table 36, respectively.

Table 37 Determined and calculated properties for the experimental data of the three rupture disk types in Table 35.

	C1	C2	C3	C4	C5	C6
R1	Calculated property	Symbol	unit	Eq.	TS0102	TS0102
R2	Superficial velocity of gas-phase	$U_{s,g}$	m/s	(76)	27.74	24.93
R3	Superficial velocity of liquid phase	$U_{s,l}$	m/s	(76)	0.19	0.13
R4	Kinematic viscosity of liquid phase	η_l	$Pa \cdot s$	DB	$1.666 \cdot 10^{-3}$	$1.061 \cdot 10^{-3}$
R5	Superficial velocity friction quotient	U_{friction}	-	(75)	$6.746 \cdot 10^{-3}$	$5.144 \cdot 10^{-3}$
R6	Two-phase Reynolds number	Re_{tp}	-	(77)	$9.789 \cdot 10^5$	$9.648 \cdot 10^5$
R7	Two-phase Darcy friction factor	λ_{tp}	-	(78)	0.016	0.016
R8	Rupture disk two-phase loss coefficient	$K_{\text{RD},0,\text{tp}}$	-	(80)	0.85	0.646
R9	Two-phase compressibility factor	F_{tp}	-	(81)	852.866	663.457
R10	Compressible two-phase pressure drop	$\Delta P_{\text{RD,tp}}$	$bar.a$	(86)	-0.138	-0.058
R11	Pressure downstream of rupture disk	P_d	$bar.a$	(89)	1.230	1.119

The value of $K_{RD,0,tp}$ is changed manually until the P_d in Figure 83 is within the range of $\pm 5\%$ of the downstream pressure profile. The rupture disk two-phase loss coefficient for rupture disk is determined as $K_{RD,0,tp}=0.850$ for TS0102 DN40 and $K_{RD,0,tp}=0.646$ for TS0202DN40. The rupture disk discharge area is the same as the one determined with the data for gas flow in Table 20 and Table 21 since the same rupture disks were used. $K_{RD,0,tp}$ is taken to be a constant value that will be used to predict the pressure-drop with two-phase flow in the following.

		TS0102 DN40			TS0202 DN40		
	Eq.	Data	Flow	Data	Flow		
β_{RD}	(40)	0.877	Table 20	gas	0.890	Table 21	gas
σ_{RD}	(40)	0.769	Table 20	gas	0.792	Table 21	gas
$K_{RD,0,tp}$	(80)	0.850	Table 35	two-phase	0.646	Table 36	two-phase

6.2.4 Prediction of the downstream pressure with a high gas mass flow quality experiment

Below, the data from two experiments with high gas mass flow quality with TS0102 DN40 and TS0202 DN40 are highlighted in Table 38 and Table 39, respectively.

Table 38: Sample measured data set from a high gas mass flow quality experiment two-phase air/water flow experiment with TS0102.

	C1	C2	C3	C4	C5	C6	C7
R1	Channel	Symbol	Mean	$\pm U$	Unit	L in mm	n
R2	Pressure at tap 01	$P_{tap,01}$	617.72	0.21	mbar, g	2470	39
R3	Pressure at tap 02	$P_{tap,02}$	562.44	0.32	mbar, g	3110	39
R4	Pressure at tap 03	$P_{tap,03}$	540.36	0.37	mbar, g	3320	39
R5	Pressure at tap 04	$P_{tap,04}$	505.38	0.83	mbar, g	3670	39
R6	Pressure at tap 09	$P_{tap,09}$	214.58	0.22	mbar, g	4230	39
R7	Pressure at tap 10	$P_{tap,10}$	179.29	0.28	mbar, g	4475	39
R8	Pressure at tap 11	$P_{tap,11}$	78.21	0.31	mbar, g	5195	39
R9	Temperature at tap 01	$T_{tap,01}$	293.05	1.00	K	-	39
R10	Temperature at tap 04	$T_{tap,04}$	292.73	1.00	K	-	39
R11	Ambient temperature	T_a	299.21	1.00	K	-	39
R12	Ambient pressure	P_a	987.77	0.40	mbar, a	-	39
R13	Mass flow rate (air)	$Q_{m,g}$	951.06	0.29	g/s	-	39
R14	Mass flow rate (water)	$Q_{m,l}$	134.49	0.04	g/s	-	39
R15	Mass flow rate (2ph)	$Q_{m,tp}$	1085.55	0.33	g/s	-	39
R16	Gas mass flow quality	x_g	0.880	0.29	-	-	39
R17	Liquid quality	x_l	0.120	0.04	-	-	39

Table 39: Sample measured data set from a high gas mass flow quality experiment two-phase air/water flow experiment with TS0202.

	C1	C2	C3	C4	C5	C6	C7
R1	Channel	Symbol	Mean	$\pm U$	Unit	L in mm	n
R2	Pressure at tap 01	$P_{tap,01}$	711.29	0.21	mbar, g	2470	55
R3	Pressure at tap 02	$P_{tap,02}$	620.96	0.32	mbar, g	3110	55
R4	Pressure at tap 03	$P_{tap,03}$	591.77	0.37	mbar, g	3320	55
R5	Pressure at tap 04	$P_{tap,04}$	544.54	0.83	mbar, g	3670	55
R6	Pressure at tap 09	$P_{tap,09}$	285.12	0.22	mbar, g	4230	55
R7	Pressure at tap 10	$P_{tap,10}$	241.14	0.28	mbar, g	4475	55
R8	Pressure at tap 11	$P_{tap,11}$	100.13	0.31	mbar, g	5195	55
R9	Temperature at tap 01	$T_{tap,01}$	292.16	1.00	K	-	55
R10	Temperature at tap 04	$T_{tap,04}$	291.65	1.00	K	-	55
R11	Ambient temperature	T_a	299.31	1.00	K	-	55
R12	Ambient pressure	P_a	987.85	0.40	mbar, a	-	55
R13	Mass flow rate (air)	$Q_{m,g}$	347.01	0.10	g/s	-	55
R14	Mass flow rate (water)	$Q_{m,l}$	224.02	0.07	g/s	-	55
R15	Mass flow rate (2ph)	$Q_{m,tp}$	571.03	0.17	g/s	-	55
R16	Gas mass flow quality	x_g	0.610	0.10	-	-	55
R17	Liquid quality	x_l	0.390	0.07	-	-	55

The downstream pressure with two-phase flow $P_{d,tp}$ will be predicted for TS0102 DN40 with $K_{RD,0,tp}=0.850$ and TS0202 DN40 with $K_{RD,0,tp}=0.646$. The following data is calculated for a high gas mass flow quality experiment with the data in Table 38 and Table 39 with TS0102 DN40 and TS0202 DN40 respectively.

Table 40 Determined and calculated properties for the experimental data of the two rupture disk types in Table 35 for TS0102 and Table 36 for TS0202.

C1	C2	C3	C4	C5	C6	
R1	Calculated property	Symbol	unit	Eq.	TS0102	TS0202
R2	Superficial velocity of gas-phase	$U_{s,g}$	m/s	(76)	407.59	144.46
R3	Superficial velocity of liquid phase	$U_{s,l}$	m/s	(76)	0.103	0.171
R4	Kinematic viscosity of liquid phase	η_l	$Pa \cdot s$	DB	$1.004 \cdot 10^{-3}$	$1.026 \cdot 10^{-3}$
R5	Superficial velocity friction quotient	$U_{friction}$	-	(75)	$2.515 \cdot 10^{-4}$	$1.180 \cdot 10^{-3}$
R6	Two-phase Reynolds number	Re_{tp}	-	(77)	$1.658 \cdot 10^7$	$5.755 \cdot 10^6$
R7	Two-phase Darcy friction factor	λ_{tp}	-	(78)	0.015	0.015
R8	Rupture disk two-phase loss coefficient	$K_{RD,0,tp}$	-	(80)	0.850	0.646
R9	Two-phase compressibility factor	F_{tp}	-	(81)	86.754	265.803
R10	Compressible two-phase pressure drop	$\Delta P_{RD,tp}$	$bar.a$	(86)	-0.249	-0.162
R11	Pressure downstream of rupture disk	P_d	$bar.a$	(89)	1.244	1.370

More data points were generated with TS0102 and TS0102 upon validation of the proposed method with 1 data point for each rupture disk type. The gas mass flow quality was varied between $0.10 < x_g < 0.90$. To also investigate whether the proposed method is valid for stationary, quasi-stationary and transient flows as is the case during emergency relief, 4274 and 3546 valid data points were collected for TS0102 and TS0202 respectively.

TS0102 DN40:

Below is the data used to evaluate the procedure for determining the pressure-drop across a rupture disk with two-phase flow with the first rupture disk type (TS0102) The data set with this device consists of 4274 data points with gas mass flow quality between $0.10 < x_g < 0.90$ as seen in Figure 84.

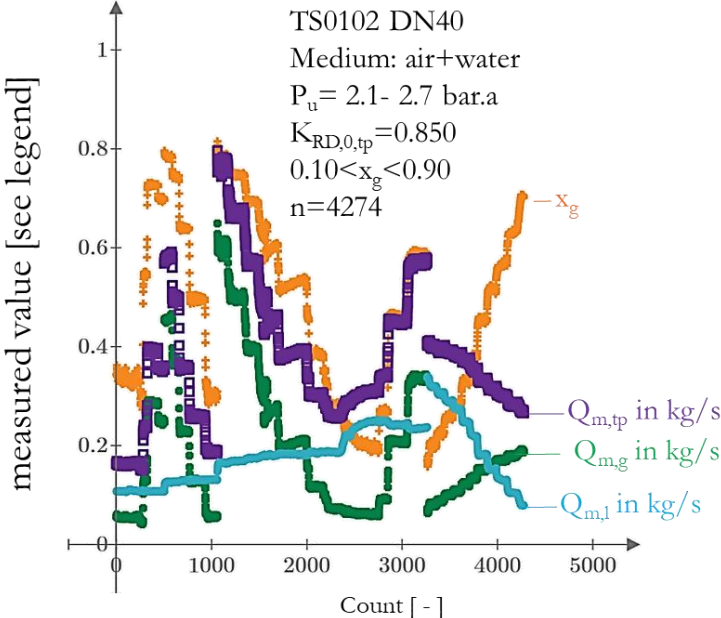


Figure 84: Raw data with TS0102 with two-phase flow with a count of 4276 data points with $0.10 < x_g < 0.90$. A zoom-in of Figure 84 with TS0102 shows that the data collected for evaluation covers (quasi) stationary flow as well as transient flow, as seen in Figure 85.

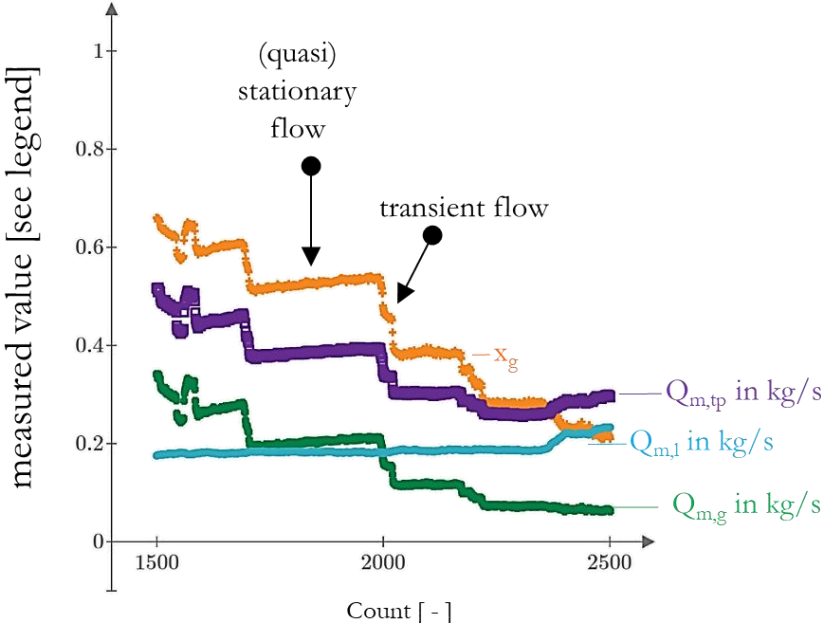


Figure 85: Zoom in of raw data with TS0102 with two-phase flow showing stationary, quasi-stationary and transient flow.

TS0102 DN40:

Below is the data used to evaluate the procedure for determining the pressure-drop across a rupture disk with two-phase flow with the first rupture disk type (TS0202) The data set with this device consists of 3546 data points with gas mass flow quality between $0.10 < x_g < 0.90$ as seen in Figure 86.

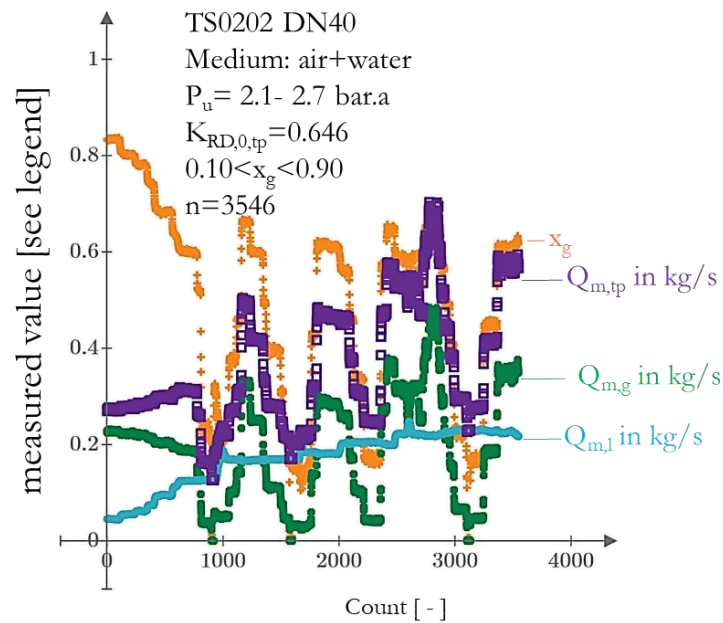


Figure 86: Raw data with TS0202 with two-phase flow with a count of 3546 data points with $0.1 < x_g < 0.90$.

A zoom-in of Figure 86 with TS0102 shows that the data collected for evaluation covers (quasi) stationary flow as well as transient flow as seen in Figure 87.

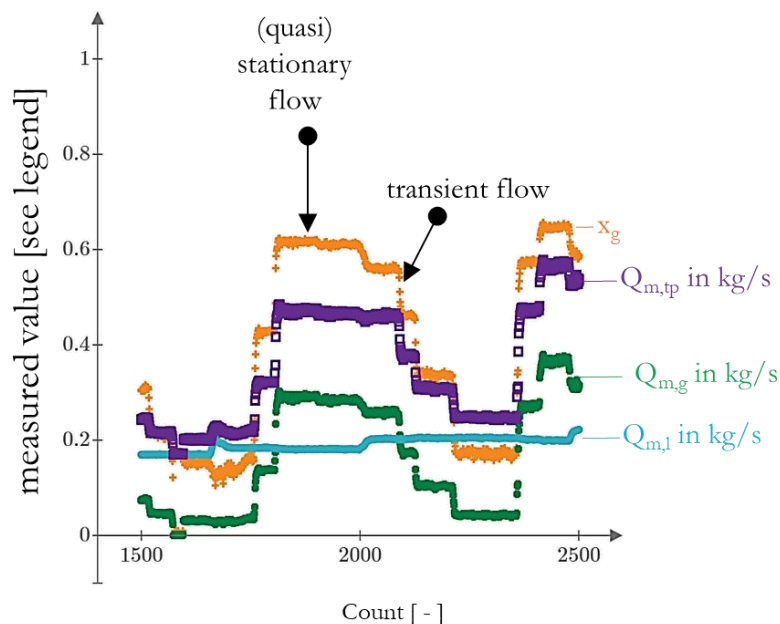


Figure 87: Zoom in of raw data with TS0202 with two-phase flow showing stationary, quasi-stationary and transient flow.

These points are representative of these types of flows. All these data points are evaluated analogously to Table 40.

The deviation of the calculated pressure downstream, P_d per eq.(89) to the experimental downstream pressure $P_{d,exp}$ calculated analogous to Table 40, is plotted in Figure 88 for the first rupture disk type TS0102. The downstream pressure predicted with the proposed procedure is mainly within $\pm 4\%$ of measured value for all 4274 data points with $0.10 < x_g < 0.90$.

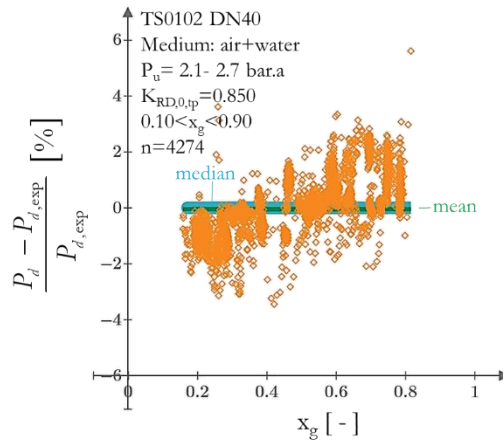


Figure 88: Deviation of the calculated pressure downstream $(P_d - P_{d,exp}) / P_{d,exp}$ in % with P_d per eq.(89) to $P_{d,exp}$ for varying x_g with TS0102.

The deviation of the calculated pressure downstream, P_d per eq.(89) to the experimental downstream pressure $P_{d,exp}$ calculated analogous to Table 40 is plotted in Figure 89 for the second rupture disk type TS0202. The downstream pressure predicted with the proposed procedure is mainly within $\pm 4\%$ of measured value for all 3546 data points with $0.10 < x_g < 0.90$.

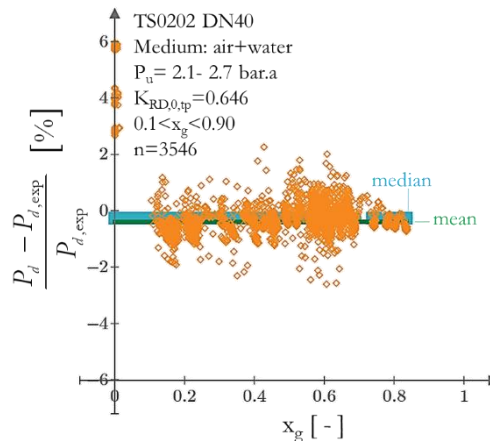


Figure 89: Deviation of the calculated pressure downstream $(P_d - P_{d,exp}) / P_{d,exp}$ in % with P_d per eq.(89) to $P_{d,exp}$ for varying x_g with TS0202.

Correlating losses observed with low-velocity flow to losses expected on high-velocity flow using equations for predicting losses in rough pipes, is also valid for two-phase flow, just like in gas flow. All the 7820 data points are predicted mainly within $\pm 4\%$ of measured value with $0.10 < x_g < 0.90$.

The proposed methodology counters current situation where there is neither a characteristic number for characterizing losses in rupture disk device nor a method to calculate the pressure-drop across a rupture disk, ΔP_{RD} with two-phase flow. This despite the fact that ΔP_{RD} is essential for the pressure-drop calculation in the entire rupture disk vent-line system to validate its capacity in sizing Step 5 in Table 1. The method is also suited to calculate the pressure-drop through rupture disk from the point of rupture disk activation (worst-case scenario) to the point when the system is fully depressurized beyond regulatory compliance. The use of the proposed procedure outside its validation range of is subject to experimental validation, especially for low gas mass flow quality with $x_g < 0.1$.

7 Conclusion and summary

This work has focused on the experimental investigation of the mass flow rate and pressure-drop through rupture disk devices with compressible gas and two-phase flow. The results are summarized as follows:

The experimental focus was in the design, construction, and commissioning of a high-capacity, high-pressure industry-scale test facility for testing small- to large-diameter rupture disks and other fittings with gas flow. The 150 bar gas rig, which is a suited industry-scale test facility for testing rupture disk devices with gas, has been designed, constructed, and put into operation. The 150 bar gas rig is the first stage of CSE HP loop, which is a high-capacity, high-pressure test-facility for testing small- to large-diameter devices at near realistic flow conditions at pressures up to 3000 bar. The 150 bar gas rig has a capacity to test rupture disks as large as DN150 and safety relief valve with a seat diameter as large as 63 mm at pressures up to 100 bar under flow conditions, which is more representative of flow during emergency relief. This work also presents the design-concept of a pilot plant for testing rupture disks with air/water two-phase flow. A test-section equipped with state-of-the-art instrumentation has been developed and used to deliver precise experimental data for validation in this work. Rupture disks can be tested on the same test section, and with the same measurement and instrumentation with gas flow, as well as with two-phase flow.

The theoretical focus was on the development of a reliable rupture disk sizing procedure for compressible gas and two-phase flow. This required phenomenological studies of flow through rupture disks with both experiments and CFD studies. Flow in a rupture disk has been visualized experimentally. A method to digitalize a rupture disk has also been developed. The digitalized model has been used in CFD-simulations to give detailed visual impressions of flow through a rupture disk.

The prediction of the dischargeable mass flow rate across a rupture disk is essential to the smallest rupture disk and pipe size, which fulfills the “dischargeable mass flow rate is larger than the minimum flow rate to be discharged,” sizing criterion. A rupture disk has thereby been modeled as an infinitely thin asymmetric bore with a large diameter ratio. The separated flow region in a rupture disk has been modeled as an apparent asymmetric nozzle, with a nozzle throat area as the rupture disk free relieving area, A_{RD} . In general, the method predicts the discharge rate within $\pm 3\%$ of the measured discharge rate. For gas flow, area-choking and fanno-choking have been investigated. The general equation for the rupture disk dischargeable mass flow rate has been achieved with mathematical coupling of the presented phenomenological relations to determine the dischargeable mass flow rate across a rupture disk for gas flow, for the full range of liquid to gas flow. With this, the smallest rupture disk and pipe size which fulfills the “dischargeable mass flow rate is larger than the minimum flow rate to be discharged” sizing criterion may be calculated from one equation with liquids, two-phase liquid-gas mixtures and with gases seamlessly.

The rupture disk free relieving area, A_{RD} is a model parameter, which is required to determine the dischargeable mass flow rate as intended. An implicit method to determine A_{RD} directly from a single experiment, with low-velocity, incompressible gas flow, with $Ma_u < 0.30$ and $Re_u > 10^5$, has been developed and validated experimentally. The method determines the discharge area precisely, with appropriate consideration of structural members, which reduce the relieving area with both the circular and segmental bores, mainly within $\pm 5\%$ of the actual area. A_{RD} as a constant characteristic number for a rupture disk type has been applied successfully as a model parameter in the phenomenological relations to determine the dischargeable mass flow rate across a rupture disk for gas flow and for two-phase flow.

The prediction of pressure-drop across a rupture disk is essential to calculate the pressure-drop in the entire rupture disk vent-line system to validate its capacity. This work also presents a method to characterize and calculate the pressure-drop across a rupture disk more reliably with gas flow and with air/water two-phase flow. The proposed method presents a relationship that more generally valid to correlate rupture disk losses observed in low-velocity flow to losses expected in high-velocity flow by factoring compressibility fully. For gas flow, this work shows that equations in literature predict the pressure-drop and pressure profile across a rupture disk accurately for low-velocity flow with Mach number upstream of rupture disk equal or less than 0.3. However, classic equations do not predict the same with acceptable accuracy for high-velocity flow with Mach number upstream of rupture disk $Ma_u > 0.3$. The predicted pressure-drop is underpredicted by up to -40% from the actual pressure-drop during relief. The root cause of this significant uncertainty is insufficient consideration of compressibility effects.

The general strategy for predicting the pressure-drop across a rupture disk with gas and two-phase flow is to correlate losses observed with low-velocity and incompressible flow to losses expected in high-velocity and compressible flow. A new characteristic number that is valid for all plausible gas flows has been proposed as the *rupture disk zero-velocity minor loss coefficient*, $K_{RD,0}$. This rupture disk characteristic number is determined experimentally with low-velocity flow with Mach number upstream of the rupture disk $Ma_u < 0.30$ and $Re_u > 10^5$. A new characteristic number that is valid for all plausible two-phase flows has also been proposed as the *rupture disk incompressible minor loss coefficient* $K_{RD,0,tp}$. This proposed characteristic number is determined experimentally with gas mass flow quality x_g , upstream of rupture disk $x_g < 0.3$. $K_{RD,0}$ and $K_{RD,0,tp}$ are taken to be constant for a rupture disk type, and nominal pipe size. $K_{RD,0}$ and $K_{RD,0,tp}$ are then used to predict the pressure-drop across a rupture disk for all other flows with a new phenomenological relationship to determine pressure-drop across a rupture disk, with an effective pipe length. The general equation for rupture disk compressible pressure-drop has been achieved with mathematical coupling of the phenomenological relations for gas flow, and for two-phase flow, for $x_g \geq 0.1$. The use of the proposed procedure outside its validation range is subject to experimental validation, especially for low gas mass flow quality $x_g < 0.1$. With this, the pressure-drop is calculated from one equation with liquids, two-phase liquid-gas mixtures, and with gases seamlessly with the determined rupture disk loss coefficients for gas flow and two-phase flow. Experiments show that the phenomenological relations described above predict the pressure-drop across a rupture disk, mainly within ± 4 % of measured value with gas mass flow quality $x_g \geq 0.1$.

8 Bibliography

- Adams, T., & Grant, C. (2012).** A Simple Algorithm to Relate Measured Surface Roughness to Equivalent Sand-grain Roughness. *International Journal of Mechanical Engineering and Mechatronics*, 1(1), 66-71.
- Ali, S. F., & Yeung, H. (2015).** Experimental Study of Two-Phase Air–Water Flow in Large-Diameter Vertical Pipes. *Chemical Engineering Communications*(202), 823-842.
- API. (2014).** Sizing, Selection, and Installation of Pressure-relieving Devices Part I—Sizing and Selection. In *API STANDARD 520*. American Petroleum Institute.
- ASME. (2014).** Pressure Relief Devices Performance Test Codes 25 (PTC 25-2014). New York: The American Society of Mechanical Engineers.
- ASME. (2017).** *BPVC Section VIII-Rules for Construction of Pressure Vessels Division 1* (2017 ed., Vols. BPVC Section VIII-Rules for Construction of Pressure Vessels Division 1). American Society of Mechanical Engineers. Retrieved from <https://www.asme.org/products/codes-standards/bpvcviii1-2017-bpvc-section-viiiirules>
- Awad, M. M., & Muzychka, Y. (2008).** Effective property models for homogeneous two-phase flows. *Experimental Thermal and Fluid Science*, 33(1), 106-113.
- Bell, I. H., Wronski, J., Quoilin, S., & Lemort, V. (2014, 05 04).** Pure and Pseudo-pure Fluid Thermophysical Property Evaluation and the Open-Source Thermophysical Property Library CoolProp. *Industrial & Engineering Chemistry Research*, 53(6), 2498-2508. doi:<http://pubs.acs.org/doi/pdf/10.1021/ie4033999>
- Beune, A. (2009).** *Analysis of high-pressure safety valves*. Eindhoven: Eindhoven University Press.
- Bhagwat, S. M., & Ghajar, A. J. (2014).** A flow pattern independent drift flux model based void fraction correlation for a wide range of gas–liquid two phase flow. *International Journal of Multiphase Flow*, 59, 186-205.
- Blank, T. (2018).** *CFD-Analyse einer Berstscheibe*. Karlsruhe: Bachelorarbeit: Karlsruhe University of Applied Sciences.
- Brkić, D. (2011).** Review of explicit approximations to the Colebrook relation for flow friction. *Journal of Petroleum Science and Engineering*(77), 34-48.
- Chen, N. H. (1979).** An Explicit Equation for Friction Factor in Pipe. *Ind. Eng. Chem. Fundam.*, 18(3), 297-297.
- Chisholm, D. (1983).** *Two phase flow in pipelines and heat exchangers*. London: Longman Group.
- Crane Co. (2009).** *CRANE Flow of Fluids - Technical Paper No. 410M*. Stamford: Crane Co.
- Darby, R. (2004).** On two-phase frozen and flashing flows in safety relief valves Recommended calculation method and the proper use of the discharge coefficient. *Journal of Loss Prevention in the Process Industries*(17), 255-259.
- Dayev, Z. A., & Sultanov, N. Z. (2018).** Comparative analysis of discharge coefficients. *Measurement Techniques*, 61(7), 718-722.
- DECHEMA. (2018).** *Die Verfügbarkeit von mechanischen Sicherheitseinrichtungen –Sicherheitsventile*. ProcessNet-Arbeitsausschuss „Sicherheitsgerechtes Auslegen von Chemieanlagen“. Frankfurt am Main: DECHEMA Gesellschaft für Chemische Technik und Biotechnologie e.V.
- Diener, R. (1999).** Berechnung und Messung der Massendurchsatzcharakteristik von Stellventilen bei Zweiphasenströmung. *Fortschritt-Berichte VDI Dusseldorf*, 7(388).
- Diener, R., & Schmidt, J. (2005).** Sizing of throttling devices for gas liquid two-phase flow, Part control valves, orifices and nozzles. *Process Safety Progress*, 24(1), 29-37.
- Ebrahimi, B., He, G., Tang, Y., Franchek, M., Liu, D., Pickett, J., . . . Franklin, D. (2017).** Characterization of high-pressure cavitating flow through a thick orifice plate in a pipe of constant cross section. *International Journal of Thermal Sciences*, 114, 229-240.
- European Commission. (1997).** *Directive 97/23/EC of the European parliament and of the council of 29 May 1997 on the approximation of the laws of the member states concerning pressure equipment*. Retrieved August 15, 2017, from <http://eur-lex.europa.eu/legal-content/EN/ALL/?uri=CELEX:01997L0023-20130101>

- Flösch, J., & Klumpp, T.** (2019). *Aufbau einer Simulation zur Untersuchung des Strömungsverhaltens einer Berstscheibe nach dem Ansprechen*. Karlsruhe: Projektarbeit: Karlsruhe University of Applied Sciences.
- Fossa, M., & Guglielmini, G.** (2002). Pressure drop and void fraction profiles during horizontal flow through thin and thick orifices. *Experimental Thermal and Fluid Science*(26), 513-523.
- Friedel, L.** (1979). Improved friction pressure drop correlations for horizontal and vertical two-phase pipe flow. *European Two-Phase Flow Group Meeting*, p. Paper E2.
- Friedel, L., & Kissner, H.** (1988). Single-phase and two-phase resistance across rupture discs. *ICHEME Symposium Series*(110), 301-329.
- Grolmes, M., & Fauske, H. K.** (1969). Propagation characteristics of compression and rarefaction pressure pulses in one-component vapor-liquid mixtures. *Nuclear Engineering and Design*(11),137-142.
- Grønnerud, R.** (1979). Investigation of liquid hold-up, flow-resistance and heat transfer in circulation type evaporators part IV: two-phase flow resistance in boiling refrigerants. Annexe 1972-1. *Bull. de l'Inst. du Froid*.
- Hamad, F., Faraji, F., Santim, C., Basha, N., & Ali, Z.** (2017). Investigation of pressure drop in horizontal pipes with different diameters. *International Journal of Multiphase Flow*(91), 120-129.
- Hanafizadeh, P., Karimi, A., Taklifi, A., & Hojati, A.** (2018). Experimental investigation of two-phase water–oil flow pressure drop. *Experimental Thermal and Fluid Science*(74), 169-180.
- Hansen, L. S., Pedersen, S., & Durdevic, P.** (2019). Multi-Phase Flow Metering in Offshore Oil and Gas Transportation Pipelines: Trends and Perspectives. *Sensors*(19), 1-26. doi:10.3390/s19092184
- Huff, J. E.** (2001). Restrictive rupture disk devices: A calculation method for certification and relief system design. *AIChE 2001 Spring National Meeting*. Houston.
- ISO.** (2003). Measurement of fluid flow by means of pressure differential devices inserted in circular cross-section conduits running full - Part 2: Orifice plates.
- ISO.** (2010). *ISO 8573-1:2010 Compressed air -- Part 1: Contaminants and purity classes*. Geneva, Switzerland: ISO.
- Kacic, O., & Nitschke, T.** (2018). *Kompressible Rohrströmung*. Karlsruhe: Projektarbeit: Karlsruhe University of Applied Sciences.
- Kong, R., Qiao, S., Kim, S., Bajorek, S., Tien, K., & Hoxie, C.** (2018). Interfacial area transport models for horizontal air-water bubbly flow in different pipe sizes. *International Journal of Multiphase Flow*(106), 46-59.
- Kurz, C.** (2017). *Experimentelle Analyse von Blenden als Ersatzmodell für die Berechnung des Massenstroms durch Berstscheiben*. Karlsruhe: Bachelorarbeit: Karlsruhe University of Applied Sciences.
- Levenspiel, O.** (1977). The discharge of gases from a reservoir through a pipe. *AIChE Journal*, 23(3), 402-403.
- Levenspiel, O.** (1998). *Engineering Flow and Heat Exchange; Revised Edition*. New York: Springer.
- Lockhart, R., & Martinelli, R.** (1949). Non-Newtonian Two-Phase Flow Characteristics across Sudden Expansion in Horizontal Rectangular Minichannel. *Chemical Engineering Progress*,(45), 28-48.
- Lu, C., Kong, R., Qiao, S., Larimer, J., Kim, S., Bajorek, S., . . . Hoxie, C.** (2018). Frictional pressure drop analysis for horizontal and vertical air-water two-phase flows in different pipe sizes. *Nuclear Engineering and Design*, 332, 147-161.
- Melkamu A., W., & J.Ghajar, A.** (2007). Comparison of void fraction correlations for different flow patterns in horizontal and upward inclined pipes. *International Journal of Multiphase Flow*, 33(4), 347-370.
- Miller, D. S.** (1984). *Compressible Internal Flow* (Vol. 10). British Hydromechanics Research Association (BHRA) the Fluid Engineering Center, Cranfield, UK.
- Miller, K. S., & Ross, B.** (1993). *An introduction to the fractional calculus and fractional differential equations* (xiii ed.). New York: Wiley.
- Miller, R. W.** (1996). *Flow Measurement Engineering Handbook* (Third Edition ed.). McGraw-Hill Education.
- Müller-Steinhagen, H., & Heck, K.** (1986). A simple friction pressure drop correlation for two-phase flow in pipes. *Chemical Engineering and Processing: Process Intensification*, 20(6), 297-308.

- Mutegi, M. K.** (2014). *Development of a test loop for safety devices for multiphase flow*. Karlsruhe: Karlsruhe Institute of Technology.
- Mutegi, M. K., & Schmidt, J.** (2016). Challenges in Sizing Rupture Disk Vent Line Systems Especially for Compressible Two-phase Flow. *Chemical Engineering Transactions*, 48, 631-636. doi:10.3303/CET1648106
- Mutegi, M. K., Schmidt, J., & Denecke, J.** (2019). Sizing Rupture Disk Vent Line Systems for High-velocity Gas Flows. *Journal of Loss Prevention in the Process Industries*, 62. doi:https://doi.org/10.1016/j.jlp.2019.103950
- NBBPVI.** (2019, 11 16). Electronic version of Pressure Relief Device Certifications. Columbus: The National Board of Boiler and Pressure Vessel Inspectors. Retrieved from <https://www.nationalboard.org/SiteDocuments/NB18/NB18.pdf>
- Nord Stream AG.** (2013). *Secure Energy for Europe - The Nord Stream Pipeline Project*. Zug, Switzerland: Nord Stream AG.
- Ould-Didi, M., Kattan, N., & Thome, J.** (2002). Prediction of two-phase pressure gradients of refrigerants in horizontal tubes. *International Journal of Refrigeration*(25), 935-947[^].
- Perry, R. H., & Green, D. W.** (2008). *Perry's Chemical Engineering Handbook (8th Edition)*. New York: McGraw-Hill. doi:10.1036/0071422943
- Petrovic, M. M., & Stevanovic, V. D.** (2016). Two-Component Two-Phase Critical Flow. *FME Transactions*(44), 109-114.
- Quibén, J. M., & Thome, J. R.** (2007). Flow pattern based two-phase frictional pressure drop model for horizontal tubes, Part II: New phenomenological model. *International Journal of Heat and Fluid Flow*, 28, 1060-1072.
- Reader-Harris, M.** (2015). *Orifice Plates and Venturi Tubes*. Heidelberg, New York, Dordrecht, London: Springer International Publishing.
- Reader-Harris, M. J., & Sattary, J. A.** (1996). The orifice plate discharge coefficient equation - the equation for ISO 5167-1. *North Sea Flow Measurement Workshop*. Peebles, Scotland; East Kilbride, Glasgow.
- Rivas-Nass, J.** (1992). Diplomarbeit , Messung der Druckverteilung in der plötzlichen Rohrverengung bei Durchströmung mit einem Gas/Flüssigkeitsgemisch. FH Frankfurt (M): FH Frankfurt (M).
- Roul, M. K., & Dash, S. K.** (2012). Single-Phase and Two-Phase Flow Through Thin and Thick Orifices in Horizontal Pipes. *Journal of Fluids Engineering*, 134(9). doi:doi:10.1115/1.4007267
- Schmidt, C.** (2016). *Messung des axialen Druckverlaufs bei Durchströmen einer Berstscheibe mit Luft*. Karlsruhe: Bachelorarbeit: Karlsruhe Institut of Technology.
- Schmidt, J.** (1993). *Berechnung und Messung der Druckänderungen über scharfkantige plötzliche Rohrerweiterungen und -verengungen bei Gas Dampf-Flüssigkeitsströmung*. Strömungstechnik. Dusseldorf: VDI-Verlag.
- Schmidt, J.** (2015). How to Size a Rupture Disk Vent-line for Two-Phase Gas/Liquid Flow based on Current Engineering Practices. *11th Global Congress on Process Safety. Austin, Texas*.
- Schmidt, J.** (2018). Kritische Massenströme durch Düsen, Ventile und Rohreinbauten. In *VDI-Wärmeatlas*. Springer Reference Technik. Springer Vieweg, Berlin, Heidelberg.
- Schmidt, J.** (2019). Auslegung von Schutzeinrichtungen für wärmeübertragende Apparate. In P. Stephan, D. Mewes, S. Kabelac, M. Kind, K. Schaber, & T. Vetzal (Eds.), *VDI-Wärmeatlas*. Springer-Verlag GmbH Deutschland.
- Schmidt, J., & Claramunt, S.** (2015). Sizing of rupture disks for two-phase gas/liquid flow according to. *Journal of Loss Prevention in the Process Industries*, 1-14. Retrieved from <http://dx.doi.org/10.1016/j.jlp.2015.12.016>
- Shannak, B.** (1998). *Kontraktion bei der Einphasigen- und Zweiphasigenströmung durch scharfkantige Blenden*. Dusseldorf: VDI-Verlag.
- Shannak, B.** (2010). Experimental and theoretical investigation of gas-liquid flow pressure drop across rupture discs. *Nuclear Engineering and Design*, 240(6), 1458-1467.

- Shannak, B. A.** (2008). Frictional pressure drop of gas liquid two-phase flow in pipes. *Nuclear Engineering and Design*, 238(12), 3277-3284. doi:10.1016/j.nucengdes.2008.08.015
- Shannak, B., Friedel, L., & Alhusein, M.** (1999). Prediction of Single- and Two-Phase Flow Contraction through a Sharp-Edged Short Orifice. *Chemical Engineering Technology*, 22(10), 865-870.
- Shannak, B.-B., Friedel, L., & Alhusein, M.** (1999). Prediction of Single- and Two-Phase Flow Contraction through a Sharp-Edged Short Orifice. *Chemical Engineering Technology*, 22(10), 865-870.
- Shapiro, A. H.** (1953). *The Dynamics and Thermodynamics of Compressible Flow*. New York: The Ronald Press Company.
- Siemens.** (STAR-CCM+ V13). STAR-CCM+. Plano: Siemens Product Lifecycle Management Software.
- Straka, M., Fiebach, A., Eichler, T., & Koglin, C.** (2018). Hybrid simulation of a segmental orifice plate. *Flow Measurement and Instrumentation*, 60, 124-133.
- Sun, L., & Mishima, K.** (2009). Evaluation analysis of prediction methods for two-phase flow pressure drop in mini-channels. *International Journal of Multiphase Flow*, 35(1), 47-54.
- Thévenin, D., & Janiga, G.** (2014). *Fluid Dynamics for Engineers*. GNU Free Documentation License.
- Thome, J. R., & Cioncolini, A.** (2015). Encyclopedia of Two-Phase Heat Transfer and Flow I. In J. R. Thome (Ed.), *Chapter 6: Two-Phase Pressure Drop* (pp. 143-176). Lausanne, Switzerland: Laboratory of Heat and Mass Transfer (LTCM), Switzerland & Ecole Polytechnique Fédérale de Lausanne (EPFL). doi:https://doi.org/10.1142/9789814623216_0023
- TORIZUMI, Y.** (1990). Flow Characteristics of Compressible Flow through Eccentric and Segmental Orifices. *Transactions of the Japan Society of Mechanical Engineers, Series B*, 142-145.
- Tribbe, C., & Müller-Steinhagen, H.** (2000). An evaluation of the performance of phenomenological models for predicting pressure gradient during gas±liquid. *International Journal of Multiphase Flow*, 26, 1019-1036.
- Truckenbrodt, E.** (2008). *Fluidmechanik Band 2; Elementare Strömungsvorgänge dichte veränderlicher Fluide sowie Potential- und Grenzschichtströmungen*. München: Springer Verlag Berlin Heidelberg.
- TÜV.** (2006). AD 2000-Merkblatt A 1, Safety devices against excess pressure – Bursting safety devices –. In *Equipment, installation and marking of pressure vessels*. Berlin: Verband der TÜV e.V.
- TÜV.** (2015). *AD 2000-Merkblatt A 2 Safety devices against excess pressure - Safety valves*. TÜV: TÜV.
- Urner, G.** (1997). Pressure loss in orifice plates according to ISO-5167-1. *Flow Measurement and Instrumentation*, 8(1), 31-41.
- Ward-Smith, A. J.** (1979). Critical Flowmetering: The Characteristics of Cylindrical Nozzles with Sharp Upstream Edges. *International Journal of Heat and Fluid Flow*(1), 123-132.
- Zande, M. v., Muntinga, J., & Broek, W. v.** (1998). Emulsification of Production Fluids in the Choke Valve, SPE Annual Technical Conference and Exhibition, 27-30 September, 1998. *SPE 49173*. New Orleans, Louisiana: Society of Petroleum Engineers, Inc. doi:https://doi.org/10.2118/49173-MS
- Zeghloul, A., Azzi, A., Saidj, F., Messilem, A., & Azzopardi, B. J.** (2017). Pressure Drop Through Orifices for Single- and Two-Phase Vertically Upward Flow — Implication for Metering. *Journal of Fluids Engineering*(139).

9 **Annex**

ANNEX I Dischargeable mass flow rate across a rupture disk device

The mass flow rate through a rupture disk device installed in a complex vent-line for gas in imperial units with (API, 2014) is per eq.(1) in chapter 3.1.

$$Q_{m,API} = K_U \cdot 1891 \cdot \psi_i \cdot D^2 \cdot \sqrt{\frac{\Delta P_i \cdot P_0}{K_{yjs} \cdot v_0}} \text{ with } i=\text{sonic or sub-sonic} \quad (1)$$

with P in PSI , v_0 in $\frac{ft^3}{lb}$ and D in in

Critical flow conditions prevail for

$$\Delta P_{sonic} < \Delta P_{sub-sonic} \quad (A-1)$$

,with the dimensionless pressure drop ΔP_{sonic} for sonic flow as a function of the only total resistance to flow K_{sum} per eq.(A-2).

$$\Delta P_{sonic} = \begin{cases} 0 & \text{for } K_{yjs} \leq 1.2 \\ 0.1107 \cdot \ln(K_{yjs}) + 0.535 & \text{for } 1.2 < K_{yjs} \leq 10 \\ 0.0609 \cdot \ln(K_{yjs}) + 0.6513 & \text{for } 10 < K_{yjs} \leq 100 \end{cases} \quad (A-2)$$

The corresponding discharge equation for sonic flow, ψ_{sonic} is

$$\psi_{sonic} = \begin{cases} 0 & \text{for } K_{yjs} \leq 1.2 \\ 0.0434 \cdot \ln(K_{yjs}) + 0.5889 & \text{for } 1.2 < K_{yjs} \leq 10 \\ 0.710 & \text{for } 10 < K_{yjs} \leq 100 \end{cases} \quad (A-3)$$

For sub-sonic flow, $\Delta P_{sub-sonic}$, is a function of the total resistance to flow K_{sum} and back-pressure P_a per eq.(A-4).

$$\Delta P_{sub-sonic} = \frac{P_0 - P_a}{P_0} \quad (A-4)$$

The corresponding discharge parameter for sub-sonic flow, $\psi_{sub-sonic}$ is

$$\psi_{sub-sonic} = 1 - \left(\frac{1 - \psi_{sonic}}{\Delta P_{sonic}} \right) \cdot \Delta P_{sub-sonic} \quad (A-5)$$

The mass flow rate through a rupture disk device with gas flow per (TÜV, 2006) is per eq.(2) are mentioned below. Sub-critical conditions prevail when

$$\frac{P_a}{P_0} > \left(\frac{2}{\kappa + 1} \right)^{\kappa/(\kappa-1)} \quad (A-6)$$

,with P_a as the absolute backpressure, p_0 as the absolute pressure in the system to protect, and κ is the isentropic exponent of the medium. Critical flow conditions prevail otherwise. The discharge parameter ψ for sub-critical flow conditions is

$$\psi = \sqrt{\frac{\kappa}{\kappa-1}} \cdot \sqrt{\left(\frac{P_a}{P_0} \right)^{2/\kappa} - \left(\frac{P_a}{P_0} \right)^{\kappa+1/\kappa}} \text{ for } \frac{P_a}{P_0} > \left(\frac{2}{\kappa+1} \right)^{\kappa/(\kappa-1)} \quad (A-7)$$

The discharge equation ψ for critical flow conditions is

$$\psi = \sqrt{\frac{\kappa}{\kappa+1}} \cdot \left(\frac{2}{\kappa+1} \right)^{1/(\kappa-1)} \text{ for } \frac{P_a}{P_0} \leq \left(\frac{2}{\kappa+1} \right)^{\kappa/(\kappa-1)} \quad (A-8)$$

The discharge coefficient of the entire relief line with the rupture disk installed is calculated per eq.(A-9).

$$C_d = \sqrt{\frac{1}{1 + 0.752 \cdot K_{yjs}^{0.876}}} \text{ with } K_{yjs} = \zeta_L \cdot \left(\frac{A_{RD}}{A_1} \right)^2 \quad (A-9)$$

The total flow resistance of the vent-line with rupture disk installed, ζ_L is

$$\zeta_L = \left[\lambda \cdot \frac{L}{D_L} + \sum_L K_i + K_{RD} \right] \cdot \frac{\bar{Z}_L}{Z} \quad (\text{A-10})$$

,where \bar{Z}_L is the average real gas factor of the fluid in pipe, while Z is the gas factor of the fluid on the pressurized system.

ANNEX II Measurement range of flow measurement unit with $U < 0.5\%$ o.r

Table 41 through Table 44 is the data given by the manufacturer. This data is used to plot the measurement range of flow measurement unit in Figure 17

Table 41 Measurement range of FI301 DN150

P bar	Q _{m,min} kg/hr	Q _{m,max} kg/hr	UQ _{m,min} % o.r.	UQ _{m,max} % o.r.
2	6,400	9,000	0.5	0.35
5	6,400	23,000	0.5	0.35
10	6,400	46,000	0.5	0.35
20	6,400	91,000	0.5	0.35
30	6,400	135,000	0.5	0.35
40	6,400	180,000	0.5	0.35
50	6,400	224,000	0.5	0.35
60	6,400	260,000	0.5	0.35
80	6,400	360,000	0.5	0.35
100	6,400	450,000	0.5	0.35

Table 42 Measurement range of FI302 DN80

P bar	Q _{m,min} kg/hr	Q _{m,max} kg/hr	UQ _{m,min} % o.r.	UQ _{m,max} % o.r.
2	1,800	3,700	0.5	0.35
5	1,800	9,200	0.5	0.35
10	1,800	18,500	0.5	0.35
20	1,800	37,000	0.5	0.35
30	1,800	55,400	0.5	0.35
40	1,800	73,700	0.5	0.35
50	1,800	91,900	0.5	0.35
60	1,800	110,000	0.5	0.35
80	1,800	145,000	0.5	0.35
100	1,800	180,000	0.5	0.35

Table 43 Measurement range of FI304 DN40

P bar	Q _{m,min} kg/hr	Q _{m,max} kg/hr	UQ _{m,min} % o.r.	UQ _{m,max} % o.r.
2	450	700	0.5	0.35
5	450	1,700	0.5	0.35
10	450	3,400	0.5	0.35
20	450	6,800	0.5	0.35
30	450	10,200	0.5	0.35
40	450	13,600	0.5	0.35
50	450	16,900	0.5	0.35
60	450	19,600	0.5	0.35
80	450	27,200	0.5	0.35
100	450	34,000	0.5	0.35

Table 44 Measurement range of FI304 DN25

P bar	Q _{m,min} kg/hr	Q _{m,max} kg/hr	UQ _{m,min} % o.r.	UQ _{m,max} % o.r.
2	113	330	0.5	0.35
5	113	830	0.5	0.35
10	113	1,600	0.5	0.35
20	113	3,300	0.5	0.35
30	113	4,900	0.5	0.35
40	113	6,600	0.5	0.35
50	113	8,300	0.5	0.35
60	113	9,900	0.5	0.35
80	113	13,200	0.5	0.35
100	113	16,600	0.5	0.35

ANNEX III The main components in zone 100

Table 45 is a list of the main components in zone 100 as presented in Figure 18 and Figure 19 in chapter 4.6.1.

Table 45 Components in Zone 100

Component	Tag	Function/Technical data
Pressure vessel	B06	Buffer tank Manufacturer: Vorwerk, MAWP=156 bar g, 25.2 m ³
Pressure vessel	B07	Buffer tank/ Manufacturer: Vorwerk, MAWP=156 bar g, 37.3 m ³
shut-off valve	V101	Manufacturer: Hartmann Type: AST
shut-off valve	V102	Manufacturer: Hartmann Type: AST
shut-off valve	V103	Manufacturer: Hartmann Type: ASF
shut-off valve	V104	Manufacturer: Hartmann Type: AST
shut-off valve	V105	Manufacturer: Hartmann Type: AST
shut-off valve	V151	Manufacturer: Hartmann Type: AST
shut-off valve	V152	Manufacturer: Hartmann Type: ASF
shut-off valve	V153	Manufacturer: Hartmann Type: AST
shut-off valve	V154	Manufacturer: Hartmann Type: AST
safety valve	SV101	Protection of container against solar radiation, 155 bar g
safety valve	SV151	Protection of container against solar radiation, 156 bar g
temperature sensor	TIz 101	iTEMP TMT82/ -100 °C-100 °C/ 4-20 mA HART/ 4- wire
temperature sensor	TIz 102	iTEMP TMT82/ -100 °C-100 °C/ 4-20 mA HART/ 4- wire
temperature sensor	TIz 103	iTEMP TMT82/ -100 °C-100 °C/ 4-20 mA HART/ 4- wire
temperature sensor	TIz 104	iTEMP TMT82/ -100 °C-100 °C/ 4-20 mA HART/ 4- wire
temperature sensor	TIz 106	iTEMP TMT82/ -100 °C-100 °C/ 4-20 mA HART/ 4- wire
temperature sensor	TIz 151	iTEMP TMT82/ -100 °C-100 °C/ 4-20 mA HART/ 4- wire
temperature sensor	TIz 152	iTEMP TMT82/ -100 °C-100 °C/ 4-20 mA HART/ 4- wire
temperature sensor	TIz 154	iTEMP TMT82/ -100 °C-100 °C/ 4-20 mA HART/ 4- wire
pressure sensor	PI 101	Cerebar S PMP71/ 0 bar- 400 bar/4-20 mA HART
pressure sensor	PI 102	Cerebar S PMP71/ 0 bar- 180 bar/4-20 mA HART
pressure sensor	PI 103	Cerebar S PMP71/ 0 bar- 180 bar/4-20 mA HART
pressure sensor	PI 151	Cerebar S PMP71/ 0 bar- 400 bar/4-20 mA HART
pressure sensor	PI 152	Cerebar S PMP71/ 0 bar- 180 bar/4-20 mA HART
pressure sensor	PI 153	Cerebar S PMP71/ 0 bar- 180 bar/4-20 mA HART

ANNEX IV The main components in zone 200

Table 46 is a list of the main components in zone 200 as presented in Figure 20 and Figure 21 in chapter 4.6.2.

Table 46 Components in Zone 200

Component	Tag	Function/Technical data
screw compressor	RSF 75-15	Maximum pressure: 15 bar g, maximum volume flow: 8.1 mN ³ /min = 486 mN ³ /h
piston compressor	GIB 24.12-75	Maximum pressure: 350 bar g, maximum volume flow: 330 mN ³ /h
oil filters	RF-C 0750	Separation of oil
tumble dryer	HL MAD 550	Air drying
fine droplet separator	AC-0550	Water separation
Oil-water separator	UFS-SP 30N	Treatment oil-water
bins	B-K-01	MAWP=16 bar g, volume: 3,65 m ³
pump	CY-6091	Cooling air supply Piston compressor
air cooler	GFH 067B	Cooling of the piston compressor with air
air purification	AKC-0870	Preparation of the air
control valve	CV202	regulation
control valve	CV205	regulation
control valve	CV251	regulation
shut-off valve	V201	Open-Close
shut-off valve	V203	Open-Close
shut-off valve	V204	Open-Close
shut-off valve	V253	Open-Close
shut-off valve	V254	Open-Close
safety valve	SV205	Protection of container against piston compressor 16bar g
safety valve	SV252	System protection against screw compressor 15bar g
safety valve	SV254	Protection of system against backflow from buffer tank 16bar g
temperature sensor	TI 201	iTEMP TMT82/ -50 °C-100 °C/ 4-20 mA HART/ 4- wire
temperature sensor	TI 204	iTEMP TMT82/ -100 °C-100 °C/ 4-20 mA HART/ 4- wire
pressure sensor	PI 201	Cerebar S PMP71/ 0 bar-50 bar/4-20 mA HART
pressure sensor	PI 202	Cerebar S PMP71/ 0 bar-50 bar/4-20 mA HART
pressure sensor	PI 203	Cerebar S PMP71/ 0 bar-50 bar/4-20 mA HART
pressure sensor	PI 204	Cerebar S PMP71/ 0 bar-50 bar/4-20 mA HART
pressure sensor	PI 205	Cerebar S PMP71/ 0 bar-50 bar/4-20 mA HART

ANNEX V The main components in zone 300

Table 47 is a list of the main components in zone 300 as presented in Figure 22 and Figure 23 in chapter 4.6.3.

Table 47 Components in Zone 300

component	Tag	Function/Technical data
control valve	CV301	regulation
control valve	CV302	Samson Typ 3730-6
control valve	CV306	regulation
control valve	CV307	Samson Typ 3730-6
control valve	CV308	Samson Typ 3730-6
flow measurement	FI301	Endress+Hauser Promass 83F1F
flow measurement	FI302	Endress+Hauser Promass 83F80
flow measurement	FI303	Endress+Hauser Promass 83F40
flow measurement	FI304	Endress+Hauser Promass 83F25
shut-off valve	V304	Open-Close
shut-off valve	V305	Open-Close
shut-off valve	V306	Open-Close
shut-off valve	V307	Open-Close
shut-off valve	V310	Open-Close
safety valve	SV301	Protection system 100bar g
safety valve	SV302	Fuse protection system 56bar g
bursting disc	BS301	Protection system 100bar g
bursting disc	BS302	Fuse protection system 56bar g
temperature sensor	TI301	iTEMP TMT82/ -100 °C-100 °C/ 4-20 mA HART/ 4- wire
pressure sensor	PI301	Cerebar S PMP71/ 0 bar-120 bar/4-20 mA HART
pressure sensor	PI304	Cerebar S PMP71/ 0 bar-120 bar/4-20 mA HART
pressure sensor	PI305	Cerebar S PMP71/ 0 bar-120 bar/4-20 mA HART

ANNEX VI The main components in zone 400

Table 48 is a list of the main components in zone 300 as presented in Figure 24 in chapter 4.6.4. This zone was not constricted because of organizational reasons.

Table 48 Components planned for Zone 400

Component	Tag	Function/Technical data
Pressure vessel	B401	Gas propulsion buffer
Pressure vessel	B402	Water vessel buffer
Control valve	CV401	Regulation of P401 and P402
Pressure sensor	PI401; PI402	Data acquisition for control unit
Temperature sensor	TI401; TI402	Data acquisition for control unit
Flow measurement	FI405	Flow measurement of water
Flow measurement	FI406	Flow measurement of air
Shut-off valve	V401	Open-Close
Shut-off valve	V402	Open-Close
Shut-off valve	V403	Open-Close
Shut-off valve	V404	Open-Close
Shut-off valve	V405	Open-Close

Component	Tag	Function/Technical data
Shut-off valve	V406	Open-Close

ANNEX VII The main components in zone 1000

Table 49 is a list of the main components in zone 1000 as presented in Figure 25 and Figure 26 in chapter4.6.5.

Table 49 Components in Zone 1000

component	Tag	Function/Technical data
control valve	V1001	Shut-off of test bench 01-B
temperature sensor	TI1016	iTEMP TMT82/ -100 °C-100 °C/ 4-20 mA HART/ 4- wire
pressure sensor	PI1001	Cerebar S PMP71/ 0 bar-120 bar/4-20 mA HART

ANNEX VIII Process Hazard Analysis of the 150 bar loop

The following Process Hazard Analysis, (PHA) and the safety concept was done and implemented in the 150 bar gas rig as illustrated in the respective PID diagrams for zone 100 (Figure 18), zone 200 (Figure 20), zone 300 (Figure 22), and zone 1000 (Figure 25), and cumulatively in the PID of the entire 150 bar gas rig (Figure 27). The Process Hazard Analysis, PHA and the safety concept starting were done on individual zones starting with zone 100.

Annex VIII-A *Buffer tank unit in zone 100*

The buffer tank zone 100 in the 150 bar gas rig consists of the tanks (B06) and (B07), have a design pressure of 150 bar g and have a volume of 25.2 m³ and 37.3 m³ respectively. The tanks are fed from the compressor part through feed lines and serve as a buffer for the test medium. The buffer tank section is controlled by the control valves (CV202, CV205, CV251) in zone 200 in the compressor section, which are monitored by temperature sensors (TIz 101, TIz 102, TIz 103, TIz 104, TIz 151, TIz 152, TIz 153) and pressure sensors (PI 101, PI 102, PI 103, PI 151, PI 152, PI 153). (See also: Figure 18)

Table 50 PHA and Safety concept for zone 100 with SV101 and SV151 (solar radiation case)

Parameter:	Pressure
Deviation:	“more”
Cause:	Solar radiation
Consequence:	Pressure increase in B06 and B07 above MAWP of 156 bar.g
Safety Concept:	Protection of the system by the safety valves (SV101) and (SV151)
Notes:	In this case, the mass flow rate required for pressure relief must be discharged via the safety valves (SV101) and (SV151)

Annex VIII-B *Compression and gas processing unit in zone 200*

The tank (B-K-01) has a design pressure of 100 bar.g. The RSF 75-15 screw compressor can generate a maximum pressure of 15 bar g. Even in the event of a malfunction of V204 behind the buffer tank, this area is intrinsically safe, as all components are designed at least in PN16.

The piston compressor GIB 24.12-75 can generate a maximum pressure of 350 bar.g. The buffer tanks B06 and B07 have a design pressure of 156 bar.g. The branch to the 800 Zone from the piston compressor to the V253 valve has a design pressure of 400 bar.g. The piping downstream has a design pressure of 156 bar.g. In case of a malfunction of the compressor or a malfunction of the valve V253, the maximum displacement of the piston compressor must be discharged through the safety valve (SV252).

Table 51 PHA and Safety Concept for zone 200 with SV252 (compressor or valve malfunction at V253 case)

Parameter:	Pressure
Deviation:	“more”.
Cause:	Compressor malfunction or valve malfunction V253
Consequence:	Pressure increase in B06 and B07 and the supply lines to the tanks
Safety Concept:	Protection of the system by the safety valve (SV252)
Notes:	The displacement (GIB24.12-75) must be discharged through the safety valve (SV252), as the buffer tanks (B06) and (B07) have a design pressure of 100 bar g 156 bar g, but the compressor can generate a maximum pressure of 350 bar g. Furthermore, the supply lines to the tanks (B06) and (B07) also have a design pressure of 156 bar g only. These are also protected by the SV252 safety valve.

Table 52 PHA and Safety Concept for zone 200 with SV254 (leakage V254 case)

Parameter:	Pressure
Deviation:	"more"
Cause:	Leakage V254
Consequence:	Pressure rise in the low-pressure supply line to the tank B-K-01 upstream of the valve V254.
Safety Concept:	Protection of the system by the safety valve (SV254)
Notes:	<p>The necessity of the safety valve (SV254) results from the consideration of two scenarios.</p> <ol style="list-style-type: none"> 1. First, the piston compressor (GIB24.12-75) displaces medium through the downstream air treatment module (AKC-0870). The control valve (CV251) and the shut-off valve (V253) are fully open, the shut-off valves (V153) and (V104) are closed so that the buffer tanks (B06) and (B07) cannot be filled. The shut-off valve (V204) on the suction side of the piston compressor is open. The shut-off valve (V254) could be leaking. The leakage flow must be discharged via the safety valve (SV254). 2. Secondly, the buffer tanks (B06) and (B07) may be compressed to 156 bar.g. The shut-off valve (V253) is closed. The shut-off valve (V153) and/or (V104) is not open as intended. The shut-off valve V254 is closed. Due to a possible leakage through V254 a pressure increase can occur. The overpressure causing leakage must be discharged via the safety valve (SV 254).

Table 53 PHA and Safety Concept for zone 200 with SV254 (operating error V254 case)

Parameter:	Pressure
Deviation:	“more”
Cause:	Operator error of V254
Consequence:	Pressure increase in the low-pressure supply line to the tank B-K-01 in the low-pressure part of the system above the design pressure 16 bar.g.
Safety Concept:	Organizational safety measure: V254 is always in the closed position and locked as intended and may only be opened if it is ensured that the pressure before V254 is less than 16 bar g and the 350 bar compressor unit is off-line. The protective measure includes a cross-check of this by at least two qualified persons. This measure is subject to documentation and approval by the person responsible for the operations of the test facility. In addition to the pressure measurement in the control unit, an analog pressure gauge is installed upstream of the valve V254 in order to read the pressure directly on site.
Notes:	<p>The necessity of the safety valve (SV254) results from the consideration of two scenarios.</p> <ol style="list-style-type: none"> 1. First, the piston compressor (GIB24.12-75) pumps the medium through the downstream air treatment module (AKC-0870). The control valve (CV251) and the shut-off valve (V253) are fully open, the shut-off valves (V153) and (V104) are closed so that the buffer tanks (B06) and (B07) cannot be filled. The shut-off valve (V204) on the suction side of the piston compressor is open. The shut-off valve (V254) could not be opened properly as a result of incorrect operation, so that the mass flow from the compressor must be discharged via the safety valve (SV254). 2. Secondly, the buffer tanks (B06) and (B07) may be under a maximum pressure of 156 bar g. The shut-off valve (V253) is closed. The shut-off valve (V153) and/or (V104) is not open as intended. When the shut-off valve (V254) is now opened, the gas flows from the buffer tank (B07) into the low-pressure section of the system.

Annex VIII-C *Flow measurement and pressure regulation unit in zone 300*

The buffer tanks (B06) and (B07) supply the flow measurement and pressure control unit. The design pressure of the regulation unit has a design pressure of 100 bar.g. The flow measurements (FI301, FI302, FI303, FI304) are regulated via the shut-off valves (V304, V305, V306, V307). The subsequent pressure regulation is carried out via the control valves (CV306, CV307, CV308).

The control valves (CV301, CV302, CV306) are controlled by the process control system via the temperature sensor (TI301) and the pressure sensors (PI301, PI304, PI305). The safety-relevant shut-off valve (V310) is also controlled via the process control system.

Table 54 PHA and Safety Concept for zone 300 with SV301 (Leakage CV301 and CV302)

Parameter:	Pressure
Deviation:	“more”
Cause:	Leakage CV301 and CV302
Consequence:	Pressure rise and exceeding of the design pressure of 100 bar g in the supply line downstream.
Safety Concept:	Protection of the system by the safety valve (SV301)
Notes:	The plant must be protected by the safety valve (SV301), as leakage through the pressure-reducing valves (CV301) and (CV302), exceeding the permissible pressure of 100 bar g in control and flow measuring section, cannot be ruled out. In this case, the mass flow must be discharged via the safety valve (SV301) to relieve the pressure.

Table 55 PHA and Safety Concept for zone 300 with BS301 (Malfunction CV301 and CV302)

Parameter:	Pressure
Deviation:	“more”
Cause:	Malfunction CV301 and CV302
Consequence:	Pressure rise and exceeding of the permissible pressure of 100 bar g in the supply line downstream.
Safety Concept:	Protection of the plant by the bursting disc (BS301).
Notes:	The system must be protected by the bursting disc (BS301), as a malfunction or malposition of the pressure-reducing valves (CV301) and (CV302) a leakage cannot be ruled out. This means that the permissible pressure of 100 bar g in the control and flow measuring section can be exceeded. In this case, the volume flow must be discharged via the bursting disc (BS301) to relieve the pressure.

Annex VIII-D *Two-phase rig in zone 400*

The design of this loop is inherently safe since all the parts have a design pressure of 16 bar.g and the only source of over-pressure is from B-K-01 in zone 200. This vessel has a maximum operating pressure of 15 bar and is subject to the PHA and safety concept of zone 200 (see also: Annex VIII-B).

Annex VIII-E *Test vessel unit in zone 1000*

The test vessel (B08) in zone 1000 has a design pressure of 100 bar.g. Test objects shall be tested in their custom made test sections. The respective test section is to be installed in test bench 01-A and test bench 01-B that are downstream of B08. The burst pressure of BS302 is 100 bar.g. The rupture disk has an operating ratio of 80 %. The operator must ensure that the pressure measured in PI1001 installed in B08 is below $0.8 \cdot 100 = 80$ bar.g to avoid activation of BS302 in DN250.

If a test section has a lower design pressure than the burst pressure of bursting disc (BS302) it shall be separately secured on a case by case basis. Restriction orifice plates shall be sized, selected and installed at the intake of the pressure vessel (B08) to limit mass flow rate reaching the test section to avoid very large safety devices while securing the test section against impermissible over-pressure. The combination of limiting orifice and safety device ensures the protection of the test-section with the respective test specimen.

ANNEX IX Operation manual for 150 bar gas rig

Annex IX-A *Testing a fitting in B08 with pressure in B06 & B07 below 15 bar.g.*

Permissible operating conditions			
Medium	air		
		min.	max.
Pressure	P‡ in bar.g	0	+15
Temperature	T‡ in °C	-10	+50

Reference: Figure 27 (PID of the 150 bar)

Operation only by qualified personnel
Wear hearing protection

A000 (Start-up of 150 bar gas rig)

1. Switch on occupancy light for 150 bar gas rig
2. Perform visual inspection on the 150 bar gas rig
3. Check that all ball valves are closed (V203, V204, V254, V253, V153, V154, V104, V105, V102, V103, V151, V152, V304, V305, V306, V307)
4. Check: V310 is closed and error-free
5. Check pressure P in bar.g < max. P‡
at the pressure measuring points PI101; PI102; PI151 & PI152
6. Check pressure P in bar.g > min. P‡
at the pressure measuring points PI 101; PI102; PI151 & PI152
7. Check temperature T in °C < max. T‡
at the temperature points TIz101; TIz103; TIz151 & TIz153
8. Check temperature T in °C > min. T‡
at the temperature points TIz101; TIz103; TIz151 & TIz153
9. Check 15 bar compressor unit is online and error-free (visual inspection)
 - a. PI204>10 bar on B-K-01
 - b. RF-C 0750 is online and error-free
 - c. HL-MSD 550 is online and error-free
 - d. AKC-0550 is online and error-free
 - e. UFS-SP-30N is online and error-free

A001 (Increase pressure in buffer vessel B06 and B07 to P<15 bar.g)

10. Ball valve V104 open
11. Ball valve V153 open
12. Ball valve V254 open
13. Ball valve V203 open
14. Switch on 15 bar compressor unit → Air flows into containers B06 and B07
15. *Monitoring:* TI204 < max. T‡ in °C
16. *Monitoring:* Temperature T in °C < max. T‡
at the temperature points TIz101; TIz103; TIz151 & TIz153

In case of error condition: Press compressor unit emergency stop

17. Switch off 15 bar compressor unit
if PI152 equals target pressure (e.g. max. P‡)
18. Switch off 15 bar compressor unit
19. Check: PI204 > 8 bar (warning: compressed air is required to operate control valves!)

Permissible operating conditions			
Medium	air		
		min.	max.
Pressure	P‡ in bar.g	0	+15
Temperature	T‡ in °C	-10	+50
A004 (Testing of a fitting)			
<p>20. Open ball valve V152 until PI154 and PI155 are at the same pressure.</p> <p>21. Open ball valve V151</p> <p>22. <i>Regulation:</i> Open control valve CV302 until PI301 equals target pressure in bar g</p> <p>23. Open ball valve V305 and/or V306 and/or V307</p> <p>24. Open ball valve V310</p> <p>25. <i>Regulation:</i> Open control valve CV307 open until PI1001 equals target pressure in bar.g</p> <p>26. Air flows from B06 and B07 into B08</p> <p>27. Carry out measurement with test specimen on B08</p> <p>28. <i>Monitoring:</i> Temperature T in °C > min. T‡ at the temperature points TIz101; TIz103; TIz151 & TIz153</p> <p>In case of error condition: Close V310 (Emergency-stop actuation)</p>			
A006 (Shut-down of 150 bar gas rig)			
<p>29. Close control valve CV307</p> <p>30. Close ball valve V310</p> <p>31. Close ball valve V305</p> <p>32. Close control valve CV302</p> <p>33. Close ball valve V151</p> <p>34. Close ball valve V152</p> <p>35. Check: PI204 > 8 bar (warning: compressed air is required to operate control valves!)</p> <p>36. If necessary: Increase pressure until PI204 > 8 bar (see steps 10-19).</p> <p>37. Perform a visual inspection of the 150 bar system.</p> <p>38. Switch off occupancy light for 150 bar system</p> <p>39. Secure all parts of the system for the operational break. and store them under lock and key in the prescribed location.</p> <p>40. Leave and close the hall Geb. 88 and close gates at exit.</p> <p>41. Return key to the operator</p>			

Annex IX-B *Testing a fitting in B08 with pressure in B06 & B07 below 154 bar g.*

Permissible operating conditions			
Medium	air		
		min.	max.
Pressure	P [‡] in bar.g	0	+154
Temperature	T [‡] in °C	-10	+50

Reference: Figure 27 (PID of the 150 bar)

Operation only by qualified personnel
Wear hearing protection

A000 **(Start-up)**

1. Switch on occupancy light for 150 bar gas rig
2. Perform visual inspection on the 150 bar gas rig
3. Check that all ball valves are closed (V203, V204, V254, V253, V153, V154, V104, V105, V102, V103, V151, V152, V304, V305, V306, V307)
4. **Cross-check that V254 is locked closed and document and file this step in documentation in the prescribed form**
5. Check V310 is closed and error-free
6. Check CV302, CV307 and CV308 are closed and error-free
7. Check pressure P in bar.g < max. P[‡]
at the pressure measuring points PI101; PI102; PI151 & PI152
8. Check pressure P in bar.g > min. P[‡]
at the pressure measuring points PI101; PI102; PI151 & PI152
9. Check temperature T in °C < max. T[‡]
at the temperature points TIz101; TIz103; TIz151 & TIz153
10. Check temperature T in °C > min. T[‡]
at the temperature points TIz101; TIz103; TIz151 & TIz153
11. Check 15 bar compressor unit is online and error-free
 - a. RF-C 0750 is online and error-free
 - b. HL-MSD 550 is online and error-free
 - c. AC-0550 is online and error-free
 - d. UFS-SP-30N is online and error-free
12. Check 350 bar compressor unit is online and error-free
 - a. GIB 24.12-75 is online and error-free
 - b. 2x AKC 0870 is online and error-free
 - c. Pump Cooling circuit in operation, pressure in the cooling circuit within permissible range.
13. Documentation of the test before commissioning
In the facility logbook (with name | date | signature)

Permissible operating conditions			
Medium	air		
		min.	max.
Pressure	P‡ in bar.g	0	+154
Temperature	T‡ in °C	-10	+50

A001 (Increase pressure in buffer vessel B06 and B07 to P<15 bar.g)

14. Open ball valve V104
15. Open ball V153
16. Check that CV251 is online
17. Open ball valve V204
18. Open ball valve V203
19. Switch on 15 bar compressor unit
20. Air flows into containers B-K-01 to inlet GIB.24.12-75
21. *Monitoring:* TI204 < max. T‡ in °C
22. *Monitoring:* 10 bar.g < PI204 > 13 bar.g
23. Switch on 350 bar compressor unit
24. Air flows into containers B06 and B07
25. *Monitoring:* Temperature T in °C < max. T‡
at the temperature points TIz101; TIz103; TIz151 & TIz153

In case of error condition: Press compressor unit emergency stop

26. Switch off 350 bar the compressor unit if PI152 equals target pressure.
(e.g. max. P‡)
27. Switch off 15 bar compressor unit

A004 (Testing of a fitting)

28. Open ball valve V152 until PI154 and PI155 at the same pressure. Only then:
29. Open ball valve V151
30. *Regulation:*
Open control valve CV302 whole PI301 < 80 bar.g
31. *Monitoring:* Pressure P in bar g < 80 bar g
at the pressure measuring points PI301 and PI304
32. Open ball valve V305 and/or, V306 and/or V307
33. Open ball valve V310
34. *Regulation:*
Open control valve CV307 or CV308 until PI1001 equals target pressure in bar.g
35. Air flows from B06 and B07 into B08
36. Carry out measurement with test specimen on B08
37. *Monitoring:* Temperature T in °C > min. T‡
at the temperature points TIz101; TIz103; TIz151 & TIz153
38. *Monitoring:* Pressure P in bar g < 80 bar.g
at the pressure measuring points PI315 and PI1001

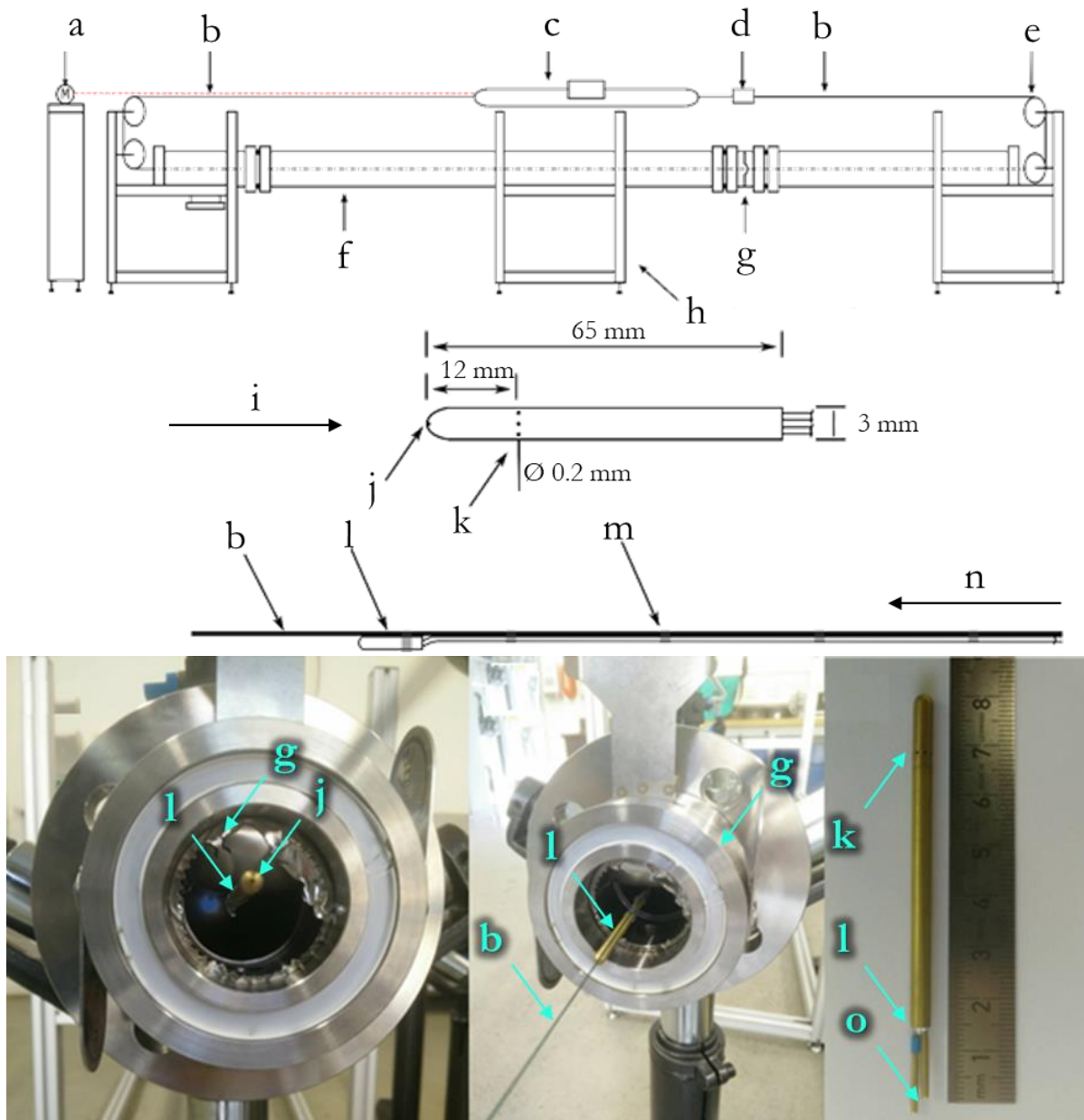
In case of error condition: Close V310 (Emergency-stop actuation)

Permissible operating conditions			
Medium	air		
		min.	max.
Pressure	P‡ in bar.g	0	+154
Temperature	T‡ in °C	-10	+50

A006 (Shut-down of 150 bar gas rig)
*If shutting down for a period longer than 14 days
discharge the pressure in B06 & B07 below 44 bar.g with steps 36 to 38*

39. Close control valve CV307
40. Close ball valve V310
41. Close ball valve V305
42. Close control valve CV302
43. Close ball valve V151
44. Close ball valve V152
45. Check: PI204 > 8 bar (warning: compressed air is required to operate control valves!)
46. If necessary: Increase pressure until PI204 > 8 bar (see steps 10-19).
47. Close ball valve V203
48. Close ball valve V204
49. Close control valve CV251
50. Close ball valve V253
51. Close ball valve V104
52. Close ball valve V153
53. Perform a visual inspection on the 150 bar gas rig
54. Switch off occupancy light for 150 bar gas rig
55. Secure all parts of the system for the operational break.
and store them under lock and key in the prescribed location.
56. Leave and close the hall Geb. 88 and close gates at exit.
57. Return key to the operator

ANNEX X Illustration of arrangement for visualization of flow with experiments



- | | |
|--|--|
| (a) Electric motor | (i) Direction of flow |
| (b) Fishing line | (j) 1 x bore for measurement of dynamic pressure on (l) |
| (c) Lashing strap | (k) 6 x bore for measurement of static pressure on (l) |
| (d) Weighing scale to set tension with c | (l) Pressure probe |
| (e) Return pulley | (m) Heat-shrink tubing |
| (f) Test section | (n) Direction of displacement of (l) |
| (g) Open rupture disk device | (o) Connection to intelligent pressure scanner (see also: Figure 29) |
| (h) Aluminium frame | |

Figure 90: Description of test arrangement to visualize flow with a rupture disk (Schmidt, 2016)

ANNEX XI Model selected for CFD modelling

Below is a listing of the CFD models selected to visualize flow across a rupture disk as presented in Figure 43, Figure 44 and Figure 45 with digitalized rupture disk in Figure 42 (Siemens, STAR-CCM+ V13).

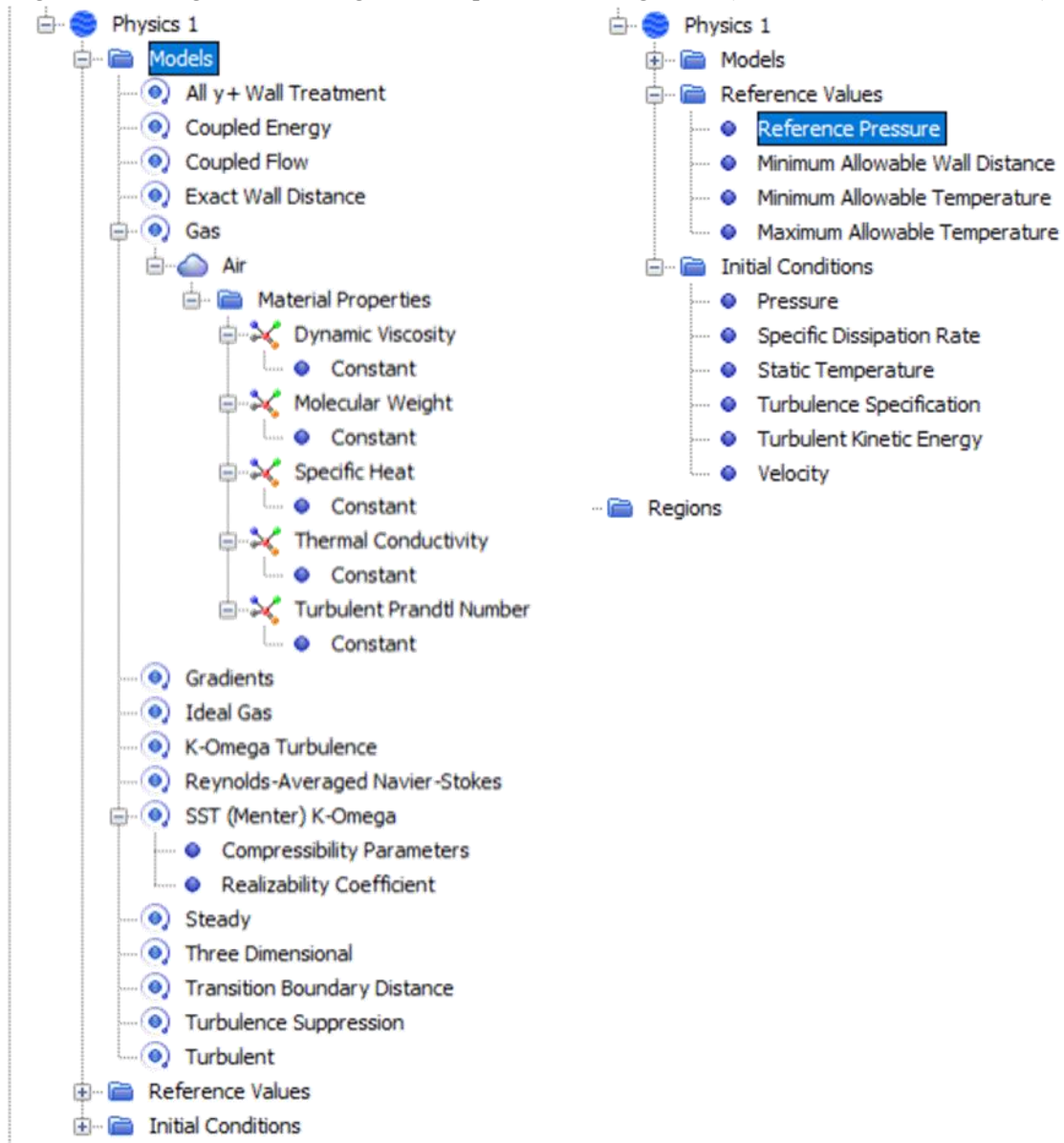

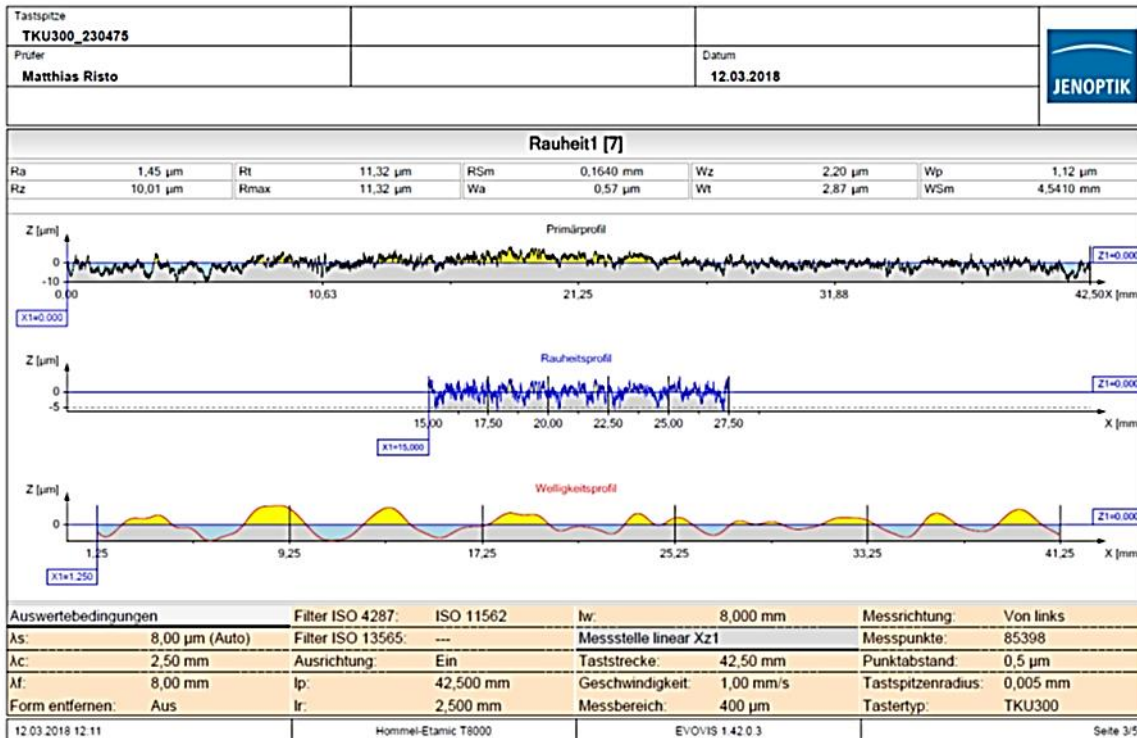
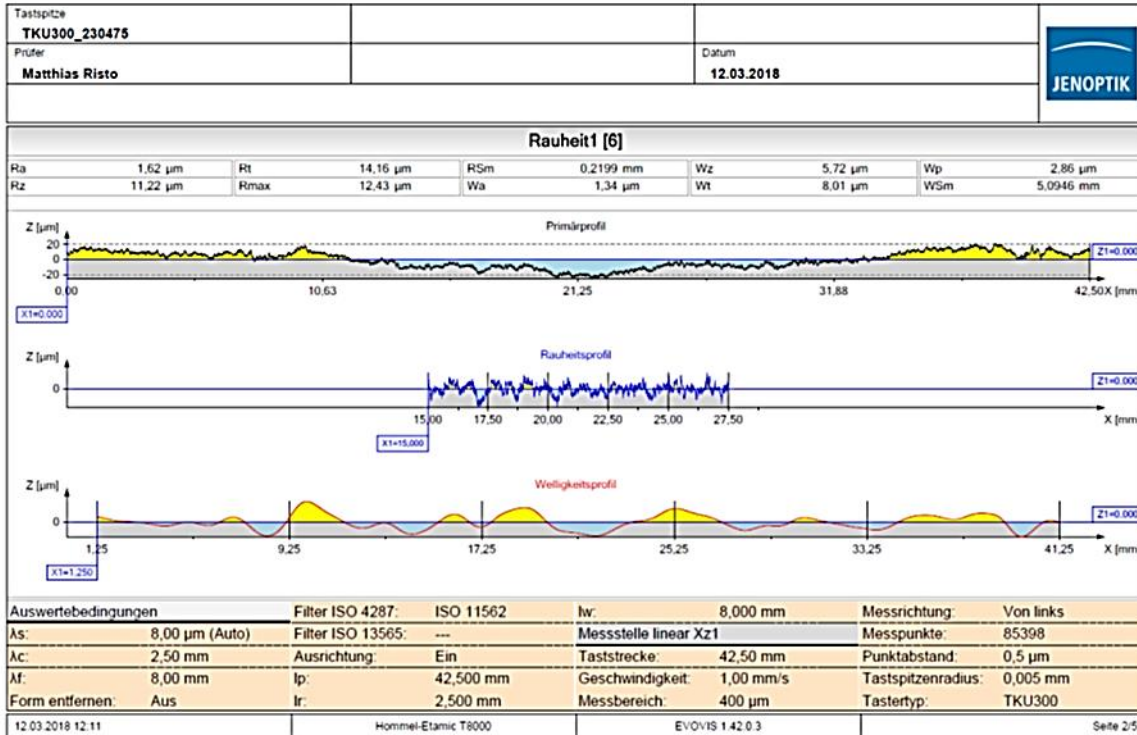


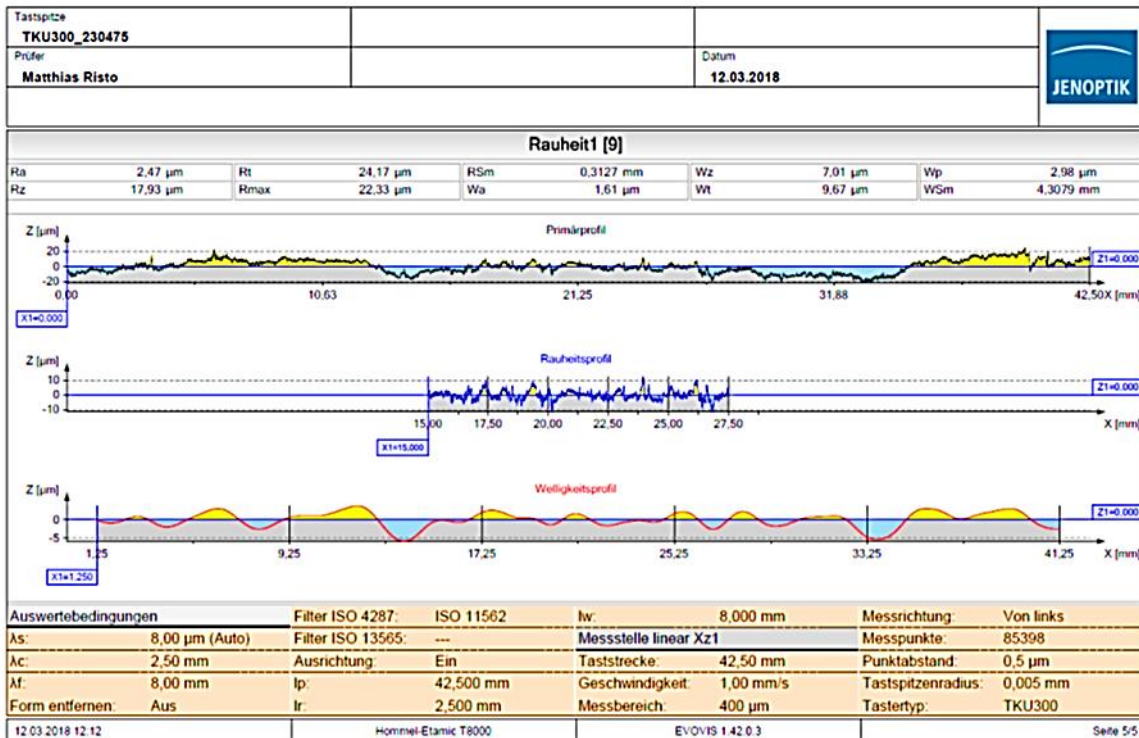
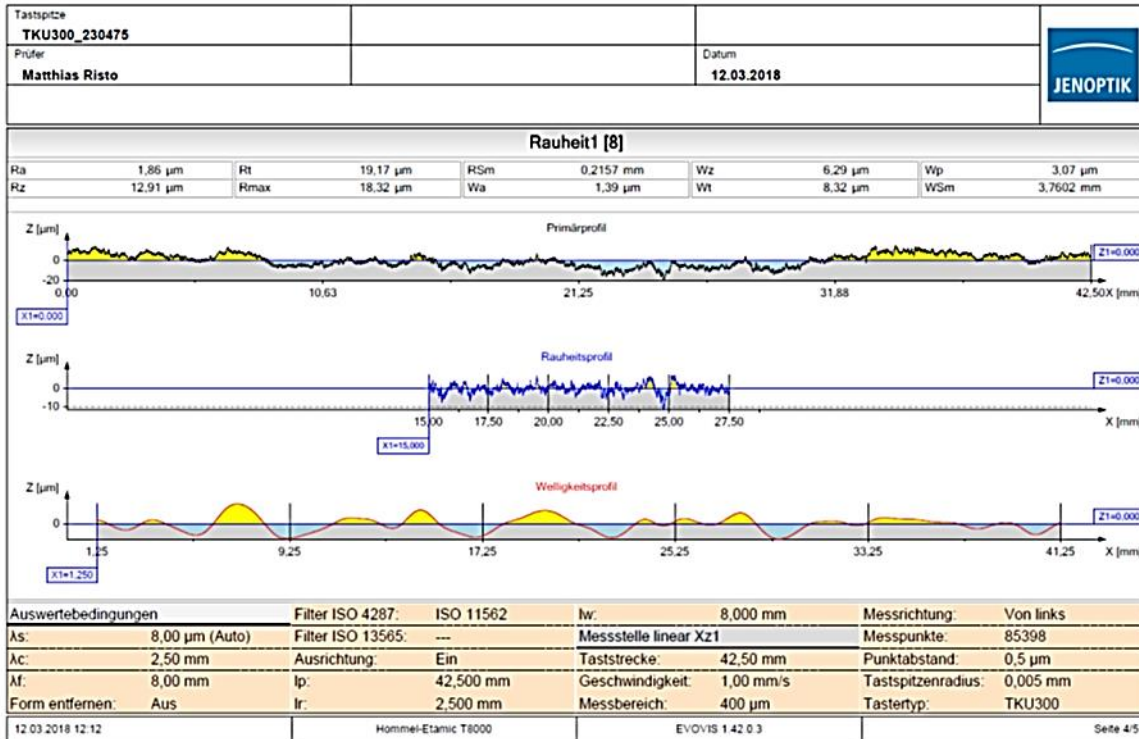
Figure 91 Description of the selected models to visualize flow with CFD's

ANNEX XII DN40 pipe roughness measurement results

The pipe roughness of the pipe used as test section in chapter 4.9. The inner pipe roughness is measured with a Hommel-Etamic T8000 device on the inner surface of the outlet pipe segment. The microscopic surface structure, or the surface roughness, of an object can be measured with the help of the stylus method. In this case, a feed device guides a probe with a wand horizontally over the surface of the object to be measured. The surface profile results from the measured change in height of the wand during the linear movement of the probe. The pipe roughness of the DN40 pipe is found to be $k_s=R_z=13\cdot 10^{-6}$ m.


Tastspitze TKU300_230475											
Prüfer Matthias Risto								Datum 12.03.2018			
Merkmalstabelle											
Nummer	Datum	Rauheit1.Ra	Rauheit1.Rz	Rauheit1.Rt	Rauheit1.Rmax	Rauheit1.RSm	Rauheit1.Wa	Rauheit1.Wz	Rauheit1.Wt	Rauheit1.Wp	Rauheit1.WSm
		µm	µm	µm	µm	mm	µm	µm	µm	µm	mm
1	03/12/2018 12:00:35	1,625	11,217	14,159	12,433	0,21986	1,338	5,715	8,012	2,860	5,09457
2	03/12/2018 12:03:30	1,454	10,005	11,317	11,317	0,16398	0,574	2,199	2,874	1,123	4,54099
3	03/12/2018 12:06:50	1,860	12,907	19,169	18,320	0,21568	1,393	6,287	8,322	3,071	3,76022
4	03/12/2018 12:08:52	2,475	17,929	24,167	22,326	0,31267	1,607	7,015	9,674	2,980	4,30766
Statistik [n=4]											
Name	Einheit	Xq	Range	S	XMax	XMin					
Rauheit1.Ra	µm	1,854	1,021	0,3867	2,475	1,454					
Rauheit1.Rz	µm	13,015	7,924	3,0188	17,929	10,005					
Rauheit1.Rt	µm	17,203	12,850	4,9060	24,167	11,317					
Rauheit1.Rmax	µm	16,099	11,009	4,4726	22,326	11,317					
Rauheit1.RSm	mm	0,228	0,149	0,0536	0,313	0,164					
Rauheit1.Wa	µm	1,228	1,033	0,3907	1,607	0,574					
Rauheit1.Wz	µm	5,304	4,816	1,8509	7,015	2,199					
Rauheit1.Wt	µm	7,221	6,800	2,5861	9,674	2,874					
Rauheit1.Wp	µm	2,509	1,948	0,8034	3,071	1,123					
Rauheit1.WSm	mm	4,426	1,334	0,4789	5,095	3,760					
12.03.2018 12:11		Hommel-Etamic T8000				EVOVIS 1.42.0.3		Seite 1/5			

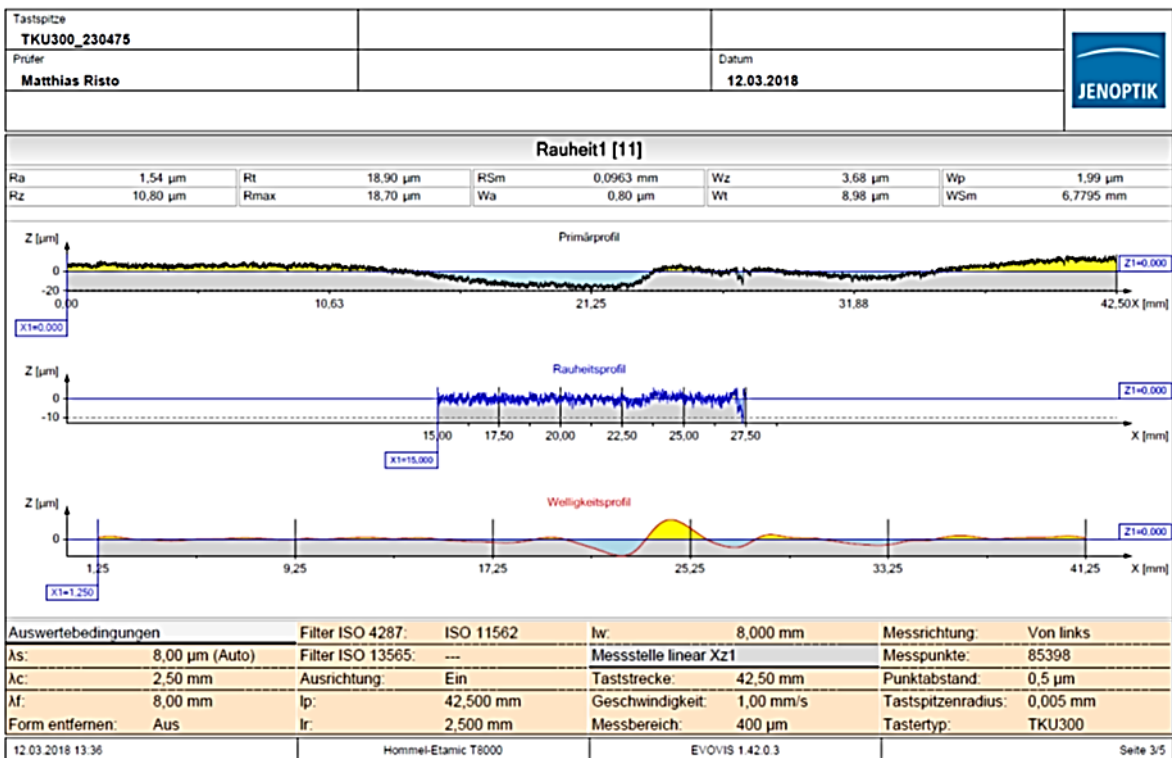
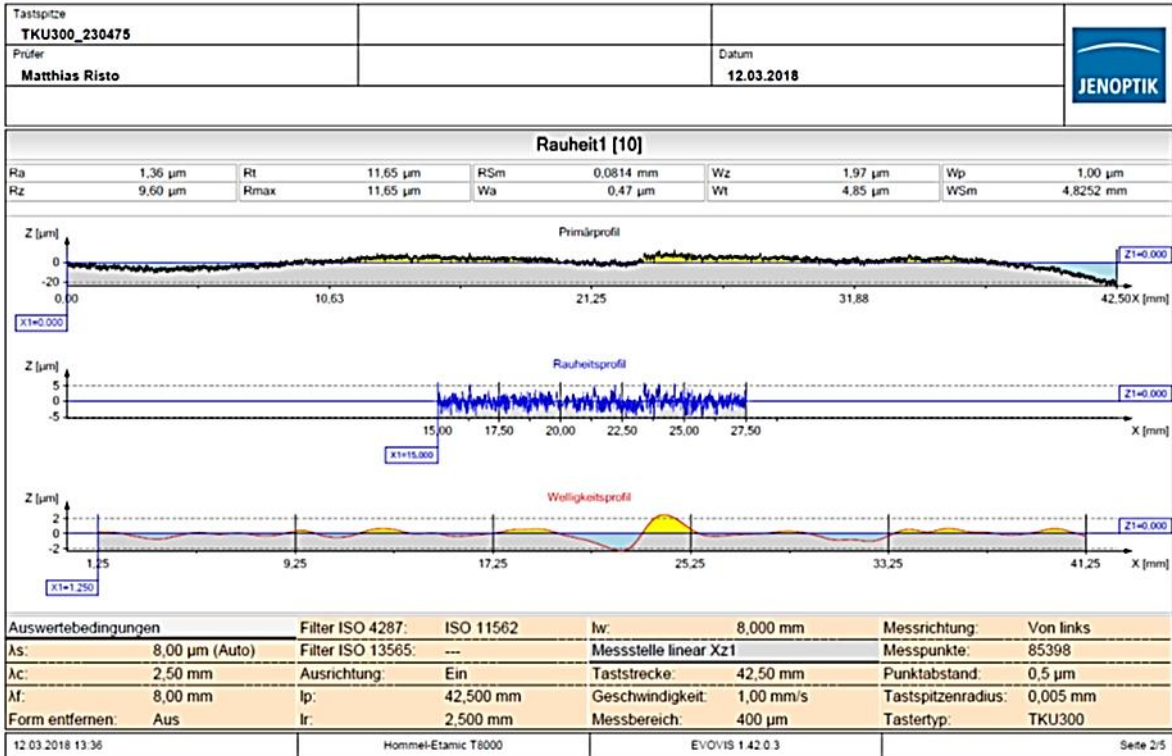


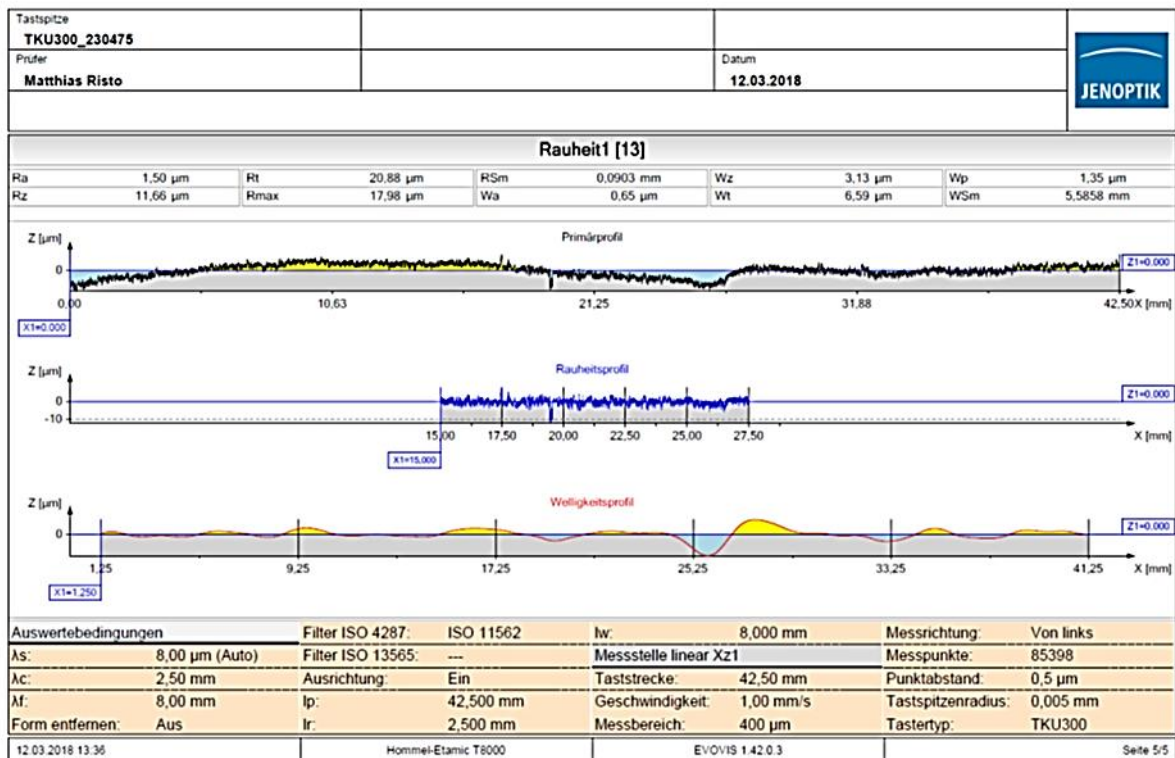
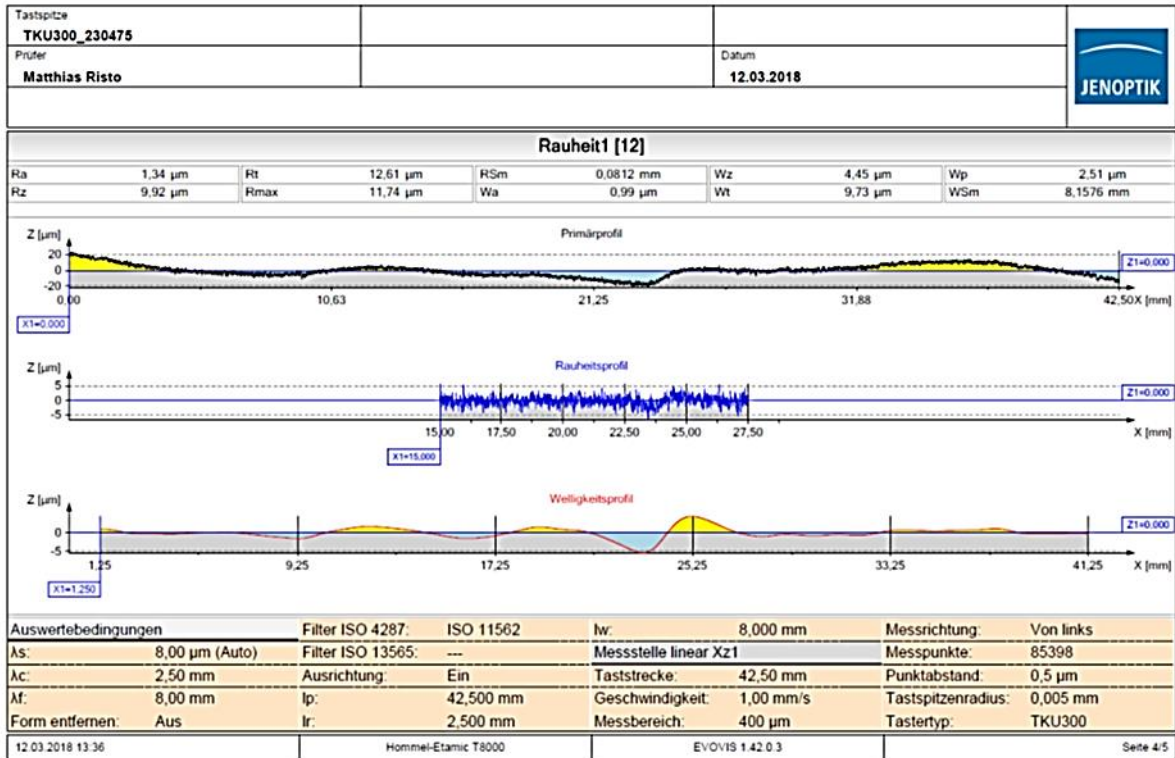


ANNEX XIII DN25 pipe roughness measurement results

The pipe roughness of the pipe used as test section in chapter 4.9. The inner pipe roughness is measured with a Hommel-Etamic T8000 device on the inner surface of the outlet pipe segment. The microscopic surface structure, or the surface roughness, of an object can be measured with the help of the stylus method. In this case, a feed device guides a probe with a wand horizontally over the surface of the object to be measured. The surface profile results from the measured change in height of the wand during the linear movement of the probe. The pipe roughness of the DN40 pipe is found to be $k_s=R_z=11 \cdot 10^{-6}$ m.

Tastspitze TKU300_230475								Datum 12.03.2018				
Prüfer Matthias Risto												
Merkmalstabelle												
Nummer	Datum	Rauheit1.Ra	Rauheit1.Rz	Rauheit1.Rt	Rauheit1.Rmax	Rauheit1.RSm	Rauheit1.Wa	Rauheit1.Wz	Rauheit1.Wt	Rauheit1.Wp	Rauheit1.WSm	
		µm	µm	µm	µm	mm	µm	µm	µm	µm	mm	
1	03/12/2018 13:25:43	1.358	9.597	11.651	11.651	0.08142	0.465	1.967	4.852	1.003	4.82520	
2	03/12/2018 13:28:09	1.539	10.800	18.900	18.703	0.09634	0.799	3.681	8.984	1.969	6.77952	
3	03/12/2018 13:30:47	1.342	9.919	12.615	11.735	0.08125	0.992	4.451	9.731	2.514	8.15757	
4	03/12/2018 13:33:33	1.505	11.659	20.877	17.980	0.09029	0.654	3.127	6.591	1.352	5.58584	
Statistik [n=4]												
Name	Einheit	Xq	Range	S	XMax	XMin						
Rauheit1.Ra	µm	1,436	0,197	0,0870	1,539	1,342						
Rauheit1.Rz	µm	10,494	2,062	0,8041	11,659	9,597						
Rauheit1.Rt	µm	16,011	9,226	3,9550	20,877	11,651						
Rauheit1.Rmax	µm	15,017	7,052	3,3342	18,703	11,651						
Rauheit1.RSm	mm	0,087	0,015	0,0064	0,096	0,081						
Rauheit1.Wa	µm	0,728	0,527	0,1932	0,992	0,465						
Rauheit1.Wz	µm	3,307	2,484	0,9051	4,451	1,967						
Rauheit1.Wt	µm	7,540	4,879	1,9372	9,731	4,852						
Rauheit1.Wp	µm	1,715	1,511	0,5814	2,514	1,003						
Rauheit1.WSm	mm	6,337	3,332	1,2610	8,158	4,825						
12.03.2018 13:36		Hommel-Etamic T8000				EVOVIS 1.42.0.3		Seite 1/5				





ANNEX XIV Calibration certificate for Ethernet Intelligent Pressure NetScanner 9116

The sensors used were selected and calibrated in a DAkkS accredited calibration laboratory. All channels used in this work have uncertainty of measurement better than 3.0 mbar after re-zero in the measurement range. Re-zero, is self-contained feature that sets the pressure of all transducers to the zero before the start of every experiment.

Werkskalibrierschein

**Kalibrierlaboratorium
für die Messgröße Druck**



WK-06451
DMT
GmbH
2016-09

DMT Druckmesstechnik GmbH
Londoner Strasse 25
48455 Bad Bentheim

Datum der Kal.: 02.09.2016
Bearbeiter: Herr Bergfeld
Seite: 1 von 3

Auftraggeber: CSE Center of Safety Excellence gGmbH
Joseph-von-Fraunhofer-Str. 9
D-76327 Pfinztal

Gegenstand: 16 Channel Pneumatik Pressure Scanner

Hersteller: Pressure Systems Inc. USA

Modell / Serien-Nr.: PSI 9116 S/N 5114

Druckbereich: 15,00 psi

zul. Fehler lt. Hersteller: 0,05% v. EW

Auflösung: 0,0001 psi

Bezugsnormal: Mensor CPC 6000
Controller

Kalibrierzeichen: D-K-15191-01-00
T-03620 / 2016-03

Druckmedium: Luft ($\rho = 1,292 \text{ kg/m}^3$ @ 0°C und 1 bar)

Druckbezugsebene: Druckanschlussfläche am KG

Kalibrierort: DMT-Labor

Ort, Datum

Bearbeiter

Stempel

Bad Bentheim, 02.09.2016

DMT
Druck Mess Technik GmbH

Londoner Str. 25, D-48455 Bad Bentheim-Gildehaus
Telefon +49 5924-78377-0; Fax: +49 5924-78377-7
www.dmt-gmbh.com

Werkskalibrierschein

Kalibrierlaboratorium
für die Messgröße Druck



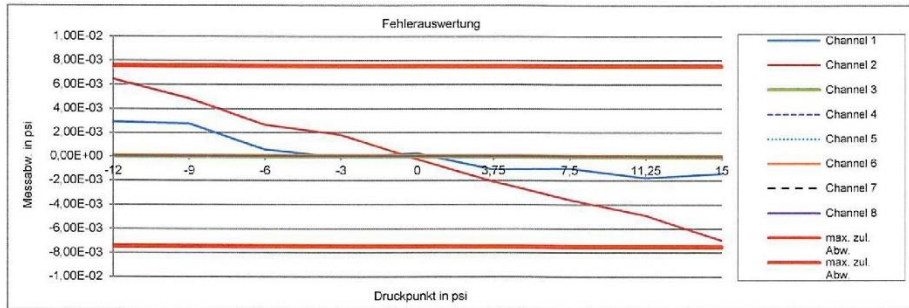
WK-06451
DMT GmbH
2016-09

DMT Druckmesstechnik GmbH
Londoner Strasse 25
48455 Bad Bentheim

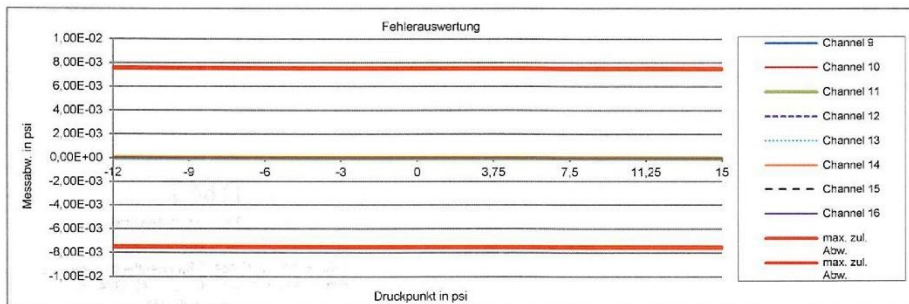
Datum der Kal.: 02.09.2016
Bearbeiter: Herr Bergfeld
Seite: 2 von 3

Messdaten wie vorgefunden:

Druckpunkt in psi	Channel 1 Messabw. in psi	Channel 2 Messabw. in psi	Channel 3 Messabw. in psi	Channel 4 Messabw. in psi	Channel 5 Messabw. in psi	Channel 6 Messabw. in psi	Channel 7 Messabw. in psi	Channel 8 Messabw. in psi
-12	0,0029	0,0064						
-9	0,0028	0,0048						
-6	0,0006	0,0026						
-3	-0,0001	0,0018						
0	0,0003	-0,0002						
3,75	-0,0011	-0,0021						
7,5	-0,0010	-0,0036						
11,25	-0,0018	-0,0049						
15	-0,0014	-0,0070						



Druckpunkt in psi	Channel 9 Messabw. in psi	Channel 10 Messabw. in psi	Channel 11 Messabw. in psi	Channel 12 Messabw. in psi	Channel 13 Messabw. in psi	Channel 14 Messabw. in psi	Channel 15 Messabw. in psi	Channel 16 Messabw. in psi
-12								
-9								
-6								
-3								
0								
3,75								
7,5								
11,25								
15								



Werkskalibrierschein

Kalibrierlaboratorium
für die Messgröße Druck



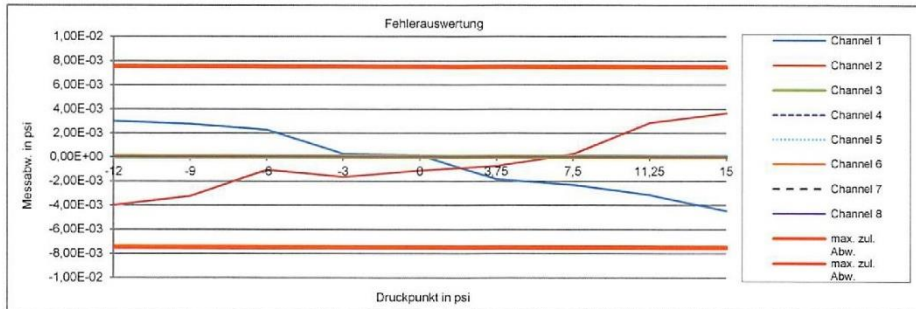
WK-06451
DMT
GmbH
2016-09

DMT Druckmesstechnik GmbH
Londoner Strasse 25
48455 Bad Bentheim

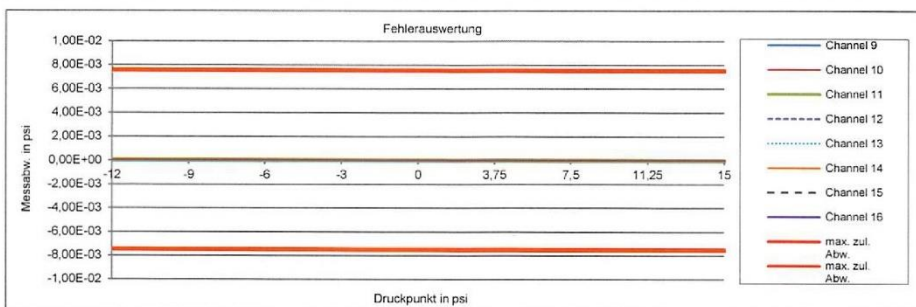
Datum der Kal.: 02.09.2016
Bearbeiter: Herr Bergfeld
Seite: 3 von 3

Messdaten wie verlassen:

Druckpunkt in psi	Channel 1 Messabw. in psi	Channel 2 Messabw. in psi	Channel 3 Messabw. in psi	Channel 4 Messabw. in psi	Channel 5 Messabw. in psi	Channel 6 Messabw. in psi	Channel 7 Messabw. in psi	Channel 8 Messabw. in psi
-12	0,0030	-0,0040						
-9	0,0028	-0,0033						
-6	0,0023	-0,0011						
-3	0,0003	-0,0017						
0	0,0001	-0,0011						
3,75	-0,0018	-0,0007						
7,5	-0,0023	0,0003						
11,25	-0,0031	0,0029						
15	-0,0045	0,0037						



Druckpunkt in psi	Channel 9 Messabw. in psi	Channel 10 Messabw. in psi	Channel 11 Messabw. in psi	Channel 12 Messabw. in psi	Channel 13 Messabw. in psi	Channel 14 Messabw. in psi	Channel 15 Messabw. in psi	Channel 16 Messabw. in psi
-12								
-9								
-6								
-3								
0								
3,75								
7,5								
11,25								
15								



Werkskalibrierschein

Kalibrierlaboratorium
für die Messgröße Druck



WK-06451
DMT
GmbH
2016-09

DMT Druckmesstechnik GmbH
Londoner Strasse 25
48455 Bad Bentheim

Datum der Kal.:
Bearbeiter:
Seite:

02.09.2016
Herr Bergfeld
1 von 3

Auftraggeber: CSE Center of Safety Excellence gGmbH
Joseph-von-Fraunhofer-Str. 9

D-76327 Pfinztal

Gegenstand: 16 Channel Pneumatik Pressure Scanner

Hersteller: Pressure Systems Inc. USA

Modell / Serien-Nr.: PSI 9116 S/N 5114

Druckbereich: 35,00 psi

zul. Fehler lt. Hersteller: 0,05% v. EW

Auflösung: 0,0001 psi

Bezugsnormal: Mensor CPC 6000
Controller

Kalibrierzeichen: D-K-15191-01-00
T-03620 / 2016-03

Druckmedium: Luft ($\rho = 1,292 \text{ kg/m}^3$ @ 0°C und 1 bar)

Druckbezugsebene: Druckanschlussfläche am KG

Kalibrierort: DMT-Labor

Ort, Datum

Bearbeiter

Stempel

Bad Bentheim, 02.09.2016

DMT
Druck Mess Technik GmbH

Londoner Str. 25, D-48455 Bad Bentheim-Gildehaus
Telefon +49 5924-78377-0; Fax: +49 5924-78377-7
www.dmt-gmbh.com

Werkskalibrierschein



Kalibrierlaboratorium
für die Messgröße Druck

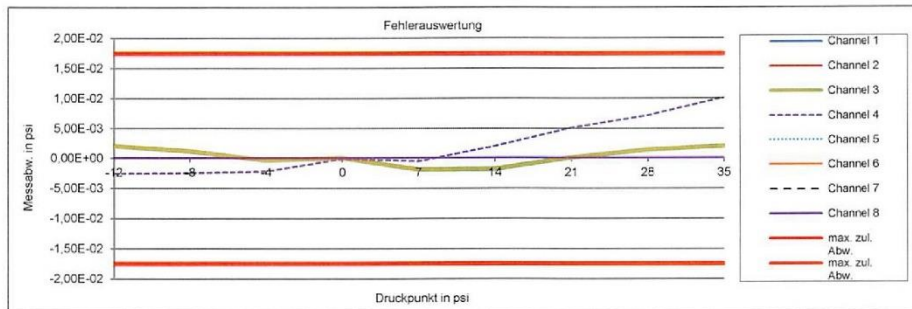
WK-06451
DMT
GmbH
2016-09

DMT Druckmesstechnik GmbH
Londoner Strasse 25
48455 Bad Bentheim

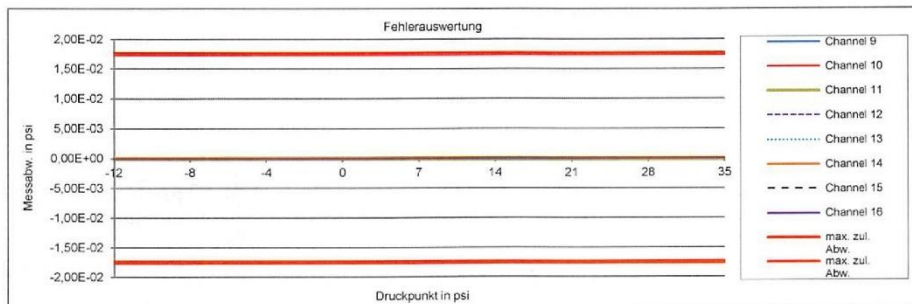
Datum der Kal.: 02.09.2016
Bearbeiter: Herr Bergfeld
Seite: 2 von 3

Messdaten wie vorgefunden:

Druckpunkt in psi	Channel 1 Messabw. in psi	Channel 2 Messabw. in psi	Channel 3 Messabw. in psi	Channel 4 Messabw. in psi	Channel 5 Messabw. in psi	Channel 6 Messabw. in psi	Channel 7 Messabw. in psi	Channel 8 Messabw. in psi
-12			0,0020	-0,0026				
-8			0,0012	-0,0025				
-4			-0,0004	-0,0022				
0			0,0000	-0,0001				
7			-0,0019	-0,0006				
14			-0,0019	0,0020				
21			0,0001	0,0051				
28			0,0014	0,0071				
35			0,0020	0,0101				



Druckpunkt in psi	Channel 9 Messabw. in psi	Channel 10 Messabw. in psi	Channel 11 Messabw. in psi	Channel 12 Messabw. in psi	Channel 13 Messabw. in psi	Channel 14 Messabw. in psi	Channel 15 Messabw. in psi	Channel 16 Messabw. in psi
-12								
-8								
-4								
0								
7								
14								
21								
28								
35								



Werkskalibrierschein



WK-06451
DMT
GmbH
2016-09

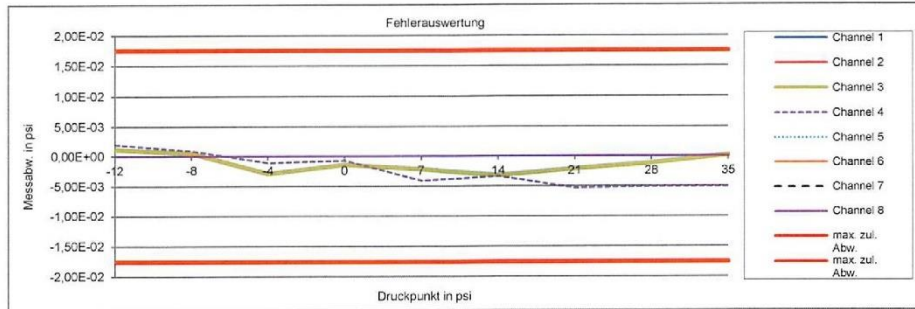
Kalibrierlaboratorium
für die Messgröße Druck

DMT Druckmesstechnik GmbH
Londoner Strasse 25
48455 Bad Bentheim

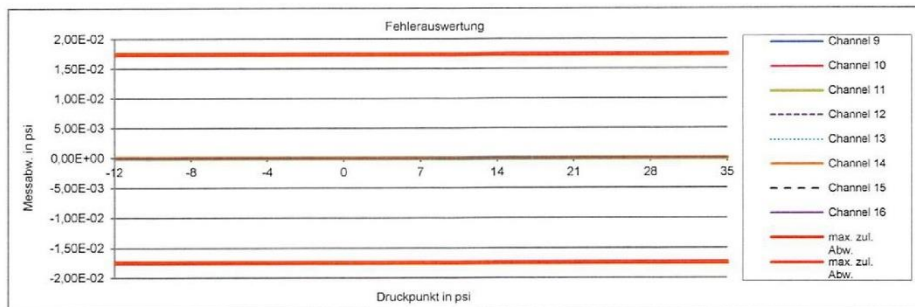
Datum der Kal.: 02.09.2016
Bearbeiter: Herr Bergfeld
Seite: 3 von 3

Messdaten wie verlassen:

Druckpunkt in psi	Channel 1 Messabw. in psi	Channel 2 Messabw. in psi	Channel 3 Messabw. in psi	Channel 4 Messabw. in psi	Channel 5 Messabw. in psi	Channel 6 Messabw. in psi	Channel 7 Messabw. in psi	Channel 8 Messabw. in psi
-12			0,0012	0,0020				
-8			0,0005	0,0009				
-4			-0,0029	-0,0011				
0			-0,0014	-0,0007				
7			-0,0021	-0,0040				
14			-0,0032	-0,0033				
21			-0,0021	-0,0053				
28			-0,0011	-0,0050				
35			0,0002	-0,0050				



Druckpunkt in psi	Channel 9 Messabw. in psi	Channel 10 Messabw. in psi	Channel 11 Messabw. in psi	Channel 12 Messabw. in psi	Channel 13 Messabw. in psi	Channel 14 Messabw. in psi	Channel 15 Messabw. in psi	Channel 16 Messabw. in psi
-12								
-8								
-4								
0								
7								
14								
21								
28								
35								



Werkskalibrierschein

Kalibrierlaboratorium
für die Messgröße Druck



WK-06451
DMT
GmbH
2016-09

DMT Druckmesstechnik GmbH
Londoner Strasse 25
48455 Bad Bentheim

Datum der Kal.: 02.09.2016
Bearbeiter: Herr Bergfeld
Seite: 1 von 2

Auftraggeber: CSE Center of Safety Excellence gGmbH
Joseph-von-Fraunhofer-Str. 9

D-76327 Pfinztal

Gegenstand: 16 Channel Pneumatik Pressure Scanner

Hersteller: Pressure Systems Inc. USA

Modell / Serien-Nr.: PSI 9116 S/N 5114

Druckbereich: 45,00 psi

zul. Fehler lt. Hersteller: 0,05% v. EW

Auflösung: 0,0001 psi

Bezugsnormal: Mensor CPC 6000
Controller

Kalibrierzeichen: D-K-15191-01-00
T-03620 / 2016-03

Druckmedium: Luft ($\rho = 1,292 \text{ kg/m}^3$ @ 0°C und 1 bar)

Druckbezugsebene: Druckanschlussfläche am KG

Kalibrierort: DMT-Labor

Ort, Datum

Bearbeiter

Stempel

Bad Bentheim, 02.09.2016

DMT
Druck Mess Technik GmbH

Londoner Str. 25, D-48455 Bad Bentheim-Gildehaus
Telefon +49 5924-78377-0; Fax: +49 5924-78377-7
www.dmt-gmbh.com

Werkskalibrierschein



Kalibrierlaboratorium
für die Messgröße Druck

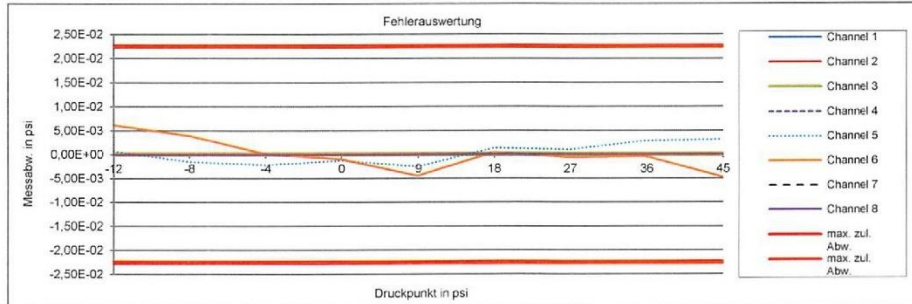
WK-06451
DMT
GmbH
2016-09

DMT Druckmesstechnik GmbH
Londoner Strasse 25
48455 Bad Bentheim

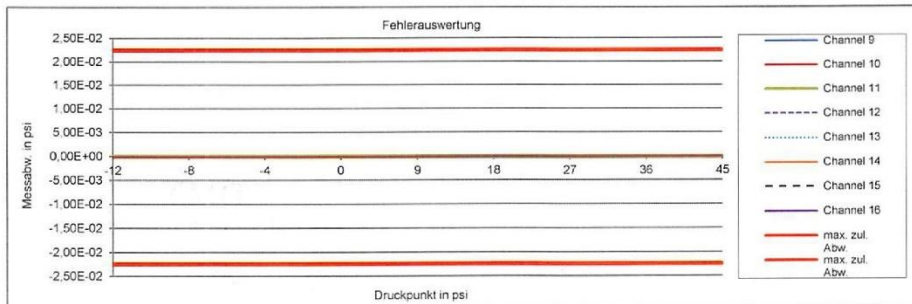
Datum der Kal.: 02.09.2016
Bearbeiter: Herr Bergfeld
Seite: 2 von 2

Messdaten wie verlassen:

Druckpunkt in psi	Channel 1 Messabw. in psi	Channel 2 Messabw. in psi	Channel 3 Messabw. in psi	Channel 4 Messabw. in psi	Channel 5 Messabw. in psi	Channel 6 Messabw. in psi	Channel 7 Messabw. in psi	Channel 8 Messabw. in psi
-12					0,0007	0,0061		
-8					-0,0015	0,0039		
-4					-0,0022	0,0002		
0					-0,0013	-0,0010		
9					-0,0025	-0,0045		
18					0,0013	0,0004		
27					0,0010	-0,0006		
36					0,0029	-0,0004		
45					0,0031	-0,0047		



Druckpunkt in psi	Channel 9 Messabw. in psi	Channel 10 Messabw. in psi	Channel 11 Messabw. in psi	Channel 12 Messabw. in psi	Channel 13 Messabw. in psi	Channel 14 Messabw. in psi	Channel 15 Messabw. in psi	Channel 16 Messabw. in psi
-12								
-8								
-4								
0								
9								
18								
27								
36								
45								



Werkskalibrierschein

Kalibrierlaboratorium
für die Messgröße Druck



WK-06451
DMT
GmbH
2016-09

DMT Druckmesstechnik GmbH
Londoner Strasse 25
48455 Bad Bentheim

Datum der Kal.: 01.09.2016
Bearbeiter: Herr Bergfeld
Seite: 1 von 3

Auftraggeber: CSE Center of Safety Excellence gGmbH
Joseph-von-Fraunhofer-Str. 9

D-76327 Pfinztal

Gegenstand: 16 Channel Pneumatik Pressure Scanner

Hersteller: Pressure Systems Inc. USA

Modell / Serien-Nr.: PSI 9116 S/N 5114

Druckbereich: 100,00 psi

zul. Fehler lt. Hersteller: 0,05% v. EW

Auflösung: 0,001 psi

Bezugsnormal: Mensor CPC 6000
Controller

Kalibrierzeichen: D-K-15191-01-00
T-03622 / 2016-03

Druckmedium: Luft ($\rho = 1,292 \text{ kg/m}^3$ @ 0°C und 1 bar)

Druckbezugsebene: Druckanschlussfläche am KG

Kalibrierort: DMT-Labor

Ort, Datum

Bearbeiter

Stempel

Bad Bentheim, 01.09.2016

DMT
Druck Mess Technik GmbH

Londoner Str. 25, D-48455 Bad Bentheim-Gildehaus
Telefon +49 5924-78377-0; Fax: +49 5924-78377-7
www.dmt-gmbh.com

Werkskalibrierschein

Kalibrierlaboratorium
für die Messgröße Druck



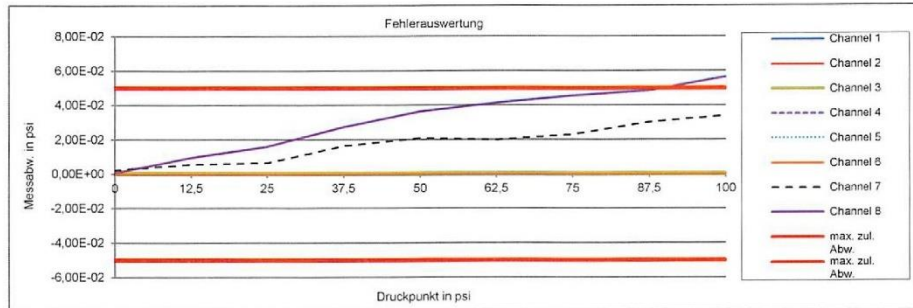
WK-06451
DMT
GmbH
2016-09

DMT Druckmesstechnik GmbH
Londoner Strasse 25
48455 Bad Bentheim

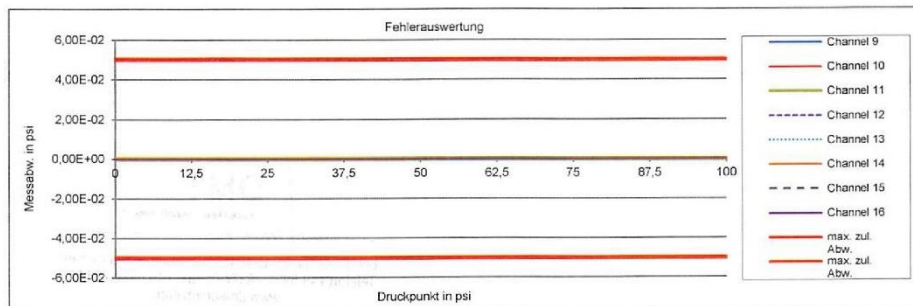
Datum der Kal.: 01.09.2016
Bearbeiter: Herr Bergfeld
Seite: 2 von 3

Messdaten wie vorgefunden:

Druckpunkt in psi	Channel 1 Messabw. in psi	Channel 2 Messabw. in psi	Channel 3 Messabw. in psi	Channel 4 Messabw. in psi	Channel 5 Messabw. in psi	Channel 6 Messabw. in psi	Channel 7 Messabw. in psi	Channel 8 Messabw. in psi
0							0,002	0,000
12,5							0,006	0,010
25							0,007	0,016
37,5							0,017	0,027
50							0,021	0,036
62,5							0,020	0,041
75							0,023	0,045
87,5							0,030	0,048
100							0,034	0,056



Druckpunkt in psi	Channel 9 Messabw. in psi	Channel 10 Messabw. in psi	Channel 11 Messabw. in psi	Channel 12 Messabw. in psi	Channel 13 Messabw. in psi	Channel 14 Messabw. in psi	Channel 15 Messabw. in psi	Channel 16 Messabw. in psi
0								
12,5								
25								
37,5								
50								
62,5								
75								
87,5								
100								



Werkskalibrierschein



WK-06451
DMT
GmbH
2016-09

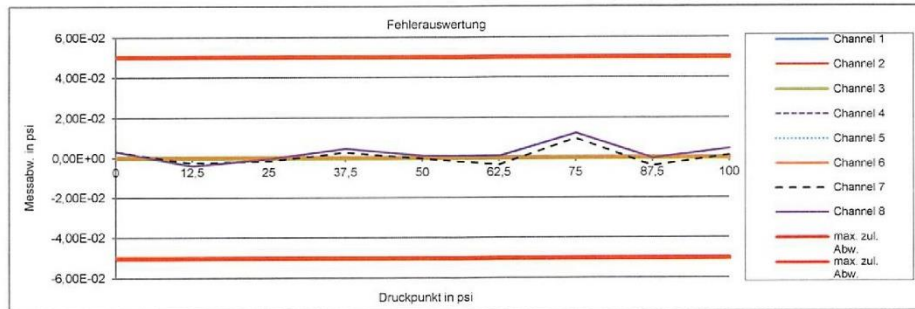
Kalibrierlaboratorium
für die Messgröße Druck

DMT Druckmesstechnik GmbH
Londoner Strasse 25
48455 Bad Bentheim

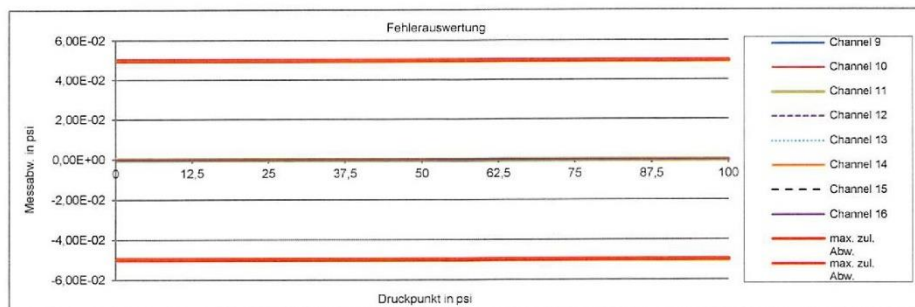
Datum der Kal.: 01.09.2016
Bearbeiter: Herr Bergfeld
Seite: 3 von 3

Messdaten wie verlassen:

Druckpunkt in psi	Channel 1 Messabw. in psi	Channel 2 Messabw. in psi	Channel 3 Messabw. in psi	Channel 4 Messabw. in psi	Channel 5 Messabw. in psi	Channel 6 Messabw. in psi	Channel 7 Messabw. in psi	Channel 8 Messabw. in psi
0							0,003	0,003
12,5							-0,002	-0,004
25							-0,002	0,000
37,5							0,003	0,005
50							0,000	0,001
62,5							-0,003	0,001
75							0,010	0,012
87,5							-0,004	0,000
100							0,001	0,004



Druckpunkt in psi	Channel 9 Messabw. in psi	Channel 10 Messabw. in psi	Channel 11 Messabw. in psi	Channel 12 Messabw. in psi	Channel 13 Messabw. in psi	Channel 14 Messabw. in psi	Channel 15 Messabw. in psi	Channel 16 Messabw. in psi
0								
12,5								
25								
37,5								
50								
62,5								
75								
87,5								
100								



Werkskalibrierschein

Kalibrierlaboratorium
für die Messgröße Druck



WK-06451
DMT
GmbH
2016-09

DMT Druckmesstechnik GmbH
Londoner Strasse 25
48455 Bad Bentheim

Datum der Kal.: 01.09.2016
Bearbeiter: Herr Bergfeld
Seite: 1 von 3

Auftraggeber: CSE Center of Safety Excellence gGmbH
Joseph-von-Fraunhofer-Str. 9
D-76327 Pfinztal

Gegenstand: 16 Channel Pneumatik Pressure Scanner

Hersteller: Pressure Systems Inc. USA

Modell / Serien-Nr.: PSI 9116 S/N 5114

Druckbereich: 750,00 psi

zul. Fehler lt. Hersteller: 0,05% v. EW

Auflösung: 0,001 psi

Bezugsnormal: Mensor CPC 6000
Controller

Kalibrierzeichen: D-K-15191-01-00
T-03578 / 2016-02

Druckmedium: Luft ($\rho = 1,292 \text{ kg/m}^3$ @ 0°C und 1 bar)

Druckbezugsebene: Druckanschlussfläche am KG

Kalibrierort: DMT-Labor

Ort, Datum

Bearbeiter

Stempel

Bad Bentheim, 01.09.2016

DMT
Druck Mess Technik GmbH

Londoner Str. 25, D-48455 Bad Bentheim-Gildehaus
Telefon +49 5924-78377-0; Fax: +49 5924-78377-7
www.dmt-gmbh.com

Werkskalibrierschein

Kalibrierlaboratorium
für die Messgröße Druck



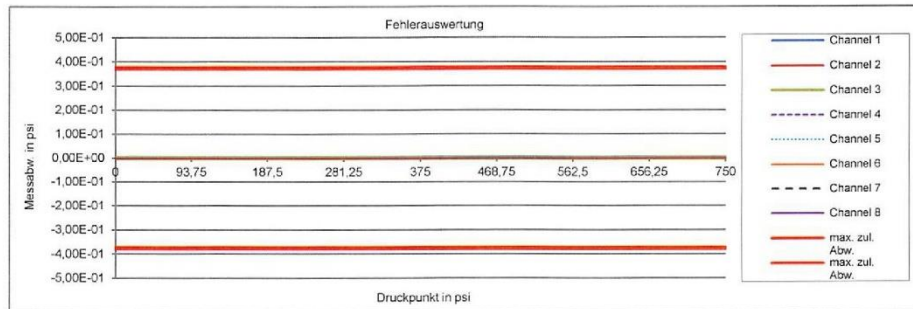
WK-06451
DMT
GmbH
2016-09

DMT Druckmesstechnik GmbH
Londoner Strasse 25
48455 Bad Bentheim

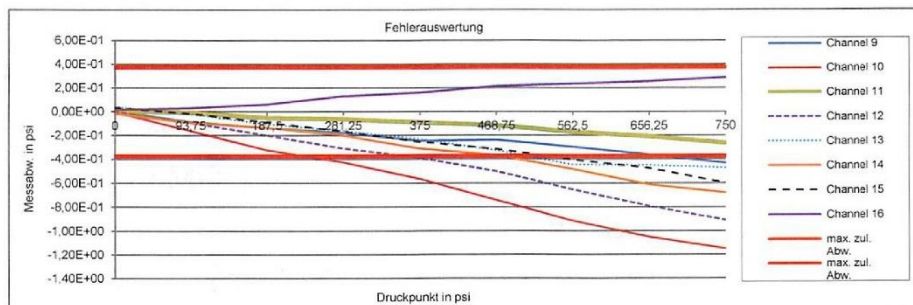
Datum der Kal.: 01.09.2016
Bearbeiter: Herr Bergfeld
Seite: 2 von 3

Messdaten wie vorgefunden:

Druckpunkt in psi	Channel 1 Messabw. in psi	Channel 2 Messabw. in psi	Channel 3 Messabw. in psi	Channel 4 Messabw. in psi	Channel 5 Messabw. in psi	Channel 6 Messabw. in psi	Channel 7 Messabw. in psi	Channel 8 Messabw. in psi
0								
93,75								
187,5								
281,25								
375								
468,75								
562,5								
656,25								
750								



Druckpunkt in psi	Channel 9 Messabw. in psi	Channel 10 Messabw. in psi	Channel 11 Messabw. in psi	Channel 12 Messabw. in psi	Channel 13 Messabw. in psi	Channel 14 Messabw. in psi	Channel 15 Messabw. in psi	Channel 16 Messabw. in psi
0	0,004	0,000	0,004	0,003	0,039	-0,016	0,035	0,017
93,75	-0,085	-0,159	-0,010	-0,093	-0,020	-0,093	-0,018	0,033
187,5	-0,135	-0,322	-0,053	-0,198	-0,107	-0,132	-0,089	0,063
281,25	-0,178	-0,424	-0,063	-0,309	-0,161	-0,199	-0,166	0,131
375	-0,246	-0,564	-0,093	-0,390	-0,232	-0,309	-0,255	0,161
468,75	-0,237	-0,741	-0,117	-0,503	-0,327	-0,366	-0,315	0,213
562,5	-0,298	-0,913	-0,171	-0,653	-0,447	-0,483	-0,405	0,234
656,25	-0,363	-1,049	-0,207	-0,791	-0,451	-0,613	-0,477	0,255
750	-0,434	-1,149	-0,265	-0,909	-0,474	-0,679	-0,601	0,287



Werkskalibrierschein



WK-06451
DMT
GmbH
2016-09

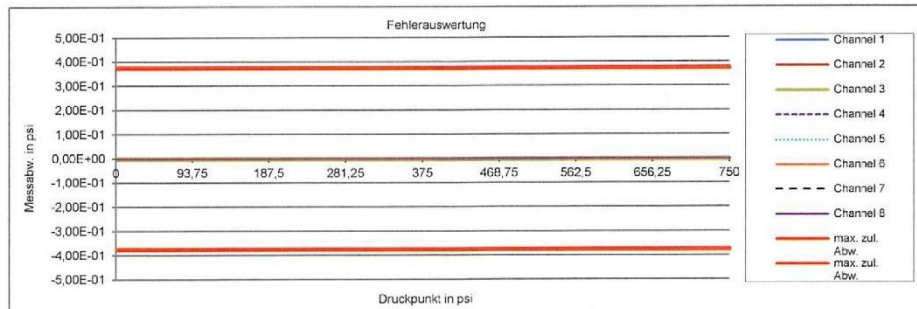
Kalibrierlaboratorium
für die Messgröße Druck

DMT Druckmesstechnik GmbH
Londoner Strasse 25
48455 Bad Bentheim

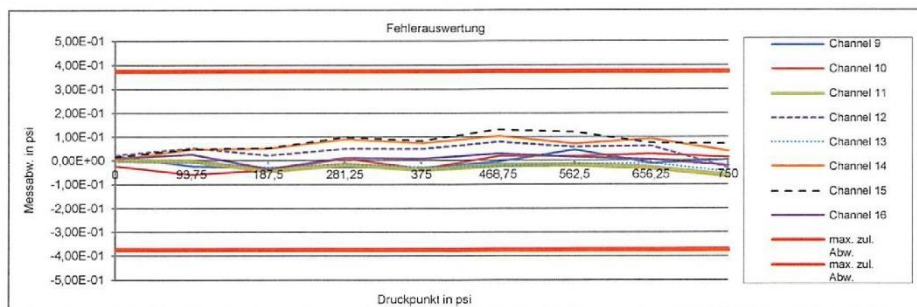
Datum der Kal.: 01.09.2016
Bearbeiter: Herr Bergfeld
Seite: 3 von 3

Messdaten wie verlassen:

Druckpunkt in psi	Channel 1 Messabw. in psi	Channel 2 Messabw. in psi	Channel 3 Messabw. in psi	Channel 4 Messabw. in psi	Channel 5 Messabw. in psi	Channel 6 Messabw. in psi	Channel 7 Messabw. in psi	Channel 8 Messabw. in psi
0								
93,75								
187,5								
281,25								
375								
468,75								
562,5								
656,25								
750								



Druckpunkt in psi	Channel 9 Messabw. in psi	Channel 10 Messabw. in psi	Channel 11 Messabw. in psi	Channel 12 Messabw. in psi	Channel 13 Messabw. in psi	Channel 14 Messabw. in psi	Channel 15 Messabw. in psi	Channel 16 Messabw. in psi
0	0,017	-0,025	0,001	0,021	-0,003	0,002	0,016	0,008
93,75	-0,025	-0,061	-0,003	0,053	-0,008	0,046	0,049	0,025
187,5	-0,033	-0,041	-0,045	0,020	-0,029	0,050	0,053	-0,037
281,25	-0,028	0,008	-0,018	0,049	-0,016	0,088	0,099	0,011
375	-0,032	-0,038	-0,039	0,048	-0,029	0,073	0,084	0,006
468,75	-0,007	0,017	-0,022	0,078	-0,025	0,102	0,130	0,027
562,5	0,044	0,016	-0,019	0,056	-0,017	0,070	0,121	0,014
656,25	-0,014	0,027	-0,032	0,061	-0,013	0,091	0,075	0,003
750	0,002	0,012	-0,065	-0,033	-0,049	0,038	0,071	-0,023



ANNEX XV Calibration certificate for Mensor absolute pressure sensor

The sensor was selected and calibrated in a DAkkS accredited calibration laboratory. All channels used in this work have uncertainty of measurement better than 3 mbar after re-zero; this is a self-contained feature that sets the pressure of all transducers to the zero before the start of every experiment

Werkskalibrierschein					
Kalibrierlaboratorium für die Messgröße Druck		<table border="1" style="border-collapse: collapse;"> <tr><td style="padding: 2px;">WK-06449</td></tr> <tr><td style="padding: 2px;">DMT GmbH</td></tr> <tr><td style="padding: 2px;">2016-08</td></tr> </table>	WK-06449	DMT GmbH	2016-08
WK-06449					
DMT GmbH					
2016-08					
DMT Druckmesstechnik GmbH Londoner Strasse 25 48455 Bad Bentheim	Datum der Kal.: Bearbeiter: Seite:	30.08.2016 H. Plescher 1 von 5			
Auftraggeber: <i>Customer</i>	CSE Center of Safety Excellence gGmbH Joseph-von-Fraunhofer-Str. 9 D-76327 Pfinztal				
Auftragsnummer: <i>Order No.</i>	-				
Gegenstand: <i>Object</i>	Digitales Druckmessgerät				
Hersteller: <i>Manufacturer</i>	Mensor, USA				
Typ: <i>Type</i>	Modell 6100				
Fabrikat / Serien-Nr.: <i>Serial number</i>	591985				
Ident-Nr.: <i>Ident number</i>	-				
<p>Dieser Kalibrierschein darf nur vollständig und unverändert weiterverbreitet werden. Auszüge oder Änderungen bedürfen der Genehmigung des ausstellenden Kalibrierlaboratoriums. Kalibrierscheine ohne Unterschrift haben keine Gültigkeit.</p> <p><i>This calibration certificate may not be reproduced other than in full except with the permission of the issuing laboratory. Calibration certificates without signature are not valid.</i></p>					
Ort, Datum <i>Location, Date</i>	Bearbeiter <i>Person in charge</i>	Stempel <i>Seal</i>			
Bad Bentheim, 30.08.2016					

Werkskalibrierschein

Kalibrierlaboratorium
für die Messgröße Druck



WK-06449
DMT GmbH
2016-08

DMT Druckmesstechnik GmbH
Londoner Strasse 25
48455 Bad Bentheim

Datum der Kal.: 30.08.2016
Bearbeiter: H. Plescher
Seite: 2 von 5

1. Kalibriergegenstand

Kalibriergegenstand : Mensor Modell 6100, digitales Druckmessgerät
Typ : Modell 6100
Seriennummer : 591985
Nenndruckbereich : 800,0 mbar bis 1150,0 mbar absolut

Abweichungsgrenzbetrag : 0,01% v.M.
Auflösung : 0,001 mbar

2. Bezugsnormal

Hersteller : DH Budenberg BN12
Modell : DPG 10A
Seriennummer : 14120
Messsystem : Druckkopf 610 14151
Erw. Messunsicherheit U : $1,5 \cdot 10^{-5} \cdot p_e + 0,8 \text{ Pa}$
Kalibrierzeichen : PTB 30064/14

3. Kalibrierverfahren

Generell erfolgt ein Vergleich der durch das verwendete Bezugsnormal bereitgestellten Werte mit den durch die Kalibriergeräte dargestellten Werte.

4. Messbedingungen

Kalibrierort : Bad Bentheim, DMT Druckmesstechnik GmbH, DAkKS-Labor
Lokale Fallbeschleunigung g_L : $(9,812783 \pm 3 \cdot 10^{-6}) \text{ m/s}^2$
Druckübertragungsmittel : Luft
Lage des Kalibriergegenstandes (Achse Druckanschluss) : Horizontal
Druckbezugsebene : Druckanschluss Dichtfläche Kalibriergegenstand

5. Umgebungsbedingungen

Temperatur : $(20,3 \pm 1)^\circ\text{C}$ bis $(20,3 \pm 1)^\circ\text{C}$
Rel. Luftfeuchte : $(45 \pm 20)\%$
Luftdruck : $(1015,7 \pm 0,1) \text{ hPa}$ bis $(1015,9 \pm 0,1) \text{ hPa}$

Werkskalibrierschein

Kalibrierlaboratorium
für die Messgröße Druck



WK-06449

DMT
GmbH

2016-08

DMT Druckmesstechnik GmbH
Londoner Strasse 25
48455 Bad Bentheim

Datum der Kal.: 30.08.2016
Bearbeiter: H. Plescher
Seite: 3 von 5

6. Messergebnisse

Tabelle 1: Eingangskennlinie für den Absolutdruckbereich von 800,0 mbar bis 1150,0 mbar

Druck in Höhe des Kalibrier- gegenstandes p_{Normal}	Ablesung am Kalibriergegenstand		Abweichungs- grenzbetrag + / -	Messabweichung	
	M1	M2		M1 - p_{Normal}	M2 - p_{Normal}
[mbar]	[mbar]	[mbar]	[mbar]	[mbar]	[mbar]
800,0743	799,6630	799,6720	0,0800	-0,4113	-0,4023
858,4231	858,0390	858,0510	0,0858	-0,3841	-0,3721
916,7635	916,4140	916,4260	0,0917	-0,3495	-0,3375
975,0838	974,7630	974,7800	0,0975	-0,3208	-0,3038
1033,4085	1033,1300	1033,1390	0,1033	-0,2785	-0,2695
1091,7527	1091,5170	1091,5220	0,1092	-0,2357	-0,2307
1150,0850	1149,9010	1149,8980	0,1150	-0,1840	-0,1870

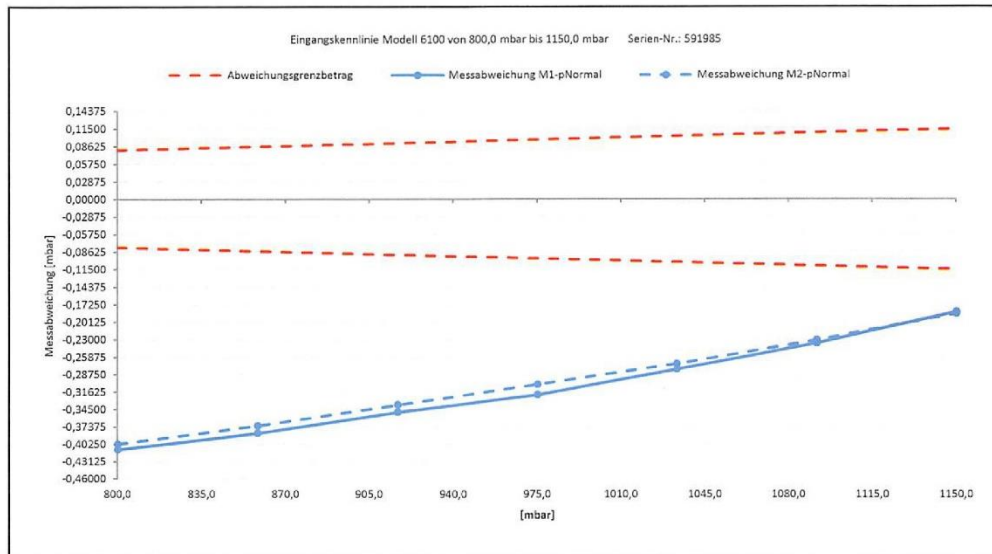


Abbildung 1

Die Messergebnisse aus Tabelle 1 und Abbildung 1 dokumentieren den Ist-Zustand des Kalibriergegenstandes im Absolutdruckbereich von 800,0 mbar bis 1150,0 mbar vor der Justage. Das Gerät wurde justiert.

Werkskalibrierschein

Kalibrierlaboratorium
für die Messgröße Druck



WK-06449

DMT
GmbH

2016-08

DMT Druckmesstechnik GmbH
Londoner Strasse 25
48455 Bad Bentheim

Datum der Kal.: 30.08.2016
Bearbeiter: H. Plescher
Seite: 4 von 5

Tabelle 2: Messergebnisse für den Absolutdruckbereich von 800,0 mbar bis 1150,0 mbar

Druck in Höhe des Kalibrier- gegenstandes p_{Normal}	Ablesung am Kalibriergegenstand		Abweichungs- grenzbetrag + / -	Messabweichung	
	M1	M2		M1 - p_{Normal}	M2 - p_{Normal}
[mbar]	[mbar]	[mbar]	[mbar]	[mbar]	[mbar]
800,0950	800,1110	800,1080	0,0800	0,0160	0,0130
835,0867	835,1050	835,0940	0,0835	0,0183	0,0073
870,0835	870,0950	870,0930	0,0870	0,0115	0,0095
905,0912	905,0970	905,0980	0,0905	0,0058	0,0068
940,0800	940,0800	940,0880	0,0940	0,0000	0,0080
975,0860	975,0790	975,0880	0,0975	-0,0070	0,0020
1010,0741	1010,0710	1010,0780	0,1010	-0,0031	0,0039
1045,0915	1045,0890	1045,0920	0,1045	-0,0025	0,0005
1080,0809	1080,0800	1080,0840	0,1080	-0,0009	0,0031
1115,0786	1115,0840	1115,0880	0,1115	0,0054	0,0094
1150,0867	1150,1000	1150,0940	0,1150	0,0133	0,0073

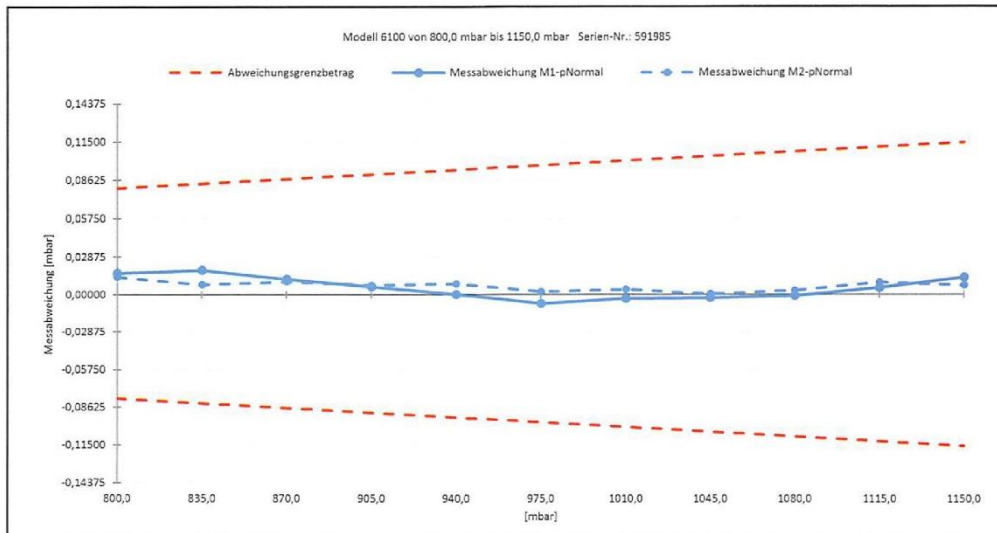


Abbildung 2

Werkskalibrierschein

Kalibrierlaboratorium
für die Messgröße Druck



WK-06449
DMT GmbH
2016-08

DMT Druckmesstechnik GmbH
Londoner Strasse 25
48455 Bad Bentheim

Datum der Kal.: 30.08.2016
Bearbeiter: H. Plescher
Seite: 5 von 5

7. Kennzeichnung

Der Kalibriergegenstand wurde mit einem Kalibrieraufkleber mit der Nr. WK-06449 gekennzeichnet.

8. Bemerkung

Die Werkskalibrierung verliert ihre Gültigkeit, wenn Einstellungen am Kalibriergegenstand verändert werden, Manipulationen durchgeführt werden, die zum Verlust der voreingestellten Parameter führen können oder Sicherungsmarken oder Plomben entfernt werden.

Ende der Eintragung

ANNEX XVI Calibration certificate for DN50 Coriolis flowmeter

Flow Calibration with Adjustment

10734351-3851071

3023379552

Purchase order number

DE-3005578288-20 / Endress+Hauser Flowtec AG

Order N°/Manufacturer

83F50-7WA2/0

Order code

PROMASS 83 F DN50 / 2"

Transmitter/Sensor

L6075202000

Serial N°

-

Tag N°

FCP-7.1.5

Calibration rig

15000 kg/h (Δ 100%)

Calibrated full scale

Service interface

Calibrated output

1.9215

Calibration factor

-17

Zero point

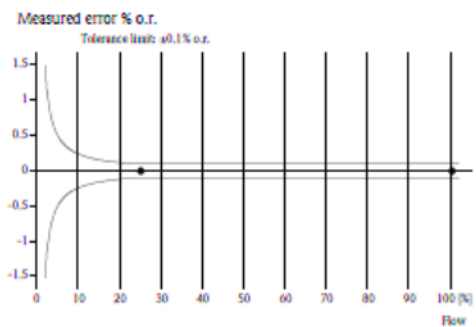
25.2 °C

Water temperature

Flow (%)	Flow (kg/h)	Duration (s)	m target (kg)	m meas. (kg)	Δ o.r.* (%)	Outp.** (mA)
24.8	3724.28	30.4	31.465	31.465	0.00	7.97
24.8	3725.97	30.4	31.481	31.481	0.00	7.97
100.4	15058.0	30.4	127.176	127.182	0.00	20.06
100.4	15062.2	30.4	127.259	127.251	-0.01	20.07
-	-	-	-	-	-	-
-	-	-	-	-	-	-
-	-	-	-	-	-	-
-	-	-	-	-	-	-
-	-	-	-	-	-	-
-	-	-	-	-	-	-

*o.r.: of reading

**Calculated value (4 - 20 mA)



For detailed data concerning output specifications of the unit under test, see Technical Information (TI), chapter Performance characteristics.

Traceability to the national standard for all test instruments used for the calibration is guaranteed.

Endress+Hauser Flowtec operates ISO/IEC 17025 accredited calibration facilities in Reinach (CH), Cernay (FR), Greenwood (USA), Aurangabad (IN) and Suzhou (CN).



15.06.2016

Date of calibration

 Endress+Hauser Flowtec AG
 Köpferstrasse 7 / Rue de l'Europe 35
 CH-4153 Reinach / F-68700 Cernay

Z. Velickovic

Operator

 Certified acc. to
 ISO 9001

ANNEX XVII Calibration certificate for DN525 Coriolis flowmeter

Flow Calibration with Adjustment

10734300-3851022

3023379552

Purchase order number

DE-3005578288-10 / Endress+Hauser Flowtec AG

Order N°/Manufacturer

83F25-7091/0

Order code

PROMASS 83 F DN25 / 1"

Transmitter/Sensor

L6074902000

Serial N°

-

Tag N°

FCP-6.5

Calibration rig

3600 kg/h

(± 100%)

Calibrated full scale

Service interface

Calibrated output

2.0524

Calibration factor

11

Zero point

25.1 °C

Water temperature

Flow (%)	Flow (kg/h)	Duration (s)	m target (kg)	m meas. (kg)	Δ o.z.* (%)	Outp.** (mA)
24.6	886.765	85.2	20.990	20.989	0.00	7.94
24.6	886.662	85.2	20.988	20.984	-0.02	7.94
99.7	3588.46	30.2	30.114	30.112	0.00	19.95
99.7	3590.41	30.2	30.129	30.129	0.00	19.96
-	-	-	-	-	-	-
-	-	-	-	-	-	-
-	-	-	-	-	-	-
-	-	-	-	-	-	-
-	-	-	-	-	-	-
-	-	-	-	-	-	-

*o.z.: of reading

**Calculated value (4 - 20 mA)

Measured error % o.r.

Tolerance limit: ±0.1% o.z.



For detailed data concerning output specifications of the unit under test, see Technical Information (TI), chapter Performance characteristics.

Traceability to the national standard for all test instruments used for the calibration is guaranteed.

Endress+Hauser Flowtec operates ISO/IEC 17025 accredited calibration facilities in Reinach (CH), Cernay (FR), Greenwood (USA), Aurangabad (IN) and Suzhou (CN).

15.06.2016

Date of calibration

 Endress+Hauser Flowtec AG
 Kägenstrasse 7 / Rue de l'Europe 35
 CH-4153 Reinach / F-68700 Cernay

A. Punzo

Operator

 Certified acc. to
 ISO 9001

ANNEX XVIII Equations for the proposed method to determine the rupture disk discharge area.

- I. The full *Reader-Harris/Gallagher 1996 equation* (Reader-Harris, 2015; Reader-Harris & Sattary, 1996)

$$\begin{aligned}
 C_d = & 0.5961 + 0.0261 \cdot \beta_{eff}^2 - 0.216 \cdot \beta_{eff}^8 + 0.000521 \left(\frac{10^6 \cdot \beta_{eff}}{Re_u} \right)^{0.7} \\
 & + (0.0188 + 0.0063 \cdot A_1) \beta_{eff}^{3.5} \cdot \max \left\{ \left(\frac{10^6}{Re_u} \right)^{0.3}, 22.7 - 4700 \cdot \left(\frac{Re_u}{10^6} \right) \right\} \\
 & + (0.043 + 0.08e^{-10L_1} - 0.123e^{-7L_1}) \cdot (1 - 0.11A_1) \cdot \frac{\beta_{eff}^4}{1 - \beta_{eff}^4} - 0.031 \cdot \\
 & (M_2 - 0.8M_2^{1.1}) \left\{ 1 + 8 \max \left(\lg \left(\frac{3700}{Re_u} \right), 0.0 \right) \right\} \beta_{eff}^{1.3} + 0.011(0.75 - \beta_{eff})
 \end{aligned} \tag{A-11}$$

with

$$L_1 = L_2 = \frac{D_n}{2} \quad \text{and} \quad M_2 = \frac{2 \cdot L_2}{1 - \beta_{eff}}$$

- II. The *Urner 1997 equation* (Urner, 1997)

This equation is also part of ISO 5167-2 (ISO, 2003) which is a working standard for flow measurement with sharp-edged orifice and is also referenced in recent work by (Reader-Harris, 2015).

$$K_R = \left[\frac{\sqrt{1 - \beta_{eff}^4} \cdot (1 - C_d^2)}{C_d \cdot \beta_{eff}^2} - 1 \right] \tag{A-12}$$

ANNEX XIX The derivation of the dischargeable mass flow rate relationship with gas flow

Restriction of flow in a rupture disk is important in the determination of the dischargeable mass flow rate. Looking at Figure 92 The measurement of a rupture disk flow restriction, $\Phi = A_i / A_{RD}$ with experimental apparatus is not trivial. It is however theoretically possible to model flow restriction in a rupture disk assuming a near-circular bore with a large diameter ratio. A rupture disk is assumed to cause separation of flow from location (u) to an unknown location (i) as illustrated by light-green dotted line in Figure 92.

Annex XIX-A Control volume

A control volume I (which is marked with a green dash-line) is the region between location (u) and (i). Separated flow in the control volume is modeled with two nozzles upstream of an abrupt expansion. The first nozzle is between (u) and (RD) while the second nozzle is between (RD) and (i).

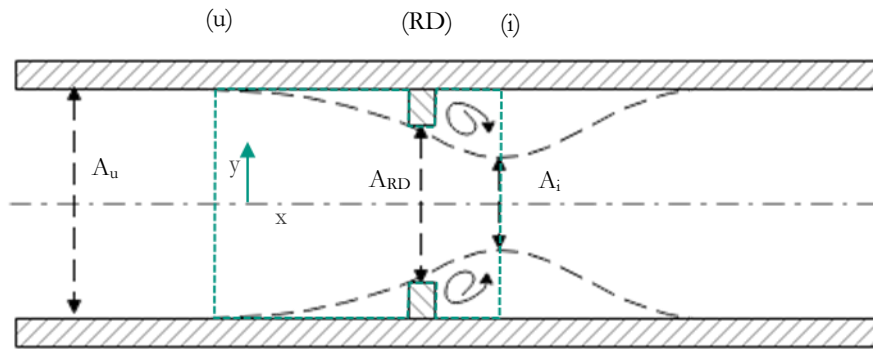


Figure 92 Illustration a control volume assuming a near-circular bore with large area ratio

Annex XIX-B Polytropic equation of state

The equation of state for assuming ideal gas is per eq.(A-13) (Levenspiel, 1998).

$$\frac{1}{\rho} = \frac{R \cdot T}{P} \quad (\text{A-13})$$

The general relationship for density ratio and pressure ratio between (u) and (i) for isentropic flow is per eq.(A-14)

$$\frac{\bar{\rho}_u}{\bar{\rho}_i} = \left(\frac{\bar{P}_u}{\bar{P}_i} \right)^{1/\kappa} = \frac{1}{\eta_i^{1/\kappa}} \quad (\text{A-14})$$

The general relationship for the temperature ratio and pressure ratio between (u) and (i) is per eq.(A-15)

$$\frac{\bar{T}_i}{\bar{T}_u} = \left(\frac{\bar{P}_i}{\bar{P}_u} \right)^{\frac{\kappa-1}{\kappa}} = \eta_i^{\frac{\kappa-1}{\kappa}} \quad (\text{A-15})$$

If the flow between (u) and (i) is taken to be isentropic change of enthalpy between (u) and (i) is per eq.(A-16) (Rivas-Nass, 1992)

$$\begin{aligned} db &= \bar{C}_p \cdot dT \\ \Delta b_{u-i} &= b_i - b_u = \bar{C}_p \cdot (\bar{T}_i - \bar{T}_u) \\ \Delta b_{u-i} &= \bar{C}_p \cdot \bar{T}_u \left(\frac{\bar{T}_i}{\bar{T}_u} - 1 \right) = \frac{\kappa}{\kappa-1} \cdot R \cdot \bar{T}_u \cdot \left(\frac{\bar{T}_i}{\bar{T}_u} - 1 \right) \end{aligned} \quad (\text{A-16})$$

Annex XIX-C **Mass balance in control volume I**

Mass balance in the control volume gives an additional relationship for change of thermodynamic properties between (u), (RD) and (i), and (out).

$$Q_m = A_u \cdot \bar{\rho}_u \cdot \bar{w}_u = A_{RD} \cdot \bar{\rho}_{RD} \cdot \bar{w}_{RD} = A_i \cdot \bar{\rho}_i \cdot \bar{w}_i = const \quad (\text{A-17})$$

Applying geometric relationships for the area ratio, and restriction factor results in the relationship for the velocity ratio between (u) and (i)

$$\begin{aligned} \frac{\bar{w}_i}{\bar{w}_u} &= \frac{A_u \cdot \bar{\rho}_u}{A_i \cdot \bar{\rho}_i} \\ \sigma_{RD} &= \frac{A_{RD}}{A_u} \text{ and } \phi = \frac{A_i}{A_{RD}} \text{ and } A_i = \phi \cdot A_{RD} = \phi \cdot \sigma_{RD} \cdot A_u \\ \frac{\bar{w}_i}{\bar{w}_u} &= \frac{\bar{\rho}_u}{\bar{\rho}_i} \cdot \frac{A_u}{A_i} = \frac{\bar{\rho}_u}{\bar{\rho}_i} \cdot \frac{A_u}{\phi \cdot A_{RD}} = \frac{\bar{\rho}_u}{\bar{\rho}_i} \cdot \frac{A_u}{\phi \cdot \sigma_{RD} \cdot A_u} = \frac{\bar{\rho}_u}{\bar{\rho}_i} \cdot \frac{1}{\phi \cdot \sigma_{RD}} \\ \frac{\bar{w}_i}{\bar{w}_u} &= \frac{\bar{\rho}_u}{\bar{\rho}_i} \cdot \frac{1}{\phi \cdot \sigma_{RD}} \text{ with } G_u = \bar{\rho}_u \cdot \bar{w}_u \\ \bar{w}_i &= \frac{G_u}{\bar{\rho}_i} \cdot \frac{1}{\phi \cdot \sigma_{RD}} \end{aligned} \quad (\text{A-18})$$

Annex XIX-D **Energy balance**

If energy losses due to gravity with gas flow are neglected in the control volume, then the energy balance is per eq.(A-19)

$$\frac{(\bar{w}_i^2 - \bar{w}_u^2)}{2} + \Delta h_{u-i} = 0 \text{ with } \Delta h_{u-i} = (h_i - h_u) \quad (\text{A-19})$$

Factoring eq.(A-18) into eq.(A-19) and algebraically rearranging it results to eq.(A-20)

$$\begin{aligned} \frac{(\bar{w}_i^2 - \bar{w}_u^2) \bar{\rho}_u^2}{2 \cdot \bar{\rho}_u^2 \cdot \bar{C}_p \cdot \bar{T}_u} + \frac{\Delta h_{u-i}}{\bar{C}_p \cdot \bar{T}_u} &= 0 \\ \frac{(\bar{w}_i^2 \cdot \bar{\rho}_u^2 - \bar{w}_u^2 \cdot \bar{\rho}_u^2)}{2 \cdot \bar{\rho}_u^2 \cdot \bar{C}_p \cdot \bar{T}_u} + \frac{(h_i - h_u)}{\bar{C}_p \cdot \bar{T}_u} &= 0 \\ \frac{(\bar{w}_i^2 \cdot \bar{\rho}_u^2)}{2 \cdot \bar{\rho}_u^2 \cdot \bar{C}_p \cdot \bar{T}_u} - \frac{(\bar{w}_u^2 \cdot \bar{\rho}_u^2)}{2 \cdot \bar{\rho}_u^2 \cdot \bar{C}_p \cdot \bar{T}_u} + \frac{\Delta h_{u-i}}{\bar{C}_p \cdot \bar{T}_u} &= 0 \\ \frac{G_u^2}{\bar{\rho}_i^2} \cdot \frac{1}{\phi^2 \cdot \sigma_{RD}^2} \cdot \frac{\bar{\rho}_u^2}{2 \cdot \bar{\rho}_u^2 \cdot \bar{C}_p \cdot \bar{T}_u} - \frac{G_u^2}{2 \cdot \bar{\rho}_u^2 \cdot \bar{C}_p \cdot \bar{T}_u} + \frac{\Delta h_{u-i}}{\bar{C}_p \cdot \bar{T}_u} &= 0 \\ \frac{G_u^2}{2 \cdot \bar{\rho}_u^2 \cdot \bar{C}_p \cdot \bar{T}_u} \cdot \left[\frac{1}{\phi^2 \cdot \sigma_{RD}^2} \cdot \frac{\bar{\rho}_u^2}{\bar{\rho}_i^2} - 1 \right] + \frac{1}{\bar{C}_p \cdot \bar{T}_u} \cdot \Delta h_{u-i} &= 0 \end{aligned} \quad (\text{A-20})$$

Annex XIX-E **Coupling of mass and energy balance with polytropic equation of state**

Eq.(A-16) is now reformulated with eq.(A-15) per eq.(A-21)

$$\Delta h_{u-i} = h_i - h_u = \frac{\kappa}{\kappa-1} \cdot \frac{\bar{P}_u}{\bar{\rho}_u} \cdot \left(\eta_i^{\frac{\kappa-1}{\kappa}} - 1 \right) \quad (\text{A-21})$$

Inserting the definition of the enthalpy drop per eq.(A-21) into eq.(A-20) yields eq.(A-22)

$$\begin{aligned} \frac{G_u^2}{2 \cdot \bar{\rho}_u^2 \cdot \bar{C}_p \cdot \bar{T}_u} \cdot \left[\frac{1}{\phi^2 \cdot \sigma_{RD}^2} \cdot \frac{\bar{\rho}_u^2}{\bar{\rho}_i^2} - 1 \right] + \frac{1}{\bar{C}_p \cdot \bar{T}_u} \cdot \frac{\kappa}{\kappa-1} \cdot \frac{\bar{P}_u}{\bar{\rho}_u} \cdot \left(\eta_i^{\frac{\kappa-1}{\kappa}} - 1 \right) &= 0 \\ \frac{G_u^2}{2 \cdot \bar{\rho}_u^2 \cdot \bar{C}_p \cdot \bar{T}_u} \cdot \left[\frac{1}{\phi^2 \cdot \sigma_{RD}^2} \cdot \frac{\bar{\rho}_u^2}{\bar{\rho}_i^2} - 1 \right] = \frac{1}{\bar{C}_p \cdot \bar{T}_u} \cdot \frac{\kappa}{\kappa-1} \cdot \frac{\bar{P}_u}{\bar{\rho}_u} \cdot \left(1 - \eta_i^{\frac{\kappa-1}{\kappa}} \right) & \\ \frac{G_u^2}{\bar{\rho}_u^2} \cdot \left[\frac{1}{\phi^2 \cdot \sigma_{RD}^2} \cdot \frac{\bar{\rho}_u^2}{\bar{\rho}_i^2} - 1 \right] = \frac{2 \cdot \kappa}{\kappa-1} \cdot \frac{\bar{P}_u}{\bar{\rho}_u} \cdot \left(1 - \eta_i^{\frac{\kappa-1}{\kappa}} \right) & \end{aligned} \quad (\text{A-22})$$

Further algebraic arrangement of eq.(A-22) with eq.(A-14) yields the general relationship that accounts for changes in thermodynamic properties between (u) and (i) due to the presence of a flow-restricting pipe element in between per eq.(A-24).

$$\frac{G_u^2}{\bar{\rho}_u^2} \cdot \left[\frac{1}{\phi^2 \cdot \sigma_{RD}^2} \cdot \frac{1}{\eta_i^{2/\kappa}} - 1 \right] = \frac{2 \cdot \kappa}{\kappa - 1} \cdot \frac{\bar{P}_u}{\bar{\rho}_u} \cdot \left(1 - \eta_i^{\frac{\kappa-1}{\kappa}} \right) \quad (A-23)$$

$$\frac{G_u^2}{1 \cdot 1} \cdot \left[\frac{1}{\phi^2 \cdot \sigma_{RD}^2} \cdot \frac{1}{\eta_i^{2/\kappa}} - \frac{\phi^2 \cdot \sigma_{RD}^2 \cdot \eta_i^{2/\kappa}}{\phi^2 \cdot \sigma_{RD}^2 \cdot \eta_i^{2/\kappa}} \right] = \frac{2 \cdot \kappa}{\kappa - 1} \cdot \frac{\bar{P}_u \cdot \bar{\rho}_u}{1} \cdot \left(1 - \eta_i^{\frac{\kappa-1}{\kappa}} \right)$$

Eq.(A-23) is simplified algebraically further by collecting the like terms yielding eq.(A-24)

$$\frac{G_u^2}{\bar{P}_u \cdot \bar{\rho}_u \cdot \phi^2 \cdot \sigma_{RD}^2 \cdot \eta_i^{2/\kappa}} \cdot \left[1 - \phi^2 \cdot \sigma_{RD}^2 \cdot \eta_i^{2/\kappa} \right] = \frac{2 \cdot \kappa}{\kappa - 1} \cdot \left(1 - \eta_i^{\frac{\kappa-1}{\kappa}} \right) \quad (A-24)$$

$$\frac{G_u^2}{\bar{P}_u \cdot \bar{\rho}_u \cdot \phi^2 \cdot \sigma_{RD}^2 \cdot \eta_i^{2/\kappa}} = \frac{2 \cdot \kappa}{\kappa - 1} \cdot \frac{\left(1 - \eta_i^{\frac{\kappa-1}{\kappa}} \right)}{\left[1 - \phi^2 \cdot \sigma_{RD}^2 \cdot \eta_i^{2/\kappa} \right]}$$

Annex XIX-F *Equation for the rupture disk flow restriction with high-velocity flow*

Eq.(A-24) is rearranged conveniently yielding the equation for rupture disk flow restriction, Φ is per eq.(A-25)

$$\frac{Q_m^2}{\bar{\rho}_u^2 \cdot A_u^2 \cdot \phi^2 \cdot \sigma_{RD}^2 \cdot \eta_i^{2/\kappa}} = \frac{2 \cdot \kappa}{\kappa - 1} \cdot \frac{\bar{P}_u}{\bar{\rho}_u} \cdot \frac{\left(1 - \eta_i^{\frac{\kappa-1}{\kappa}} \right)}{\left[1 - \phi^2 \cdot \sigma_{RD}^2 \cdot \eta_i^{2/\kappa} \right]}$$

$$\phi^2 = \frac{Q_m^2}{\bar{\rho}_u^2 \cdot A_u^2 \cdot \sigma_{RD}^2 \cdot \eta_i^{2/\kappa}} \cdot \left(\frac{2 \cdot \kappa}{\kappa - 1} \cdot \frac{\bar{P}_u}{\bar{\rho}_u} \cdot \frac{\left(1 - \eta_i^{\frac{\kappa-1}{\kappa}} \right)}{\left[1 - \phi^2 \cdot \sigma_{RD}^2 \cdot \eta_i^{2/\kappa} \right]} \right)^{-1} \quad (A-25)$$

$$\phi = \frac{Q_m}{\bar{\rho}_u \cdot A_u \cdot \sigma_{RD} \cdot \eta_i^{1/\kappa}} \cdot \left(-\Delta h_i \cdot \frac{2}{\left[1 - \phi^2 \cdot \sigma_{RD}^2 \cdot \eta_i^{2/\kappa} \right]} \right)^{-\frac{1}{2}}$$

Annex XIX-G *Equation for mass flow rate through a rupture disk*

Eq.(A-24) is rearranged conveniently in terms of Q_m per eq. (A-26)

$$\frac{G_u^2}{\bar{P}_u \cdot \bar{\rho}_u \cdot \phi^2 \cdot \sigma_{RD}^2} = \frac{2 \cdot \kappa}{\kappa - 1} \cdot \frac{\eta_i^{2/\kappa} \cdot \left(1 - \eta_i^{\frac{\kappa-1}{\kappa}}\right)}{\left[1 - \phi^2 \cdot \sigma_{RD}^2 \cdot \eta_i^{2/\kappa}\right]} \quad (\text{A-26})$$

$$\frac{Q_m^2}{\bar{\rho}_u^2 \cdot A_u^2 \cdot \phi^2 \cdot \sigma_{RD}^2 \cdot \eta_i^{2/\kappa}} = \frac{2 \cdot \kappa}{\kappa - 1} \cdot \frac{\bar{P}_u}{\bar{\rho}_u} \cdot \frac{\left(1 - \eta_i^{\frac{\kappa-1}{\kappa}}\right)}{\left[1 - \phi^2 \cdot \sigma_{RD}^2 \cdot \eta_i^{2/\kappa}\right]}$$

Eq.(A-26) is rearranged conveniently yielding the equation for the mass flow rate across a rupture disk, Q_m per eq.(A-27)

$$Q_m = \bar{\rho}_u \cdot A_u \cdot \phi \cdot \sigma_{RD} \cdot \eta_i^{1/\kappa} \cdot \left(\frac{\kappa}{\kappa - 1} \cdot \frac{\bar{P}_u}{\bar{\rho}_u} \cdot \left(1 - \eta_i^{\frac{\kappa-1}{\kappa}}\right) \cdot \frac{2}{\left[1 - \phi^2 \cdot \sigma_{RD}^2 \cdot \eta_i^{2/\kappa}\right]} \right)^{\frac{1}{2}} \quad (\text{A-27})$$

$$Q_m = \bar{\rho}_u \cdot A_u \cdot \phi \cdot \sigma_{RD} \cdot \eta_i^{1/\kappa} \cdot \left(-\Delta h_{u-i} \cdot \frac{2}{\left[1 - \phi^2 \cdot \sigma_{RD}^2 \cdot \eta_i^{2/\kappa}\right]} \right)^{\frac{1}{2}}$$

ANNEX XX Recommendations for rupture disk performance testing

- i. The rupture disk device should be characterized by the following characteristic numbers:
 - a. Rupture disk free relieving area A_{RD}
 - b. Rupture disk zero-velocity minor loss coefficient, $K_{RD,0}$ for gas service
 - c. Rupture disk incompressible minor loss coefficient $K_{RD,0,tp}$ for liquid and two-phase service
- ii. Rupture disk free relieving area A_{RD} per eq.(40) and zero-velocity minor loss coefficient, $K_{RD,0}$ per eq.(40) should be determined from the same experiment with low-velocity flow with Mach number upstream of the rupture disk, $Ma_u < 0.30$ and $Re_u > 105$ and taken to be constant for a rupture disk type, and nominal pipe size.
- iii. Rupture disk incompressible minor loss coefficient $K_{RD,0,tp}$ per eq.(80) should be determined with gas mass flow quality upstream of rupture disk $x_g < 0.3$ and taken to be constant for a rupture disk type, and nominal pipe size.
- iv. The test-section with its instrumentation is recommended for consideration as the standard test section for determining the three rupture disk characteristic numbers mentioned above. Rupture disks can be tested on the same test section, and with the same measurement and instrumentation with liquids, two-phase flow and gases.
- v. Small diameter rupture disk with a nominal pipe size less than DN40 may be tested with the test section in this work.
- vi. Large diameter rupture disk with nominal pipe size larger than DN40 should be tested with shorter test sections, such as the one proposed in (Mutegi, 2014) since the dimensions of the test-section used in this work are otherwise impracticable.

ANNEX XXI Calculation of the gas void fraction in Mathcad

The detailed work by (Bhagwat & Ghajar, 2014) introduces a flow-pattern independent void fraction, ϵ_{ip} , that is valid generally. This two-phase mixture void fraction, ϵ_{ip} formulation is key because it significantly simplifies two-phase flow. It is the first general flow pattern-based model available in literature that does not require flow maps at all. It also considers the inclination of the pipe. Since it is a drift-flux based model, it is independent of the slip velocity. Therefore, function to calculate ϵ_{ip} is formulated in MatchCAD with the method and equations in (Bhagwat & Ghajar, 2014) as follows:

Theory inputs

General formulation of void fraction per Thome/Cioncolini, BII, chap 04, p19,eq. 26
superficial velocity of gas phase
Cioncolini, 2015 eq.27

$$U_{sg}(x_g, Q_{m_gl}, D_i, p, T) := \frac{x_g \cdot q_m(Q_{m_gl}, D_i)}{\rho_g(p, T)}$$

superficial velocity of liquid phase
Cioncolini, 2015 eq.27

$$U_{sl}(x_g, Q_{m_gl}, D_i, p, T) := \frac{(1-x_g) \cdot q_m(Q_{m_gl}, D_i)}{\rho_l(p, T)}$$

two-phase mixture velocity
Awad Two-Phase Flow, Chap 11, 2012, eq.13

$$U_m(x_g, Q_{m_gl}, D_i, p, T) := U_{sg}(x_g, Q_{m_gl}, D_i, p, T) + U_{sl}(x_g, Q_{m_gl}, D_i, p, T)$$

two-phase mixture Reynolds number
Bhagwat & Ghajar 2014 eq.14

$$Re_{ip_Bhagwat}(x_g, Q_{m_gl}, D_i, p, T) := \frac{U_m(x_g, Q_{m_gl}, D_i, p, T) \cdot \rho_l(p, T) \cdot D_i}{\eta_l(p, T)}$$

Gas volumetric flow fraction,
Bhagwat & Ghajar 2014 eq.15

$$\beta_{fg}(x_g, Q_{m_gl}, D_i, p, T) := \frac{U_{sg}(x_g, Q_{m_gl}, D_i, p, T)}{U_{sg}(x_g, Q_{m_gl}, D_i, p, T) + U_{sl}(x_g, Q_{m_gl}, D_i, p, T)}$$

Two-phase fanning friction factor
Bhagwat & Ghajar 2014 eq.13

$$f_{tp_iter}(x_g, Q_{m_gl}, D_i, p, T, k_r, f_{tp}) := \left(-4 \cdot \log \left(\frac{k_r}{3.7 D_i} + \frac{1.256}{Re_{ip_Bhagwat}(x_g, Q_{m_gl}, D_i, p, T) \cdot (f_{tp})^{0.5}} \right) \right)^{-2}$$

$$f_{tp_x} := 0.01$$

$$f_{tp}(x_g, Q_{m_gl}, D_i, p, T, k_{pipe}) := \text{root}(f_{tp_x} - f_{tp_iter}(x_g, Q_{m_gl}, D_i, p, T, k_{pipe}, f_{tp_x}), f_{tp_x})$$

$$\lambda_{tp}(x_g, Q_{m_gl}, D_i, p, T, k_{pipe}) := 4 \cdot f_{tp}(x_g, Q_{m_gl}, D_i, p, T, k_{pipe}) \quad \text{formulation to Darcy form}$$

Constant in eq. 11
0.2 for circular/annular pipes
0.4 for rectangular pipes
Bhagwat & Ghajar 2014 eq.11
 $C_1 := 0.2$

Bhagwat & Ghajar 2014 eq.11

$$C_{01_sort}(x_g, Q_{m_gl}, D_i, p, T) := \left(C_1 - C_1 \cdot \left(\frac{\rho_g(p, T)}{\rho_l(p, T)} \right)^{0.5} \right) \cdot \left((2.6 - \beta_{fg}(x_g, Q_{m_gl}, D_i, p, T))^{0.15} - (f_{tp}(x_g, Q_{m_gl}, D_i, p, T, k_{pipe}))^{0.5} \right) \cdot (1 - x_g)^{1.5}$$

Bhagwat & Ghajar 2014 eq.8
Froude number based in the superficial gas velocity

$$Fr_{sg}(x_g, Q_{m_gl}, D_i, p, T, \theta) := \left(\frac{\rho_g(p, T)}{\rho_l(p, T) - \rho_g(p, T)} \right)^{0.5} \cdot \frac{U_{sg}(x_g, Q_{m_gl}, D_i, p, T)}{(g \cdot D_i \cdot \cos(\theta))^{0.5}}$$

Term in eq. 12
Bhagwat & Ghajar 2014 eq.11

$$C_{01}(x_g, Q_{m_gl}, D_i, p, T, \theta) := \begin{cases} \text{if } 0 \text{ deg} \leq \theta \leq 50 \text{ deg} \wedge Fr_{sg}(x_g, Q_{m_gl}, D_i, p, T, \theta) \leq 0.1 \\ 0 \\ \text{else} \\ C_{01_sort}(x_g, Q_{m_gl}, D_i, p, T) \end{cases}$$

eq. 10

Bhagwat & Ghajar 2014 eq.10

$$C_0(x_g, Q_{m_gl}, D_i, p, T, \theta, \alpha) := \frac{2 - \left(\frac{\rho_g(p, T)}{\rho_l(p, T)}\right)^2}{1 + \left(\frac{Re_{tp_Bhagwat}(x_g, Q_{m_gl}, D_i, p, T)}{1000}\right)^2} + \frac{\left(\frac{1 + \left(\frac{\rho_g(p, T)}{\rho_l(p, T)}\right) \cdot \cos(\theta)}{1 + \cos(\theta)}\right)^{(1-\alpha)^{\frac{2}{5}}}}{1 + \left(\frac{1000}{Re_{tp_Bhagwat}(x_g, Q_{m_gl}, D_i, p, T)}\right)^2} + C_{01}(x_g, Q_{m_gl}, D_i, p, T, \theta)$$

Term in eq. 16

Bhagwat & Ghajar 2014 eq.17

$$C_2(p, T) := \begin{cases} \left\| \frac{\eta_l(p, T)}{Pa \cdot s} \right\| & \text{if } \frac{Pa \cdot s}{0.001} > 10 \\ \left\| \left(\frac{0.434}{\log\left(\frac{Pa \cdot s}{0.001}\right)} \right)^{0.15} \right\| & \\ \left\| 1 \right\| & \text{else} \end{cases}$$

Laplace variable in eq. 18

Bhagwat & Ghajar 2014

$$La(D_i, p, T) := \frac{\left(\frac{\sigma_{sl}(p, T)}{g \cdot (\rho_l(p, T) - \rho_g(p, T))}\right)^{0.5}}{D_i}$$

Term in eq. 16

Bhagwat & Ghajar 2014 eq.18

$$C_3(D_i, p, T) := \begin{cases} \left\| \left(\frac{La(D_i, p, T)}{0.025} \right)^{0.9} \right\| & \text{if } La(D_i, p, T) < 0.025 \\ \left\| 1 \right\| & \text{else} \end{cases}$$

$$C_4(x_g, Q_{m_gl}, D_i, p, T, \theta) := \begin{cases} \left\| -1 \right\| & \text{if } 0 \leq deg < \theta \leq -50 \text{ deg} \wedge Fr_{sg}(x_g, Q_{m_gl}, D_i, p, T, \theta) \leq 0.1 \\ \left\| 1 \right\| & \text{else} \end{cases}$$

Drift velocity

Bhagwat & Ghajar 2014 eq.16

$$U_{drift}(x_g, Q_{m_gl}, D_i, p, T, \theta, \alpha) := (0.35 \sin(\theta) + 0.45 \cos(\theta)) \cdot \left(\frac{g \cdot D_i \cdot (\rho_l(p, T) - \rho_g(p, T))}{\rho_l(p, T)}\right)^{0.5} \cdot (1-\alpha)^{0.5} \cdot C_2(p, T) \cdot C_3(D_i, p, T) \cdot C_4(x_g, Q_{m_gl}, D_i, p, T, \theta)$$

Iteration and solving for void fraction

two-phase void fraction

Cioncolini, 2015 eq.26 equivalent to Bhagwat & Ghajar 2014 eq.1

$$\alpha_{iter}(x_g, Q_{m_gl}, D_i, p, T, \theta, \alpha) := \frac{U_{sg}(x_g, Q_{m_gl}, D_i, p, T)}{C_0(x_g, Q_{m_gl}, D_i, p, T, \theta, \alpha) \cdot (U_{sl}(x_g, Q_{m_gl}, D_i, p, T) + U_{sg}(x_g, Q_{m_gl}, D_i, p, T)) + U_{drift}(x_g, Q_{m_gl}, D_i, p, T, \theta, \alpha)}$$

$$\alpha_{tp_x} := 0.01$$

$$\alpha_{tp}(x_g, Q_{m_gl}, D_i, p, T, \theta) := \text{root}(\alpha_{tp_x} - \alpha_{iter}(x_g, Q_{m_gl}, D_i, p, T, \theta, \alpha_{tp_x}), \alpha_{tp_x})$$

$$\varepsilon_{tp}(x_g, Q_{m_gl}, D_i, p, T, \theta) := \alpha_{tp}(x_g, Q_{m_gl}, D_i, p, T, \theta)$$

Publications and conferences

#	Duration	Type	Title and Description
(1)	12.11.2014 - 13.11.2014	Diploma Degree	“Development of a test facility for safety devices for multiphase flow”, Engler-Bunte-Institut, Karlsruhe Institut of Technology
(2)	10.06.2015 - 12.06.2015	Conference	“Experimental Investigation and Modeling of Rupture Disk Vent Line Systems in Two-Phase Gas/Liquid Flow” Joint US and European DIERS User Group Meeting, Düsseldorf, 2015
(3)	25.04.2016 - 27.04.2016	Conference	“Experimentelle Untersuchung und Modellierung des Massenstroms durch Berstscheiben-Abblaseleitungen bei kompressiblen Strömungen”, 3. Wangerooger Sicherheitstage, 2016
(4)	05.06.2016 - 08.06.2016	Conference	“Challenges in sizing rupture disk devices especially for compressible two-phase flow” presented at the 15 th International Symposium on Loss Prevention and Safety Promotion in the Process Industries, Freiburg, 2016
(5)	2016	Publication	Mutegi, M. K., & Schmidt, J. (2016). “Challenges in Sizing Rupture Disk Vent Line Systems Especially for Compressible Two-phase Flow.” Chemical Engineering Transactions, 48, 631-636. DOI:10.3303/CET1648106
(6)	16.11.2017 - 17.11.2017	Conference	“Experimentelle Untersuchung von Blenden als Ersatzmodell für die Berechnung des Massenstroms durch Berstscheiben” presented at the 13. Fachtagung Anlagen-, Arbeits- und Umweltsicherheit in Köthen
(7)	23.04.2018 - 25.04.2018	Conference	“Ersatzmodell für die Berechnung des Massenstroms durch Berstscheiben Teil I Druckabfall”, CSE-Sicherheitstage 2018
(8)	09.09.2018 - 13.09.2018	Conference	“On the High-Velocity Compressible Gas Flow Pressure-drop in a Rupture Disk Relief Line”, presented at the 12th European Fluid Mechanics Conference in Vienna, Austria.
(9)	23.10.2018 - 25.10.2018	Conference	“Sizing Rupture Disk Vent Line Systems for High-Velocity Gas Flows Part 1: Pressure profile in a pipe with rupture disk device installed” , presented at the Mary Kay O'Connor Process Safety Center International Symposium, "Beyond Regulatory Compliance, Making Safety Second Nature" In Association with IChem in College Station, TX, US
(10)	22.05.2019 - 24.05.2019	Conference	“Sizing Rupture Disk Vent Line Systems for Two-Phase Flows”, presented at the 2019 Joint DIERS User Group Meeting in Karlsruhe, Germany.
(11)	2019	Publication	Mutegi, M. K., Schmidt, J., & Denecke, J. (2019). Sizing Rupture Disk Vent Line Systems for High-velocity Gas Flows. Journal of Loss Prevention in the Process Industries, 62. DOI: https://doi.org/10.1016/j.jlp.2019.103950

Curriculum vitae

Surname Mutegi
Name Mondie Kimandi

Education

2006-2014
Chemical Engineering
Karlsruhe Institute of Technology (KIT), Karlsruhe, Germany.

Scientific Experience

Since October 2014
Project Engineer
REMBE® GmbH Safety + Control GmbH, Brilon Germany.

2015 - 2020
Research Scientist
CSE Center of Safety Excellence gGmbH (CSE-Institut), Pfinztal, Germany.

2015 - 2020
External Ph.D Student
The Department of Mechanical and Process Engineering at the University of
Kaiserslautern, Germany.